PERFORMANCE OF ULTRA-HIGH PERFORMANCE FIBRE REINFORCED CONCRETE PLATES UNDER IMPACT LOADS

by

Hesham Adel Bassuni Othman

M.Sc., Menofiya University, Egypt, 2011
B.Sc. (Hons), Zagazig University, Egypt, 2004

A dissertation

presented to Ryerson University

in partial fulfillment of the

requirements for the degree of

Doctor of Philosophy

in the program of

Civil Engineering

Toronto, Ontario, Canada, 2016

AUTHOR'S DECLARATION

I hereby declare that I am the sole author of this dissertation. This is a true copy of the dissertation, including any required final revisions, as accepted by my examiners.

I authorize Ryerson University to lend this dissertation to other institutions or individuals for the purpose of scholarly research

I further authorize Ryerson University to reproduce this dissertation by photocopying or by other means, in total or in part, at the request of other institutions or individuals for the purpose of scholarly research.

I understand that my dissertation may be made electronically available to the public.

ABSTRACT

PERFORMANCE OF ULTRA-HIGH PERFORMANCE FIBRE REINFORCED CONCRETE PLATES UNDER IMPACT LOADS

Hesham Othman

Doctor of Philosophy, Civil Engineering

Ryerson University, Toronto, 2016

The next generation of concrete, Ultra-High Performance Fibre Reinforced Concrete (UHP-FRC), exhibits exceptional mechanical characteristics. UHP-FRC has a compressive strength exceeding 150 MPa, tensile strength in the range of 8-12 MPa, and fracture energy of several orders of magnitudes of traditional concrete. The focus of this research is to investigate and analyze the advantage of using UHP-FRC in impact resistance structures. To achieve these goals, two experimental testing programs and major numerical investigations have been conducted.

The material experimental investigation has been conducted to determine the effects of strain rate on UHP-FRC. Two parameters are investigated, namely: compressive strength (80, 110, 130, and 150 MPa); and steel fibre content (0, 1, 2, and 3%). Experimental results showed that the rate sensitivity decreases with the increase in the compressive strength; and the dynamic enhancement of tensile strength is inversely proportional to the fibre content.

The structural impact testing program focuses on the dynamic response of full-scale reinforced concrete plates as well as generating precise impact measurements. Twelve reinforced plates with identical dimensions are tested under high-mass low-velocity multi-impacts. The investigated parameters include: concrete type (NSC, HSC, and UHP-FRC), fibre volume

content, and steel reinforcement ratio. The results showed that the use of UHP-FRC instead of NSC or HSC is able to change the failure mode from punching to pure flexural; and UHP-FRC containing 3% fibre has superior dynamic properties. For plates with identical steel reinforcement, the total impact energy of UHP-FRC plate containing 3% fibres is double the capacity of UHP-FRC plate containing 2% fibres, and 18 times the capacity of NSC plate.

A three-dimensional finite element analysis has been performed using ABAQUS/Explicit to model multi-impacts on RC plates and the applicability is verified using existing experimental data. Concrete damage plasticity (CDP) model is adapted to define UHP-FRC. The CDP constitutive model parameters for the new material are calibrated through a series of parametric studies. Computed responses are sensitive to CDP parameters related to the tension, fracture energy, and expansion properties. The analytical results showed that the existing CDP model can predict the response and crack pattern of UHP-FRC reasonably well.

ACKNOWLEDGEMENTS

The research work presented in this PhD dissertation was carried out at the department of civil engineering, Ryerson University under the supervision of Professor Hesham Marzouk. This research program was financially supported by the Natural Sciences and Engineering Research Council of Canada (NSERC), Prof. Marzouk, and Ryerson University. This support is gratefully acknowledged. I would like to acknowledge Lafarge North America for UHP-FRC material donation.

First and foremost, I would like to express my sincere appreciation and gratitude to my supervisor, Prof. Marzouk for his invaluable guidance, encouragement, endless patience, and support throughout the course of my PhD study, not to mention his helpful advice and unsurpassed knowledge. It was my great pleasure working under his supervision.

I also would like to thank my colleagues Aria Aghajani-Namin, Mahmoud Sayed-Ahmed, and Seyed Masoud Sadri for their moral support and help in carrying out the experimental phase.

In addition, I wish to extend my appreciation and thanks to the committee members, Prof. Reza Kianoush, and Dr. Jinyuan Liu for dedicating their valuable times to review my dissertation.

I am deeply thankful to my family for their love, support, sacrifices and encouragement throughout my extended educational career. Most of all I must thank my father, to whom I owe it all. To my wife, I could not have done this without you. To my dear kids Mohamed and Lana, thank you for keeping daddy extra busy during these years.

TABLE OF CONTENTS

LIST OF TABLES

LIST OF FIGURES

LIST OF ABBREVIATIONS

2D-FE: Two-dimensional Finite Element

3D-FE: Three-dimensional Finite Element

B31: Three-dimensional two node beam element

C3D8R: Three-dimensional eight node continuum solid element with reduced integration

CDP: Concrete Damage Plasticity material model

DIF: Dynamic Increase Factor

DSP: Densified Small Particles

FE: Finite Element

FRC: Fibre Reinforced Concrete

FRCC: Fibre-reinforced Cementitious Composites

HSC: High Strength Concrete

HSS: Hollow Structural Steel

MDF: Macro-Defect-Free Concrete

NSC: Normal Strength Concrete

RC: Reinforced Concrete

RPC: Reactive Powder Concrete

UHP-FRC: Ultra-High Performance Fibre Reinforced Concrete

1 INTRODUCTION

1.1 Background

Low-velocity impact is of growing concern to structural engineers since this loading rate range is relevant to most common accidental loading cases in civil engineering structures. Typical low-velocity impact scenarios include transportation structures subjected to vehicle collisions, airport runway platforms during aircraft landing, and offshore structures subjected to ice and/or ship impact. Dynamic loads arising from natural hazards such as tornadoes and earthquakes are also related to low-velocity impact (CEB-FIP, 1988).

Ultra-high performance fibre reinforced concrete (UHP-FRC) seems to be the best choice to fit evolving static, dynamic, and durability properties needed in many structures. UHP-FRC is a new generation of fibre cementitious composites which has been developed in the last two decades (Schmidt and Fehling, 2005). UHP-FRC exhibits outstanding mechanical, and durability properties. Such properties include: ultra-compressive strength exceeding 150 MPa, enhanced tensile strength, ductility, flexibility, toughness, impact resistance, dimensional stability, durability, corrosion resistance, and abrasion resistance (Walraven, 2009). It should be pointed out that UHP-FRC has high resistance to spalling, scabbing, and fragmentation (Riisgaard et al., 2007). The use of UHP-FRC in impact resistance structures is growing. However, there are insufficient studies to fully describe the dynamic behaviour of UHP-FRC materials (Habel and Gauvreau, 2008). Additionally, there is no available data in literature related to the behaviour of UHP-FRC members under low-velocity impact loading conditions. Most of the promising performance is based on static simple bending tests at the material level. Even the static load-bearing capacity and the failure mode of reinforced UHP-FRC plates have not been widely investigated. Therefore, this research is a stepping stone.

The use of numerical technique such as finite element (FE) to predict structural response in dynamic event is inevitable due to the limitation of analytical and empirical methods (Li et al. 2005). However, nonlinear FE modelling of reinforced concrete (RC) members subjected to impact load is still a challenging topic for researchers, as there are many aspects which still require wide discussion and exploration to accurately model RC structures under impact loading such as, defining strain rate effect on concrete and steel reinforcement material models, mesh dependency of results, and modelling the dynamic contact between impacted bodies. Several investigations have shown that the mechanical properties of UHP-FRC material (Wille et al., 2010; Wille et al., 2011; Wille et al., 2012) and the strain rate effects (Riisgaard et al., 2007; Ngo et al., 2007) are different from traditional concrete, in particular the tensile response. These differences in material behaviour might result in more complexity to the FE simulation of UHP-FRC under impact loads.

1.2 Research Scope

The primary focus of this research is to investigate, analyze, and report the potential and the advantage for the use of UHP-FRC material for impact resistance structures. To achieve these goals, two experimental testing programs and major numerical investigations have been conducted. The first testing program aims to investigate the strain rate effect on the mechanical properties of UHP-FRC material, while the second testing program focuses on the advantage of using UHP-FRC in impact resistance structural elements. Reinforced normal strength concrete (NSC), high strength concrete (HSC), and UHP-FRC plates are tested under drop-weight impact.

Parameters investigated include: concrete type, fibre volume content, and steel reinforcement ratio.

Impact testing techniques are generally more complicated than static one, since there are many other parameters involved that may mislead the interpretation of test results and must be filtered out. Among such parameters to be analyzed carefully is the frequency range of test specimens and expected impact load. Therefore, another testing series constructed using HSC has been conducted to be used in the validation processes of developed impact test setup and data analysis. At the same time, this testing series is used to investigate the influence of different steel reinforcement ratio and layout on the dynamic response and failure mode of RC plate.

The second phase of this research program aims to develop an accurate three-dimensional finite element (3D-FE) model capable of analyzing and predicting the dynamic response of the RC members under impact loads. The FE analysis has been performed using a general-purpose program; ABAQUS/Explicit software (Simulia, 2016). Concrete damage plasticity (CDP) model is adapted to consider nonlinearity, stiffness degradation, and strain rate effects of concrete materials. The material models are adapted using the results of materials investigation and the simulation results are validated with the results of the tested HSC plates. Thereafter, the calibrated FE model are extended to model the experimentally tested UHP-FRC plates in order to assess whether the existing CDP constitutive material model with adjustable material parameters may be able to accurately replicate the response of UHP-FRC member.

1.3 Objectives

Due to the large scope, this research program involves the following objectives:

1) To investigate the mechanical properties of UHP-FRC materials at high strain rates corresponding to low-velocity impact, as well as evaluate the quasi-static mechanical properties of concrete materials and steel reinforcement that are required to define materials constitute models in FE simulations. The materials investigation includes the following tasks:

    - Identify the influence of matrix strength and fibre volume content on the mechanical properties of UHP-FRC matrices at high strain rates;

    - Examine the applicability of CEB-FIP Model Code (2010) to model UHP-FRC response under high strain rates;

    - Generate accurate input data for HSC, UHP-FRCs, and steel reinforcement constitutive models that are required in the numerical FE simulation phase.

2) To design and conduct an experimental testing program focuses on the structural behaviour of full-scale NSC, HSC, and UHP-FRC plates subjected to drop-weight impact. The detailed objectives of this testing program can be summarized as follows:

    - Validate the developed drop-weight impact setup, implemented instrumentation, selected sampling rate of data acquisition system, and filtering process;

    - Identify the influence of the bottom steel reinforcement ratio (1.0, 2.0, and 3.0%); and the steel reinforcement arrangement (single or doubly reinforced plates) on the impact response and failure mode;

    - Address the advantage of using UHP-FRC in impact resistance structural members;

    - Identify the influence of fibre volume content and the steel reinforcement ratio on dynamic response, failure mode, and impact capacity of UHP-FRC plates;

- Provide test data in a research area where no testing has been performed: low-velocity impact response of UHP-FRC plates.

3) To develop an accurate 3D-FE model capable of analyzing and predicting the dynamic response of the RC members under low-velocity impact loads using ABAQUS/Explicit software (Simulia, 2016) with following tasks:

   - Develop a rational procedure for the structural analysis of RC members subjected to repeated impact loads;
   - Validate the implemented loading technique, contact modelling, and boundary conditions;
   - Use the mass participation factor of modal shape analysis to estimate the deformed shape of RC members under impact load and compared with experimental observation deformed shape;
   - Calibrate the FE model by comparing numerical with experimental results of the tested specimen constructed using HSC through a series of parametric studies;
   - Investigate the influence of strain rate effect, and damping parameters on the numerical results and damage pattern;
   - Assess whether the existing CDP constitutive model with adjustable material parameters may be able to accurately replicate the UHP-FRC members' response.

1.4 Outlines and Methodology

The structure of this dissertation follows the methodology used in establishing the research program. The dissertation is divided into the following seven chapters.

Chapter one: Presents a brief introduction to identify the problems, objectives, and the outline of the research program.

Chapter two: provides the fundamental basics and background information related to the present work with a focus on mechanical properties of UHP-FRC, strain rate effect, plate response to impact loading, nonlinear numerical simulation of RC plates under dynamic loads, brief description of the important features of explicit analysis, and adapted materials constitutive models available in ABAQUS/Explicit. Additionally, a comprehensive review of relevant experimental testing and numerical simulation of RC plates under low-velocity impact loading conditions are presented and discussed.

Chapter three: presents the materials experimental investigation under different loading rates, with emphasis on the loading rate dependent compressive strength, elastic modulus, and flexural tensile strength of five different UHP-FRC mixes and one control HSC mix. The details of the concrete mixes, test specimens, test setups, instrumentation, adapted loading rates, test results and observations are described. This chapter reports also the quasi-static results of steel reinforcements and concrete materials that are needed to develop the numerical models.

Chapter four: describes the drop-weight low-velocity impact investigation of full-scale RC plates. This chapter reports the details of test specimens, developed impact test setup, instrumentations, and loading protocol that have been utilized in the experimental program of RC plates.

Chapter five: presents the drop-weight impact testing results in both quantitative and qualitative forms. The measurements of the tested plates are reported in details in order to facilitate and validate the development of numerical 3D-FE models. In addition, selected results are presented to characterize the influence of studied parameters on the impact response and failure pattern of the tested plates.

Chapter six: presents a detailed explanation of the developed methodology for nonlinear 3D-FE simulations of RC plates under impact loads. Several parametric studies have been conducted to calibrate and investigate the significance of various input parameters based on test measurements of HSC series. The applicability of the existing CDP model in ABAQUS for modelling UHP-FRC material under impact loading conditions is addressed. For both HSC and UHP-FRC series, the computed responses and damage patterns are compared to the experiments.

Chapter seven: presents the main findings and conclusions of the experimental and numerical investigations. This chapter also includes recommendations for future studies.

2 BACKGROUND AND LITERATURE REVIEW

2.1 Introduction

The demand for impact resistant design has a wide spectrum in many applications, such as offshore platform, rock sheds, protective structures, transportation structures, etc. UHP-FRC has been identified as one of the promising ways to innovate in impact resistance structures.

This chapter provides a brief discussion of the development, mixture compositions, and the mechanical properties of UHP-FRC material. This chapter also presents a thorough background on strain rate effect, RC plate response to impact loading, nonlinear numerical simulation of RC plates under dynamic loads, brief description of the important features of explicit analysis, and materials constitutive models available in ABAQUS/Explicit (Simulia, 2016). Thereafter, a comprehensive review of both experimental and numerical investigations of related studies is presented and discussed.

The objectives of this chapter are to provide the fundamental background and the past findings of the behaviour and failure modes of RC plates under low-velocity impact, and to address the advantage of using UHP-FRC material in impact resistance structures.

2.2 Ultra-High Performance Fibre Reinforced Concrete (UHP-FRC)

UHP-FRC is a relatively new generation of fibre cementitious composites which has been developed to give a significantly higher material performance than other concrete classes. UHP-FRC exhibits outstanding mechanical, and durability properties. Such properties include: ultra-compressive strength exceeding 150 MPa (AFGC, 2002), enhanced tensile strength, high elastic modulus and high elastic limit, post-peak ductility, strain hardening in tension (Wille et al., 2010), toughness, dimensional stability, impermeability, corrosion resistance, abrasion resistance, and aggressive environment resistance (Wille et al., 2012). Despite its vastly superior material properties, the structural application of UHP-FRC is still not widespread because of material expensive cost and the lack of practical design code regulations. Since the late 1990's there are several research programs have been conducted with a focus on finding methods to reduce the production cost (Rong et al., 2010; Roth et al., 2010). On the other side, the structural behaviour of UHP-FRC members needs to be thoroughly understood to allow rational models and appropriate analytic approaches to be defined.

2.2.1 History and development of UHP-FRC

The development of advanced concretes dates back to the 1970s with the investigations on enhancing the concrete characteristics based on the principle of lowering water-cement ratio and decreasing the porosity of cementitious materials (Yudenfreund et al., 1972) or improving the cement paste by applying heat-curing and pressure technique (Roy et al., 1972). With the development of superplasticizers and pozzolanic admixtures in the 1980's, the development of fine grained concretes started and concrete mixes became more compact. Bache (1981) introduced a technique to increase the compressive strength and decrease porosity by improving the homogeneity of the raw mix. Micro-silica and superplasticizer are interacting in the mix design. This class of concretes is known as densified small particles (DSP). Another approach was used towards improving the strength of concrete by adding water-soluble polymers; this developed class is a polymer modified cementitious material. It based on the concept of macro-defect-free concretes (MDF) (Wille et al., 2012). The last step taken to enhance matrix ductility was adding discontinuous fibres to decrease brittleness. The development of UHP-FRC was initiated by the introduction of Reactive powder concrete (RPC) by Richard and Cheyreezy

(1995). The technology of UHP-FRC is based on all above mentioned developments: the advances in concrete, nanotechnology of using the polymer modified cementitious materials, and the use of steel fibre.

2.2.2 Principles of UHP-FRC

The principle concept of UHP-FRC relies on improving homogeneity, packing density, microstructure, and ductility. The first three principle aspects are fulfilled by the use of fine compositions with various diameters and possible heat treatment. On the other hand, the ductility is achieved by the use of fibres. The basic principles of mixture design of UHP-FRC can be detailed as follows:

- Elimination of coarse aggregates: in order to enhance the homogeneity and decrease the mechanical effects of heterogeneity, According to the Japanese recommendations maximal aggregate size should be less than 2.5 mm (JSCE, 2008);
- A low water-cement ratio (0.2 to 0.25): this maintains the small spacing of the cement grains, resulting in a dense and strong structure of the hydration products and minimizing the capillary pores;
- Optimizing packing density: using well distributed fine grained of silica fume, very fine sand, and cement, so that each size of grains fills the voids of the larger size. The dense packing results in increasing the strength and lowering the porosity;
- Adding admixtures: to achieve sufficient workability of the fresh mix;
- Optionally, the microstructure can be further enhanced during the production process by applying pressure, heat curing, or both;
- Adding fibres: in order to enhance the ductility and post-peak behaviour.

2.2.3 UHP-FRC compositions

As mentioned, UHP-FRC generally consists of optimized combination of cement, fine sand, micro-silica fume, superplasticizer, water, and fibres. Typically, UHP-FRC mixes have very low water-cement ratio (w/c), below 0.25 and containing at least 20% micro-silica fume. Normally, short high strength steel fibres are used (Wille et al., 2012).

Different types of UHP-FRCs are currently available on the market. The sources of differences are mainly lie in the composition of the mixture, fibre type, fibre volume fracture, and curing process (with or without heat). Examples of UHP-FRCs currently marketed are the following:

- **Ductal® concrete:** developed by Bouygues, Lafarge and Rhodia, and marketed by Lafarge (Lafarge, 2016),
- **Ceracem® concrete:** developed by Sika in association with Eiffage company (formerly BSI "Béton Spécial Industriel"),
- **Cemtec® $_{\textbf{multiscale}}$:** developed by Rossi et al. (2005) at the Laboratoire Central des Ponts et Chaussees (LCPC) in Paris.

In the present study, the UHP-FRC used is Ductal® specified by Lafarge North America. Typical compositions of Ductal® containing 2% short straight steel fibres are shown in **Table 2.1**.

Table 2.1 – Typical composition of UHP-FRC (Graybeal, 2005).

Material	Bulk density (kg/m^3)	Percent by weight (%)
Portland cement	712	28.5
Fine sand (size < 0.5 mm)	1020	40.8
Silica fume	231	9.3
Ground quartz	211	8.4
Superplasticizer	30.7	1.2
Accelerator	30	1.2
Steel fibres	156	6.2
Water	109	4.4

2.2.4 Mechanical properties of UHP-FRC

The mechanical properties presented in this section are the important quasi-static properties related to the current study. **Table 2.2** summarizes the average quasi-static mechanical properties of Ductal® as specified by Lafarge North America (Lafarge, 2016).

Table 2.2 – Typical mechanical properties of UHP-FRC (Graybeal, 2005)

Mechanical characteristic	Range
Compressive strength	150-200 MPa
Direct tensile strength	8-15 MPa
Flexural strength	30-40 MPa
Elastic modulus	45-55 GPa
Poisson's ratio	0.2
Density	2500 kg/m^3

2.2.4.1 Compressive behaviour

Typical quasi-static compressive stress-strain curve of UHP-FRC is shown in **Figure 2.1**. The behaviour of UHP-FRC in compression is characterized by very high strength, greater than 150 MPa, a high elastic modulus, a high strain of 4-5 ‰ at compressive strength and a significant post-peak ductility.

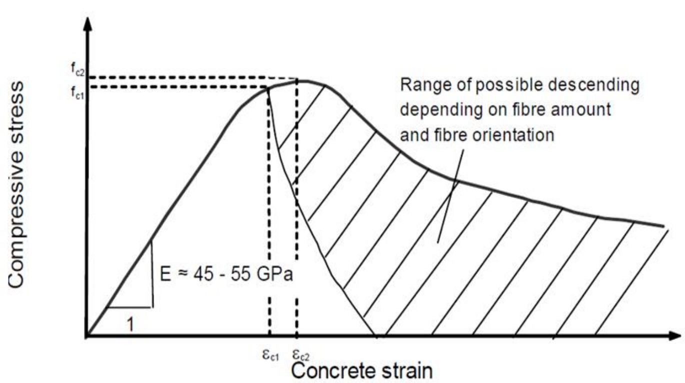

Figure 2.1 – Typical compressive stress-strain curve of UHP-FRC (Fehling and Bunje, 2004)

In general, the effect of steel fibres on the compressive strength and elastic modulus is low (Naaman, 2007; Millard et al., 2010). On the other hand, the post-peak behaviour is influenced mainly by fibre type, fibre content, fibre orientation, and bond of fibres and matrix (Wille et al., 2010).

Typically, the Poisson's ratio of UHP-FRC is slightly higher than NSC and HSC, and its value remains constant up to 80 % of compressive strength (Tue et al., 2004). **Figure 2.2** shows a comparison between the Poisson's ratios of UHP-FRC and NSC developed over compressive stress.

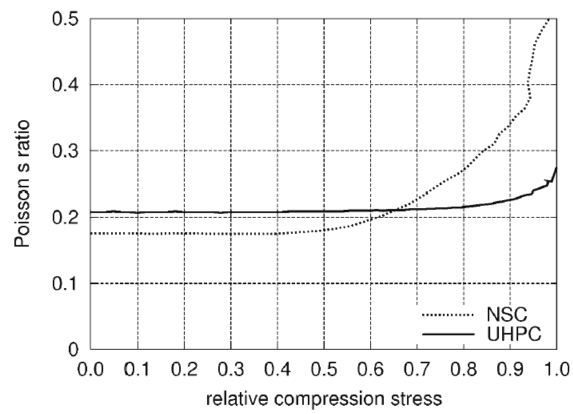

Figure 2.2 – Variation of Poisson’s ratio with compression stress (Tue et al., 2004)

2.2.4.2 Tensile behaviour

The tensile strength of UHP-FRC is in the range of 8 to 15 MPa (Chanvillard and Rigaud, 2003), as shown in **Figure 2.3**. The tensile behaviour of UHP-FRC is characterized by: linear-elastic to the stress level corresponding to matrix tensile strength, strain hardening behaviour corresponding to non-continuous micro-cracks in the cementitious paste ended by single crack localization. Thereafter, the resistance drops and strain softening behaviour till complete failure. Steel fibre content has a strong effect on the tensile strength and post-cracking nonlinear descending branch of the stress-strain curve.

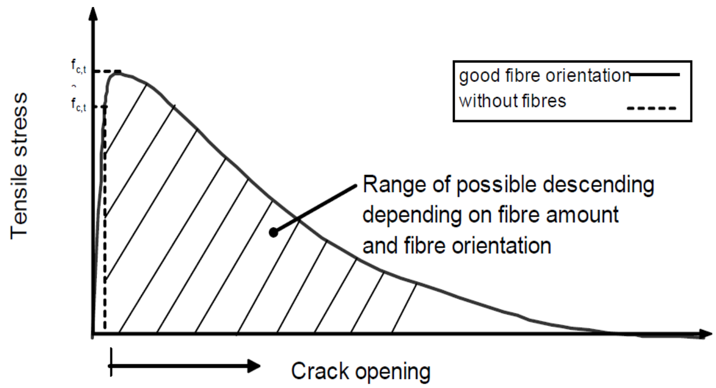

Figure 2.3 – Typical tensile stress-strain response of UHP-FRC (Fehling and Bunje, 2004)

2.2.4.3 Fracture energy

The fracture toughness is anther tensile property that has a significant effect on the structural behaviour of concrete. In general the fracture toughness of concrete is quantified by determining the fracture energy (G_F). Fracture energy is the amount of energy required to produce a continuous crack of unit area within the damage zone. Fracture energy is an important parameter for defining the cracking and post-cracking behaviour of concrete and it is significant for any accurate FE analysis (Marzouk and Chen, 1993). For plain concrete and fibre reinforced concrete (FRC), the fracture energy can be determined as the area under stress-opening crack width softening branch of uniaxial controlled tensile test (Bazant and Cedolin, 1980; Hillerborg et al., 1976; Marzouk and Chen, 1995). On the other hand, the fracture energy of UHP-FRC is comprised of two parts, the energy dissipated during strain hardening through concrete matrix and that during softening through fibres pull-out (Xu and Wille, 2015). **Figure 2.4** illustrates the difference between the fracture energy of strain softening and strain hardening materials. It is worth noting that the fracture energy dissipated during strain hardening is very small (approximately 1% of G_F) in comparison to the dissipated energy during softening or fibres pull-out (Xu and Wille, 2015).

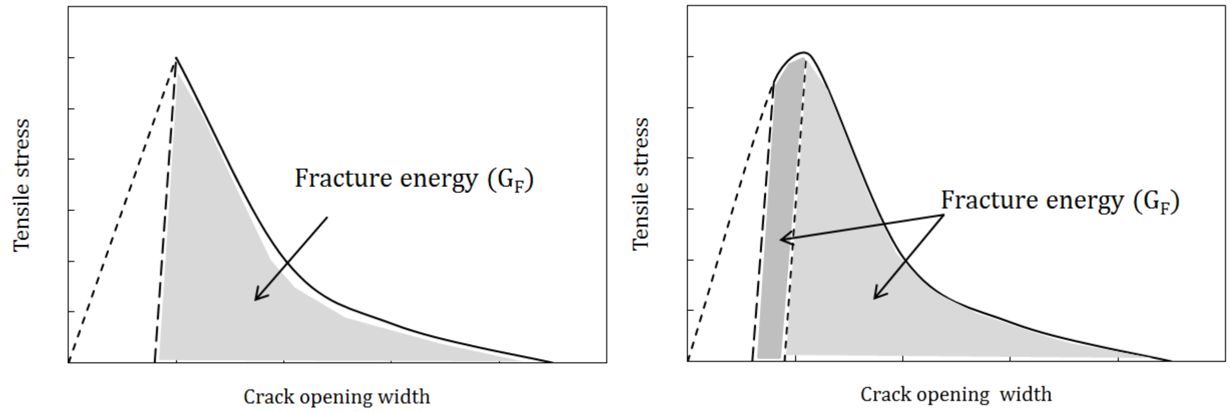

Figure 2.4 – Fracture energy of (left:softening concrete materials; right: UHP-FRC)

Fracture energy of UHP-FRC is strongly dependent on the fibre type, geometry, and volume content as well as on the matrix properties. Increasing the fibre volume fraction leads to higher fracture energy. In literature, reported fracture energy values of UHP-FRC are ranging from 14,000 to 40,000 N/m (Wille and Naaman, 2010; Voit and Kirnbauer, 2014; Xu and Wille, 2015; Tran et al., 2016) in comparison with 100 and 160 N/m for NSC, and HSC, respectively (Marzouk and Chen, 1995). It is evident from this comparison that the fracture energy of UHP-FRC is several orders of magnitudes of NSC and HSC, making it promising candidate for blast- and impact-resistant structures.

2.3 Materials Behaviour at High Strain Rates

In general, materials subjected to dynamic effects, such as impact loading, response over a relatively short period of time. As a result of such loading rate, the strain rates reach magnitudes considerably higher than that of static conditions (CEB-FIP, 1988). Typical strain rates occurring in various dynamic loading scenarios are summarized in **Table 2.3**.

It is well known that high strain rates result in enhancing mechanical properties in most materials. This includes the constituents of RC structures, namely: concrete and steel reinforcement. Although the reason for this enhancement is not entirely understood, it is widely considered to be a material property. Dynamic increase factor (DIF) is the most popular method for taking account of strain rate effects on both deformation and failure (Li et al., 2005). DIF is defined as the ratio of the dynamic to static strength. DIF generally reported as a function of strain rate. Most reported relations of DIF and strain rate are linear-logarithmic or double logarithmic. It is important to mention that DIFs is of direct use in FE analysis of structures subjected to dynamic loading conditions (Li et al., 2005; Othman and Marzouk, 2014).

Table 2.3 – Typical strain rates for various types of loading (CEB-FIP, 1988)

Load case	Strain rate (s^{-1})
Traffic	$10^{-6} – 10^{-4}$
Gas explosions	$5\times10^{-5} – 5\times10^{-4}$
Earthquake	$5\times10^{-3} – 5\times10^{-1}$
Pile driving	$10^{-2} – 10^{0}$
Aircraft impact	$5\times10^{-2} – 2\times10^{0}$
Hard impact	$10^{0} – 5\times10^{1}$
Hypervelocity impact	$10^{2} – 10^{6}$

2.3.1 Properties of concrete at high strain rate

2.3.1.1 Strain rate effect on plain concrete

Abrams was the first researcher who observed, in 1917, the effect of changing strain rates on concrete response (Li et al. 2005; Bischoff and Perry 1991). Further, numerous experimental studies have demonstrated the strain rate effect on compressive strength, tensile strength, modulus of elasticity, and fracture energy of concrete (Malvar and Ross, 1998; Bischoff and Perry, 1991; Williams, 1994; Ross et al., 1995; Li and Huang, 1998; Weerheijm and Van Doormaal, 2007; Zhang et al., 2009). Such studies typically proposed models to be used to estimate the concrete DIFs at a certain strain rate. These models are mainly functions in concrete compressive strength, and quasi-static and dynamic strain rate (Malvar and Ross, 1998).

Although, there are some difference in estimated values at a certain strain rate using these models, all these studies typically concluded that: the stiffness and strength properties of concrete increase significantly under high strain rates, DIFs are higher for concretes with lower strengths, the strength enhancement is different for compression and tension (Malvar and Ross, 1998; Bischoff and Perry, 1991), the increase in the modulus of elasticity and the peak strain corresponding to the peak stress is relatively small (Malvar and Ross, 1998). The fracture energy and crack opening are unaffected by strain rates up to 23 s^{-1} (Weerheijm and Van Doormaal, 2007; Zhang et al., 2009). **Figure 2.5** summarized the most frequently used DIFs models at different strain rates for concrete materials with a compressive strength of 30 MPa.

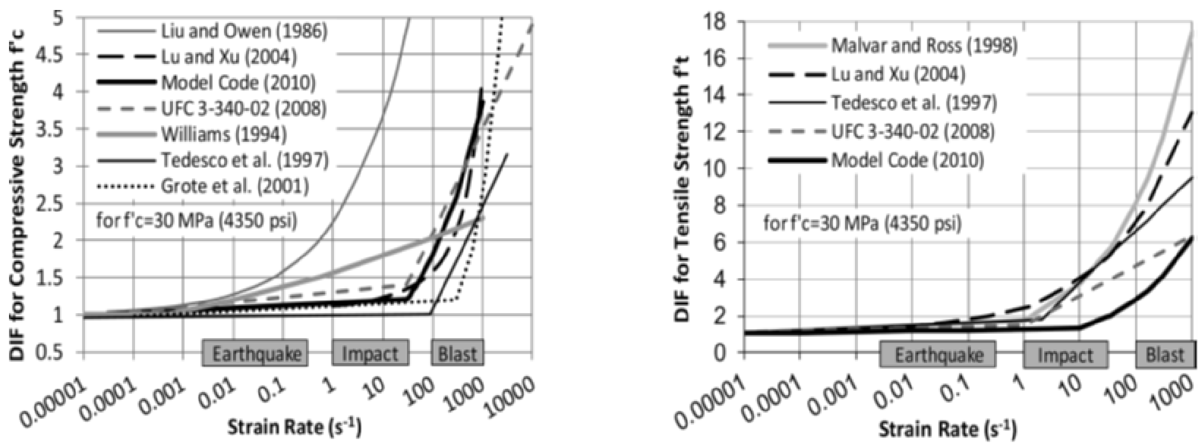

(a) Compressive strength (b) Tensile strength

Figure 2.5 – Summary of mathematical strain rate effect models (Guner and Vecchio, 2013)

2.3.1.2 Strain rate effect on fibre reinforced cementitious composites

This section presents the strain rate effect on fibre-reinforced cementitious composites (FRCC) including all concrete classes that containing fibres. Several experiments have been undertaken to develop a fundamental understanding of strain rate effect on FRCC with different objectives (Bischoff and Perry, 1991; Banthia et al., 1996; Gopalaratnam and Shah, 1986; Maalej et al., 2005; Millard et al., 2010; Habel and Gauvreau, 2008). These experimental investigations have revealed that: FRCC exhibits enhanced impact resistance compared to plain concrete (Bischoff and Perry, 1991; Millard et al., 2010; Banthia et al., 1996); Fibres volume content has little effect on compressive strength and elastic modulus (Habel and Gauvreau, 2008; Millard et al., 2010). On the other hand, fibres enhance significantly tensile/flexural, shear, and ductility properties (Millard et al., 2010; Wille et al., 2010).

Different conclusions have been drawn for fibres volume content effect on the strain rate effect behaviour of FRCC including UHP-FRC materials. Gopalaratnam and Shah (1986), and Maalej et al. (2005) concluded FRCC are more rate-sensitive than plain matrices. On the other hand, the results of Gao et al. (2006), and Millard et al. (2010) showed that the DIF is greater for specimens without fibres and decrease with the increase of fibre contents. It should be pointed out that the rate sensitivity of pull-out of short straight fibres has been shown to be independent of strain rate (UN Gokoz and Naaman, 1981; Suaris and Shah, 1982).

The behaviour of UHP-FRC subjected to high strain rates are not well established, particularly in terms of response at the material level. AFGC (2002) suggests DIF for UHP-FRC in compressive and tensile strength of 1.5 and 2, respectively, for strain rate range of 10^{-3} to 1 s^{-1}.

A series of impact tests were carried out by Ngo al. (2007) to estimate strain rate effects on compressive strength for three concrete classes, including NSC, HSC, and UHP-FRC. The UHP-FRC used in the study was Ductal®. The strain rates were applied using the split Hopkinson pressure bar (SHPB) setup. The tested cylinders were of 50 mm diameter and had a static compressive strength of 160 MPa. Cylinders were tested in compression at strain rates range 3×10^{-5} s^{-1} (quasi-static rate) up to 264 s^{-1} (dynamic rate). The testing results showed that Ductal® is less strain-rate sensitive than NSC and HSC. **Figure 2.6** shows the testing results of Ngo et al. (2007).

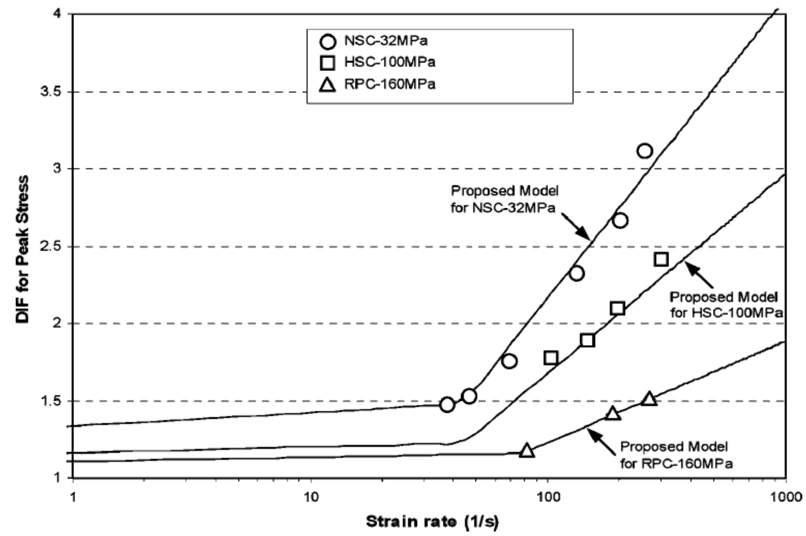

Figure 2.6 – DIF for different concrete types (Ngo et al., 2007)

An extensive review of experimental data for all concrete classes, including UHP-FRC under a wide range of strain rates was carried out by Pajak (2011). Pajak summarized all available experimental data of compressive and tensile strength, and the corresponding strain rate. Pajak concluded that the values of DIF obtained from testing UHP-FRC materials are same as NSC tests. As a result, same DIFs equations of plain concrete can be used to estimate UHP-FRC behaviour at high strains.

Based on contradictory information in the literature and the lack of data for UHP-FRC, the strain rate effect on UHP-FRC is in need to experimentally investigate.

2.3.2 Properties of reinforcing steel at high strain rate

As well as concrete, the mechanical properties of reinforcing steel are also enhanced by high strain rates. Several researchers have experimentally studied the effect of strain rate on steel reinforcement properties (Malvar and Crawford, 1998; Asprone et al., 2009). All studies typically demonstrated that both the yield stress and ultimate strength enhanced due to strain rate increase; the yield stress is enhanced more significantly than the ultimate strength (Malvar and

Crawford, 1998; Asprone et al., 2009); the effect of strain rate on the elastic modulus and peak strain are negligible (Malvar and Crawford, 1998).

Commonly, mathematical models proposed by Malvar and Crawford (1998) is used in FE numerical simulation for estimating the DIFs for yield and ultimate strengths (Eqs. **2.1** and **2.2**, respectively). These models were developed based upon an extensive review of experimental data. The model is applicable for strain rate ranging from 1×10^{-4} (reference quasi-static rate) up to 225 s^{-1}, and is valid for static yield stresses ranging from 290 to 710 MPa.

$$\mathrm{DIF_Y} = \left(\frac{\dot{\varepsilon}}{10^{-4}}\right)^{0.074-0.04\left(\frac{f_y}{414}\right)} \tag{2.1}$$

$$\mathrm{DIF_U} = \left(\frac{\dot{\varepsilon}}{10^{-4}}\right)^{0.019-0.009\left(\frac{f_y}{414}\right)} \tag{2.2}$$

Where,

$\mathrm{DIF_Y}$ = DIF for yield stress; $\mathrm{DIF_U}$ = DIF for ultimate strength;

$\dot{\varepsilon}$ = strain rate (s^{-1}); f_y = steel yield stress (MPa).

2.4 Impact Loading Terminology

RC structural member subjected to impact loading scenarios deform over a relatively short period of time, the effect of strain rate, lateral confinement, and inertia force become more significant. As a result, the structural response and failure mode may be different from those under static loads (Li et al., 2005; Chen and May, 2009). This section focuses on the terminology of impact loading, structural response, and failure modes.

Impact loading may be classified as hard or soft impact, depending on the deformation of the impactor (projectile) with respect to the deformation of the target. In hard impact, the deformation of the impactor is considerably negligible compared with target's deformation. In such impact type, the impactor is considered rigid. In contrast, in soft impact, the impactor itself undergoes significant deformation and must be considered in the analysis of impact problem (Li et al., 2005). In either of two impact types, the response as well as the failure mode of the concrete target may be classified as follows:

- **Global response:** the RC member responds globally with a deformation of entire member. There are two failure modes of global response for RC members: flexural failure and punching shear failure. Both failure modes are caused by the elastic-plastic response. **Figure 2.7** shows the two modes of global response. The majority of global response investigations were carried out on RC beams.

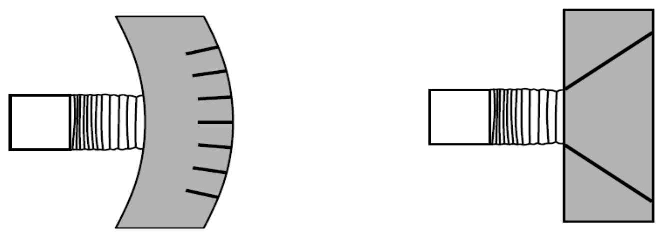

(a) Flexural failure (b) Punching Shear failure

Figure 2.7 – Global response of RC target (Martin, 2010)

- **Local response:** the RC member responds locally and the impact energy is dissipated around the impact zone. Most of local impact investigations were carried out on RC plates. Local impact effect is briefly sub-divided into seven phenomena as classified in (Kennedy, 1976; Li et al. 2005): a) penetration, b) cone cracking and plugging, c) spalling, d) radial cracking associated to (i) impact face and (ii) back face, e) scabbing ejection of fragments from the back face of the target, f) perforation. Local impact damage mechanisms are illustrated in **Figure 2.8**.

- **Combined response:** the impact energy is dissipated through a combination of local and overall structure deformations.

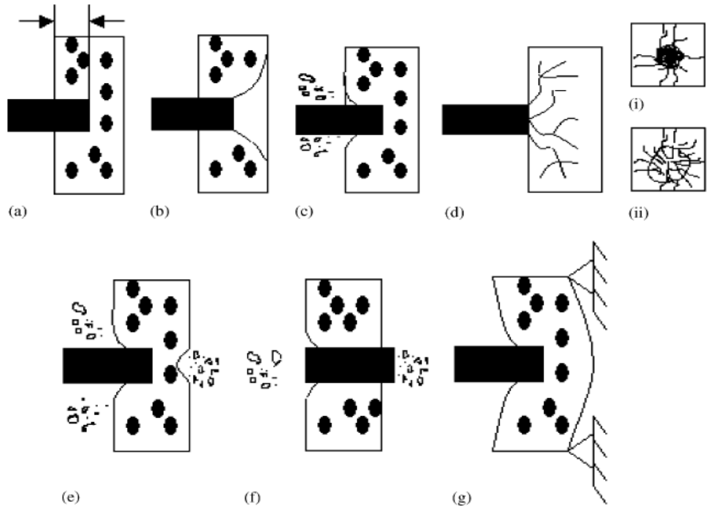

Figure 2.8 – Impact effects on concrete targe (Li et al., 2005)

According to Li et al. (2005) all above impact effects can be quantified using the following measurements:

Penetration depth: depth to which the impactor reaches into concrete target without perforation.

Scabbing limit: minimum thickness of the concrete target to prevent scabbing.

Perforation limit: minimum thickness of the concrete target to prevent perforation.

Ballistic limit: minimum initial impact velocity required to perforate concrete target.

2.5 Review of Previous Low-velocity Impact Experiments

Although, numerous experimental investigations have been performed on the impact behaviour of RC members, most of earliest studies are carried out by those associated with military and nuclear sectors. In such investigations, the impactor has small size hitting a massive target with high velocity in the range of 40 m/s to 300 m/s. In this type of impact, the loading impulse acts over a very short time, much shorter the natural period of structural member vibration by perhaps one or two orders of magnitude. As a result, the entire member has no time to respond globally and the failure of beams or plates is localized in the form of punching ejection cone. However, the resulting crack pattern and displacements map indicate that both flexural and shear failure are involved. For impact with higher velocity >1000 m/s, only local failures are developed. More details regarding high-velocity impact can be found elsewhere (Li et al., 2005; Barr et al., 1982). A worth of mention here the results of these investigations are almost qualitative and often in the form of impact-resistant empirical formulas. However, there is no standard test technique for impact loading condition (Li et al., 2005). Therefore, most of the developed empirical formulas are applicable for certain condition and loading range.

In general, low-velocity impact is relevant to most common dynamic accidental loading cases in civil engineering structures (CEB-FIP, 1988). Low-velocity impact tests are commonly based on large mass low-velocity technique using the potential energy method to generate the impact energy. Examples of such setups include falling drop-weight and pendulum-type. This section provides a comprehensive review of experimental investigations that related to low-velocity impact loading on RC plates.

2.5.1 Review of RC plates experimental impact testing

Sawan and Abdel-Rohman (1987) carried out low-velocity tests on 750 mm square RC plates, 50 mm thick. The plates were impacted at their midpoint by free fall steel ball of 120 mm diameter from several heights up to 1200 mm. The aim of the study was to investigate the effect of impact velocity and steel reinforcement ratio on the dynamic deflection. The results showed steel reinforcement has a little effect on reducing the dynamic deflection of RC slabs.

Kishi et al. (1997) tested nine large rectangular plates of dimensions 4×5 m under repeated impact. The plate thicknesses were varied (250, 500, 750 mm), plates were impacted at their centre by free fall masses of (1000, 3000, 5000 kg) depending on the thickness. The failure was assumed when the accumulated residual deflection under repeated impact exceeds 1/200th the span. The variations of reinforcement ratio (0.5, 1.0%), reinforcement arrangement (single and double layers) were considered. The purpose of the Kishi et al. (1997) experiments were to investigate the impact behaviour by recording maximum impact load, reactions, residual displacements and crack patterns. The results showed that the maximum impact force was affected by plate thickness rather than reinforcement ratio and reinforcement arrangement.

Murtiadi and Marzouk (2001) tested sixteen 950 mm square plates, 100 mm thick under both static and dynamic loads. A free fall solid steel cylinder of 220 kg mass with contact diameter of 304.5 mm was used to apply the impact load. The drop-weight was dropped from variable heights of up to 4 m. The variations of concrete strength (NSC and HSC), boundary conditions (fixed and simply supported), and steel reinforcement ratio (1.0, 2.5% in tension face, and 0.7, 0.8% in compression face) were considered. The structural behaviour with respect to displacement, concrete and steel strains, failure mode, and energy absorption were investigated. The experimental results showed that; the impact punching load at failure was about twice the static punching shear capacity, and supporting conditions had little influence on the impact response.

Chen and May (2009) investigated a series of high-mass, low-velocity drop-weight impact tests on RC beams and plates. The purpose of the tests was to generate high quality input data to validate FE models. Four 760 mm square plates, 76 mm thick, and two 2320 mm square plates, 150 mm thick were tested. Different drop-mass up to 380 kg were used to apply the impact load with velocities up to 8.7 m/s. Supports were provided by clamping the corners to restrain horizontal and vertical movement. Measurements included transient impact loads, accelerations and reinforcement strains. Additionally, the impact events were recorded using a high-speed video camera operated at rate up to 4500 frames per second. The tests confirmed the findings of Murtiadi and Marzouk (2001) that supports have limited influence on the impact response.

2.5.2 Review of FRC plates experimental impact testing

Steel fibres are the most used type in impact resistance structures. Many researchers have concluded that fibre reinforced concrete (FRC) members exhibit better impact resistance compared to structural members constructed using plain concrete (Gopalaratnam and Shah, 1986; Banthia et al., 1996; Ong et al., 1999b; Hrynyk and Vecchio, 2014).

Ong et al. (1999a) tested fibre concrete plates without conventional steel reinforcement under low-velocity repeated drop-weight impact. Ten 1000 mm square plates, 50 mm thick were tested. The main objective of this investigation was to assess the effect of fibres type and fibre volume contents on the impact resistance. Three different types of fibres namely: polyolefin, polyvinyl alcohol and steel fibres were investigated. The volume content of fibres examined were 0%, 1% and 2%. Impact was applied by dropping hemispherical impactor of 43 kg mass from a height of 4 m. Test results indicate that end-hooked steel fibre concrete plates have better cracking characteristics, energy absorption and resistance to shear plug formation compared to plates reinforced with other fibre types. Additionally, plates reinforced with polyvinyl alcohol fibres exhibited higher fracture energy values compared to plates reinforced with polyolefin fibres.

Ong et al. (1999b) carried out a complimentary study using same test setup, loading protocol, and plates' dimensions, but plates were reinforced by steel bars of diameter 6.5 mm. Only end-hooked steel fibres were used. Two different drop-weight impact loading conditions were considered: a 20 kg hemispherical drop-weight from a height of 1.5 m, and a 20 kg flat drop-weight from a height of 4.5 m. Experimental results showed that the addition of steel fibres up to 2.0 % by volume increased the number of impacts to failure by at least seven times. The plate maximum deflection was found to decrease with increasing fibre content, and additional conventional steel reinforcement placed as compression reinforcement was also found to increase the impact resistance, particularly in the case of the hemispherical impactor.

Hrynyk and Vecchio (2014) tested seven plates to failure under sequential drop-weight impacts. The plates were 1800 mm square, 130 mm thick, and were doubly reinforced with equal top and bottom steel reinforcement. Three plates were constructed using plain concrete, while the other four slabs were constructed from a steel FRC with varied volumes of end-hooked steel fibres. Two parameters were investigated namely: steel reinforcement ratio (0.273, 0.420, and 0.592%); and fibre volume content (0, 0.5, and 1.5%). The data from the test program were used to assess the performance of steel FRC in impact resistant applications. Additionally, the generated high quality experimental data were used to calibrate FE simulation. The test results showed that the plates constructed using FRC exhibited superior performances when compared with non-fibrous RC plates. The addition of the steel fibres was effective in increasing plate impact capacity, stiffness, reducing crack widths, and mitigating local damage under impact. On the other hand, limited benefits were attained as a result of increasing steel reinforcement ratios of the RC plates.

2.5.3 Review of UHP-FRC plates experimental impact testing

Several experimental investigations at material level have demonstrated that UHP-FRC exhibits excellent dynamic properties (Parant et al., 2007; Habel and Gauvreau, 2008; Millard et al., 2010). However, experimental investigations on the dynamic response of UHP-FRC structural members (i.e., beams and slabs) are limited. Most of the available data in the literature are related to extreme loading conditions, such as blast and explosion loading (Cavill et al., 2006; Ngo et al., 2007; Yi et al., 2012) and high-velocity impact simulation using a shock tube (Ellis et al., 2014). In summary, all these investigations have confirmed that UHP-FRC has improved performance and superior damage control properties under extreme load conditions compared to conventional concrete. However, there is no available data in literature related to the behaviour of UHP-FRC members subjected to low-velocity impact load.

2.5.4 Summary of previous low-velocity impact experiments

In conclusion, several low-velocity precision impact experiments that related to this research have been undertaken to understand the dynamic response of RC and FRC members. In particular, RC slabs under drop-weight impact tests. These low-velocity impact experimental investigations have revealed that: punching shear is the predominate failure pattern (Murtiadi and Marzouk, 2001; Zineddin and Krauthammer, 2007; Chen and May, 2009; Hrynyk and Vecchio, 2014); the impact punching capacity is twice the static one (Murtiadi and Marzouk, 2001); the supporting conditions have limited effect on RC plate response, failure pattern, impact capacity, and maximum impact force (Kishi et al., 1997; Murtiadi and Marzouk, 2001; Chen and May, 2009); the plate thickness has significant effect on impact capacity and maximum impact force (Kishi et al., 1997); FRC members exhibit much better impact resistance properties compared to plain RC members (Hrynyk and Vecchio, 2014; Gopalaratnam and Shah, 1986; Banthia et al., 1996); and steel reinforcement ratio has a significant effect in controlling spalling (Zineddin and Krauthammer, 2007).

2.6 Finite Element Modelling of RC Members under Impact Loading

Finite element is one of the most effective and accurate numerical methods to simulate the dynamic response of structures under impact/blast loading (Belytschko et al., 2014). In this research, FE analysis is performed using general purpose program ABAQUS/Explicit, version 6.14 (Simulia, 2016). This section presents the important features of explicit analysis. This section also describes the geometrical, constitutive material models, and impact load modelling techniques, followed by a review of previous related numerical studies of RC members subjected to dynamic loads.

2.6.1 ABAQUS finite element software

ABAQUS is one of the most popular FE programs, commercial sold by Dassault Systèmes as part of their SIMULIA Product software tools. ABAQUS is a three-dimensional finite element package with advanced modelling capabilities. ABAQUS has a huge library of elements and material constitutive models to simulate the behaviour of most typical material with any geometry. ABAQUS is available in three different products: Standard, Explicit and CFD. ABAQUS/Standard and ABAQUS/Explicit are the two products used for structural modelling.

ABAQUS/Standard can be used to solve both static and dynamic problems using the implicit integration. The implicit integration is a direct-integration analysis method that solves a set of simultaneous equilibrium equations at each time step. In other words, implicit analysis requires the full formulation of the global stiffness matrix and its inversion. This is computationally expensive since equilibrium equations must be satisfied at each step. It should be pointed out that, it may be not possible to obtain efficient solution with ABAQUS/Standard in problems with significant discontinuities in the solutions that may be resulted from sudden impact, and/or material degradation such as cracking of concrete. ABAQUS/Explicit has been particularly designed to efficiently solve discontinues nonlinear dynamic problems such as impact and blast loads (Simulia, 2016). ABAQUS/Explicit uses explicit integration in which the equations of motion are satisfied at the current time step, and extrapolated to determine the solution of the next time step i.e. the values of nodal accelerations, velocities and displacements at the end of any time increment are merely based on the same quantities as at the beginning of the current time step, which explains why this method is considered explicit. Therefore, explicit analysis requires less computational time and disk space since there is no need to form the global stiffness matrix (Chopra, 2012). ABAQUS/Explicit contains many modelling capabilities that do not exist in ABAQUS/Standard. For example, material failure with element deletion for elastic-plastic materials and the contact algorithm that does not add additional degrees of freedom to the mode. Thus, explicit analysis requires less computational time and disk space. More information about ABAQUS can be found in the ABAQUS Keyword User's Manual and the ABAQUS Theory Manual (Simulia, 2016).

2.6.2 Explicit time integration algorithm

As mentioned before explicit dynamics is a mathematical technique for integrating the equations of motion (**Eq. 2.3**) through time. It is also known as the forward Euler or central difference time integration rule.

$$\mathrm{M}\ddot{\mathrm{u}}^{\mathrm{i}} = \mathrm{P}^{\mathrm{i}} - \mathrm{I}^{\mathrm{i}} \qquad (2.3)$$

The dynamic quantities (accelerations, velocities, displacements, stresses and strains) are integrated over the time increment by employing an explicit dynamic finite element formulation in which the dynamic quantities are extracted kinematically from the current time increment to the next one. The equation of motion is just used at the beginning of each step to calculate the nodal acceleration ($\ddot{u}^i$) using the diagonal lumped element mass matrix (M), the applied external load vector (P^i) and the internal force vector (I^i) as given in **Eq. 2.4**. It should be mentioned the lumped mass matrix is used because its inverse is simple to compute.

$$\ddot{\mathrm{u}}^{\mathrm{i}} = \mathrm{M}^{-1}.(\mathrm{P}^{\mathrm{i}} - \mathrm{I}^{\mathrm{i}}) \qquad (2.4)$$

Further the current acceleration is integrated used central finite difference method to obtain the nodal velocity ($\dot{u}^i$) and displacement (u^i) at next step using **Eqs. 2.5** and **2.5.**

$$\dot{u}^{i+\frac{1}{2}} = \dot{u}^{i-\frac{1}{2}} + \frac{\Delta t^{i+1} + \Delta t^{i}}{2}\,\ddot{u}^{i} \qquad (2.5)$$

$$u^{i+1} = u^{i} + \Delta t^{i+1}.\dot{u}^{i+\frac{1}{2}} \qquad (2.6)$$

Finally the internal forces can be computed. Then the next integration step can be performed following same procedures. The following steps in the explicit calculation are to determine the strain increments in the elements and then the stresses.

It is evident from previous procedures that, the explicit integration scheme requires nodal mass or inertia to be defined at all activated degrees of freedom. The initial velocity ($\dot{u}^0$) and acceleration ($\ddot{u}^0$) at first step must be defined. Additionally, the time increment size is the critical factor in explicit analysis, the time increment has to be within a certain range to ensure stability and accuracy of the solutions since explicit analysis assumes the acceleration is constant throughout the time increment. Failure to use an adequate small time increment results in an unstable solution. When the solution becomes unstable, the time history response of solution variables such as strains and displacements will oscillate with increasing amplitudes and the total energy balance will also change significantly. Theoretically, the time increment (Δt) must be smaller than the stability limit of the central-difference operator given in Eq. **2.7** (Chopra, 2012).

$$\Delta t \le \frac{2}{\omega_{max}}(\sqrt{1+\xi^2} - \xi) \qquad (2.7)$$

Where, ω_{max} is the highest frequency in the system, and ξ is the damping ratio (a fraction of critical damping). In ABAQUS/Explicit a small amount of damping is introduced in the form of bulk viscosity to control high frequency oscillations. Determination of the exact highest natural frequency in case of nonlinear response is complicated and computationally expensive. Alternately, ABAQUS/Explicit estimates an automatic approximation of the stable limit based on the smallest transit time of a dilatational wave across the meshed elements using **Eq. 2.8**.

$$\Delta t \cong \frac{L_{min}}{C_d} \qquad (2.8)$$

Where L_{min} is the smallest dimension of elements in mesh, C_d is the propagation wave speed calculated using **Eq. 2.9** for a linear elastic material with Poisson's ratio equal to zero; where E is the elastic modulus and ρ is the mass density of material.

$$C_d = \sqrt{\frac{E}{\rho}} \qquad (2.9)$$

The most important advantage of small time increment is to allow accurate capturing of the transition from linear to non-linear behaviour. In conclusion, explicit analysis is more suitable for modelling non-linear dynamic events with strong discontinuous geometrical or material responses such as impact problems involving contact.

2.6.3 Energy balance

As mentioned in previous section the explicit integration method can introduce errors if the time increment is not small enough. The energy balance can be used to determine the plausibility of the analysis and check the used time increment. In ABAQUS/Explicit the energy balance equation for the entire model can be defined according to **Eq. 2.10**.

$$E_{total} = E_I + E_V + E_{FD} + E_{KE} - E_W = \text{constant} \qquad (2.10)$$

Where, E_{total} is the total energy for the entire model; E_I is the internal energy, E_V is the viscous energy dissipated by damping mechanisms; including bulk viscosity damping and material damping; E_{FD} is the friction energy dissipation; E_{KE} is the kinetic energy; and E_W is the work done by externally applied loads.

In general, the total energy (E_{total}) of any system remains constant since the energy cannot disappear only it can be transformed. Therefore, check the total energy of the system is a good way to verify the stability of the analysis. In numerical analysis, the total energy is not completely constant and varies with time. ABAQUS specifies an error limit of 1% in total energy variation throughout the time duration to accept the stability of solution (Simulia, 2016).

In addition to monitor the total energy time history, it is important to check different components of internal energy (**Eq. 2.11**). The internal energy (E_I) is equal to the summation of recoverable elastic strain energy (E_E), the energy dissipated through inelastic plasticity processes (E_P), the energy dissipated through viscoelasticity or creep (E_{CD}), and the artificial strain energy or hourglass energy (E_A). The artificial strain energy is used to suppress hourglass modes and it includes energy stored in hourglass resistances and transverse shear in shell and beam elements. The artificial energy is anther useful quality check. It should be minimal, typically not exceed 5% of internal energy (Simulia, 2016). Large values of artificial strain energy indicate that mesh refinement is necessary.

$$\mathrm{E_I = E_E + E_P + E_{CD} + E_A} \qquad (2.11)$$

2.6.4 Different techniques for impact load modelling

Free fall impact can be modelled in ABAQUS using different techniques. One obvious way is to define an amplitude variation of impact load resulting from test as an input. However, ABAQUS offers two easy techniques without prior knowledge of the impact load. First technique, the drop-weight can be modelled at its initial drop-height above the specimen and allow ABAQUS to calculate the motion under the influence of applied gravity acceleration; or alternatively the drop-weight can be modelled at a position very close to the specimen surface with a predefined initial impact velocity. The first option is less practical because of the large number of increments required to complete the falling part of the simulation. The latter is the most efficient technique and it has been used throughout the numerical simulations of the current research (see, Chapter 6).

2.6.5 Geometrical modelling

In general, the geometry of RC members should be modelled as close as possible to the real structure. The majority of numerical simulations of RC members have been carried out using two-dimensional idealization, which is valid for most cases that involving static loading. However, impact-contact problems require adequate representation of local and global responses. 3D-FE modelling would enable accurate simulation of RC plates under impact load since stresses and strains distributions are in three dimensions especially at impact zone (Belytschko et al., 2014). Additionally, three-dimensional modelling takes into account some critical aspect such as confinement effect, punching, transverse shear, and dilation of concrete, which are difficult to model using two-dimensional simplification.

To model the geometry of concrete member in 3D-FE, tetrahedral or hexahedral elements can be used. One of the most important choices in FE modelling are choosing either first or second order element, reduced or full integration. First order element has nodes only at the corners and use linear interpolation to find displacements at any other points with element. Second order element has a node in element middle and use quadratic interpolation rather than linear. The reduced integration technique uses fewer Gaussian integration points than the full integration scheme. ABAQUS/Explicit adopts only first-order reduced-integration elements to integrate various response outputs over the element (Simulia, 2016). Linear interpolation elements with reduced integration have been found to be very efficient compared to fully integrated element in modelling contact impact or large distortions problems (Belytschko et al., 2014). The reason may be return to that first-order element has a lumped mass formulation which is suitable for explicit dynamic analysis. It should be mentioned that first-order reduced-integration elements have been frequently used in most of the previous dynamic numerical studies (Sangi and May, 2009; Martin, 2010; Kishi et al., 2011).

Steel reinforcement and its interface with concrete can be modelled in several ways; as smeared reinforcement in the concrete, discrete one-dimensional element, embedded one-dimensional element or solid element. In case of smeared technique, the reinforcement is modelled as a composite layer. This technique is usually used to simulate the global response without taking local response effect into consideration or when the simulation results for reinforcement is unnecessary. In discrete element, steel is modelled by using truss or beam element. The main drawback of this technique is the concrete mesh is restricted by reinforcement location (**Figure 2.9-a**). On the other hand, embedded technique overcomes this problem by allowing the placement of reinforcement beam element in anywhere regardless of concrete mesh nodes, and then the embedment constraint is applied (Simulia, 2016). The embedded constraint ties the nodes of the reinforcement to the nodes of the concrete without need to share nodes with surrounding concrete (**Figure 2.9-b**).

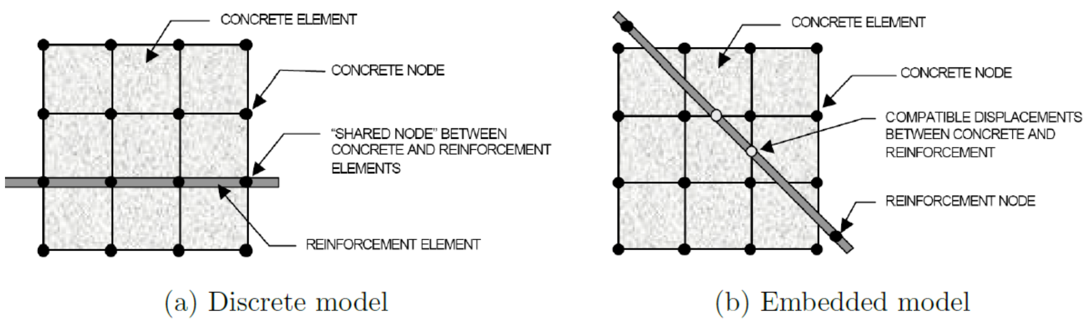

Figure 2.9 – Modelling of reinforcement and its interface with concrete (Belytschko et al., 2014)

The last technique is using three dimensional solid elements. Commonly, this technique is time consuming since unnecessary to introduce the complexities of multi-axial constitutive relationships for steel, additionally the complexity of the FE model would be increased exponentially if the reinforcement had been modelled as a solid element.

2.6.6 Materials modelling

The adopted material constitutive model must be capable of tracing the development and propagation of the yielding and inelastic flow of the material up to the failure point. In addition, the strain rate effect is another important issue that must also be simulated properly. In ABAQUS/Explicit, density must be defined in order to form the lumped mass matrix in explicit analysis. The elastic behaviour of material is specified by defining elastic modulus and Poisson's ratio. The inelastic behaviour is defined using the true stress-logarithmic plastic strain curve.

The following subsections present brief descriptions of selected constitutive material models that are used to model the concrete and steel behaviours. The detailed description of background theory and their models will not be given, for more details see (Dunne and Petrinc, 2005; Simulia, 2016).

2.6.6.1 Concrete damage plasticity model

Nonlinear behaviour of concrete has been defined using built-in concrete damage plasticity (CDP) model available in ABAQUS. CDP model can be used to model the behaviour of plain or RC under different loading conditions. The model was proposed by Lublinear et al. (1989) for monotonic loading, and later was developed by Lee and Fenves (1998) to consider the dynamic and cyclic loadings. CDP model is selected because of several distinguishing features; it allows for separate yield strengths, strain rates, and damage parameters in tension and compression. Additionally, CDP model provides an advanced representation of various concrete types using a set of adjustable parameters that can be measured experimentally. These parameters are used mainly to define the yield surface and flow rule in the three-dimensional space of stresses. The details of the mathematical formulation of the CDP model are given in (Lublinear et al., 1989; Lee and Fenves, 1998) and the ABAQUS theory and analysis manual (Simulia, 2016).

Uniaxial behaviour

The typical uniaxial compressive and tensile stress-strains curves characterized by CDP model are shown in **Figure 2.10**. Under uniaxial compression the response is modelled in three phases. The first two phases describe the ascending branches: linear elastic until the value of the initial yield (σ_{co}); followed by the plastic stress hardening response until the ultimate stress (σ_{cu}) is reached. The third branch is descending or strain softening response (**Figure 2.10-a**). Under uniaxial tension the stress-strain response follows a linear elastic relationship until the value of the failure stress (σ_{to}) is reached. Beyond the failure stress the formation of micro-cracks is represented with a softening stress-strain response, which induces strain localization in the concrete structure (**Figure 2.10-b**).

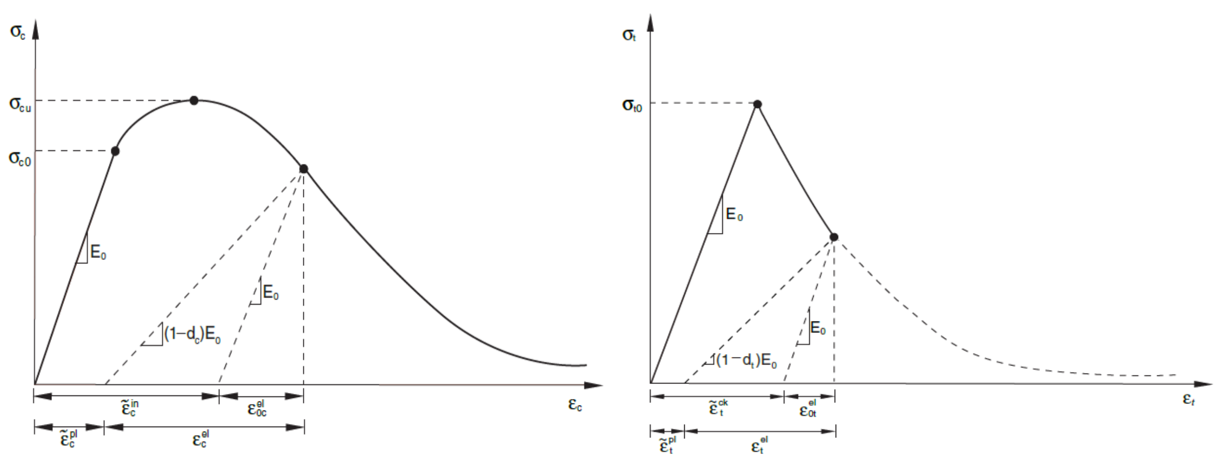

a) Compresive behaviour b) Tension behaviour

Figure 2.10 – Uniaxial stress-strain curves in CDP model (Simulia, 2016)

In ABAQUS, the uniaxial nonlinear behaviour of concrete in compression and tension are defined as tabular input in the form of stress-inelastic strain. The inelastic/cracking strains can be calculated as illustrated in **Figure 2.10** as follows:

$$\varepsilon_c^{in} = \varepsilon_c - \frac{\sigma_c}{E_0} \qquad (2.12)$$

$$\varepsilon_t^{in} = \varepsilon_t - \frac{\sigma_t}{E_0} \qquad (2.13)$$

Where, the subscripts c and t refer to compression and tension, respectively; ε_c^{in} and ε_t^{in} are the inelastic strains, ε_c and ε_t are the total strains, σ_c and σ_t are the stresses, E_0 is the initial (undamaged) elastic modulus.

In general, concrete tends to lose its stiffness with loading. The loading and unloading paths are different from the initial loading slope (elastic modulus). This stiffness degradation behaviour is more pronounced in strain-softening branch and related to the damage caused by micro-cracks. This behaviour can be observed in cyclic loading experiments (Sinha et al. 1964; Reinhardt et al. 1986). In CDP model, the stiffness degradation is taken into account by defining two scalar variables; compressive damage variable (d_c), and tensile damage variable (d_t) which are assumed to be functions of plastic strains. It should be pointed out that CDP model assumes unloading and subsequent reloading up to the monotonic path occur linearly with no hysteretic loops. The damage variables can take value from zero, representing the undamaged material to one, which represents complete damage (Simulia, 2016). The damage variables can be defined using **Eqs. 2.14** and **2.15**.

$$d_c = 1 - \frac{\sigma_c {E_0}^{-1}}{\sigma_c {E_0}^{-1} + \varepsilon_c^{in}(1 - b_c)} \qquad (2.14)$$

$$d_t = 1 - \frac{\sigma_t {E_0}^{-1}}{\sigma_t {E_0}^{-1} + \varepsilon_t^{in}(1 - b_t)} \qquad (2.15)$$

The b_c and b_t are proportional factors represent the relation between plastic and inelastic strains with values range of $0 \leq b_c, b_t \leq 1$. These proportional factors can be determined experimentally based on result of curve-fitting of cyclic uniaxial compressive and tension tests.

ABAQUS automatically converts the inelastic strains (ε_c^{in} and ε_t^{in}) to plastic strains (ε_c^{pl} and ε_t^{pl}) using the provided inelastic strain and damage variables (**Eqs. 2.16** and **2.17**). It should be mentioned that, in the absence of damage variables the plastic strains are taken equal to inelastic strains.

$$\varepsilon_c^{pl} = \varepsilon_c^{in} - \frac{d_c}{(1 - d_c)} \frac{\sigma_c}{E_0} \qquad (2.16)$$

$$\varepsilon_t^{pl} = \varepsilon_t^{in} - \frac{d_t}{(1 - d_t)} \frac{\sigma_t}{E_0} \qquad (2.17)$$

The stiffness recovery plays an important role in the mechanical response of concrete under cycling and dynamic loading. ABAQUS allows direct user specification two different stiffness recovery factors for compression (ω_c) and tension (ω_t). Based on experimental observation of concrete materials under reverse cycling loads, the compressive stiffness is recoverable upon crack closure as the load changes from tension to compression, i.e., $\omega_c = 1$. On the other hand, the tensile stiffness is not recoverable as the load changes from compression to tension once crushing micro-cracks have developed, i.e., $\omega_t = 0$. This behaviour is the default used by ABAQUS. **Figure 2.11** illustrates a uniaxial load cycle assuming the default stiffness recovery factors.

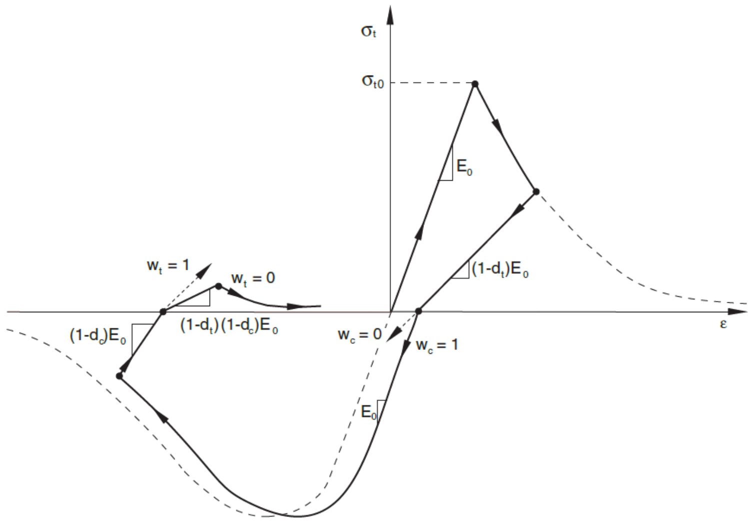

Figure 2.11 – Uniaxial load cycle of CDP model assuming default stiffness recovery factors

Yield surface and plastic flow rule

When the load exceeds the elastic limit (yield load), the deformation is no longer fully recoverable. Some part of the deformation will remain when the load is removed. The yield stresses are defined by a three-dimensional yield surface which generalizes the concept of yield load. The yield surface of CDP model is a modification of the Drucker–Prager strength hypothesis (Lublinear et al., 1989; Lee and Fenves, 1998). **Figure 2.12** illustrates the yield surface and flow potential function of CDP model. According to the modification, the yield surface of CDP model in the deviatoric plan is not a circle to allow for different yield tri-axial tension and compression stresses (**Figure 2.12-a**). This noncircular yield surface is governed by shape parameter (K_c). Physically, parameter K_c is interpreted as a ratio of second stress invariant for tension and compression at same hydrostatic stress (Simulia 2016). This ratio must satisfy the condition $0.5 \leq K_c \leq 1$ (default K_c value is 2/3). It should be mentioned that when $K_c = 1$ the yield stresses in tri-axial tension and compression are the same and the deviatoric plane of the failure surface becomes a circle as in the classic Drucker–Prager hypothesis.

In CDP model, the Drucker-Prager hyperbolic plastic potential function is used. The parameters needed to define the plastic flow are dilation angle (ψ), and flow potential eccentricity (ϵ). A geometric interpretation of ψ and ϵ are shown in **Figure 2.12-b**.

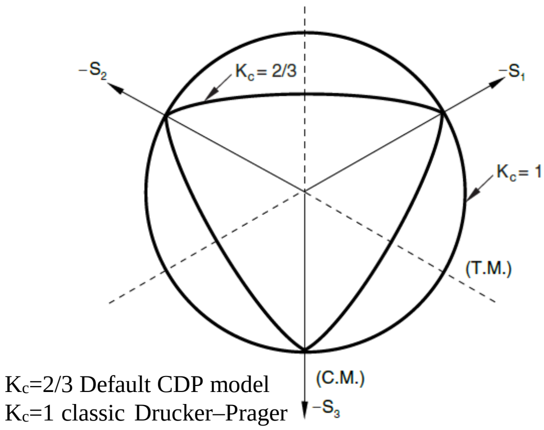

a) Yield surfaces in deviatory plane for different K_c

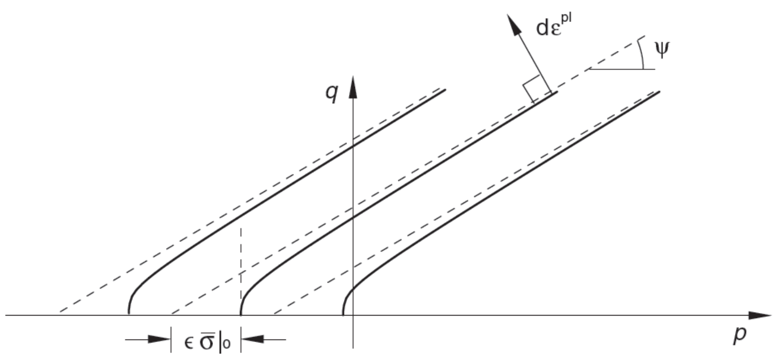

b) Yield surface and hardening in meridian plane

Figure 2.12 – Illustration of concrete damage plasticity model general shape (Simulia, 2016)

Physically, the dilation angle controls the amount of plastic volumetric strain developed during plastic shearing and is assumed constant during plastic yielding. In associated flow, dilation angle (ψ) is equal to concrete internal friction angle (β). Although CDP model assumes non-associated potential plastic flow where ψ<β, ABAQUS allows to approximate ψ=β in case of confined inelastic deformation since the difference between ψ and β is not large (Simulia 2016).

The eccentricity (ϵ) is a parameter that defines the rate at which the flow function approaches the asymptote. This parameter allows increasing the material dilation at low confinement. The function approaches the linear Drucker-Prager flow potential asymptotically at high confining pressure stress and intersects the hydrostatic pressure axis at 90° (**Figure 2.12-b**). The default flow potential eccentricity is $\epsilon = 0.1$ (Simulia 2016), which implies that the concrete has almost same dilation angle over a wide range of confining pressure stresses. Increasing the value of ϵ provides more curvature to the flow potential and dilation angle increases more rapidly as the confining pressure decreases. When ϵ value tends to zero the flow surface in the meridional plane becomes a straight line as in classic Drucker-Prager hypothesis.

Another parameter describing the state of the material is the ratio of the strength in the biaxial state to the strength in the uniaxial state (σ_{bo}/σ_{co}). The default stress ratio of σ_{bo}/σ_{co} is 1.16 (Simulia 2016).

The CDP model does not consider the strain rate effect automatically. Different tension and compression curves must be specified as a tabulated function of inelastic strain rate manually (Simulia, 2016).

2.6.6.2 Steel reinforcement constitutive model

Classical metal plasticity model has been chosen to define the full response of the steel reinforcement. This model assumes that the behaviour of the reinforcing steel is equal in tension and in compression. This model uses von Mises yield criterion assuming isotropic hardening. Strain rate effect is one of the most important material dynamic phenomena that must be included in the impact analysis of structures. Three different methods, the Cowper-Symonds over-stress power law (Cowper and Symonds, 1957), Johnson-Cook plasticity model (Simulia, 2016), and tabular input of enhanced yield stresses are offered in ABAQUS/Explicit to define the strain rate effect in the classical metal plasticity model.

2.6.7 Mesh size dependency

One of complexity associated with FE analysis of RC structures is mesh dependency of results. Several numerical studies reported that both tensile and compressive post-peak behaviour of concrete is mesh size dependent, in which the numerical results do not converge to a unique solution as the mesh is refined (Vebo and Ghali, 1977; Bazant and Cedolin, 1980). It is more affected by the in-elastic uniaxial tensile response rather than compression softening behaviour (Grassl and Jirasek, 2006). This problem is not limited to the static or low loading rates cases, but manifests identically in the dynamic loading case (Kwak and Gang, 2015). Mesh dependency typically occurs when a constitutive model based on smeared cracking approach is used to trace the damage progression in material with stress-strain softening response (Rabczuk et al., 2005). Intensive researches have been undertaken to overcome this drawback, particularly through the application of fracture energy concept (Marzouk and Chen, 1993a; Marzouk and Chen, 1993b; Kishi and Bhatti, 2010; Kwak and Gang, 2015).

CDP model offers the use fracture energy cracking criterion by defining the post-peak tensile stress-opening crack width response rather than stress-strain softening to minimize mesh dependency of results (Simulia, 2016). In general, a bilinear softening curve is the simplest function that describes concrete tension stiffening behaviour reasonably well and it has been used successfully in several FE analyses of RC members (Rabczuk et al., 2005; Genikomsou and Polak, 2015). In this dissertation, the fictitious crack model proposed by Hillerborg (1985) is used to define the descending branch of uniaxial tensile stress-crack displacement response. **Figure 2.13** illustrates the simplified uniaxial tensile response that is used as input in the numerical investigation phase. Three parameters are needed to define the adapted uniaxial tensile curve, namely: the elastic modulus (E), Tensile strength (f_t), and fracture energy (G_F). The determination of these parameters is provided in Chapters 3 and 6.

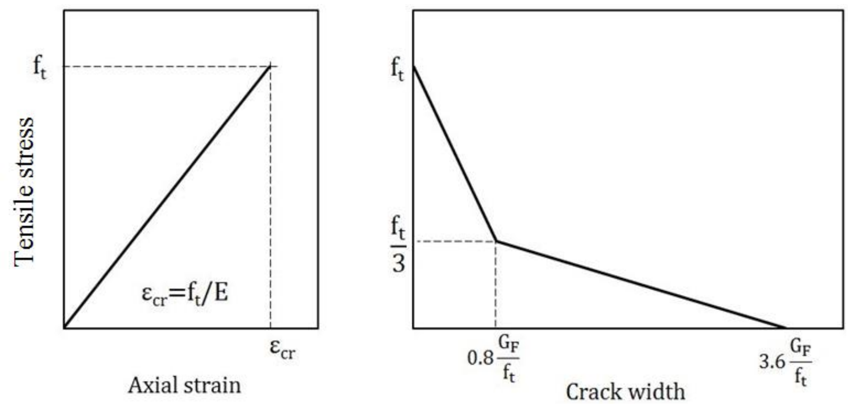

Figure 2.13 – Adapted uniaxial tensile relationshipe for concrete based on fracture energy

2.7 Review of Previous Numerical Investigations

In this section, a selection of previously developed numerical procedures that are relevant to the current study is described.

Miyamoto et al. (1991) investigated the ultimate behaviours and failure modes of doubly RC plates using nonlinear FE method. The concrete and steel reinforcement are modelled as smeared layers. The doubly reinforced plate was divided into eight layers, six layers to represent concrete and two layers to represent steel reinforcement. Out of plane shear stresses computed on the basis of the bending and twisting moments were used to modify the in plane stress conditions. The distribution of the out of plane shear stress was assumed to be parabolic through the thickness of the plate. Concrete was modelled using Drucker-Prager. While steel was modelled using elastic prefect plastic model. The external impulse load was applied at midpoint. The numerical model was verified using experimental test results from a series of RC plates tested by the same authors. Maximum deflections at mid-span and impulse load from zero to ultimate load were examined. The impact load-displacement responses of the slabs were estimated reasonably well from the FE analyses. The limitations of their study were the use of two-dimensional finite element (2D-FE), strain rate was not considered, and steel reinforcement was modelled using smeared reinforcement technique. This method is a suitable approach for overall global analysis of RC plates when the details of reinforcement are unnecessary.

Sangi and May (2009) modelled the RC plates tested by Chen and May (2009). The 3D-FE was conducted using LS-DYNA (J. Hallquist 2007). Concrete was modelled using 8 node solid elements with reduced integration. Two different built-in material constitutive models: Winfrith concrete and Concrete damage, were examined. Steel reinforcement was modelled using truss element using a simple bilinear model to define steel behaviour. The strain rate effect on steel was modelled using the Cowper and Symonds strain rate model. The modelling results showed the response shape and impact durations matched reasonably well with the experimental data, but the peak impact force was overestimated by up to 40 %.

Kishi and Bhatti (2010) proposed an equivalent fracture energy concept in order to reduce the mesh size dependency of the FE analysis of RC girders subjected to falling-weight impact loading. Assuming that the tensile fracture energy is the same for all elements irrespective of their sizes, fictitious tensile stress-strain relations are defined for the elements. The 3D-FE was applied using LS-DYNA code (J. Hallquist, 2007). Concrete geometry was modelled using eight-node solid elements with reduced integration and steel reinforcement was modelled using two-node beam elements assuming prefect bond between concrete and steel reinforcement. The concrete behaviour was modelled using a bilinear model in compression, and a cutoff model in tension. The applicability of equivalent tensile fracture energy concept was investigated numerically by comparison with experimental tests conducted by the same authors. It was observed that similar results can be obtained irrespective of element sizes when applying this method.

Kishi et al. (2011) performed a series of nonlinear 3D-FE analyses to simulate the behaviour of RC plates under drop-weight impact. The plates were 2,000 mm square, 180 mm thick, and were impacted at their midpoints using a 300 kg mass with an impact velocity of 4.0 m/s. The FE analyses of the plates were performed using LS-DYNA (J. Hallquist, 2007). Elements used in modelling the geometry as well as materials constitutive models for concrete and steel reinforcement were similar to those described above in Kishi and Bhatti (2010). The impact force-time, support reactions-time, and displacement-time histories computed numerically were in good agreement with the experimental data in terms of response shapes and frequencies. On the other hand, the peak amplitudes of the impact forces and midpoint displacements were underestimated. The previous two studies used too simple concrete model to show the complex behaviour of concrete under impact loads. For example, the stiffness degradation especially the post-peak softening response cannot be captured in Drucker–Prager model and the bilinear model on the compression side with a tension cutoff to simulate the uniaxial nonlinear dynamic response are too simple to describe the full response of material.

3 MATERIALS INVESTIGATION

3.1 Introduction

The material properties of UHP-FRC have been extensively studied, and its superior mechanical properties are well known (Graybeal, 2005; Graybeal, 2007; Roth et al., 2010; Wille et al., 2010; Wille et al., 2011; Wille, et al., 2012). Despite the obvious advantage of UHP-FRC mechanical and durability properties, its structural application is not very widespread. The expensive cost of patented UHP-FRC compositions, and high energy consumption during the production and curing, limits its commercial development and application in practical engineering (Rong et al., 2010). Additionally, the dynamic behaviour of UHP-FRC is not well established, particularly in terms of the enhancement in mechanical properties at high strain rates.

This investigation is motivated by the expensive production cost of UHP-FRC and the lack of dynamic increase factor (DIF) models that can be used in FE numerical simulation of impact loading scenarios on UHP-FRC material. In the present chapter, the developments of two UHP-FRC mixes are reported in details. Thereafter, the mechanical properties of HSC and UHP-FRC materials are investigated under various strain rates ranging from the static to impact level. This strain domain is the most relevant to common load cases in civil engineering structures. **Figure 3.1** shows typical orders of magnitude of strain rates for different loadings with a focus on the strain rate range corresponding to the loading rate of the present study. The DIFs determined based on the experimental tests are fitted with DIFs of latest CEB-FIP Model Code (2010) to examine the applicability of CEB-FIP in modelling UHP-FRC response under high strain rates.

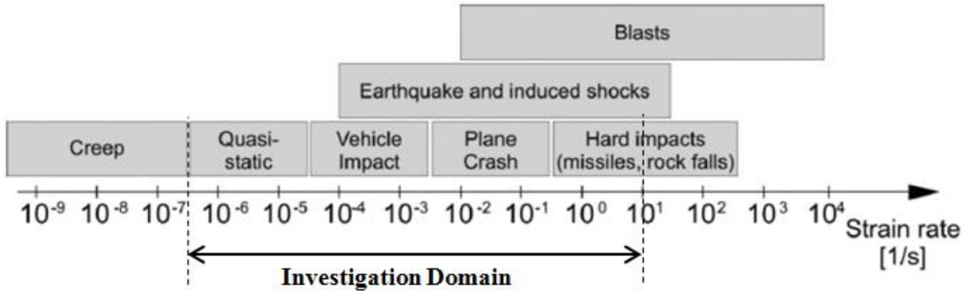

Figure 3.1 – Various loads cases and corresponding strain rates (Riisgaard et al., 2007)

The ultimate objective of the current materials investigation is to develop a fundamental understanding of the strain rate effect on the behaviour of UHP-FRC materials. Two parameters are investigated namely: compressive strength; and steel fibre content. As a second objective of this investigation is to generate accurate input data at different strain rates for HSC, UHP-FRCs, and steel reinforcement constitutive models that are required in the numerical simulation phase of this research program.

3.2 DIFs Formulas of CEB-FIP (2010)

The most comprehensive formulas for predicting the strain rate enhancement of concrete are presented by the CEB-FIP Model Code (2010). The DIFs formulas of CEB-FIP Model Code (2010) are based on the CEB *Bulletin 187* (1988). The CEB *Bulletin 187* itself is based on work by Reinhardt in 1985 (Malvar and Ross, 1998). The provisions of the CEB-FIP Model Code (2010) cover concretes up to characteristic strength of 120 MPa, including new fibre-reinforced cementitious materials. CEB-FIP proposes a series of strain-rate dependent relationships for concrete in both compression and tension. These relationships are independent of concrete strength and are applicable for strain rate up to 3×10^2 s^{-1}. All DIFs equations of CEB-FIP Model Code (2010) are presented in the following subsections and summarized in **Figure 3.2**.

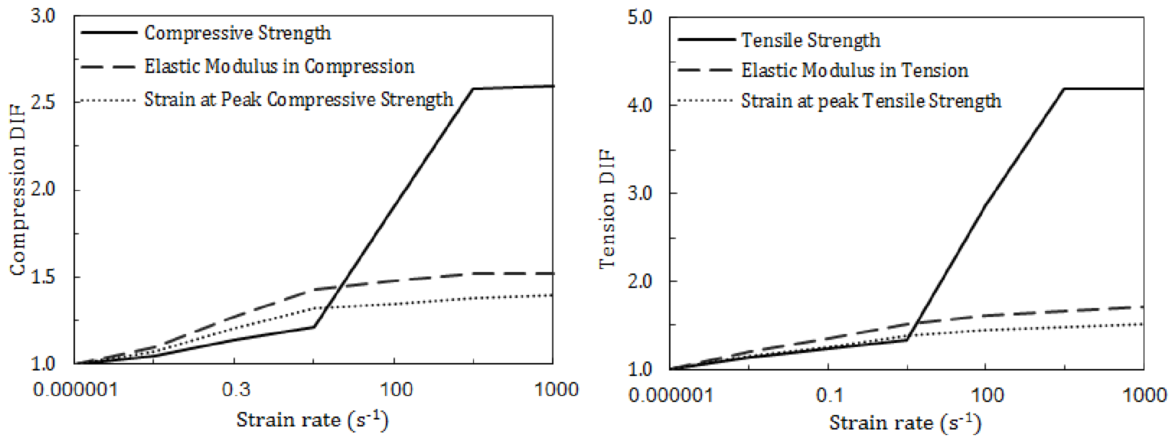

a) Concrete in compression b) Concrete in tension

Figure 3.2 – Summary of concrete DIFs according to CEB-FIP (2010)

3.2.1 CEB-FIP compression DIF model

The compression CEB-FIP model is applicable for strain rate ($\dot{\varepsilon}_c$) ranging from 30×10^{-6} (reference quasi-static rate) up 300 s^{-1}.

<u>The DIF of compressive strength (DIF_{fc}) is computed using:</u>

$$\mathrm{DIF_{fc}} = \frac{f_{cd}'}{f_c'} = \left(\frac{\dot{\varepsilon}_c}{30\times10^{-6}}\right)^{0.014} \qquad \text{for} \quad \dot{\varepsilon}_c \le 30\ \mathrm{s^{-1}} \qquad (3.1a)$$

$$\mathrm{DIF_{fc}} = \frac{f_{cd}'}{f_c'} = 0.012\left(\frac{\dot{\varepsilon}_c}{30\times10^{-6}}\right)^{1/3} \qquad \text{for} \quad 30 < \dot{\varepsilon}_c \le 300\ \mathrm{s^{-1}} \qquad (3.1b)$$

Where:

f_{cd}' = the compressive strength corresponding to strain rate of $\dot{\varepsilon}_c$;

f_c'= the compressive strength corresponding to the reference static strain of 30×10^{-6} s^{-1}

<u>The DIF of compressive elastic modulus (DIF_{Ec}) is computed using:</u>

$$\mathrm{DIF_{Ec}} = \frac{E_{cd}}{E_c} = \left(\frac{\dot{\varepsilon}_c}{30\times10^{-6}}\right)^{0.026} \qquad \text{for} \quad 30\times10^{-6} \le \dot{\varepsilon}_c \le 300\ \mathrm{s^{-1}} \qquad (3.2)$$

Where:

E_{cd}= the elastic modulus corresponding to strain rate of $\dot{\varepsilon}_c$;

E_c =the elastic modulus corresponding to the reference static strain of 30×10^{-6} s^{-1}

And strain at peak compressive strength ($DIF_{\varepsilon o}$) is computed using:

$$DIF_{\varepsilon o} = \left(\frac{\dot{\varepsilon}_c}{30 \times 10^{-6}}\right)^{0.02} \qquad \text{for} \quad 30 \times 10^{-6} \leq \dot{\varepsilon}_c \leq 300\ \mathrm{s}^{-1} \qquad (3.3)$$

3.2.2 CEB-FIP tension DIF model

The tension CEB-FIP model is applicable for strain rate ($\dot{\varepsilon}_t$) ranging from 1×10^{-6} (reference quasi-static rate) up 300 s^{-1}.

The DIF of concrete tensile strength (DIF_{ft}) is computed using:

$$DIF_{ft} = \frac{f_{td}}{f_t} = \left(\frac{\dot{\varepsilon}_t}{1 \times 10^{-6}}\right)^{0.018} \qquad \text{for} \quad \dot{\varepsilon}_t \leq 10\ \mathrm{s}^{-1} \qquad (3.4a)$$

$$DIF_{ft} = \frac{f_{td}}{f_t} = 0.0062\left(\frac{\dot{\varepsilon}_t}{1 \times 10^{-6}}\right)^{1/3} \qquad \text{for} \quad 10 < \dot{\varepsilon}_t \leq 300\ \mathrm{s}^{-1} \qquad (3.4b)$$

Where:

f_{td}= the tensile strength corresponding to strain rate of $\dot{\varepsilon}_t$;

f_t =the tensile strength corresponding to the reference static strain of 1×10^{-6} s^{-1}

The DIF of tensile elastic modulus (DIF_{Et}) is computed using:

$$DIF_{Et} = \frac{E_{td}}{E_t} = \left(\frac{\dot{\varepsilon}_t}{1 \times 10^{-6}}\right)^{0.026} \qquad \text{for} \quad 1 \times 10^{-6} \leq \dot{\varepsilon}_c \leq 300\ \mathrm{s}^{-1} \qquad (3.5)$$

Where:

E_{td}= the tensile elastic modulus corresponding to strain rate of $\dot{\varepsilon}_t$;

E_t =the tensile elastic modulus corresponding to the reference static strain of 1×10^{-6} s^{-1}

The DIF of strain corresponding to peak tensile strength ($DIF_{\varepsilon t}$) is computed using:

$$DIF_{\varepsilon t} = \left(\frac{\dot{\varepsilon}_t}{1 \times 10^{-6}}\right)^{0.02} \qquad \text{for} \quad 1 \times 10^{-6} \leq \dot{\varepsilon}_c \leq 300\ \mathrm{s}^{-1} \qquad (3.6)$$

3.3 Development of UHP-FRC

This section reports the mix designs of two developed UHP-FRC during the preparation phase of the current research program. The two mixes have been developed using locally available materials in Canada. The mix designs are resulted from a series of trial mixtures and modifications on the composition developed by Rossi et al. (2005).

In general, a standard mixture design for UHP-FRC does not exist. However, all UHP-FRCs types are originally based on the same principles of improving homogeneity, packing density, and ductility. The developed matrices are based on almost same general principle of UHP-FRC reported in Chapter 2. The principles of the two developed UHP-FRC mixes can be summarized as follows: The homogeneity of the mix is enhanced by replacing coarse aggregate by fine sand with a maximum size of 500 μm; the properties of cement matrix is improved by the addition of pozzolanic admixture (silica fume) in the range of 20% to 25% of the cement weight; water-cement ratio is reduced to below 0.23; superplasticizer is included to decrease water demand and improve workability; short steel fibres with a content of 2% by volume is added to achieve ductility; the mixing and curing procedures are maintained as existing practice in order to decrease the production cost.

Table 3.1 summarizes the mix proportions and the compressive strength of the two developed UHP-FRC matrices. The selection of raw materials and mixing proportions are based on extensive review of the previous research on the development of UHP-FRC materials, such as (Richard and Cheyreezy, 1995; Rossi et al., 2005; Roth et al., 2010; Wille, et al., 2011; Wille, et al., 2012), as well as the availability and the cost of raw materials. The details of the used constituents and mix proportions are presented in the following subsections. Mixing process, workability characteristics and mechanical properties are presented in the materials investigation section with other tested concrete materials.

Table 3.1 – Mix proportions of the two developed UHP-FRC

Target compressive strength, f_c' (MPa)		105-115	125-140
Material	Product	Proportion by weight	
Cement	GU Lafarge Portland cement	1	1
Silica fume	Eucon MSA (Grey SF)	0.20	0.24
Fine sand	foundry grade Ottawa sand	0.67	0.60
Water	Tap water	0.22	0.19
Superplasticizer	Plastol 6200EXT (40% solid content)	0.030	0.038
Steel fibres (2%)	Nycon-SF® (aspect ratio of 13/0.2)	0.163	0.149

3.3.1 Cement type

Typically, Portland cement Type I ASTM standard is used in UHP-FRC mixes. Wille et al. (2011) tested fifteen different mixtures with different cement types, the result of the study showed that best results in terms of strength and workability were achieved with Portland cement Type I, also Type II/V Portland cements showed good properties with respect to compressive strength and spread value, but the availability of Type II/V may be limited compared to Type I. Therefore, ordinary Portland cement (GU Lafarge Portland Cement) supplied by Lafarge North America conforming to ASTM C150 is used. This cement has a specific gravity of 3.15.

3.3.2 Silica fume

Silica fume is one of the principal constituents of the UHP-FRC. Silica fume reacts chemically with the calcium hydroxide in the cement paste, which yields a calcium silicate hydrate gel that significantly enhances strength, durability and reduces pore sizes. The fine micro-silica also fills the empty spaces between cement particles creating a very dense, less permeable concrete matrix. It should be mentioned that, the effect of silica fume type on the compressive strength of

UHP-FRC is negligible (Wille et al., 2011). The optimum silica fume content is around 25% of cement weight (Wille et al., 2011; Habel et al., 2008). However, the high cost of silica fume leads most manufacturers to recommend the dosage below 15%. In this study, grey silica fume (trade name Eucon MSA) with a specific gravity of 2.20 and conforms to the requirements of ASTM C1240 is used. The content of silica fume in the concrete mix is selected to be close to the optimum content (i.e., 25% of cement weight).

3.3.3 Aggregates

As mentioned before, no coarse aggregates are used in UHP-FRC mixes. Fine foundry grade Ottawa sand is selected in the current study. The particles of Ottawa sand are round with mean, and maximum sizes of 250, and 500 μm, respectively. The specific gravity of sand particles is 2.65.

The ratio of sand/cement in the original mix design proposed by Rossi et al. (2005) was 0.48 which is too low compared to a ratio of greater than 1.00 in most commercial UHP-FRC mixes (Graybeal, 2005). Based on the trial mixes results, the sand/cement ratio can be increased up to 0.67 to keep cement as low as possible.

3.3.4 Water-cement ratio

UHP-FRC mixes are made with a very low water-cement (w/c) ratio. Typically, w/c less than 0.25 is used (Schmidt and Fehling, 2005). The influence of the w/c on the compressive strength of UHP-FRC was studied by Wille et al. (2011). All tested UHP-FRC mixes were containing 2.5% fibres by volume. The lowest reported compressive strength was 115 MPa at w/c of 0.26 and the highest compressive strength was 206 MPa at w/c of 0.2. The water-binder ratio is another parameter that should be taken into account in selecting the water content. The binder is the sum of the cement and the silica fume. Typically, UHP-FRC and RPC mixes have water-binder ratio between 0.14 and 0.2 (Richard and Cheyreezy, 1995; Rossi et al., 2005; Schmidt and Fehling, 2005). Based on the presented ratios and conducted trial mixes, the upper limit of w/c is restricted to 0.23. It is worth mention, UHP-FRC does not exhibit any weight loss or drying shrinkage because of the very low w/c ratio.

3.3.5 Superplasticizer

Superplasticizer is essential in UHP-FRC mixes to decrease water demand, and improve workability. The superplasticizer product used is (Plastol 6200EXT), which is a high-range water-reducing admixture polycarboxylate type with a 40% solid content by mass. This product conforms to ASTM C494/C494M Type A. Plastol 6200EXT was sourced from a local supplier (Euclid Chemical Company) in Toronto, Canada. The superplasticizer content of the original mix is 4% of cement weight (Rossi et al., 2005). Wille et al. (2011) recommended an optimum range of 1.4 to 2.4% of cement weight. In the current mixes, the superplasticizer content in range of 3 to 4% is selected based on the observation of mixing process and workability tests of the trial mixes.

3.3.6 Fibres

Fibres play the key role in improving the ductility, tensile strength, and fracture properties of UHP-FRC matrix. Commonly used straight, smooth, high-strength steel fibres are selected. Type I copper-coated steel fibres (Nycon-SF®) is used based on the required geometrical aspect ratio, availability, and price. These fibres have a small diameter of 0.2 mm and are 13 mm long. This fibre geometry has an aspect ratio of 65, offering a trade-off between good workability and high pull-out resistance (Wille et al., 2010). Only fibre content of 2% by volume is considered in the mixes because this fibre content has been found to be the optimum out of thousands of tests with high bending and direct tensile strength (Acker and Behloul, 2004). Additionally, this fibre content is a commonly used percent in the industry.

3.4 Experimental Investigation of HSC and UHP-FRCs

An experimental program has been conducted to investigate compressive strength, elastic modulus, and flexural strength of HSC and UHP-FRCs at six different strain rates ranging from static to impact level. Five UHP-FRC matrices and one control HSC are tested. Two parameters are investigated namely: steel fibre volume content (1.0, 2.0, and 3.0%); and matrix strength (110, 130, 150 MPa). **Figure 3.3** shows a flowchart depicting the experimental program for this study.

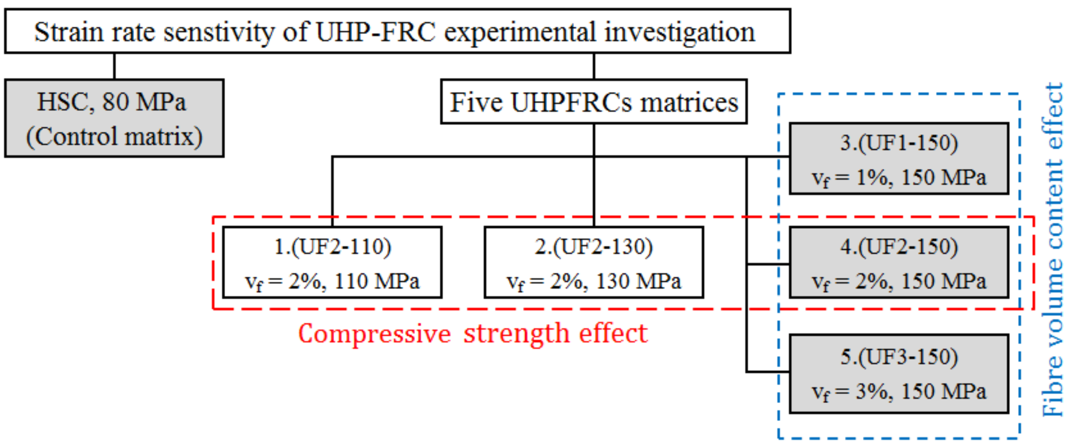

Figure 3.3 – Details of experimental investigation of strain rate effect

For easier reference, the UHP-FRC matrices are named according to their fibre volume content (v_f) and characteristic compressive strength (e.g., UF_1-150 for UHP-FRC matrix containing 1% fibres and compressive strength of 150 MPa). All tests have been carried out at the age of 56 days to allow materials reach their maximum strength. Identical specimens are used in both static and dynamic tests with similar loading and support conditions to avoid size effect. Two types of specimens (cylinders and prisms) are used for compressive and flexural strength tests, respectively, leading to twelve series of tests.

3.4.1 Materials

Table 3.2 provides the mix proportions of concrete materials used throughout this investigation. The control matrix is a conventional plain HSC with target 56-day cylinder-compressive strength of 80 MPa. The mix design of HSC matrix includes ordinary Portland cement, quartzite sandstone, crushed granite of 12 mm maximum nominal size, 6% silica fume, and water-cement ratio of 0.35. This matrix is based on the composition developed and used previously in (Marzouk, 1991; Marzouk and Hussein, 1992; Marzouk and Chen, 1995).

The other five concrete matrices are UHP-FRC with target 56-day cylinder compressive strengths ranging from 100 to 150 MPa. The first and second UHP-FRC matrices (UF_2-110 and UF_2-130) are containing 2% steel fibre by volume with 56-day compressive strengths of 110 and 130 MPa, respectively. The details of mix proportions and raw materials of UF_2-110 and UF_2-130 are provided in the previous section. The remaining three UHP-FRCs matrices are proprietary product Ductal® specified by Lafarge North America (Lafarge, 2016). These three matrices (UF_1-150, UF_2-150, and UF_3-150) have target 28-day compressive strength of 150 MPa with different volume contents of 1, 2, and 3%, respectively. UF_1-150, UF_2-150, and UF_3-150 mixes have identical mix proportions with exception of fibre volume dosage. The manufacturer supplied the Ductal® constituents in three separate groups: premix, fibres, and superplasticizer. The batched premix consists of a blend of all cementitious, fine sand, and silica fume materials. The superplasticizer is a high-range water-reducing admixture.

Short straight steel fibres are used in all UHP-FRC mixes. The fibre manufacturer's specified the following nominal properties: minimum tensile strength of 2,600 MPa, elastic modulus of 205 GPa, mass density of 7850 kg/m^3, diameter of 0.2 mm, and length of 13 mm.

Table 3.2 – Mixtures proportions by weight (kg/m^3)

Constituent	**HSC**	**UF$_2$-110**	**UF$_2$-130**
Portland cement	450.0	960.0	1050.0
Silica fume	30.0	190.0	250.0
Fine sand (size < 0.5 mm)	550.0	650.0	630.0
Coarse aggregate (size < 12 mm)	1100.0	n/a	n/a
Water	220.0	210.0	200.0
Superplasticizer	20.0	30.0	40.0
Steel fibres (% by volume)	n/a	156 (2%)	156 (2%)
Ductal® (Proprietary mixture design)	**UF$_1$-150**	**UF$_2$-150**	**UF$_3$-150**
Premix	2195.0		
Superplasticizer	30.0		
Water	130.0		
Steel fibres (% by volume)	79 (1%)	156 (2%)	234 (3%)

It should be mentioned that the matrices shaded in grey in **Figure 3.3** and **Table 3.2** are cast as companion specimens alongside the full-scale RC plates (see, Chapters 4 and 5) using same concrete batches, to ensure having same mechanical properties of full-scale plates.

3.4.2 Mixing procedures and workability characteristics

To ensure the consistency and the quality of UHP-FRCs mixes, all UHP-FRCs are mixed following the same procedures using an in-house shear mixer located in the Structural laboratory of Ryerson University. The dry materials (cement, fine sand and silica fume) are mixed for 5 minutes, and then water and the superplasticizer are added slowly over the course of 2 minutes. Continue mixing as the UHPC changes from dry powder to paste (it normally took from 4 to 6 minutes). When the mixture became flowable, the fibres are added slowly over the course of 2 minutes, continue mixing for additional 10 minutes to ensure that fibres are spatially distributed well.

Because of the large concrete volume required to cast the control HSC small-scale specimens of material investigation, and the six full-scale HSC plates (see, Chapters 4 and 5), The HSC is mixed by a local ready-mix concrete company using the mix proportions reported in **Table 3.2** and delivered to the structural laboratory of Ryerson University.

The workability is tested subsequently using a flow table test in accordance with ASTM C1437. The mini slump cone is filled with UHP-FRC then removed to allow the concrete to flow freely without applying any external force. Ones the UHP-FRC reached the steady state the average diameter is calculated using three different measurements. Then, the flow table is dropped 20 times. Again, the average diameter is recorded after the concrete is settled. **Figure 3.4** shows the final flow diameter of the two kinds of UHP-FRC matrices, locally developed and Ductal®. According the research investigation conducted by Graybeal (2005), a flow measure that is above 200 mm is consistent with UHP-FRC that is easy to place. The two matrices locally developed (UF_2-110 and UF_2-130) showed final diameters ranged from 170 to 188 mm. Such flow values indicate that UHP-FRC would have some difficult to cast outside of a laboratory setting. The flowability can be improved by using two or more different size of fine sand and fine filler materials (Wille et al., 2011). Additionally, a series of trial mixes with different ratios of cement: superplasticizer: sand is required. However, this is not the focus of this research program and the objective of the two developed UHP-FRCs is achieved by generating test series with different strengths in the strain rate sensitivity study (refer to **Figure 3.3**). On the other hand, commercial Ductal® UHP-FRC mixes (UF_1-150, UF_2-150, and UF_3-150) show excellent flow characteristics with diameter equal the brass table diameter (250 mm) even before applying the 20 times drops.

Figure 3.4 – Flow table test (left: UF_2-110; right: UF_2-150)

The casting of all specimens is completed within 20 minutes after the completion of mixing. No heat is used during casting or curing. All specimens are cured following the same procedures: under moist burlap for 1 week. Then, all specimens are taken out of their moulds and stored in a moist-curing chamber at a temperature of 20^{o}C for an additional 3 weeks, then placed to dry in laboratory air conditions until testing at the age of 56 days. **Figure 3.5** summarizes typical casting and curing processes.

3.4.3 Adapted basic quasi-static strain rates

As mentioned before, DIF is defined as the ratio of the dynamic to static strength. To develop DIF versus strain rate relationships, all results of experiments conducted at different strain rates must be related to static strength measured at a specific quasi-static strain rate. This strain rate is called basic quasi-strain rate where DIF is taken equal to 1. In the literature, this strain rate is varied from $1{\times}10^{-8}$ to $1{\times}10^{-5}$ s^{-1} (Malvar and Crawford, 1998). Since the results of these experiments would be fitted with CEB-FIP Model Code 2010 formulas, the basic quasi-static strain rates of CEB-FIP are used; quasi-static strain rates of 3×10^{-5}, and 1×10^{-6} s^{-1} are adapted for the reported experimental compressive, and bending tests, respectively (CEB-FIP, 2010).

a) Preparation and casting process

b) Curing process (Left: under moist burlap for 1 week; right: curing chamber for 3 weeks)

Figure 3.5 – Typical casting and curing of test specimens

3.4.4 Compressive strength test procedures

Compressive strength and elastic modulus tests have been conducted on 100×200 mm cylinders. A hydraulic servo-controlled testing machine (MTS 815) is used to conduct the compression testing for both the quasi-static and dynamic ranges (**Figure 3.6**). For each tested matrix, three specimens are tested at each strain rate. Compressive tests are conducted according to ASTM C39 and the capture of the strain is completed according to ASTM C469.

Figure 3.6 – Compressive strength tests for all strain rates.

Figure 3.7 – Preparation and casting of cylinders with embedded fibre-optic sensors

As shown in **Figure 3.7**, the cylinders tested at basic quasi-static strain rate are equipped with an embedded fibre-optic sensor capable of measuring longitudinal deformations over a gauge length of 150 mm. The embedded fibre-optic sensors are used to verify the displacement rate reading of the machine, and to capture the descending response of stress-strain curve. More details about fibre-optics sensors and the calibration process are given in Ref. (Yazdizadeh, 2014). The loading rate is set through the software of the controlling computer as a displacement rate. As listed in **Table 3.3**, there are six different series of compressive strength tests at six different strain rates. The adapted basic displacement rate for the first static test is 0.36 mm/min that corresponds to the quasi-static strain rate of 3×10^{-5} s^{-1}. The highest loading rate used in this investigation is 1200 mm/min, which corresponds to strain rate of 10^{-1} s^{-1}. This high strain rate can represent values resulted during seismic loading, or from vehicle impact on bridge piers (CEB-FIP, 1988). It is clear that the ratio of the highest to the lowest strain rate is 3,300. This rate range is sufficient for impact analysis; however, for strain rate corresponding to blast and explosion, a special Hoskins bar test is required.

Table 3.3 – Summary of compressive strength and elastic modulus tests

<table>
<tr><th colspan="6">Matrix</th><th>Loading range</th><th>Strain rate (s^{-1})</th><th>Loading rate (mm/min)</th></tr>
<tr><td rowspan="6">HSC</td><td rowspan="6">UF_2-110</td><td rowspan="6">UF_2-130</td><td rowspan="6">UF_1-150</td><td rowspan="6">UF_2-150</td><td rowspan="6">UF_3-150</td><td>Quasi-static</td><td>3×10^{-5}</td><td>0.36</td></tr>
<tr><td rowspan="5">Dynamic range</td><td>3×10^{-4}</td><td>3.60</td></tr>
<tr><td>3×10^{-3}</td><td>36.0</td></tr>
<tr><td>1×10^{-2}</td><td>120</td></tr>
<tr><td>3×10^{-2}</td><td>360</td></tr>
<tr><td>1×10^{-1}</td><td>1200</td></tr>
</table>

The loading rate of the machine is verified by comparing the strain time histories calculated based on the machine and the other extracted from the fibre-optic sensor (**Figure 3.8**) and the results showed that the machine accurately recorded the displacement and time. The calculation of displacement rates that correspond to adapted strain rates are documented in **Appendix A**.

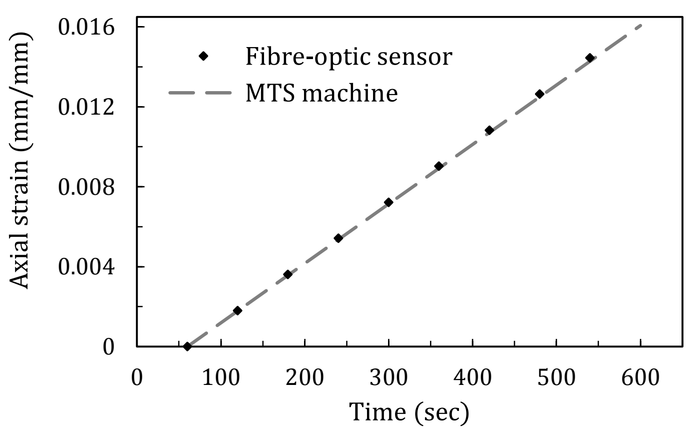

Figure 3.8 – Verification of MTS loading rate (UF_2-150, strain rate $=3\times10^{-5}$ s^{-1})

3.4.5 Flexural strength test procedures

Three-point bending tests have been conducted on 100×100×400 mm prisms with a clear span of 300 mm. Specimens are rotated 90 degrees from their casting position to reduce the effects of casting direction on the results. For each test series, three specimens are tested at each strain rate. Testing and the analysis of results have been carried out according to ASTM C1609. **Table 3.4** summarizes the conducted flexural tests and loading rates used. The loading rates are calculated assuming engineers' theory of bending and based on Young's modulus values resulted from compressive strength experimental tests at the quasi-static strain rate. More details about the calculation of loading rates are provided in **Appendix A.**

Table 3.4 – Summary of flexural strength tests

<table>
<tr><th colspan="6">Matrix</th><th colspan="2">Machine</th><th>Strain rate (s^{-1})</th><th>Loading rate (mm/min.)</th></tr>
<tr><td rowspan="6">HSC</td><td rowspan="6">UF_2-110</td><td rowspan="6">UF_2-130</td><td rowspan="6">UF_1-150</td><td rowspan="6">UF_2-150</td><td rowspan="6">UF_3-150</td><td rowspan="3">MTS 793</td><td>Quasi-static</td><td>1×10^{-6}</td><td>0.009</td></tr>
<tr><td rowspan="2">Low rates</td><td>1×10^{-5}</td><td>0.090</td></tr>
<tr><td>1×10^{-4}</td><td>0.90</td></tr>
<tr><td rowspan="3">Drop weight</td><td rowspan="3">High rates</td><td>From testing</td><td>150 [1]</td></tr>
<tr><td>From testing</td><td>300 [1]</td></tr>
<tr><td>From testing</td><td>600 [1]</td></tr>
</table>

[1] Drop-height in (mm)

A second hydraulic servo-controlled testing machine (MTS 793), shown in **Figure 3.9**, is used to perform tests for the first three loading rate ranges (**Table 3.4**). The load value and loading rate of the machine is verified by testing two prisms supported on load cells, and the results showed that the machine accurately recorded the force and time. For UHP-FRC matrices, the three-point bending test has been terminated when the measured localized crack width (macro-crack) associated with strain softening response is equal to 4 mm. This limit has been choosing since the deformation capacity of UHP-FRC is typically related to half fibre length (Habel and Gauvreau, 2008; Wille et al., 2012).

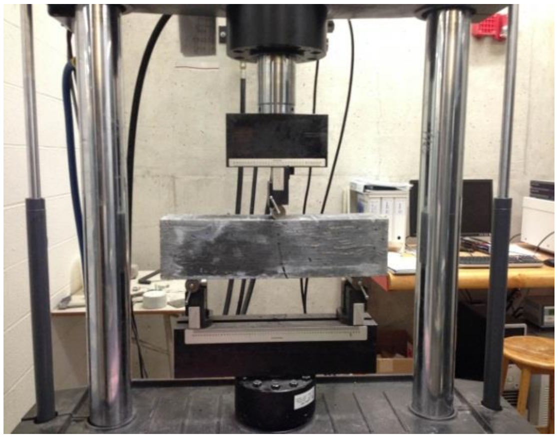

Figure 3.9 – Three-point bending tests for lower three strain rates (10^{-6} to 10^{-4} s^{-1})

The loading rates tests that are over the rate capacity of the hydraulic testing machine have been conducted using drop-weight impact technique. A small drop-hammer apparatus is designed, and developed especially to test prisms under high strain rates (**Table 3.4**). The schematic diagram of the setup and the test configuration is illustrated in **Figure 3.10**. The system has the capacity to drop a 37.5 kg mass from heights of up to 1200 mm. The drop-hammer is a solid steel cylinder and it is supported and guided by a steel frame. The striking surface of the drop-hammer is flat and circular of 51 mm diameter. In this study, three drop-heights (150, 300, and 600 mm) are considered, and three specimens are tested at each height.

The impact force is determined from the average reading of two (±2000*g*) accelerometers mounted to the drop-hammer. The reaction forces between the support and the specimens are measured using quartz cells. The raw data are sampled with a rate of 5 kHz using a digital dynamic data acquisition system ECON (model MI-7008). No damping materials are used in the contact zone between the hammer and the specimen during the tests, as that inadvertently reduces the strain rate. Additionally, all specimens are visually inspected after testing. To absorb the vibration results from impact and minimize the quantity of noise in the acquired data, a 50 mm fine sand layer is used as a support for the concrete platform.

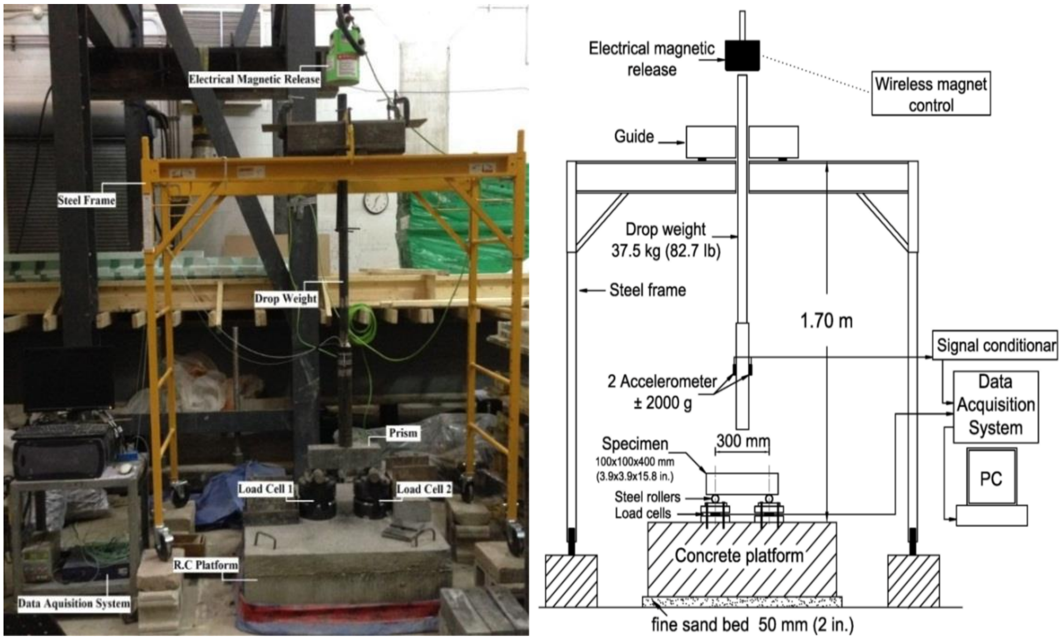

Figure 3.10 – Drop-hammer impact test setup for the higher three loading rates.

Figure 3.11 shows the impact and the reaction forces time histories curves. Comparing the impact force with the total reaction force, it is obvious that the peak of the impact force is greater than that of the reaction force. The reason is that most of the impact force is used to balance the inertia force, while a small portion of impact force is used to deform and fracture the specimen. Therefore, the inertia force has to be filtered out; otherwise, the material properties are significantly overestimated. To eliminate the inertia force effect and true flexural strength is obtained; the flexural loads and loading rates are calculated based on the total reaction time history (see, **Appendix A**). This approach has been used frequently by other researches (Soleimani and Banthia, 2014; Zhang et al., 2009) and verified experimentally by Soleimani et al. (2007).

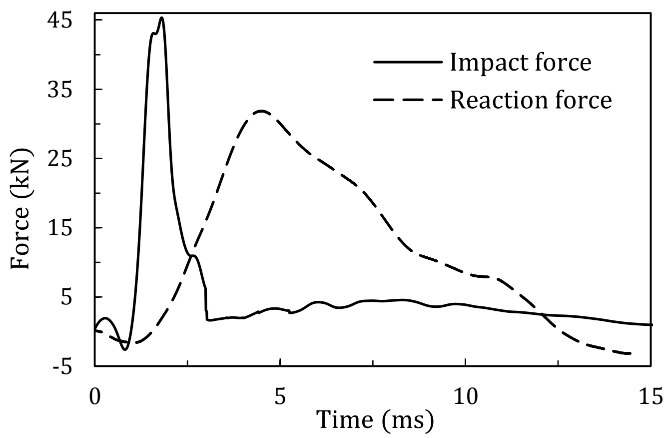

Figure 3.11 – Typical impact and reaction forces time histories (UF_2-110, height = 150 mm)

3.5 Experimental Results and Discussions

3.5.1 Basic static mechanical properties

The characteristic mechanical properties tested at the lowest (basic quasi-static) strain rate are summarized in **Table 3.5**. Each data point in the table is averaged from three specimens. The results of all tests are reported in **Appendix B**. In addition to tested properties, mass density and splitting tensile strength of concrete materials (HSC, UF_1-150, UF_2-150, and UF_3-150) are measured in order to supplement the geometrical and mechanical properties for concrete materials of the full-scale tests that are required in the numerical simulations (see, Chapters 4-6). The densities of concrete materials are estimated by taking the average mass of three cylinders. Splitting tensile tests are conducted according to ASTM C496 with a loading rate of 0.05 mm/min.

Figures 3.12 and **3.13** show the quasi-static response of all tested UHP-FRC matrices in comparison to HSC. It can be first observed that UHP-FRCs matrices exhibited ductile compressive and tensile response compared to free fibre HSC matrix. It is also evident that UHP-FRC matrices show strain hardening behaviour under both compression and flexural loading. It should be mentioned that the failure of HSC under compression test is of explosive nature and brittle sudden under flexural tests. HSC reached its compressive strength at a strain of 2.35 ‰. On the other hand, UHP-FRCs matrices do not exhibit explosive failure and specimens remained intact after testing. All UHP-FRC matrices reached the compressive strength at strains in the range of 4 – 4.5 ‰ regardless of fibre content and matrix strength.

Table 3.5 – Characteristic mechanical properties

Concrete Matrix	Density (kg/m^3)	Compressive strength f_c', (MPa)	Elastic modulus E_c, (GPa)	Flexural strength f_r, (MPa) [1]	Splitting strength f_{tsp}, (MPa)
HSC	2,540	83.1	30.2	8.0	4.51
UF_2-110	NA	110.8	33.8	12.1	NA
UF_2-130	NA	132.7	39.3	13.7	NA
UF_1-150	2,600	154.8	47.0	8.5	7.32
UF_2-150	2650	162.4	48.8	19.2	11.11
UF_3-150	2,710	158.7	49.3	28.3	14.03

NA not measured [1]based on the assumption of uniform, elastic, un-cracked cross-section

3.5.1.1 Effect of matrix strength on quasi-static response

Figure 3.12 shows the influence of matrix strength on the behaviour of all tested materials under basic quasi-static compression and flexural tests. It is evident that the compressive strength, elastic modulus, flexural strength and the post-cracking response are improved with matrix strength increase. A worth of mentioning here that the descending branches of all UHP-FRC curves have approximately the same slope because all of these matrices contain 2% fibres by volume.

The three-point tests for UF_2-110 and UF_2-130 reached the test termination criteria of 4 mm crack width at low levels of deformation compared to UF_2-150. The maximum mid-span displacement is around 4 mm at target crack width. On the other hand, the UF_2-150 reached a displacement of 6 mm at same crack width. This large difference in deformation capacity is not related to the matrix strength only. It is also depending on fibre-matrix bond properties during cracking-bridging mechanism which is more pronounced in UF_2-150 matrix (Ductal® mix) compared to UF_2-110 and UF_2-130. The fibre-matrix bond effect is also showed up clearly in enhanced strain hardening and elevated flexural strength value of UF_2-150 matrix (**Figure 3.12-b**).

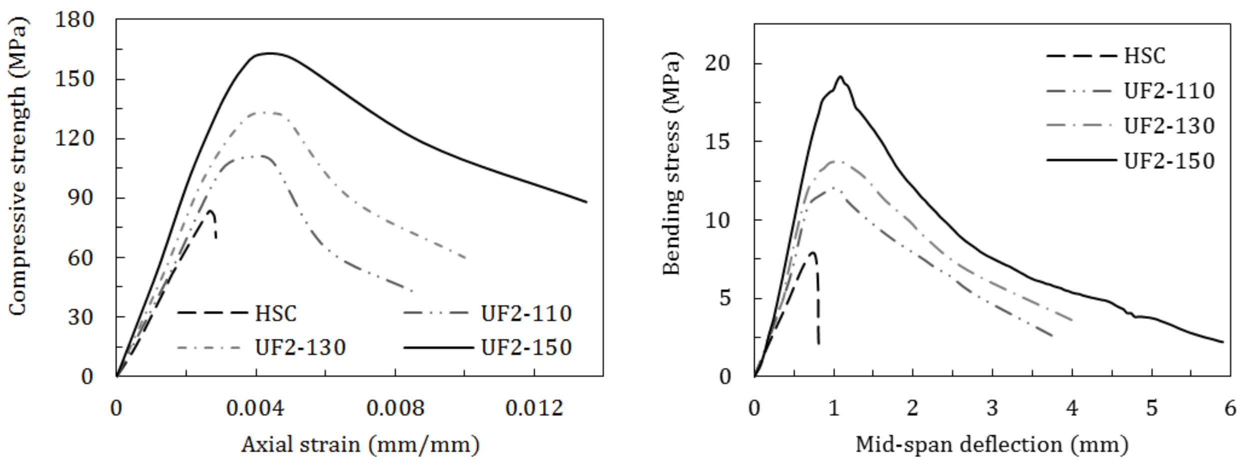

a) Compression response of cylinders b) Flexural response of prisms

Figure 3.12 – Influence of matrix strength on quasi-static response (average curves)

3.5.1.2 Effect of fibre volume content on quasi-static response

Figure 3.13 shows the influence of fibre volume content on the behaviour of UHP-FRC materials under basic quasi-static compression and flexural tests in comparison to the behaviour of HSC. It is evident that increasing fibre volume content from 1 to 3% led to significant post-peak ductility in both compression and flexural tension responses. The contribution of fibres is more pronounced in splitting (refer to **Table 3.5**) and flexural strength values (i.e., tensile strength) than in compressive strength and elastic modulus values. The effect of increasing the fibre content on compressive strength is found to be insignificant. Several researches have reported same observation (Mangat and Azari, 1984; Millard et al., 2010).

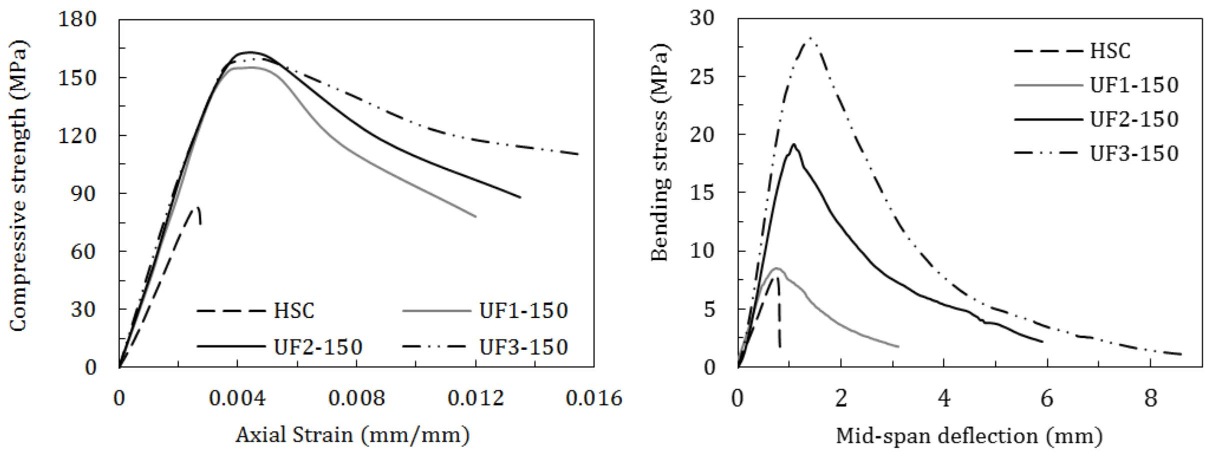

a) Compression response of cylinders b) Flexural response of prisms

Figure 3.13 – Influence of fibre volume content on the quasi-static response (average curves)

3.5.2 DIFs of compressive strength and modulus of elasticity

One hundred and eight cylinders are tested to determine the strain rate effect on compressive strength and elastic modulus. **Table 3.6** summarizes the test results for all matrices. Each data point in the table is averaged from three specimens. Comparison between DIF derived from tests and CEB-FIP (2010) for compressive strength and elastic modulus are given in **Figures 3.14** and **3.15**.

It is evident from **Figure 3.14** and **3.15** that, the mechanical properties increase with the increase in the loading rate; the CEB-FIP Model Code (2010) gives matching results for HSC, however, overestimates both compressive strength and elastic modulus enhancement for UHP-FRC matrices; DIF is higher for matrices with lower strengths and decrease with the increase of compressive strength for both compressive strength and elastic modulus (**Figure 3.14**); the DIF is different for compression and elastic modulus; and fibre volume content has no clear effect on the enhancement of compressive strength and elastic modulus (**Figure 3.15**).

Table 3.6 – DIFs experimental results for compressive strength and elastic modulus

Matrix	strain rate (s^{-1})	3×10^{-5}	3×10^{-4}	3×10^{-3}	1×10^{-2}	3×10^{-2}	1×10^{-1}
HSC	f_c' [1] (MPa)	83.1	85.5	89.4 [4]	90.8	93.3	94.7
	DIF[3]	1.00	1.03	1.08	1.09	1.12	1.14
	E_c [2] (GPa)	30.2	31.9	34.4 [4]	35	36.7	38.4
	DIF[3]	1.00	1.06	1.14	1.16	1.21	1.27
UF_2-110	f_c' [1] (MPa)	110.8	112.8	114	117.9	119.5 [4]	120.8
	DIF[3]	1.00	1.02	1.03	1.06	1.08	1.09
	E_c [2] (GPa)	33.8	34.7	35.5	36.8	37.9 [4]	39.8
	DIF[3]	1.00	1.03	1.05	1.09	1.12	1.18
UF_2-130	f_c' [1] (MPa)	132.7	133.9	136.1	137	139.1	143
	DIF[3]	1.00	1.01	1.03	1.03	1.05	1.08
	E_c [2] (GPa)	39.3	40.1	42.1	42.9	45	44.9
	DIF[3]	1.00	1.02	1.07	1.09	1.14	1.14
UF_1-150	f_c' [1] (MPa)	154.8	156.8	160.1	160.6	163.3	164.5
	DIF[3]	1.00	1.01	1.03	1.04	1.05	1.06
	E_c [2] (GPa)	47.0	48.5	48.9	50.8	50.9	50.9
	DIF[3]	1.00	1.03	1.04	1.08	1.08	1.08
UF_2-150	f_c' [1] (MPa)	162.4	164.3	165.6	168.2	171.1	173.5
	DIF[3]	1.00	1.01	1.02	1.04	1.05	1.07
	E_c [2] (GPa)	48.8	50.3	51.2	51.8	53.1	54.1
	DIF[3]	1.00	1.03	1.05	1.06	1.09	1.11
UF_3-150	f_c' [1] (MPa)	158.7	160.3	163.5	163.55	166.6	171.4
	DIF[3]	1.00	1.01	1.03	1.03	1.05	1.08
	E_c [2] (GPa)	49.3	50.5	52.1	52.3	53.0	54.1
	DIF[3]	1.00	1.02	1.06	1.07	1.07	1.10

[1] Compressive strength, [2] Elastic Modulus
[3] DIF = dynamic increase factor with respect to static case, [4] Average of two readings

It is obvious also from **Figure 3.15** that, there is scatter observed among DIFs results of specimens with different fibre contents, however, it is insignificant. The DIFs for all UHP-FRC matrices with compressive strength of 150 MPa have almost same slope regardless fibre dosage, which means that fibre content has no effect on the dynamic enhancement of compressive strength and elastic modulus. A worth of mentioning here similar conclusion has been drawn by Lok and Zhao (2004). In their investigation, steel fibre reinforced concrete with static compressive strength of 91 MPa has been tested under compression at strain rates between 20 and 100 s^{-1} using a split Hopkinson's pressure bar. It was concluded that the DIF of compressive strength of FRC increases with strain rate in the same way as plain concrete of same compressive strength (Lok and Zhao, 2004).

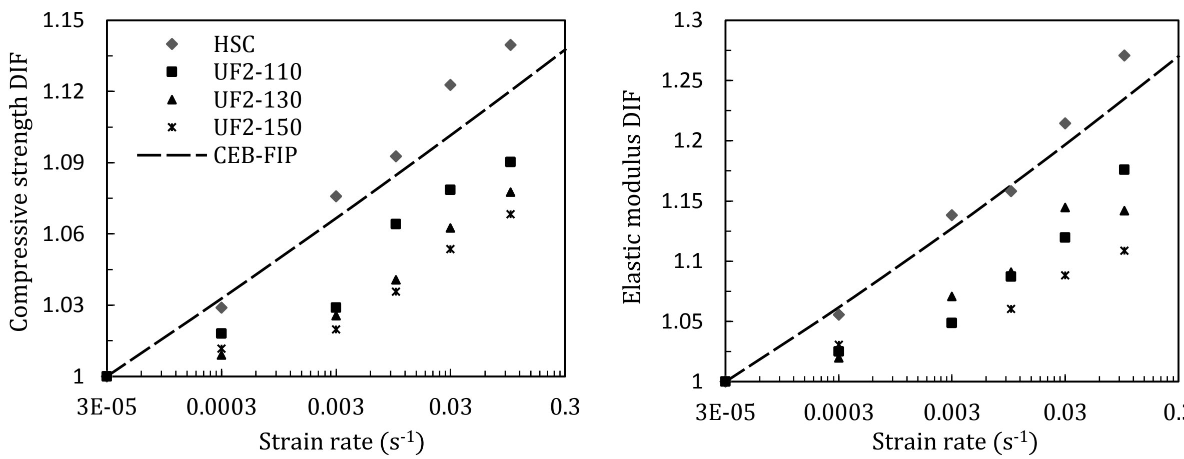

Figure 3.14 – Influence of matrix strength (left: Compressive strength; right: Elastic modulus)

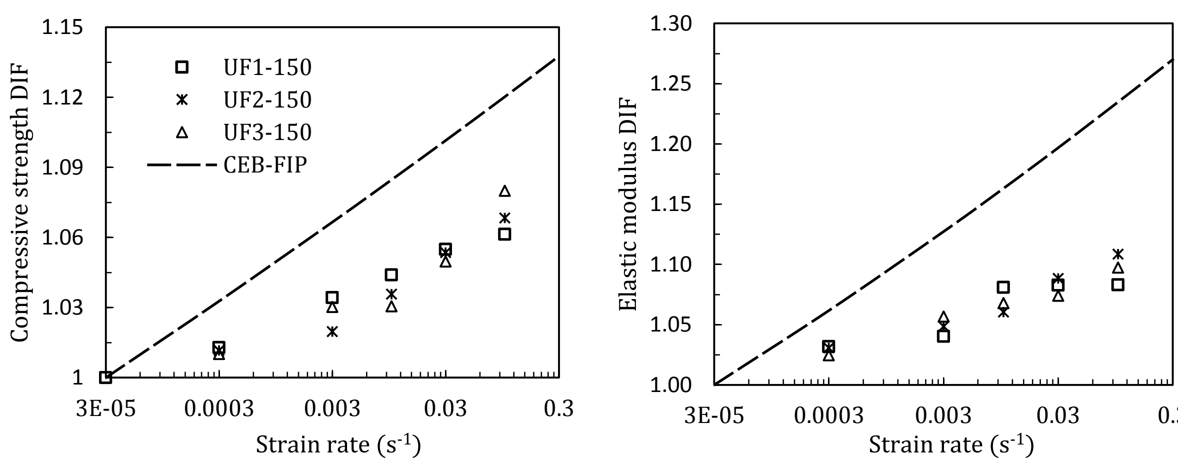

Figure 3.15 – Influence of fibre content (left: Compressive strength; right: Elastic modulus)

3.5.3 DIFs of flexural strength

Table 3.7 shows the flexural strengths for the lower three strain rates obtained using the hydraulic servo-controlled testing machine (MTS 793), and results from the dynamic flexural tests are given in **Table 3.8**. Analyzing the test results, the flexural tensile strength is more sensitive than the compressive strength and elastic modulus at same strain rate. Additionally, DIF is higher for matrices with lower strengths.

Table 3.7 – Rate effect on flexural strength for rate range 10^{-6} to 10^{-4} s^{-1}.

Matrix	HSC		UF_2-110		UF_2-130		UF_1-150		UF_2-150		UF_3-150	
Strain rate (s^{-1})	f_r[1]	DIF[2]	f_r[1]	DIF[2]	f_r[1]	DIF[2]	f_r[1]	DIF[2]	f_r[1]	DIF[2]	f_r[1]	DIF[2]
10^{-6}	8.00	1.00	12.10	1.00	13.7	1.00	8.50	1.00	19.21	1.00	28.31	1.00
10^{-5}	—	—	12.40	1.02	13.9	1.01	8.61	1.01	19.52	1.02	28.43	1.00
10^{-4}	8.95	1.23	12.65	1.05	14.12	1.03	8.95	1.05	19.80	1.03	28.63	1.01

Table 3.8 – Rate effect on flexural strength in high loading rates

Matrix	Drop-height (mm)	150	300	600
HSC	Strain rate (s^{-1})	0.32	1.63	2.55
	f_r [1] (MPa)	10.05	10.45	10.65
	DIF[2]	1.26	1.31	1.33
UF_2-110	Strain rate (s^{-1})	0.15	1.55	2.58
	f_r [1] (MPa)	13.80	14.25	14.51
	DIF[2]	1.14	1.18	1.20
UF_2-130	Strain rate (s^{-1})	0.79	1.33	2.50
	f_r [1] (MPa)	15.25	15.40	15.75
	DIF[2]	1.11	1.12	1.15
UF_1-150	Strain rate (s^{-1})	0.21	1.01	2.10
	f_r [1] (MPa)	9.65	10.00	10.21
	DIF[2]	1.14	1.18	1.20
UF_2-150	Strain rate (s^{-1})	0.10	0.99	2.05
	f_r [1] (MPa)	20.555	20.86	21.12
	DIF[2]	1.07	1.09	1.10
UF_3-150	Strain rate (s^{-1})	0.185	0.95	1.95
	f_r [1] (MPa)	29.40	29.65	30.02
	DIF[2]	1.04	1.05	1.06

[1] Flexural tensile strength,
[2] DIF = dynamic increase factor with respect to static case.

The dynamic flexural strength enhancement of the experimental results is shown in **Figure 3.16**. The results are compared with the model for strain rate enhancement of tensile strength of CEB-FIP Model Code (2010). DIF is higher for matrices with lower strengths and decrease with the increase of compressive strength (**Figure 3.16-left**). The dynamic enhancement is inversely proportional to the fibre content (**Figure 3.16-right**). It can be seen also CEB-FIP (2010) model overestimates the tensile enhancement for all UHP-FRC matrices. The maximum difference between DIF derived from CEB-FIP (2010) and experimental results is greater than 20%, which is significant when compared with the difference in compressive strength. On the other hand, CEB-FIP (2010) model gives matching results for HSC matrix.

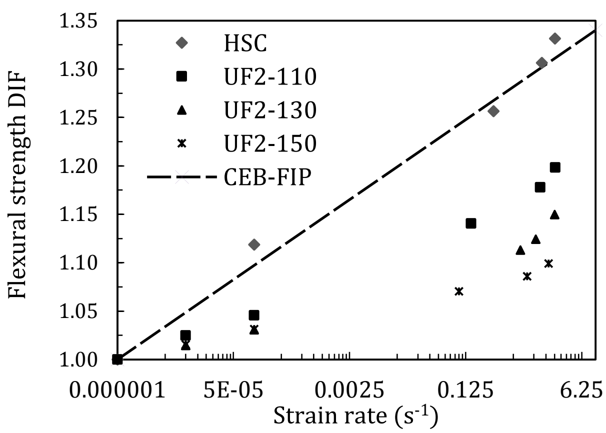

a) Influence of matrix strength

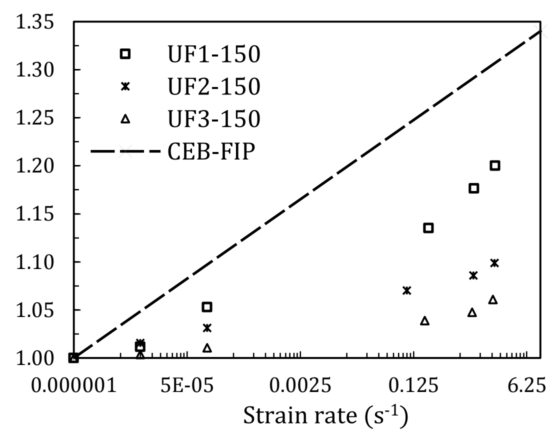

b) Influence of fibre content

Figure 3.16 – Comparison between DIF derived from tests and CEB-FIP for tensile strength

As shown in **Figure 3.17**, there is no significant variation in crack pattern observed for different strain rates, even at higher strain rates using drop-hammer impact setup. The cracking mode indicated that the specimens are failed in bending (tension side). No compression damage or inclined cracks are observed in all specimens, regardless concrete material, matrix strength, and fibre content. All HSC specimens failed suddenly in two pieces. On the other hand, UHP-FRCs specimens remained intact after testing and showed enhanced damage control properties. The damage level and crack width are correlated to the steel fibre content. Under same loading rate, specimens with higher fibre volume content showed less damage. Fibre pull-out is the only observed mode of fibres failure in all UHP-FRC specimens. Pull-out of short straight fibre has previously been shown to be independent of strain rate (UN Gokoz and Naaman, 1981; Suaris and Shah, 1982).

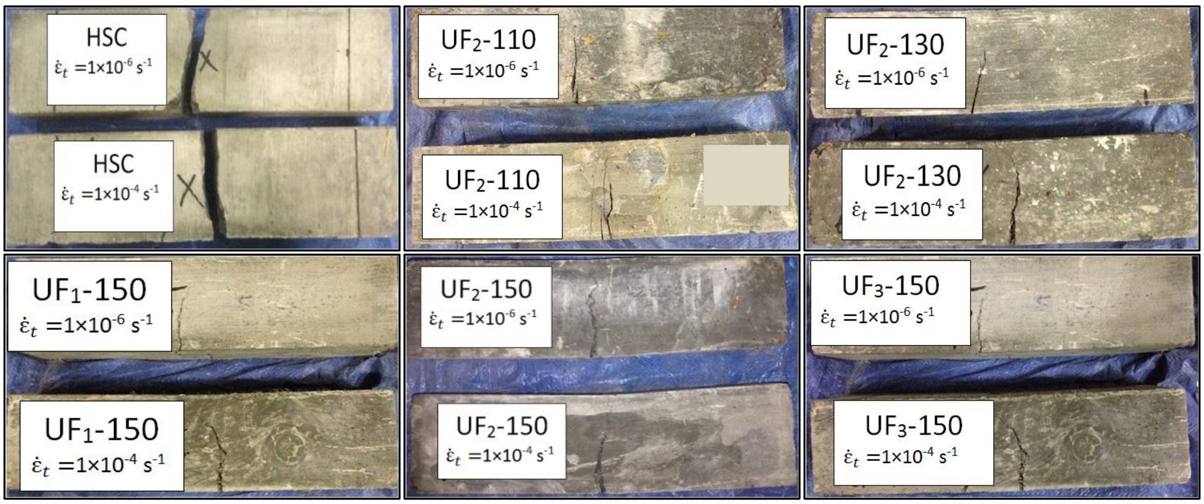

a) Low loading rates (MTS 793 machine)

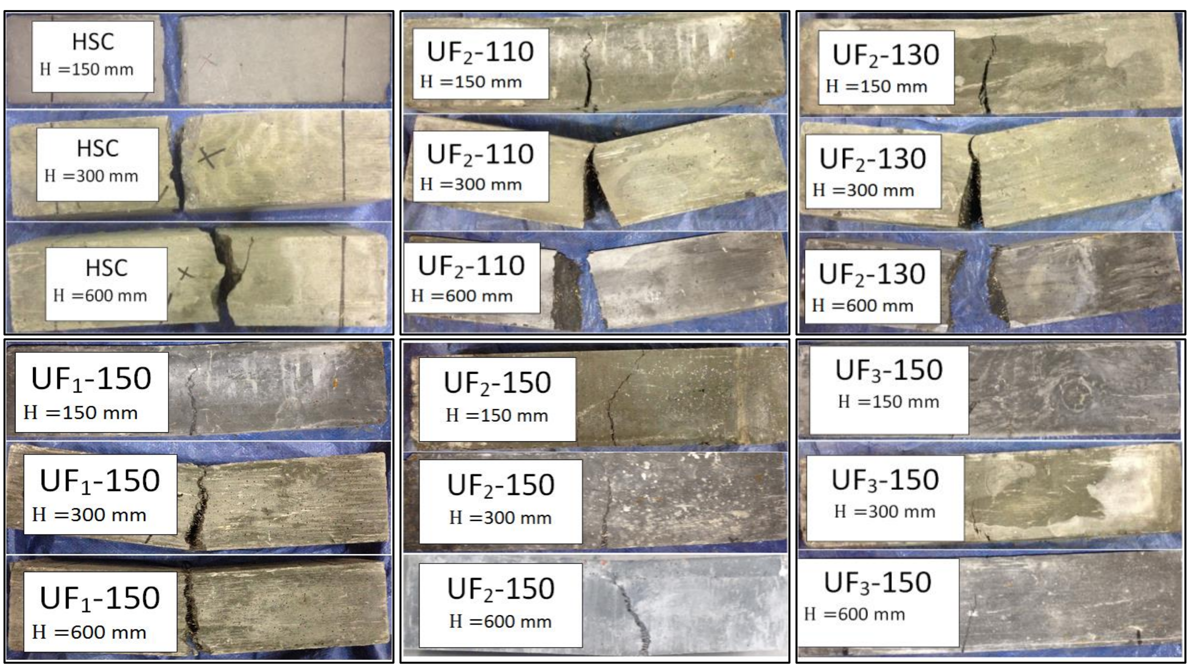

b) High loading rates (Drop-hammer test, H is the drop-height)

Figure 3.17 – Failure patterns of fleuxral test specimens

3.6 Steel Reinforcement Properties

Based on the second objective of this chapter, the material properties of steel reinforcement are measured. CSA standard Grade 400 deformed steel bars are used as longitudinal reinforcement in full-scale RC plates impact testing. Three typical bars sizes of 10M, 15M, and 20M are used as specimens' reinforcement (see, Chapter 4). The tested geometrical and mechanical properties of steel reinforcement are summarized in **Table 3.9**. Tensile coupon tests are carried out to determine the mechanical properties of steel reinforcement bars (**Figure 3.18**). The density is determined by weighting one meter length of steel bars. Each data in the table is averaged from three readings. The measurements of all tests are reported in **Appendix B**.

Table 3.9 – Material properties of steel reinforcement

Steel bar size	Diameter (mm)	Mass (kg/m)	Yield stress f_y, (MPa)	Ultimate strength f_{ult}, (MPa)	Elastic modulus E_s, (GPa)
10M	11.29	0.775	433.4	621.70	201.1
15M	15.95	1.560	435.00	618.30	204.24
20M	19.53	2.345	451.20	629.10	198.60

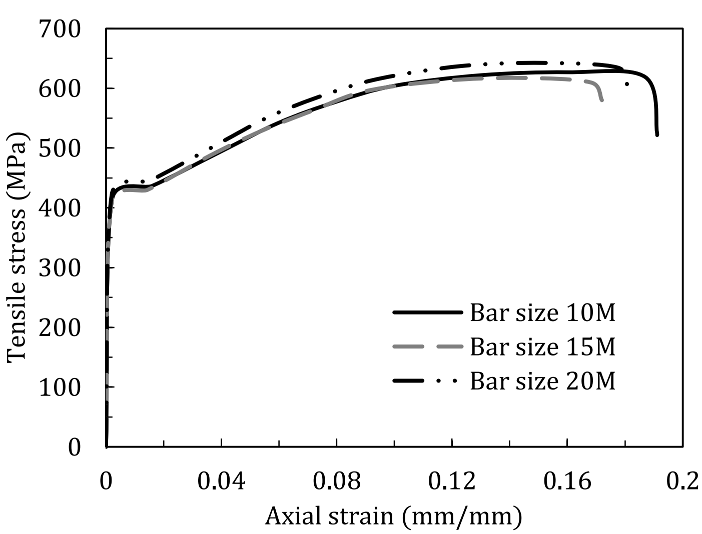

Figure 3.18 – Steel reinforcement stress-strain behaviour (average curves)

3.7 Summary of Material Investigation

The development of two UHP-FRC mixes using locally available materials in Canada is reported in details. Thereafter, an experimental investigation has been conducted to determine the dynamic behaviour of HSC and UHP-FRC materials. Two parameters are investigated namely: compressive strength; and steel fibre content. Compressive strength, modulus of elasticity, and flexural tensile strength has been investigated under six different strain rates, ranging from the static to the seismic and/or impact level. Additionally, accurate input data for HSC, UHP-FRCs, and steel reinforcement constitutive models that are needed in the numerical simulation phase of this research program have been generated. The following conclusions can be drawn from this materials investigation:

1. Based on the limited numbers of trial mixes, the production of UHP-FRC is no longer limited within the domain of patented or commercial product materials and the mix design will be available in near future.
2. Under compression tests, the failure of HSC is of explosive nature. HSC reached its compressive strength at a strain, ranging from 2.3 – 2.6 ‰. On the other hand, UHP-FRCs matrices do not exhibit explosive failure and cylinders remained intact after the test. All UHP-FRC matrices reach the compressive strength at a strain in the range of 4 – 4.5 ‰ regardless of fibre content.
3. Increasing fibre volume content from 1 to 3 % significantly increases the quasi-static tensile properties and post-peak ductility, however, fibre volume content has shown a limited effect on quasi-static compression properties.

4. The compressive strength, elastic modulus, and the flexural tensile strength increased with the increase of strain rates. However, the flexural tensile strength is more sensitive than both compressive strength and elastic modulus at same strain rate.

5. DIFs are higher for matrices with lower strengths and decrease with the increase of matrix strength for compressive strength, elastic modulus, and flexural strength.

6. The dynamic enhancement of flexural (tensile) strength is inversely proportional to the fibre content. On the other hand, the effect of fibre content on dynamic enhancement in compression is insignificant. All UHP-FRCs matrices exhibited almost same compressive DIFs regardless of fibre content.

7. The DIFs formulas of CEB-FIP Model (2010) fit reasonably well with HSC results in both compression and tension. On the other hand, the CEB-FIP Model (2010) overestimates DIFs for all UHP-FRC matrices, especially matrices of compressive strength greater than 110 MPa. The difference between CEB-FIP and experimental results was found to be more pronounced in tension since fibre contribution is much more effective.

8. Quasi-static and drop-weight bending tests have identical failure patterns for all concrete matrices: cracking started on the tension side of high moment zone regardless of concrete material, matrix strength, and fibre content. All HSC specimens split suddenly into two pieces. On the other hand, UHP-FRCs specimens remained intact after testing and showed enhanced damage control properties. The damage level and crack width were correlated to the steel fibre content. Under same loading rate, specimens with higher fibre volume content showed less damage. Fibre pull-out is the only observed mode of failure for fibres in all UHP-FRC specimens.

4 IMPACT TESTING OF RC PLATES

4.1 Introduction

The experimental program presented in this chapter focuses on the structural behaviour of full-scale RC plates, as well as generating precise low-velocity impact measurements that are required to calibrate the FE models. Two different series of low-velocity impact tests on RC plates using the same test setup have been conducted in the Structural Laboratory of Ryerson University. The first series, plates are cast using conventional non-fibrous HSC of 80 MPa target compressive strength. The main objectives of this series are to investigate: the effect of main bottom steel reinforcement ratio; and the steel reinforcement arrangement (single or doubly reinforced plates) on the behaviour and failure mode of the RC plate under impact loading. This test series has also served as a pilot test to check the developed drop-weight impact setup, implemented instrumentation, selected sampling rate of data acquisition system, and filtering process. The second testing series focuses on assessing the advantage of using UHP-FRC in impact resistance structural elements. The main objectives of this series are to investigate the effect of concrete matrix, fibres volume content and steel reinforcement ratio, on dynamic response and impact capacity of UHP-FRC plates. Specimens of the second series are cast using UHP-FRCs of 150 MPa target compressive strength. In addition, two control specimens constructed using NSC and HSC of compressive strengths of 40 and 80 MPa, respectively, are tested in this series.

This chapter provides a description of RC specimens, developed drop-weight impact test setup, instrumentations, and loading protocol that have been utilized in this experimental investigation.

The results and discussions are given in the next chapter. The details of concrete materials proportions, and tested geometrical and mechanical properties are given in Chapter 3.

4.2 Test Specimens

In total, twelve RC plate specimens of nominal identical geometry are constructed and tested under drop-weight low-velocity impact loading conditions. One specimen is cast using NSC, six specimens are cast using HSC, and the remaining five plates are cast using UHP-FRCs. Manufacturing of formworks and castings are carried out in the Structural Laboratory of Ryerson University. All plate specimens are 1950 mm square with a total thickness of 100 mm and 15 mm clear cover to reinforcement. Specimens are designed such that, under static monotonic loading conditions, a ductile tension failure of reinforcement governed ultimate capacity. As mentioned before, there are two test series with quite different parameters and objectives. Therefore, the details of each test series are presented separately in the following subsections.

4.2.1 Details of HSC series

Five HSC plates with identical dimensions and reinforcement spacing are constructed and tested. The concrete mix used in this series is a conventional non-fibrous HSC with target 56-day cylinder-compressive strength of 80 MPa previously described in Chapter 3. To address the effect of steel reinforcement distribution, two parameters are investigated namely: main bottom steel reinforcement ratio (1.0, 2.0, and 3.0%); and steel reinforcement arrangement (single or doubly reinforced plates). The variation in main bottom steel reinforcement ratios is achieved by increasing the bar size while reinforcement spacing is kept constant and equal to 100 mm. CSA standard Grade 400 deformed steel bars are used as longitudinal reinforcement (CSA A23.3, 2004). Three typical bars sizes of 10M, 15M, and 20M are used as specimens' reinforcement. Single and doubly reinforced plates are constructed as pairs with identical main bottom reinforcement. For doubly reinforced plates, the top reinforcement is kept constant, CSA Standard 10M bars with spacing 210 mm are used as minimal top reinforcement. Plates' identification, dimensions, reinforcement details, and cross sections are shown in **Figure 4.1**

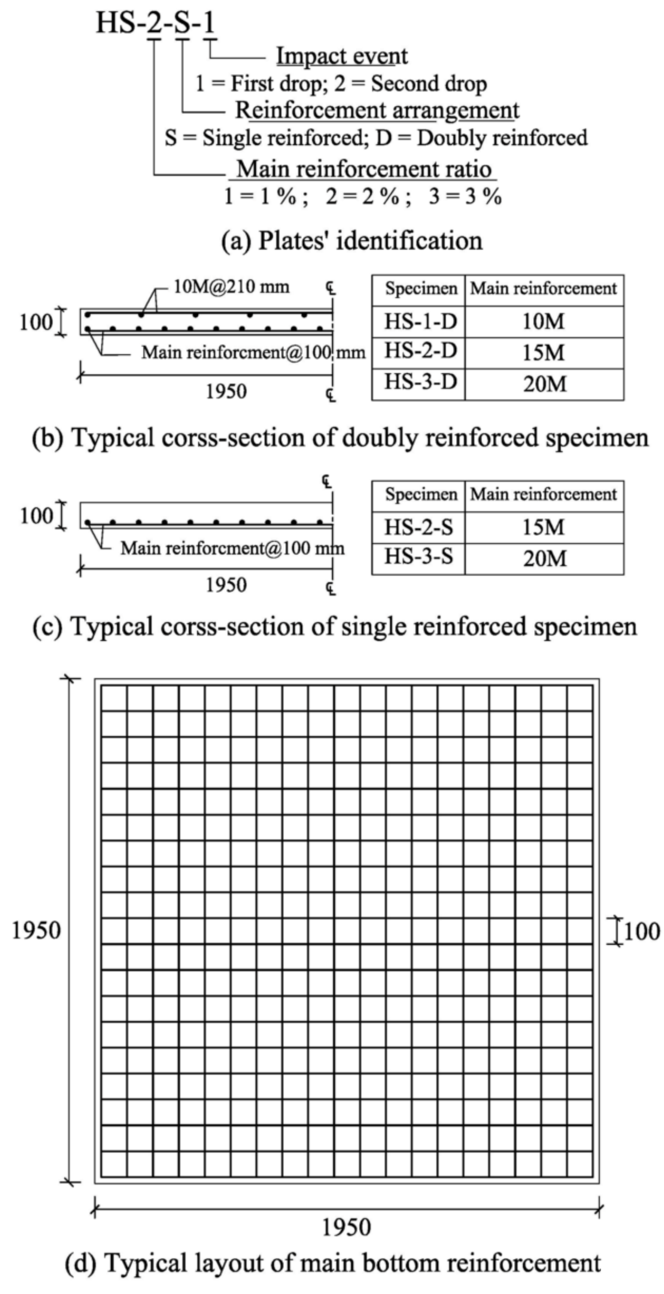

Figure 4.1 – Details of HSC specimens (dimensions in mm)

HSC specimens are designed to collapse in bending failure mode under midpoint static loading conditions with bending-punching capacity ratios range from 0.3 to 0.9. Static flexural capacity (P_{us}) and punching-shear capacity (V_{us}) are calculated using conventional prediction equations. Canadian code CSA A23.3 (2004) is followed to estimate ultimate static bending moment and punching-shear ultimate load of plates. Additionally, the nominal flexural loads (P_{us}) are estimated using yield line theory (Kennedy and Goodchild, 2004). Details of individual specimen's reinforcement, and their static bending and shear capacities are given in **Table 4.1**, and the calculations are documented in **Appendix C**.

Table 4.1 – Steel reinforcement details and static capacities of HSC specimens

Plate's ID	Bottom reinforcement		Top reinforcement		Static capacities		
	Dai./spacing (mm)	Ratio[1] (%)	Dai./spacing (mm)	Ratio[1] (%)	P_{us}[2] (kN)	V_{us}[3] (kN)	P_{us} / V_{us}[4]
HS-1-D	10M/100	1.00	10M/210	0.48	130	440	0.30
HS-2-D	15M/100	2.00	10M/210	0.48	240	400	0.60
HS-2-S	15M/100	2.00	----	----	240	400	0.60
HS-3-D	20M/100	3.00	10M/210	0.48	320	360	0.90
HS-3-S	20M/100	3.00	----	----	320	360	0.90

[1]based on total section height = 100 mm, per direction. [2]P_{us}= Ultimate static flexural capacity.
[3]V_{us} = Ultimate static punching capacity. [4]P_{us} /V_{us} = Flexural-punching capacity ratio.

In order to have identical concrete properties and to avoid the development of cold-joints, all specimens are cast at the same time using single concrete batch. Specimens are also cured following the same procedures, under moist burlap and plastic for seven days. Afterwards, the specimens are taken out of their moulds and placed to dry in laboratory air conditions until testing at the age of 56 days. Manufacturing and casting of HSC specimens are presented in **Figure 4.2**.

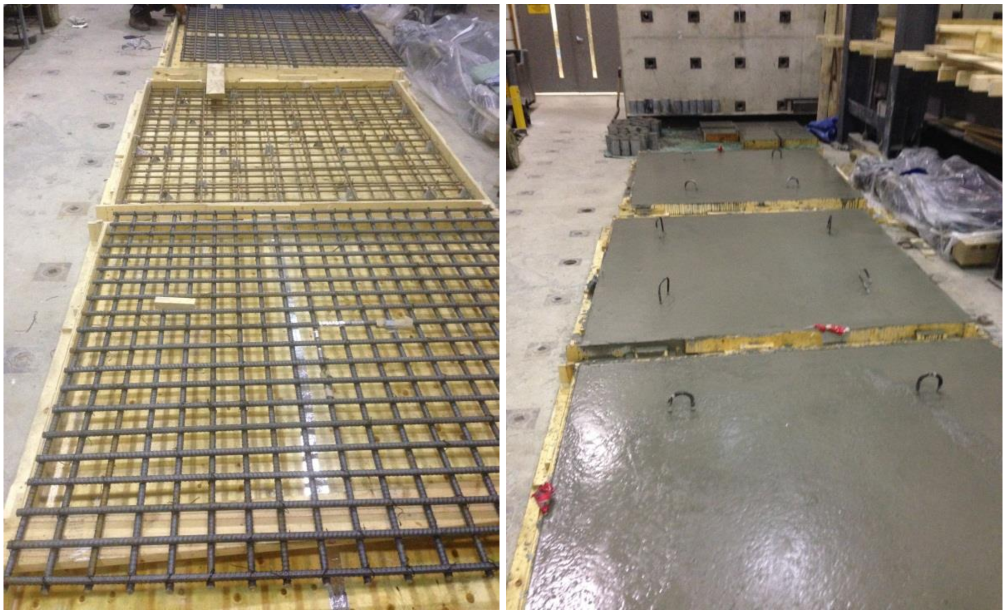

Figure 4.2 – Manufacturing and casting of HSC specimens series

4.2.2 Details of UHP-FRC series

This testing series consists of seven RC plates with identical dimensions of 1950×1950×100 mm. Five UHP-FRC specimens, and two control specimen cast using NSC and HSC are constructed and tested under drop-weight impact load. All plates are doubly reinforced with equal top and bottom orthogonal steel reinforcement mats. 10M CSA standard deformed steel bars of Grade 400 are used as longitudinal reinforcement in all plates (CSA A23.3, 2004). Three parameters are considered in the current investigation, namely: concrete matrix (NSC, HSC and UHP-FRC); fibre volume content (1, 2, and 3%); and steel reinforcement ratio (0.47, 0.64, and 1.00% per layer/direction). Plates' identification, dimensions, reinforcement details, and cross section are shown in **Figure 4.3**. Additionally, a summary of the different study parameters for the seven specimens is presented in **Table 4.2**.

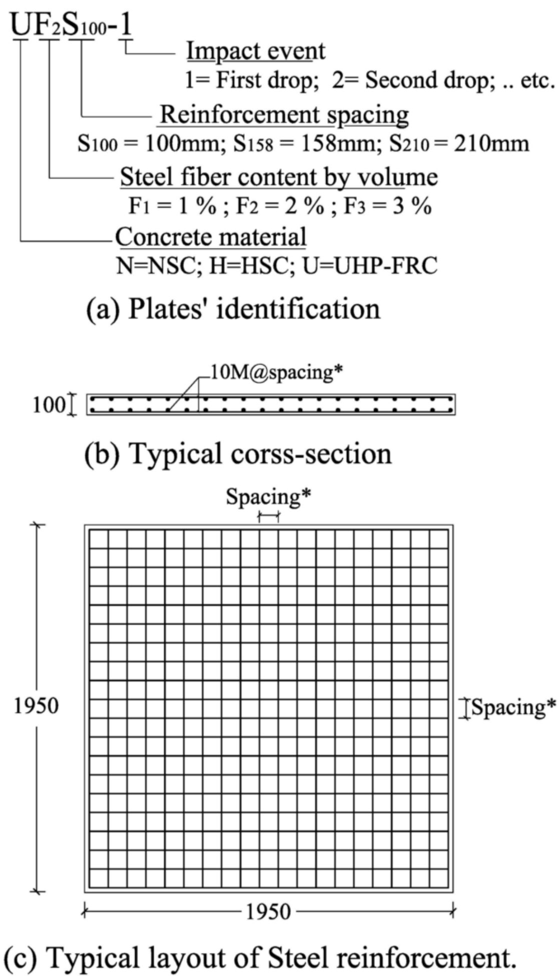

Figure 4.3 – Details of UHP-FRC plates (dimensions in mm)

Table 4.2 – Summary of UHP-FRC plates

Plate's ID	Fibre Content v_f (%)	Longitudinal Reinforcement	
		Dai./Spacing[1] (mm)	Ratio[2] (%)
NS_{100}	---	10M/100	1.00
HS_{100}	---	10M/100	1.00
UF_1S_{100}	1	10M/100	1.00
UF_2S_{100}	2	10M/100	1.00
UF_3S_{100}	3	10M/100	1.00
UF_2S_{158}	2	10M/158	0.64
UF_2S_{210}	2	10M/210	0.48

[1]per layer; per direction, [2] based on total section height = 100 mm.

To address the advantage of using UHP-FRC and the effect of steel fibre content in impact resistance members, the concrete mix is varied amongst five plates which are constructed using identical doubly reinforced steel mats using bar size 10M with spacing 100 mm per layer. Two plates are constructed using plain NSC and HSC mixes, while the other three are constructed using UHP-FRC with varied steel fibre volume contents of 1, 2, and 3%, respectively. To address the effect of steel reinforcement ratio on impact response of UHP-FRC plates, the steel reinforcement ratio is varied from 0.476 to 1.00% amongst three specimens. These three specimens are constructed using same UHP-FRC containing 2% steel fibre by volume. The variation in steel reinforcement ratios is achieved by changing reinforcement spacing while the bar size is kept constant. The NSC is cast using a ready-mix concrete with 10 mm maximum aggregate size provided by a local concrete company (Dufferin Custom Concrete Group). The concrete manufacturer's specified a nominal compressive strength of 25 MPa and 100 mm slump. The average tested mechanical properties of NSC at same time of impact test are as follow: compressive strength of 41.1 MPa, splitting tensile strength of 3.95 MPa, and flexural strength or modulus of rupture of 6.8 MPa. HSC specimen is cast from same concrete batch of the HSC testing series. The UHP-FRC concrete mixes used in this series is the proprietary product Ductal® specified by Lafarge North America (Lafarge, 2016). The details of the mix proportions and tested material properties of HSC and UHP-FRCs are reported in Chapter 3.

Figure 4.4 shows the manufacturing of UHP-FRC specimens. The workability and flow characteristics of UHP-FRC was observed during the discharge and batching of the specimens as shown in **Figure 4.4-b**. Specimens are cured following the same procedures without heat curing, under moist burlap and plastic for seven days. Afterwards, the specimens are taken out of their moulds and placed to dry in laboratory air conditions until testing at the age of 56 days.

a) Preparation process (formwork and reinforcement)

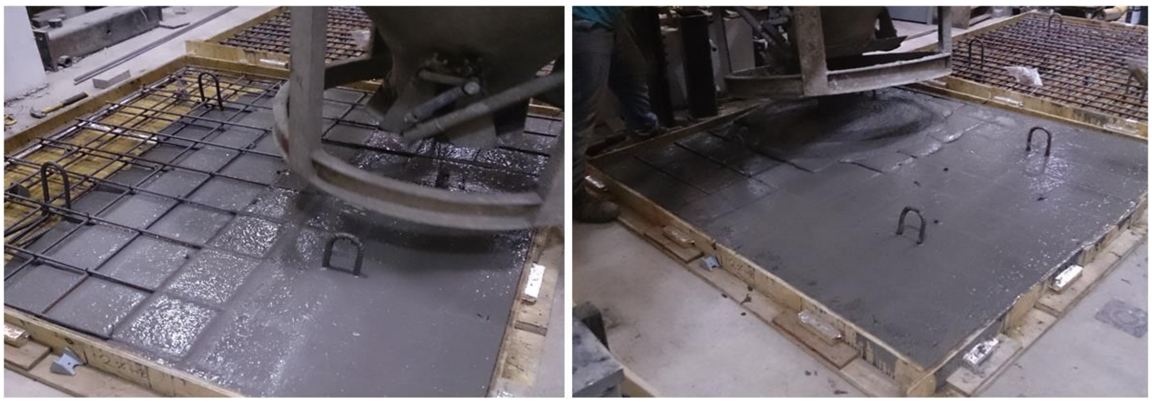

b) Casting of UHP-FRC specimens

Figure 4.4 – Manufacturing of UHP-FRC test series

4.3 Drop-weight Impact Testing Setup

The schematic diagram of the testing setup is illustrated in **Figure 4.5**. The drop-weight low-velocity impact setup has been designed and fabricated, especially for this research project, in the structural laboratory of Ryerson University with a capacity of 19.30 kJ. The dimensions of drop-weight mass and the drop-height are governed by the required impact energy and the available vertical space capacity of the laboratory. Additionally, the dimension of the overhead crane hook is a factor since the crane has to go between the guides to lift drop-weight after the test as shown in **Figure 4.5**. During the test, the drop-weight is elevated to a desired height above specimens using an electromagnetic hoist and then the mass is released to hard impact the specimen with a velocity that depends on the dropping height.

The impact setup can be divided into three subsystems, namely: drop-weight impact frame, supporting system, and instrumentation. Details about different subsystems are given in next subsections.

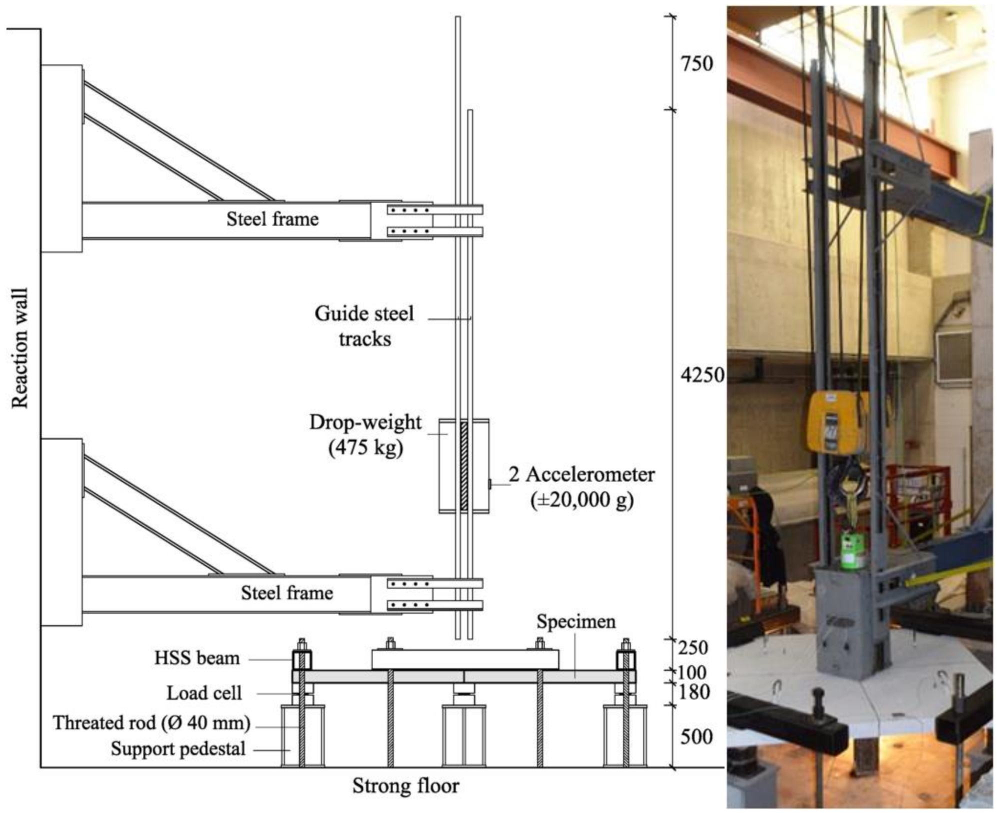

Figure 4.5 – Drop-weight impact test setup (dimensions in mm)

4.3.1 Drop-weight impact frame

The drop-weight impact frame is capable of dropping a 475 kg mass from a height of up to 4.15 m. In order to ensure hitting the specimens' midpoint and avoid the damage of instrumentation during the test, a tower frame with four vertical steel tracks is used to guide the drop-weight. The guiding frames are mounted to the strong 1 m-thick reaction wall of the structural laboratory (**Figure 4.5**).

The drop-weight mass is manufactured by filling hollow structural steel (HSS) section with concrete (**Figure 4.6**). The HSS section is a 400 mm square, 750 mm in length and with a minimum thickness of 12 mm. Two thick square steel plates with dimensions of 400×400×25 mm are welded to the top and bottom of the HSS section as end caps. The mass of the drop-weight is measured using calibrated load cell (**Figure 4.7**).

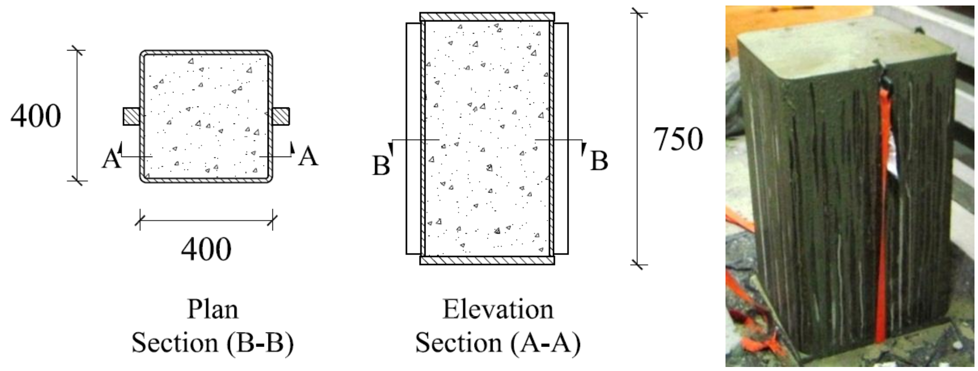

Figure 4.6 – Details of drop-weight mass (dimensions in mm)

Figure 4.7 – Measurement of drop-weight mass

In order to have a free fall condition with minimal friction, a 10 mm clearance between the drop-weight guide and the steel tracks is considered during the fabrication. Additionally, before each test the steel tracks of the tower are lined with grease to reduce any possible friction. **Figure 4.8** shows the arrangement used to guide the drop-weight.

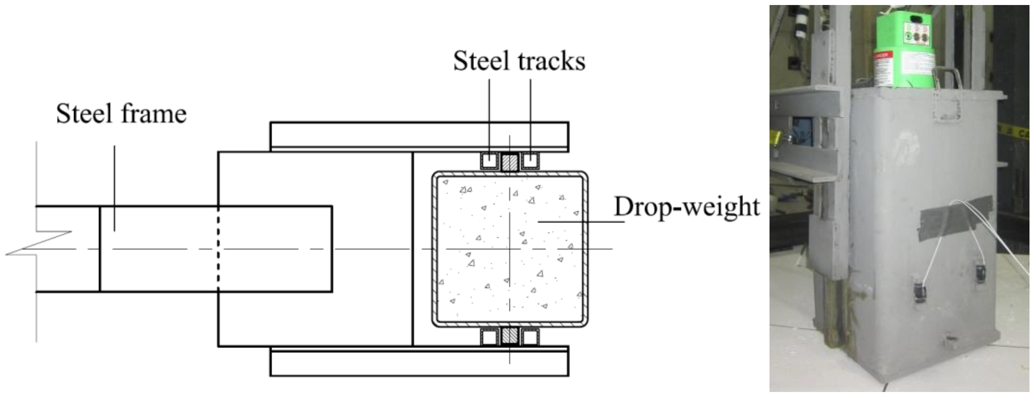

Figure 4.8 – Fitting of drop-weight between the guiding tracks

4.3.2 Supporting system

Previous study carried out by Soleimani and Banthia (2014) showed that the reactions recorded by the support load cells for two identical impact tests without preventing vertical movements were entirely different. On the other hand, when the vertical movement was restrained the measured reaction forces were in good agreement. Therefore, preventing uplift or vertical movement at supporting points is required.

The supporting system has been designed to prevent the uplift of supports without creating any significant restraint moments. The specimens are supported at the four corners. The use of corner supports is selected to reduce the measurement of the reaction forces to specific points, i.e., corners. The uplift of each corner is prevented by holding down the specimen's corner using a special tie-down frames consist of a stiff hollow structural section (HSS) anchored at both ends to the strong floor of the laboratory using two high strength threaded rods with a diameter of 40 mm. The tie-down frame allows a sufficient amount of rotation for concrete members, up to 5^{o}. This methodology has been used frequently in most of the previous impact tests (Kishi et al., 2002; Hrynyk and Vecchio, 2014; Chen and May, 2009; Soleimani and Banthia, 2014; Saatci and Vecchio, 2009). Details of the supporting system arrangement are shown in **Figure 4.9**.

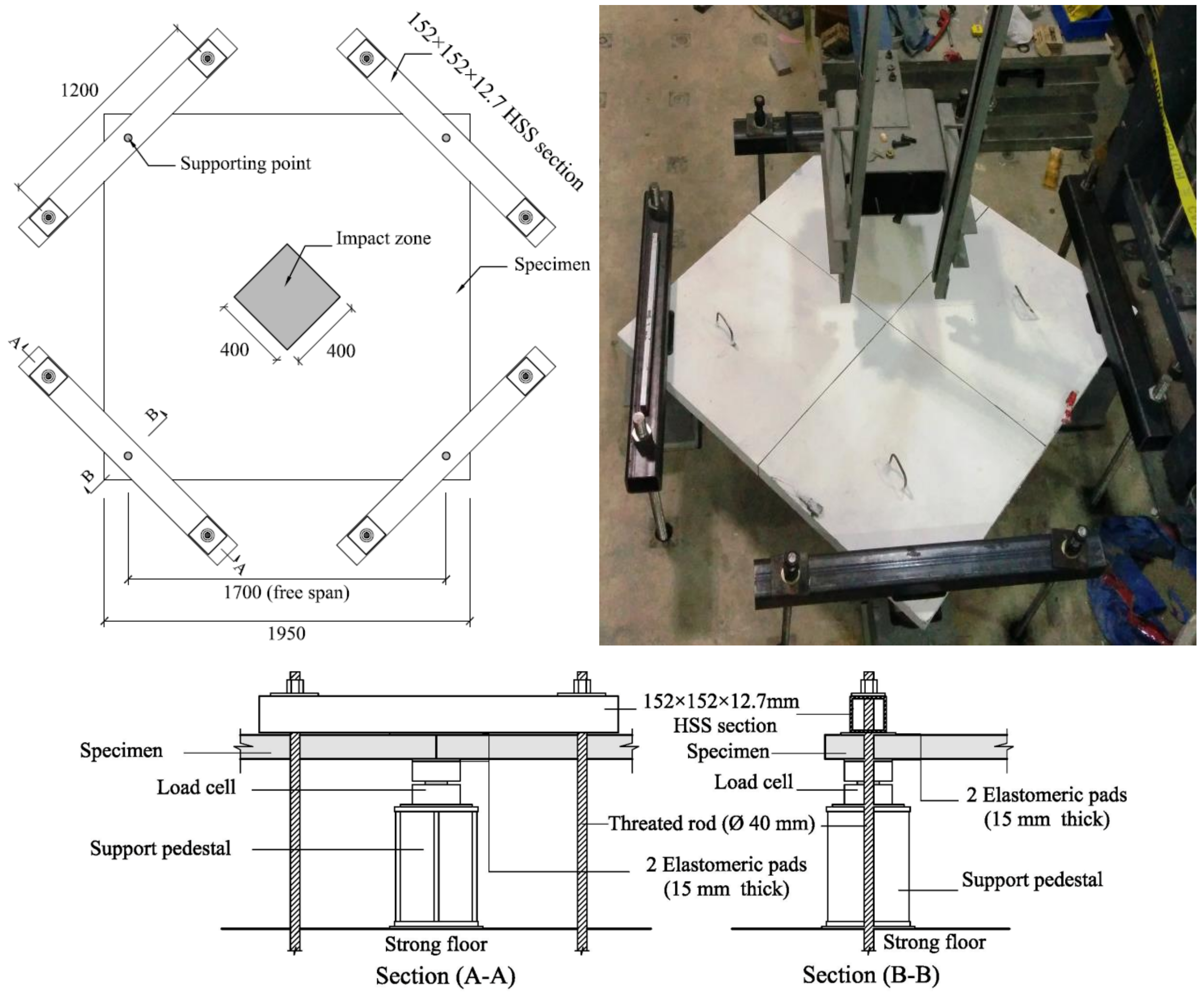

Figure 4.9 – Supporting system of RC plates (dimensions in mm)

4.4 Instrumentation

The impact testing setup is equipped with sophisticated instrumentation to monitor applied impact force, reaction forces, displacements, and reinforcing bar strains. The used instrumentations are outlined in the following subsections.

4.4.1 Accelerometers

Two accelerometers with a maximum capacity range of ±20,000 g are mounted to the drop-weight (where g is the Earth's gravitational acceleration) (refer to **Figure 4.8**). The used accelerometers are products of Kistler Instrument Corporation (model 8742A20). These two accelerometers are used to determine the impact force excited in the falling drop-weight using Newton's 2nd law. The calibrations of the accelerometers are provided by the supplier.

4.4.2 Quartz dynamic load cells

The reaction forces between the supports and specimen are measured using quartz load cells. Each load cell consists of a quartz force sensor sandwiched between two thick steel caps to protect the electrical connector from any potential damage during testing. **Figure 4.10** shows the quartz load cell during assembly and after installation. The used quartz force sensors are also manufactured by Kistler Instrument Corporation (model 9107A) with a capacity of 650 kN. In general, quartz force sensors have exceptional characteristics for measuring dynamic force and quasi-static forces compared to strain gauge type. Quartz force sensors are small in size and stiff as solid steel. Stiffness and small size provide high frequency response permitting accurate capture of short-duration impulse force data. It should be pointed out that quartz force sensors are not practical to measure static or long-term loading forces, since the measurement signal generated by a quartz force sensor will decay over time.

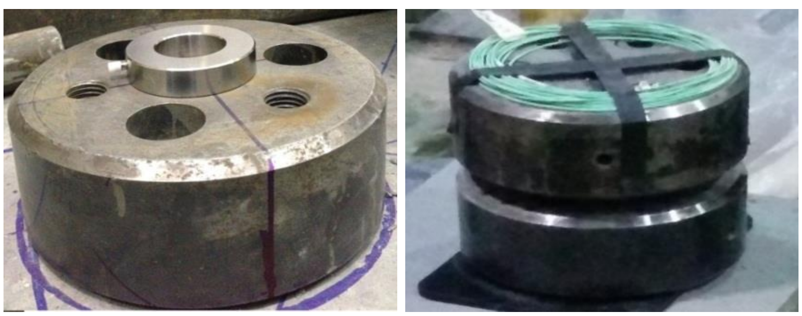

Figure 4.10 – Load cell a) Positioning of force sensor during assembly b) After installation

The quartz force sensors are delivered uncalibrated and must be calibrated in situ after installation in the mounting structure, i.e., after steel caps are screwed tightly over the force sensor in order to obtain absolute measurements. It should be noted that the load cell must be calibrated again if there is any change in the preloading screws. The load cells are calibrated using hydraulic servo-controlled testing machine (MTS 815). Anther calibrated external load cell is used also to verify load values obtained from the machine (**Figure 4.11**). Each load cell is calibrated under quasi-static load up to 70 % of its rated capacity. Outputs of the load cell with 0 to 500 kN loads at 50 kN increments are recorded. The measurements are carried out 4 times. First two calibrations are performed using ascending load while the other two are performed using descending load. Calibration process and results of load cell 1 are shown in **Figure 4.11**. It can be seen that the relation between the output voltage signal and the load is perfectly linear for both loading and unloading with the absence of any significant hysteretic losses.

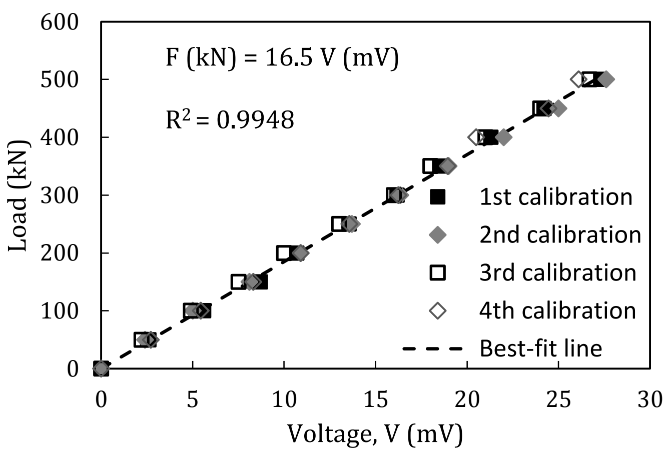

Figure 4.11 – Calibration process (load cell 1)

In order to verify the reliability of the calibration process, simple tests are conducted by applying measurable impact load onto the calibrated load cell. Each calibrated load cell is subjected to 4 impact tests using DYTRAN (model 5803A) impulse hammer. A typical load cell reading, along with impulse hammer reading are shown in **Figure 4.12**. In general, there is a strong agreement between the load cell and impulse hammer reading in terms of both magnitude and shape over the impact time duration.

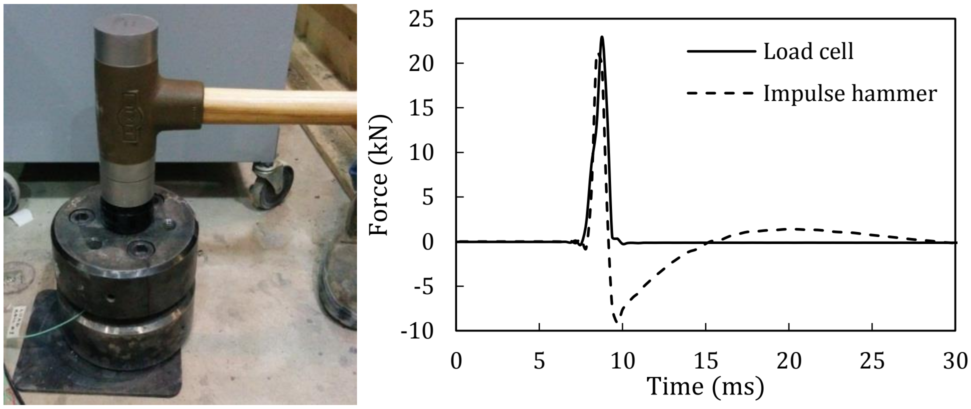

Figure 4.12 – Validation test of calibrated load cells using impulse hammer

4.4.3 Strain gauges

Strain gauges are used to determine the magnitude and rate of strain in the steel reinforcement. The gauges are manufactured by Tokyo Sokki Kenkyujo Co. Ltd. (model TML FLA-5-11) with 5 mm gauge lengths. Two strain gauges are glued to the surface of bottom longitudinal reinforcement at the midpoint zone of each specimen in both directions. The steel reinforcement surface at midpoint is lightly grinded and cleaned using alkaline and acidic chemicals, strain gauge is attached using glue provided by the manufacturer. **Figure 4.13** shows glued strain gauge, before and after covered with protection layer of paraffin wax and aluminium tape to decrease the probability of damage during the casting.

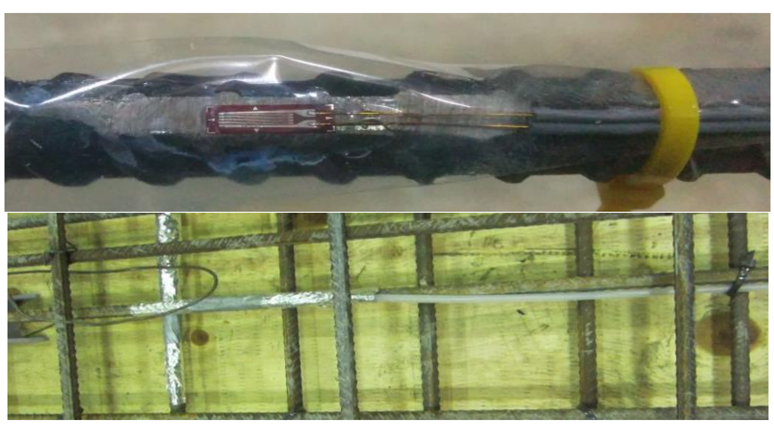

Figure 4.13 – Installation of strain gauge to steel reinforcement

4.4.4 Displacement laser sensors

Most of the previous impact investigations declared that some of the displacement data are lost due to the damage of displacement sensor or its connection to impacted specimen. Therefore, the decision was to use contact-less laser sensor to avoid the high probability of damage of traditional displacement gauge with physical connection to specimen, e.g., Potentiometer and LVDT. Two contacts-less laser KEYENCE (model IL-300) sensors are used to measure displacements. One laser displacement sensor placed at the midpoint and the other place at the mid-quarter point on the axis connecting diagonal supports (**Figure 4.14**). The KEYENCE IL-300 sensor has a semi-conductor laser with a wavelength of 655 nm and a measuring range of 290 mm.

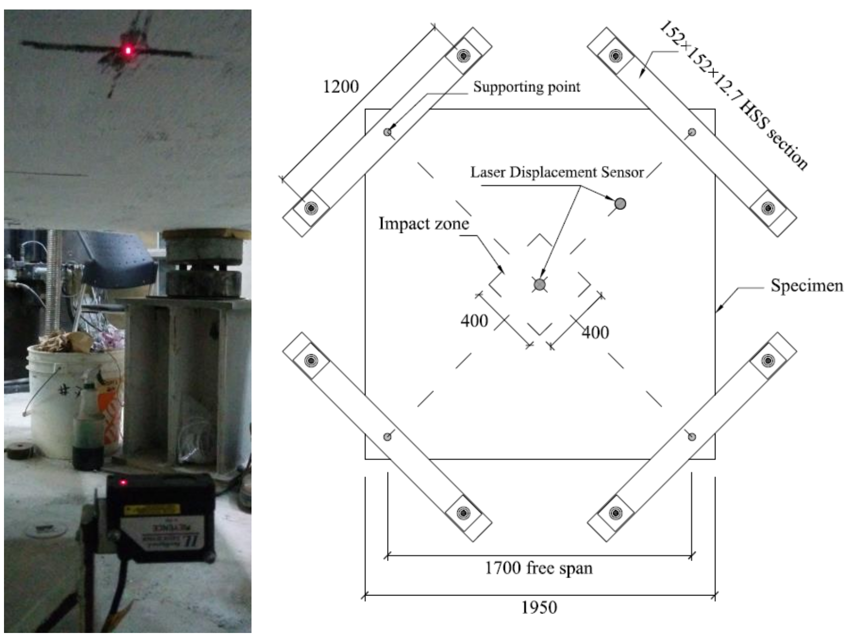

Figure 4.14 – Typical locations of laser displacement sensors

4.4.5 Data acquisition system

Raw acquired data are recorded using a digital dynamic data acquisition system ECON (model MI-7008). All measurements are stored in text files where they can later be analyzed by MATLAB or similar software. In this investigation, the data that are most likely to have large amplitude and high frequency content are acceleration and reaction forces. Therefore, the collected data from the accelerometers and load cells are sampled at rate of 100 kHz. On the other hand, displacement and strain are sampled at rate of 5 kHz since these data are lower in frequency content by nature. A worth of mentioning here, these sampling rates are selected based on preliminary FE analysis of drop-weight impact tests conducted by Murtiadi and Marzouk (2001) (Othman and Marzouk, 2014).

4.4.6 Video camera and image analyzer

The impact tests are recorded using a digital camera with a framing rate of 240 fps (frames/second) and posterior analysis of recorded videos is performed using Tracker® image analysis software (Brown, 2016). The camera is focused on the last two meters of the guide tracks and the image analysis of recorded video is performed for last meter of the guide to evaluate the impact velocity, contact time duration, and rebound velocity (refer to **Figure 4.15**).

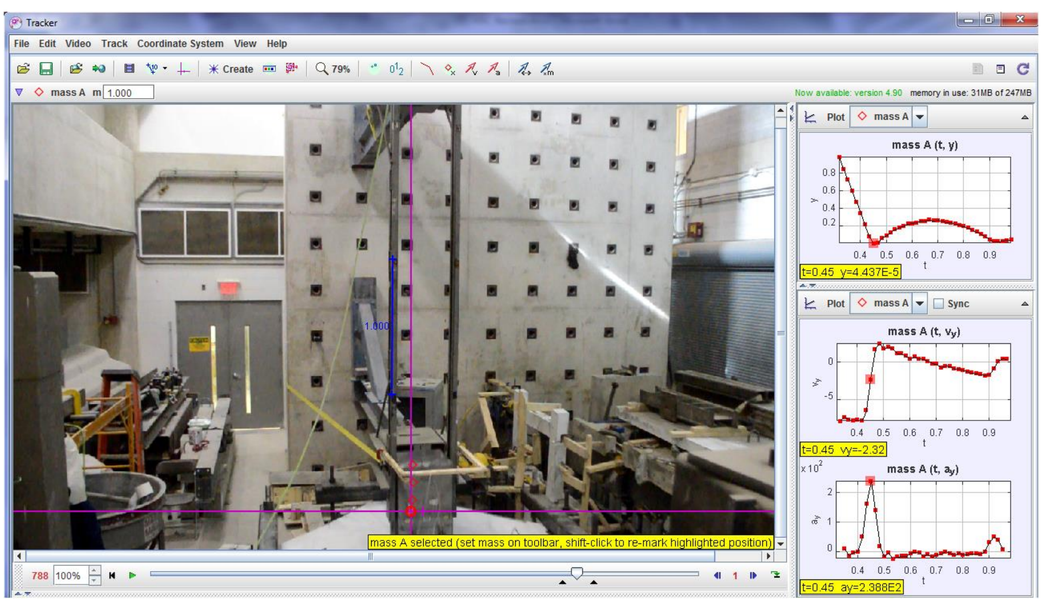

Figure 4.15 – Image analysis of recorded video (user interface of Tracker® software)

4.5 Loading Protocol and Test Termination

In general, there is no standard test technique to assess the impact resistance of concrete members. ACI Committee 544 (1988) proposed a repeated drop-weight impact test for testing FRC materials, in which the number of drops necessary to cause prescribed levels of damage in the specimen is the main parameter and the drop-height is kept constant. Relative impact resistance of specimens with identical dimensions cast using different materials can be evaluated using this technique. Same procedures are followed in this investigation. All plates are subjected to multi-impact tests by dropping a steel mass of 475 kg from a constant height of 4.15 m, resulting 9.00 m/s theoretical impact velocity.

- For the first series (HSC series), each plate is subjected to the predefined impact loads twice. As a result, the total kinetic energy imparted to each plate is nominally the same. Experimental results of HSC series are evaluated focusing on the impact force characteristics, the impact response of HSC plates, and damage characteristics.

- For the second series (UHP-FRC series), it has been observed during the materials investigation phase that small-scale UHP-FRC prisms can reach 8 times the serviceability limit of deflection under multi-impact tests without significant fragmentations. Therefore, for this testing series, it has been decided to conduct the impact testing till cumulative residual midpoint displacement of 65 mm is reached under repeated impact loads, or severe punching damage took place with high probability of instrumentation damage. The deflection limit of 65 mm is approximately equal to 8 times the serviceability deflection limit specified by Canadian code CSA A23.3 (2004). Maximum and residual displacement, accumulated energy absorption capacity, and crack pattern against multiple impacts are aspects of assessing the impact performance of UHP-FRC specimens.

4.6 Dynamic Characteristics of Plates

The dynamic characteristics (natural damped frequencies and damping ratio) of the tested plates are determined experimentally in order to acquire reliable impact testing data that can be used to verify numerical models. The intact plates (i.e., before testing) are excited using DYTRAN (model 5803A) sledge hammer at their midpoint to generate free vibration. The plate's response is captured by two ±500g accelerometers and the quartz load cells (refer to **Figure 4.16**).

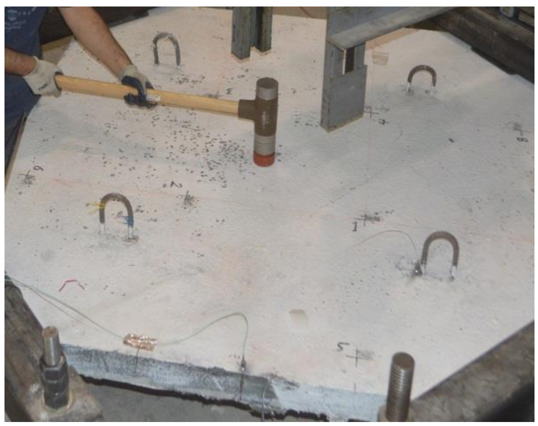

Figure 4.16 – Typical dynamic charactristics testing of plates.

5 RESULTS AND DISCUSSIONS OF IMPACT TESTING

5.1 Introduction

Two series of low-velocity impact tests on RC plates using same drop-weight test setup have been conducted. Description of the developed drop-weight impact setup and details of two test series are provided in the previous chapter. In this chapter, the results of the two testing series are presented in two separate sections because each series has its own objectives. In each section, the impact test results are presented in both quantitative and qualitative forms. The measurements and the dynamic properties of the tested plates are reported in details. In addition, selected results are presented to characterize the influence of studied parameters on the impact response and failure pattern of tested plates.

The captured data by the data acquisition system are very large in size and contained redundant parts that would cause unnecessary time consumption during the data processing. Therefore, entire data for each impact are scanned and clipped into manageable size which started just before impact and ended when the dynamic responses are damped out. MATLAB program has been used to process and analyze the measured responses (MathWorks, 2015).

5.2 Results of HSC Series

As explained in the previous chapter a total of 10 impact tests are conducted on HSC plates, including two tests on each specimen. Based on the objective of this testing series the results are presented in three different subsections: first section describes the validation process of developed test setup; second section documents the measurements that are used to facilitate and validate the development of numerical FE models; third section illustrates the influence of main reinforcement ratio and reinforcement arrangement on the impact response.

5.2.1 Function tests of developed impact setup

Impact tests are generally much more complicated than static ones. The experimental measurements must be carefully examined to ensure that the data are valid and as accurate as possible before using the experimental results in further interpretation studies.

5.2.1.1 Impact velocity

In general, the initial impact velocity (v_i) depends on the drop-height and independent of the mass. The initial impact velocity can be estimated based on the law of conservation of energy, assuming that air resistance is negligible, i.e., neglecting drag forces caused by air resistance. The velocity of free falling mass can be obtained using:

$$v_i = \sqrt{2gh} \qquad (5.1)$$

Where, g is the standard gravitational acceleration of 9.806 m/s^2; h is the drop-height.

To investigate the effect of the friction between the drop-weight and guide tracks, eight impact tests are conducted and recorded using a high speed camera. These impact tests are conducted over a large sand bag before testing the actual HSC specimens. Four different drop-heights, including two tests for each height are considered. **Figure 5.1** shows the comparison between theoretical free fall velocities estimated using **Eq. 5.1**, and experimental velocities calculated using image analyses of recorded videos. It can be noted that the experimental and theoretical velocities are close that indicates that the friction between the drop-weight and steel guides is practically small. The data also show that the difference between experimental and theoretical velocities is more significant for test cases with drop-heights greater than two meters, which means the friction is significant for drop-heights exceeds 2 meters. Based on this investigation, the impact velocity of drop-weight can be estimated using **Eq. 5.1** for tests with a drop-height less than 2 meters and for drop-heights greater than 2 meters the impact velocity should be extracted experimentally. Since the drop-height used in all RC plates testing is 4.15 m, the decision was to record all tests using a digital camera in order to calculate the impact velocity.

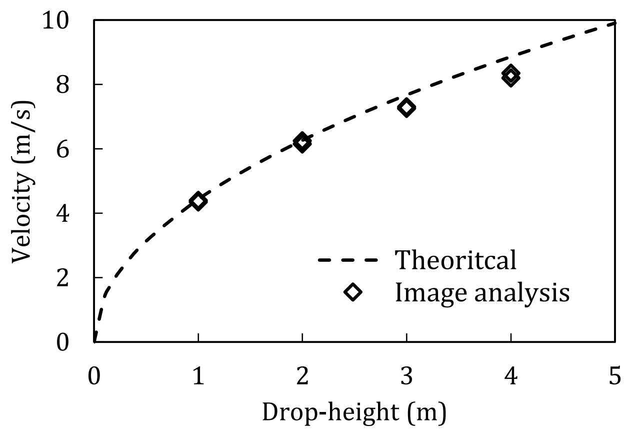

Figure 5.1 – Experimental and theoretical impact velocity as a function of drop-height.

5.2.1.2 Acceleration data evaluation and correlation

The drop-weight accelerometers data are noisy and contain high frequencies that may mask the fundamental pulse and make the data too difficult to interpret. The drop-weight acceleration data of impact event HS-D-3-2 is used to demonstrate the evaluation and correlation process that have been used typically as a quality check throughout all impact tests (**Figure 5.2**). The raw data from the two accelerometers are integrated to generate velocity curve and compared to the velocity curve extracted from recorded video. It is evident from **Figure 5.2-b** that the velocity curve resulted from integrating raw accelerometer (1) data is corrupted since the curve does not produce the rebound velocity and the data must be disregarded. On the other hand, the velocity curve resulted from accelerometer (2) data is reliable and plausible. The rebound velocity goes to

+ 2.10 m/s (upward) in a contact time duration of 29.98 ms. The calculated values are correlated well with the values obtained from image analysis of recorded video.

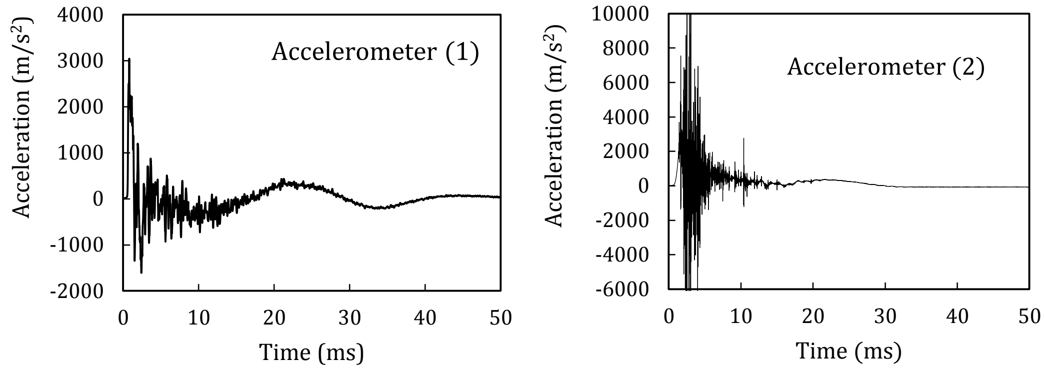

a) Raw acceleration data

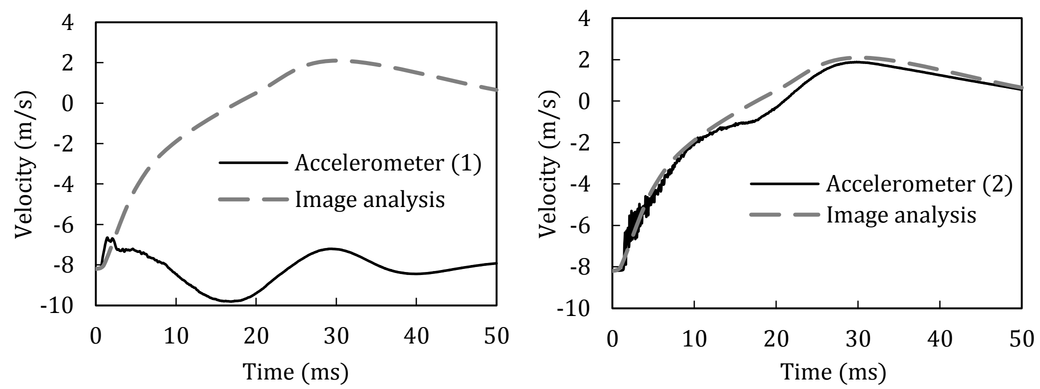

b) Velocity obtained from integrating the raw acceleration data

Figure 5.2 – Accelerometers data evaluation process (test: HS-3-D-2).

5.2.1.3 Acceleration data filtering

In general accelerometers data are noisy and required extensive post-test filtering. The filtering process of the acceleration data of impact event HS-D-3-2 is used to demonstrate the applied filtering technique. The filter is applied using *'filtfilt'* command built-in MATLAB that is a forward-backward filtering algorithm, i.e., does not shift the time phase (MathWorks, 2015). Valid accelerometers data that passed the previous quality check are filtered using low-pass second order Butterworth filter. It should be mentioned as a guide before filtering, an approximate value of the peak acceleration value of 2490 m/s^2 or 254 g's can be obtained by simply computing the maximum slope of the velocity curve shown in **Figure 5.2-b**. Cutoff frequencies ranging from 1.25 kHz to 10.0 kHz are examined to select the appropriate cutoff frequency that produces the fundamental acceleration pulse without over filtering the data. To check the cutoff frequencies, the velocity curve resulted from raw data is compared with others resulted from filtered data. As shown in **Figure 5.3-a**, each of the filtered accelerations is integrated to obtain the corresponding velocity responses. It is evident from **Figure 5.3-a** that the velocity curves obtained by integrating the 2.5, 5.0, and 10.0 kHz filtered accelerations follow the velocity response of raw acceleration data quite well which means no physical data are filtered. On the other hand, the velocity response obtained by integrating the 1.25 kHz filtered acceleration distorts the original velocity trace which means actual physical data are filtered. Based on this investigation, a cutoff frequency of 2.5 kHz is selected (**Figure 5.3-b**).

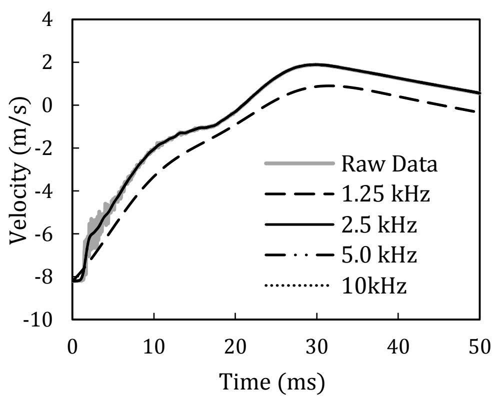

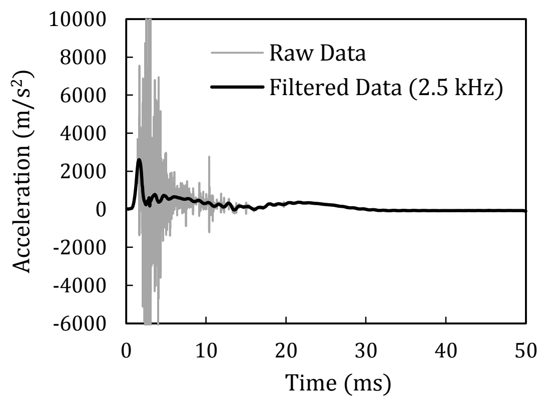

a) Velocity curves of raw and examined filters b) Raw and selected filtered acceleration

Figure 5.3 – Accelerometers data filtering process (test: HS-3-D-2)

It is worth mentioning here that the peak acceleration of filtered acceleration using 2.5 kHz cutoff frequency is 2600 m/s^2 or 265 g's. This value is close to the approximate value that is estimated using the maximum slope of the velocity curve before applying the filter.

5.2.1.4 Impact force validation and characteristics

The impact force excited in the falling steel weight is determined by Newton's 2nd law using the reading of the filtered acceleration data of drop-weight. Impulse-momentum theorem is implemented to validate the accuracy of impact testing setup and filtering process. Impulse-momentum theorem states the impulse is equal to the change of momentum (Millard et al., 2010). The impulse (I_p) is the time integration of impact force, i.e., the area under the impact force-time curve. Momentum is described as a kind of moving inertia that its magnitude does not vary regardless of the target details, i.e., steel reinforcement ratio and/or extend of specimen damage. The change of momentum (ΔM) at the instance of impact can be calculated as the product of impact-weight mass (m) and the change of velocity using **Eq. 5.2.**

$$\Delta M = m \times (V_i - V_b) \qquad (5.2)$$

As mentioned before, all tested plates are impacted by a drop-weight of 475 kg mass (m) from a constant height of 4.15 m. This means that all plates subjected to same nominal momentum. Thus, it is expected that all impact tests have same impulse. **Figure 5.4** shows the impulse of all impact tests compared to the nominal change of momentum. Nominal change of momentum is calculated using the theoretical initial (V_i) and rebound velocities (V_b) of – 9.0 and + 2.2 m/s, respectively. This step is important as a quality check before processed in detailed analysis. It is evident from **Figure 5.4** that the impulse is equal to the change of momentum and its magnitude do not vary regardless of the longitudinal steel reinforcement ratio, reinforcement arrangement, or extend of plate damage.

Table 5.1 summarizes the validation process and the characteristic values of impact force. The reported impact velocity (V_i, downward is negative), The rebound velocity (V_b, upward is positive), and the impact time duration (T_d) are calculated using image analysis of recorded videos frames. Absorbed energy (E_{ab}) is the integration of impact force-displacement curve. Input kinetic energy (E_k) is the maximum kinetic energy at the instant of impact ($1/2\ mV_i^2$).

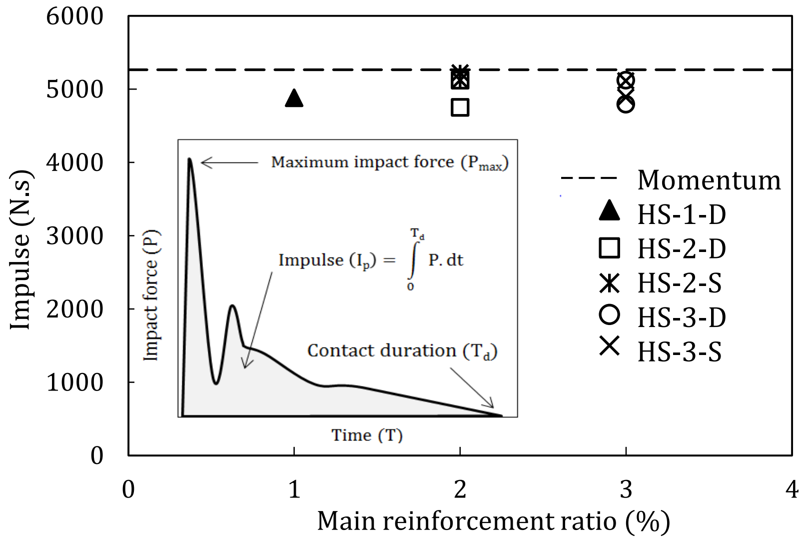

Figure 5.4 – Validation of estimated impact force using impulse-momentun therom

Table 5.1 – Impact force characteristic values

Impact test	Impact velocity (m/s)	Rebound velocity (m/s)	Contact duration (ms)	Momentum, ΔM (kg.m/s)	Impulse, I_p (Ns)	$I_p/\Delta M$	Absorbed energy, E_{ab} (kJ)	Input energy, E_k (kJ)	E_{ab}/E_k
HS-1-D-1	-8.30	1.95	33.10	4868.75	4789.05	0.98	6.48	16.36	0.39
HS-1-D-2	-8.50	2.15	36.40	5058.75	4879.00	0.96	6.87	17.16	0.40
HS-2-D-1	-8.85	2.20	32.60	5248.75	5117.94	0.98	8.19	18.60	0.44
HS-2-D-2	-8.50	2.10	33.20	5035.00	4748.80	0.94	8.93	17.16	0.52
HS-3-D-1	-8.95	2.10	26.10	5248.75	5117.23	0.97	7.99	19.02	0.42
HS-3-D-2	-8.35	2.08	30.00	4954.25	4791.86	0.97	8.44	16.56	0.51
HS-2-S-1	-9.00	2.20	40.55	5320.00	5220.35	0.98	7.72	19.24	0.40
HS-2-S-2	-8.90	2.15	43.70	5248.75	5117.40	0.97	8.25	18.81	0.44
HS-3-S-1	-9.00	2.20	34.50	5320.00	5109.70	0.96	8.82	19.24	0.46
HS-3-S-2	-8.80	2.15	37.10	5201.25	4887.50	0.94	NA	18.39	NA

NA is data not available due to faulty sensors.

It should be pointed out that the maximum difference between the impulse and the actual change of momentum is equal 6 % (refer to **Table 5.1**). This means that the drop-weight impact testing setup can fulfil the design objectives and the proposed filter and selected cutoff frequency produces the desired effect without distorting actual data.

5.2.2 Impact test measurements of HSC series

In this section, the measurements of the tested plates are reported in details to facilitate the development of the numerical FE models. **Table 5.2** reports the peak measurements and the corresponding time of all conducted impact experiments. The reported peak reaction is the maximum total reaction force determined by summing the measurements of four load cells since reaction force responses from load cells at the four corner supports are typically similar in terms of magnitude and time response. The peak displacement is the maximum midpoint displacement measured by contact-less laser (Keyence IL-300) sensor. The reported displacement and steel strain of second impact test represent event measurements and do not include the accumulation of residual values from the first impact test.

Table 5.2 – Impact test results of HSC series

Impact test	Impact force		Total reaction force		Steel strain		Midpoint displacement	
	Peak (kN)	Time (ms)	Peak (kN)	Time (ms)	Peak (με)	Time (ms)	Peak (mm)	Time (ms)
HS-1-D-1	980.10	1.75	950.0	14.25	2117	7.00	29.03	27.20
HS-1-D-2	680.05	1.80	669.0	17.60	2114	7.80	37.54	30.00
HS-2-D-1	1616.90	0.85	1182.00	11.00	2433	10.20	26.51	19.00
HS-2-D-2	1613.15	1.00	987.65	14.45	2096	11.60	32.52	21.40
HS-3-D-1	1479.80	1.65	1089.95	12.90	2432	4.80	22.99	18.40
HS-3-D-2	1237.30	1.65	929.60	15.30	2399	6.00	29.57	23.20
HS-2-S-1	1065.00	1.70	1034.95	13.80	2804	8.20	35.87	25.40
HS-2-S-2	996.80	1.85	852.10	18.55	1450	8.00	42.11	31.00
HS-3-S-1	1464.05	1.10	938.75	12.80	2635	7.40	37.15	25.60
HS-3-S-2	1128.35	1.05	806.00	18.00	1510	7.60	NA	NA

NA is data not available due to faulty sensors.

Figure 5.5 shows typical impact test measurements time histories of impact tests for three different plates. The measurements include: impact force, total reaction force, midpoint displacement, and strain of bottom steel reinforcement located at midpoint of the tested plates.

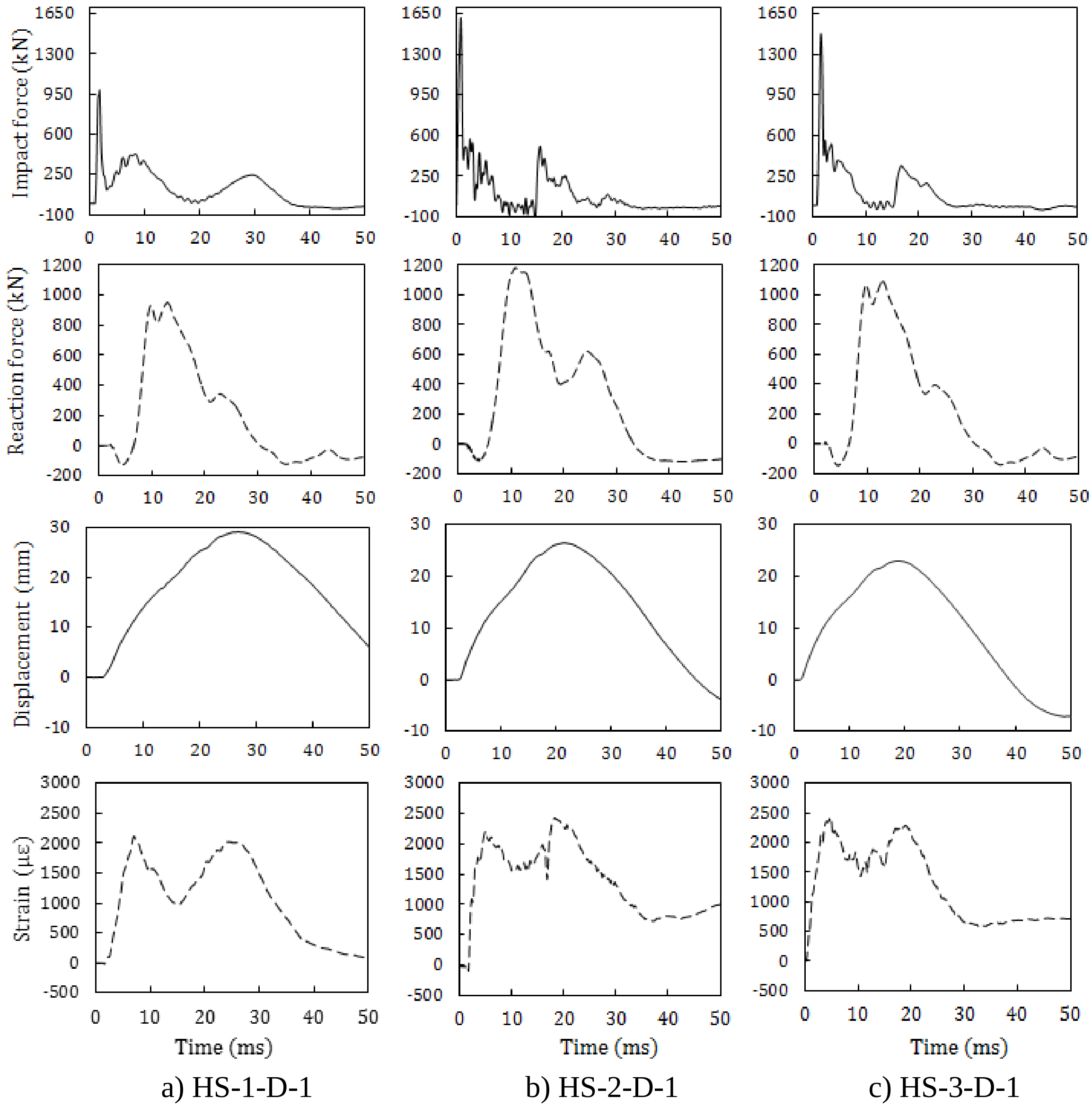

Figure 5.5 – Typical time histories of different measurements of HSC series (1st impact)

Comparing the impact force to the reaction force, the peak amplitude of impact force is greater than that of reaction force. The reason is most of impact force is used to balance the inertia force or accelerate the plate, while a small portion of impact force is used to deform and fracture the specimens. Normally, there is a time lag between the maximum impact force and the maximum reaction force. This time lag is due to the stress wave propagation travel from the impact zone to the supports. These observations were also documented by other researchers (Hrynyk and Vecchio, 2014; Saatci and Vecchio, 2009; Soleimani and Banthia, 2014).

5.2.3 Influence of steel reinforcement on HSC plates impact response

5.2.3.1 Contact time duration

The contact time duration for all impact tests in the range of 25 to 45 ms (refer to **Table 5.1**). **Figure 5.6** shows the influence of the main reinforcement ratio and steel arrangement on the contact time duration between the drop-weight and specimen during the impact test. A tendency is observed that the contact time duration is decreased when the reinforcement ratio is increased for both types; single and doubly reinforced plates. The contact time duration is longer for second drop (damaged plate) compared to first drop (intact plate). This indicates that the contact duration is inversely proportional to plate's stiffness for plates with the same reinforcement layout.

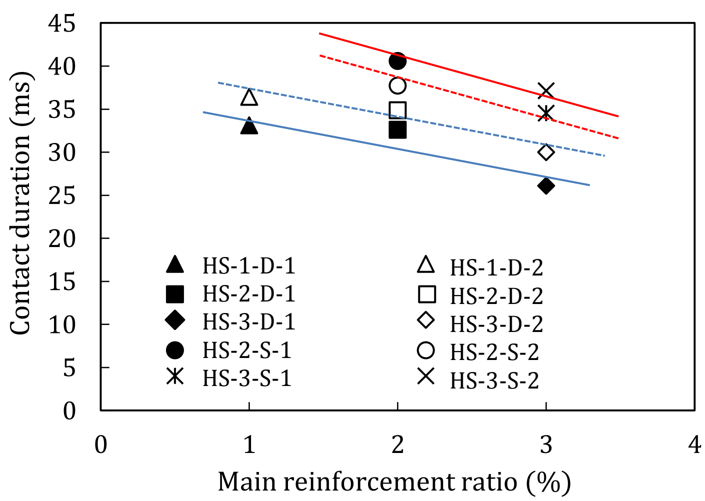

Figure 5.6 – Influence of main reinforcement ratio on contact time duration

It is evident from **Table 5.2** and **Figure 5.6** that the maximum impact force amplitude and the corresponding contact duration are affected by the stiffness of the specimen. The maximum amplitude of impact force is larger and the corresponding contact time duration is smaller for specimens with higher stiffness and vice versa.

5.2.3.2 Absorbed energy

The influence of the main reinforcement ratio and steel arrangement on the absorbed energy is shown in **Figure 5.7**. The absorbed energy values of all impact tests are also listed in **Table 5.1**. The energy ratio of absorbed to input kinetic energy is used in **Figure 5.7** to take account of input energy loss due to friction between the drop-weight and the guides. It can be seen the energy ratio values are distributed in the range from 0.44 to 0.52.

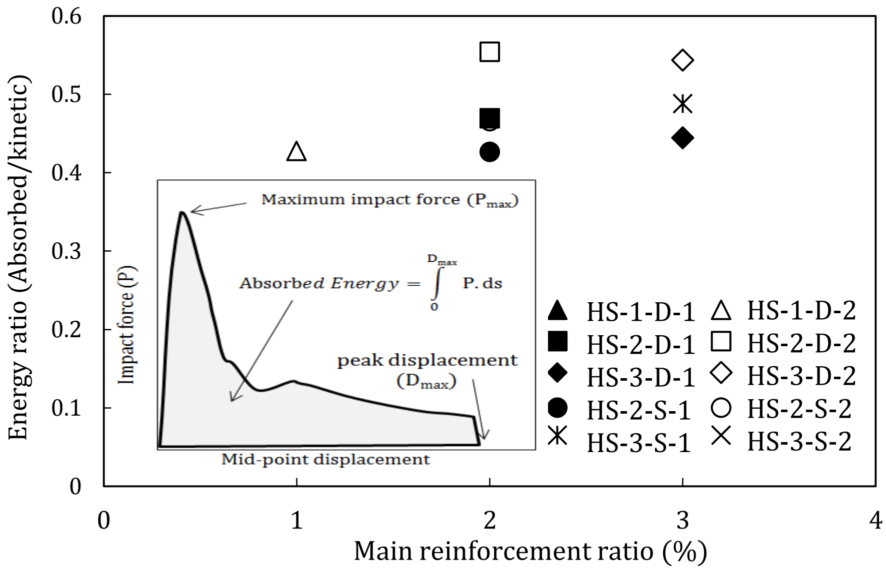

Figure 5.7 – Influence of main reinforcement ratio on absorbed energy

5.2.3.3 Midpoint displacement response

The displacement-time histories for all plates are found to response typically as shown in **Figures 5.8** to **5.10**. Under each impact test, the plate starts to vibrate in the same direction of drop-weight motion. The displacement achieves the peak value rapidly. Thereafter, the plate vibrates at a high frequency in the equilibrium position. When there is no plastic deformation or damage occurred in the pate during impact, the plate is in a free vibration at zero equilibrium position and there is no offset. On the other hand, if the plastic deformation is occurred, the plate will vibrate at a new equilibrium position. The new equilibrium position is called permanent displacement offset (the position about which the subsequent free vibrations of the nonlinear system occur). A summary of maximum midpoint displacements and the corresponding time of all tested plates are reported in **Table 5.2**.

Figure 5.8 shows displacement-time histories for first and second impact tests of doubly and single reinforced plates with identical bottom reinforcement of 2% (plates HS-2-D and HS-2-S). Typically, the displacement responses exhibit progressively increasing peak followed by residual displacement. The effect of damage level or stiffness loss shows up clearly in this comparison; under first impact there is no permanent displacement offset which indicates only slight deformation took place. On the other hand, the displacement histories of second impact tests show larger peak and permanent displacement offset. This clearly demonstrates that there is substantial permanent or plastic deformation took place.

It is also evident from **Figure 5.8** that the natural period of second drop has increased compared to first impact. This period elongation resulted from stiffness loss of damaged plates. It should be mentioned that the displacement-time histories of second impact events for single reinforced plates (i.e., HS-2-S-2 and HS-3-S-2) were not completely captured due to massive concrete scabbing that blocked the laser beam path of displacement sensor. However, the trend of recorded period of the responses show that single reinforced plates exhibit higher substantial permanent deformation compared to doubly reinforced plates (refer to **Figure 5.8-right**).

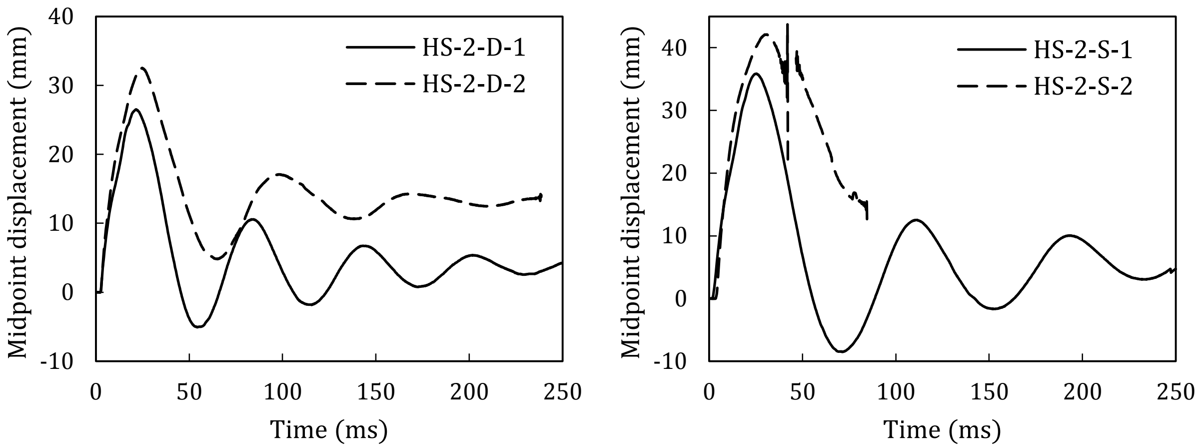

Figure 5.8 – Midpoint displacement-time histories for plates HS-2-D and HS-2-S

a) <u>Influence of steel reinforcement layout</u>

Figure 5.9 shows the influence of steel reinforcement arrangement on the displacement response. It is clearly illustrated that the addition of minimal top steel reinforcement layer reduced the peak and residual displacements. **Figure 5.9** can be used to demonstrate the effect of reinforcement arrangement on controlling damage level; doubly reinforced plate exhibits limited permanent displacement offset compared to single reinforced plate especially for plates with main reinforcement ratio of 3 % (**Figure 5.9-right**). Also, the time period is less for doubly reinforced plate which means it has higher stiffness.

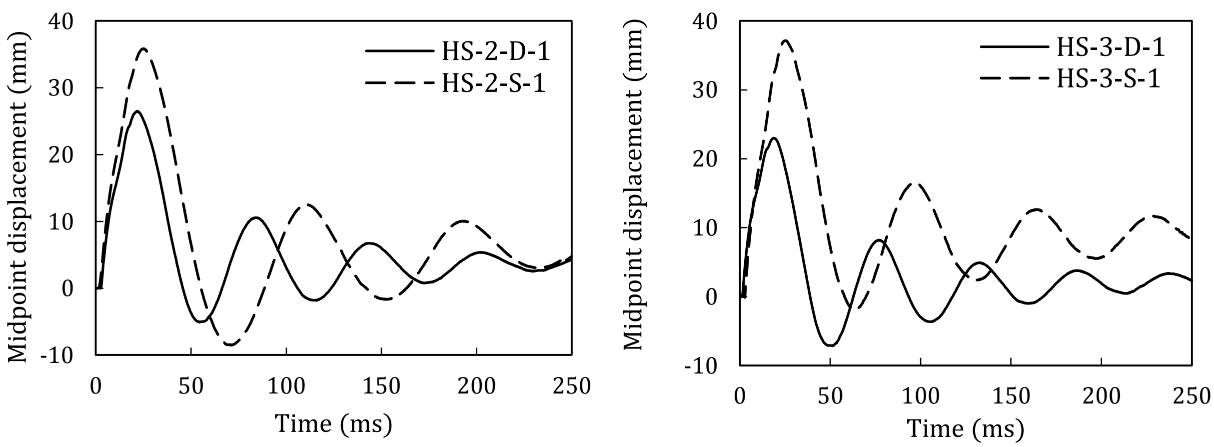

Figure 5.9 – Influence of reinforcement arrangement on midpoint displacement (1st impact)

b) <u>Influence of bottom reinforcement ratio</u>

The effect of main steel reinforcement ratio is presented in **Figure 5.10**. For doubly reinforcement specimens, main reinforcement ratio plays important role in limit peak displacement and residual displacement (**Figure 5.10-left**). On the other hand, increasing the bottom reinforcement ratios of the single reinforced plates has limited influence on midpoint displacement amplitudes (**Figure 5.10-right**). Additionally, permanent displacement offset of impact test on specimen HS-3-S-1 is larger than obtain from impact test on HS-2-S-1.

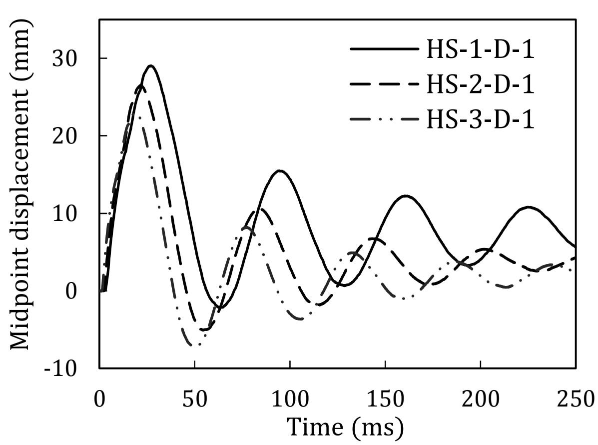

Figure 5.10 – Influence of main reinforcement ratio on midpoint displacement (1st impact)

This means that increasing reinforcement ratio increases the damage level for the singly reinforced plates. The reason of such behaviour is returned to the effect of the stiffness on peak impact force. Specimen HS-3-S has higher stiffness than HS-2-S. As observed in Section **5.2.3.1**, increasing the stiffness leads to less contact time duration and larger peak impact force. The peak impact force of test HS-3-S-1 is 37 % higher than test HS-2-S-1 (refer to **Table 5.2**). This should be mentioned side by side with single reinforced plates under impact loads are mainly responded locally and failed in punching shear mode, which affected by concrete strength rather than flexural steel reinforcement ratio. This means increasing the reinforcement ratio in single reinforced plate has a negative effect; it increases the peak impact force without any significant contribution in punching resistance.

5.2.3.4 Damage characteristics and crack patterns

Based on the observed damage and crack development in the tested specimens, crack pattern is found to be depending on reinforcement layout rather than main reinforcement ratio. All single reinforced specimens (HS-2-S and HS-3-S) are typically failed by localized sudden punching. Shear cracks are observed before any significant bending cracks developed. Under the first impact drop, visible penetration of the drop-weight and wide circumferential cracks around the impact zone at the bottom surface are observed. In addition, partial scabbing is observed in circumferential crack zone. Under second impact, residual circumferential cracks from the previous impact are widened significantly led to excessive penetration and concrete scabbing associated with punching shear in the outside perimeter under impact loading zone. Visible narrow radial cracks on top and bottom surfaces are also developed. The final cracking pattern for specimen HS-3-S is presented in **Figure 5.11-a**. Single reinforced specimens (HS-2-S and HS-3-S) almost have same small value of permanent displacements (refer to **Table 5.3**) regardless reinforcement ratio.

The addition of top steel reinforcement layer strongly limits the development of the localized damage. All doubly reinforced specimens (HS-1-D, HS-2-D, and HS-3-D) typically failed in a ductile punching mode, i.e., the crack pattern indicates that both bending and shear cracks are developed. Under the initial impact, cracking patterns aligned with steel reinforcement grids are developed on both top and bottom surfaces of the plates indicating flexural bending behaviour. No concrete scabbing, only limited penetration is observed. Under the second drop, visible penetration is observed and also inherited hairline cracks from the first impact are widened. In addition to such cracks, new radial and circumferential cracks are developed, that led to partial concrete scabbing. The final cracking pattern for HS-3-D plate is presented in **Figure 5.11-b**.

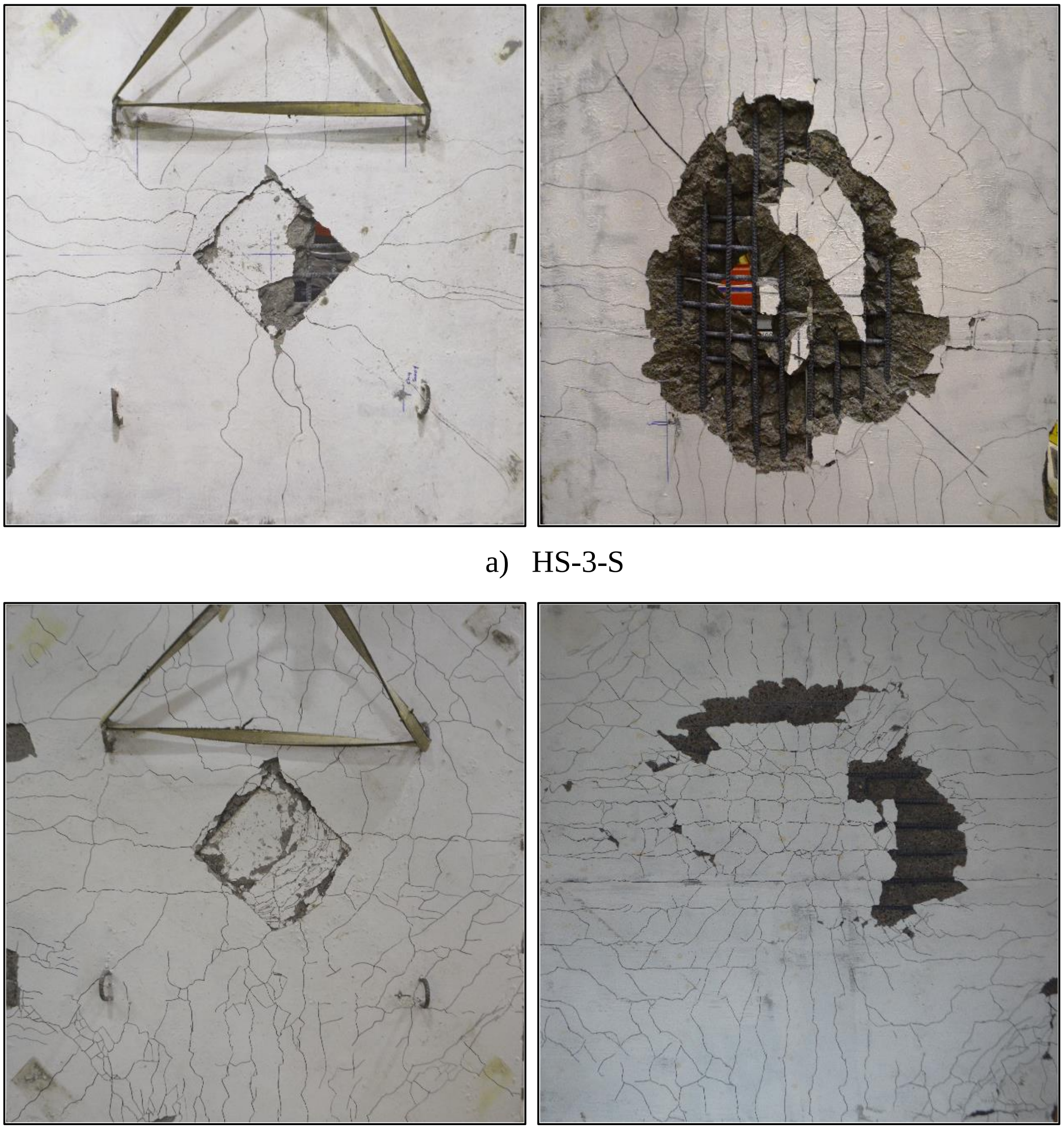

a) HS-3-S

b) HS-3-D

Figure 5.11 – Final crack patterns (left: top surface; right: bottom surface)

Table 5.3 summarizes final damage measurements of all tested HSC specimens. It is obvious from measurements that the addition of minimum top reinforcement layer plays an important role in controlling the damage. For specimens with identical main bottom steel reinforcement the ejected scabbing concrete weight is decreased by more than 60% and the penetration depth is decreased by approximately 40% when minimum top steel reinforcement layer is added. The main reinforcement ratio is found to have influence on the residual displacement of doubly reinforced specimens (refer to **Table 5.3**). The residual displacement values are decreased with the increase of main reinforcement ratio. It should be noted that doubly reinforced plates have higher residual displacement compared to single reinforced ones. This observation confirms that doubly reinforced plates are responded globally and failed by ductile punching shear mode and single reinforced plates are responded locally and failed in pure punching mode. Scabbing mass is also affected by the main reinforcement ratio. More concrete is ejected from the back surface of the plates with the least amount of reinforcement.

Table 5.3 – Damage measurements of HSC plates

Plate's ID	Penetration depth (mm)	Punching diameter (mm)	Punching cone angle (degree)	Scabbing mass (kg)	Residual displacement (mm)
HS-1-D	20.0	1040	24.0	28.4	32.5
HS-2-D	17.5	1045	23.0	24.0	20.3
HS-3-D	12.2	940	29.7	9.7	15.3
HS-2-S	29.1	1165	19.7	66.1	11.3
HS-3-S	23.8	1200	18.4	61.5	11.8

The above mentioned failure modes can be verified using strain-time histories of steel reinforcement at the midpoint zone. Steel strain-time histories of single and doubly reinforced specimens with identical main bottom reinforcement ratio of 2 % are shown in **Figure 5.12**. These plates are selected to show the correlation between steel strain-time history and failure mode. Since there is no significant lose in the stiffness at the start of first test, the measured strain-time histories under first impact show same trend for all specimens, regardless reinforcement arrangement or main reinforcement ratio. Typically, as shown in **Figure 5.12-left**, strain gauges measured large peak strain values beyond the yield strain followed by residual strain. Under the second impact (**Figure 5.12-right**), steel strain-time history is influenced by reinforcement arrangement. Steel strain in case of single reinforced plate does not reach yield strain. This means the plate response locally and failed by a sudden failure of concrete before any significant flexural deformation. On the other hand, steel strain in the case of doubly reinforced plate reaches higher strain level over the yield limit compared to first impact. This means the doubly reinforced plate still response globally indicating that there is a flexural deformation.

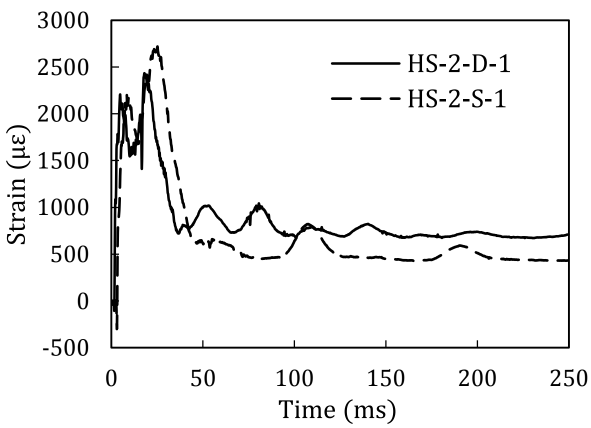

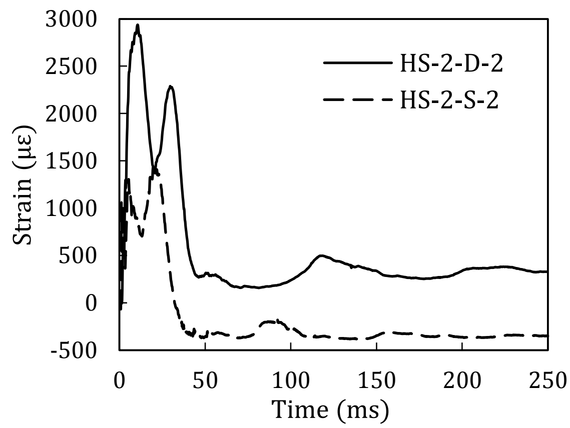

Figure 5.12 – Strains-time histories for HS-2-D and HS-2-S (left:1st impact; right: 2nd impact)

5.3 Results of UHP-FRC Series

As explained before the results of the impact tests are presented in both quantitative and qualitative forms. The measurements of the tested plates are reported in details to facilitate the development of the numerical FE model. In addition, selected results are presented to characterize the influence of steel fibre content, and reinforcement ratio on the impact capacity and failure pattern of tested plates. It should be recalled from Chapter 4 that five UHP-FRC specimens and two control specimen (NSC and HSC) have been tested under repeated impact load by dropping a 475 kg drop-weight from a fixed height of 4.15 m and the testing is terminated when the cumulative residual midpoint displacement of repeated impacts exceeds 65 mm or sever punching damage take place.

5.3.1 Impact test measurements of UHP-FRC series

Table 5.4 summarizes the results of conducted first four impact tests for each plate. The number between brackets beside the specimen name is the total number of impact tests that applied to the plate until reaching one of the two testing termination criteria. The results are reported in terms of impact load characteristics and plate response. The reported impact velocity (V_i) and rebound velocity (V_b) are calculated using image analysis of the recorded videos. The impact force (P) excited in the falling drop-weight is determined using the average reading of the two ±20,000g accelerometers mounted to the drop-weight. The impulse (I_p) is the time integration of impact force, i.e., the area under impact force-time curve. It should be mentioned as a validation of impact force calculation process that all impact tests have almost the same impulse with an average of 5.06 kN.s and coefficient of variance of 4.1%. This behaviour can be easily explained by using the impulse-momentum theorem as discussed before. Imparted kinetic energy (E_k) is the kinetic energy at instant of impact ($1/2\ mV_i^2$). The peak reaction (R) is the maximum total reaction force determined by summing the measurements of four load cells. The reported midpoint peak displacement (Δ_{peak}), residual displacement (Δ_{Res}), and steel reinforcement strain (ε_{steel}) represent the measurements of individual impact tests and do not include the accumulation of residual values from previous tests.

Figure 5.13 and **5.14** show the typical time histories of impact tests measurements for control (NSC and HSC), and UHP-FRC plates, respectively. All measurements time histories have the same trend regardless the concrete material, steel reinforcement, damage level, and fibre content;

the peak amplitude of impact force is greater than that of reaction force. Additionally the time of peak impact force is different from those of peak reaction force, displacement, and steel reinforcement strain.

Table 5.4 – Impact tests measurements of UHP-FRC series

Plate	Test no.	Impact load characteristics					Plate response			
		V_i (m/s)	V_b (m/s)	P(kN)	I_p (kN-s)	E_k (kJ)	R (kN)	Δ_{peak}[1] (mm)	$\Delta_{Res.}$[1] (mm)	ε_{Steel}[1] (με)
NS_{100}	1	-8.90	2.00	1085.5	5.30	18.8	802.8	78.10	29.3	2012
HS_{100} (3)	1	-8.60	1.85	1080.0	4.97	17.6	950.0	30.0	9.8	2119
	2	-8.55	1.75	996.0	4.89	17.4	823.4	15.1	15.1	2205
	3	-8.65	1.50	1160.0	4.81	17.8	790.9	22.7	22.7	2075
UF_1S_{100} (7)	1	-9.00	2.35	1530.7	5.47	19.2	1055.1	44.7	9.0	3963
	2	-8.85	5.25	1479.6	5.18	18.6	NA	46.2	7.8	4250
	3	-8.75	2.20	1406.5	4.95	18.2	1134.2	46.5	7.2	4300
	4	-8.90	2.40	1438.0	5.21	18.8	1101.4	53.3	11.2	NA
UF_2S_{100} (9)	1	-8.95	2.10	1576.5	5.18	19.0	969.6	42.5	10.4	3992
	2	-9.05	2.30	1610.0	5.12	19.5	1210.6	44.7	8.8	4150
	3	-8.70	1.85	1453.2	4.77	18.0	1040.0	45.3	7.4	4520
	4	-8.80	1.90	1461.2	4.97	18.4	1014.5	45.5	5.4	4755
UF_3S_{100} (18)	1	-9.00	2.40	1762.8	5.50	19.2	1008.9	33.6	4.9	3303
	2	-8.95	2.20	1703.0	5.17	19.0	1333.9	35.9	4.2	2980
	3	-9.00	2.30	1695.7	5.09	19.2	1303.0	36.4	2.9	3037
	4	-8.95	2.15	1660.0	5.11	19.0	1250.0	36.6	2.1	4186
UF_2S_{158} (4)	1	-8.80	2.10	1550.0	5.12	18.4	1038.4	42.4	10.3	4701
	2	-8.85	2.05	1513.3	5.12	18.6	1165.3	51.1	15.4	NA
	3	-8.65	1.90	1492.0	4.91	17.8	1102.8	56.9	18.0	2846
	4	-8.55	1.50	1483.0	4.58	17.4	1178.0	64.8	24.1	2444
UF_2S_{210} (4)	1	-8.80	2.20	1534.8	4.99	18.4	918.9	47.0	15.2	5631
	2	-8.65	1.75	NA	NA	17.8	NA	50.0	15.8	5352
	3	-8.95	2.05	1320.6	5.24	19.0	882.6	58.6	23.9	4581
	4	-8.80	1.80	1050.3	4.99	18.4	996.0	65.7	26.2	6863

[1] Not include cumulative measurement of previous tests
NA is data not available due to faulty sensors or broken wire.

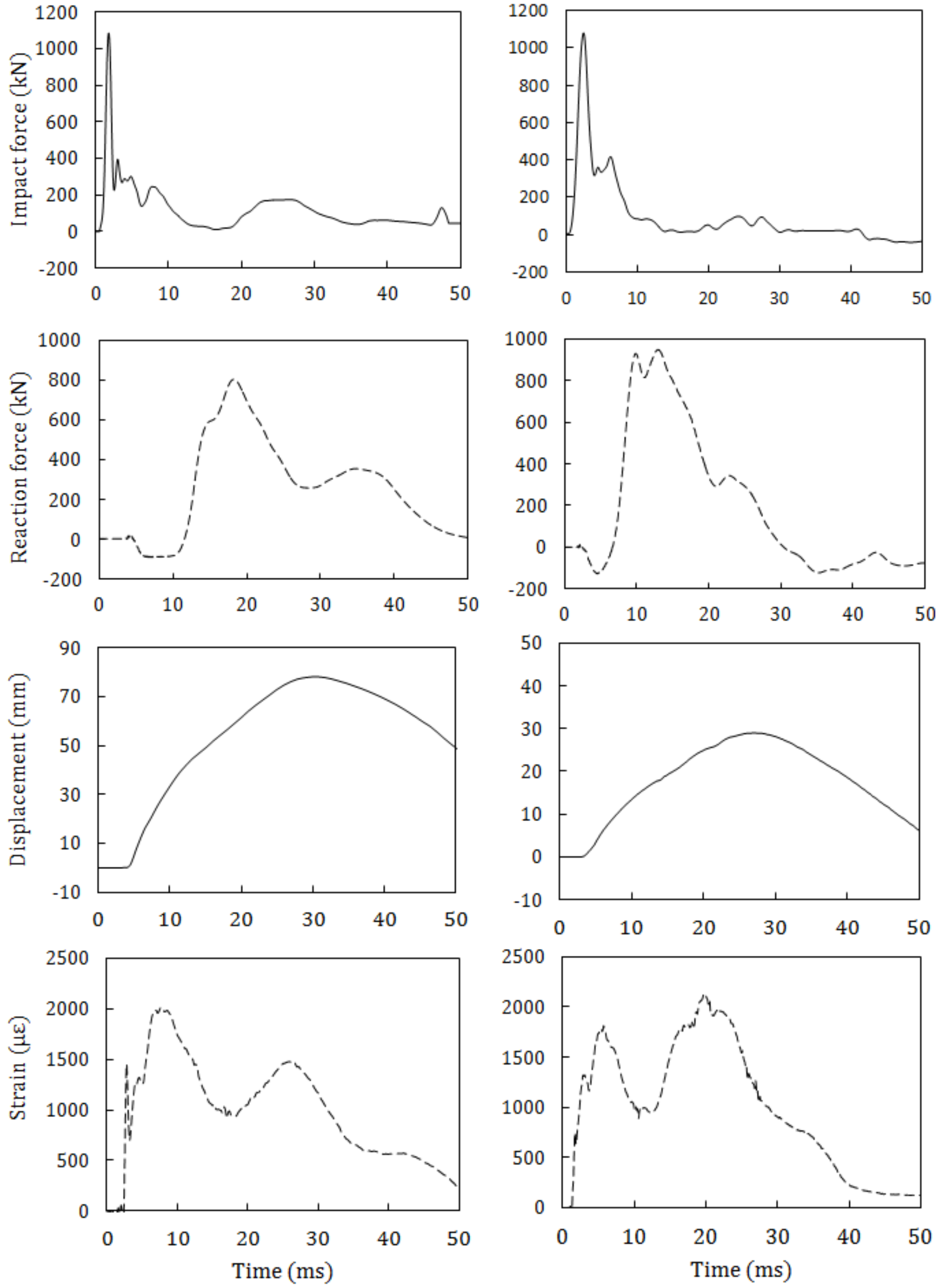

a) NS_{100} b) HS_{100}

Figure 5.13 – Typical time histories of different measurements of control specimens (1st test)

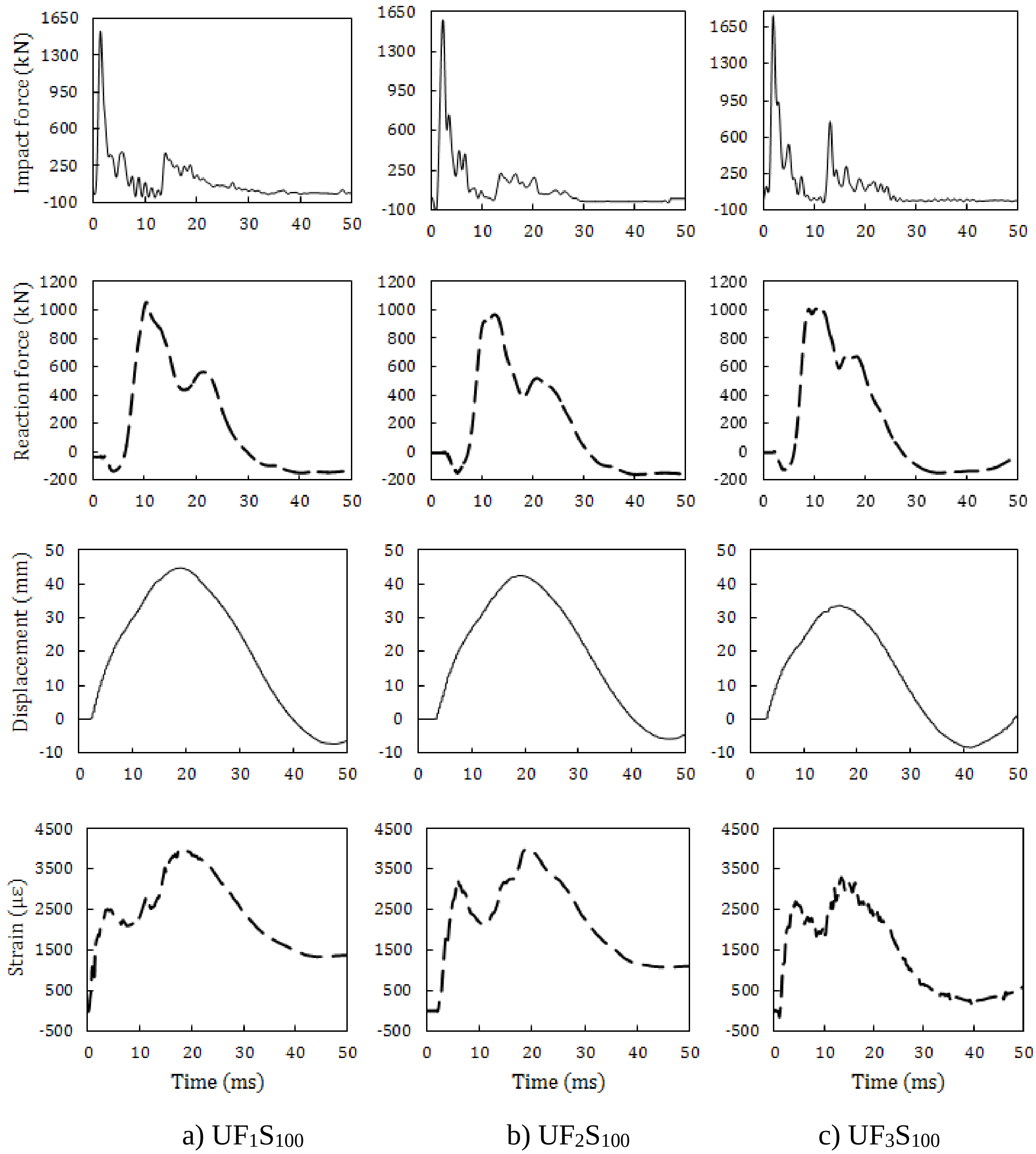

Figure 5.14 – Typical time histories of different measurements of UHP-FRC specimens (1st test)

5.3.2 Impact capacity

Previous study carried out by Kurihashi et al. (2006) showed that the impact capacities were the same for two identical FRC specimens subjected to two different low-velocity impact loading protocols (single impact or sequential impacts). Therefore, in this investigation, the total kinetic energy ($E_k = \Sigma 1/2\ mV_i^2$) imparted to each specimen is used to provide an estimate of the impact capacity. It should be pointed out that all plates have been tested under same loading and supporting conditions, and subjected to uniform testing termination criteria. **Table 5.5** summarizes the impact capacities of tested plates. Clearly, the cumulative residual displacements of some plates were exceeded extensively the limit (65 mm) during the last impact test. For example, specimen UF_2S_{158} experienced extensive residual displacement after the fourth impact of 67.9 mm; on the other hand, UF_2S_{210} experienced 81.0 mm after same number of impact tests. Therefore, interpolation is used to estimate the impact capacity of tested plates by fitting polynomial curve to energy vs cumulative displacement data.

Table 5.5 – Impact capacities of UHP-FRC series

Plate's ID	No. of impacts	Final residual displacements (mm)	Total kinetic energy, E_k	
			(kJ)	Normalized [2]
NS_{100}	1	29.30[1]	18.8	1
HS_{100}	3	47.60[1]	53.1	2.8
UF_1S_{100}	7	65.68	129.8	6.9
UF_2S_{100}	9	65.28	167.7	8.9
UF_3S_{100}	18	65.03	333.8	17.75
UF_2S_{158}	4	67.86	70.0	3.7
UF_2S_{210}	4	81.00	63.2	3.4

[1] Test terminated due to punching shear criteria
[2] Normalized with respect to NSC plate (NS_{100})

The influence of the steel fibre volume content and the longitudinal steel reinforcement ratio on the impact capacities of UHP-FRC plates are shown in **Figure 5.14**. The impact capacity of NSC and HSC specimens are included as well. It is evident from **Table 5.5** and **Figure 5.14**, the use of UHP-FRC material enhances the impact capacity significantly. Comparing the capacity of UHP-FRCs to NSC and HSC plates that are constructed using same steel reinforcement ratio, the total imparted energy to UHP-FRC plates is being in range of 7 to 18 times the capacity of NSC plate. The increased capacities of UHP-FRC plates are correlated to the steel fibre content. A worth of mentioning here that increasing of fibre content from 1 to 2% has limited effect on the impact capacity compared to increasing the fibre content from 2 to 3%. Steel reinforcement ratio is found also to have significant influence on increasing the impact capacity (refer to **Figure 5.15**). This behaviour indicates that UHP-FRC plates are responded globally.

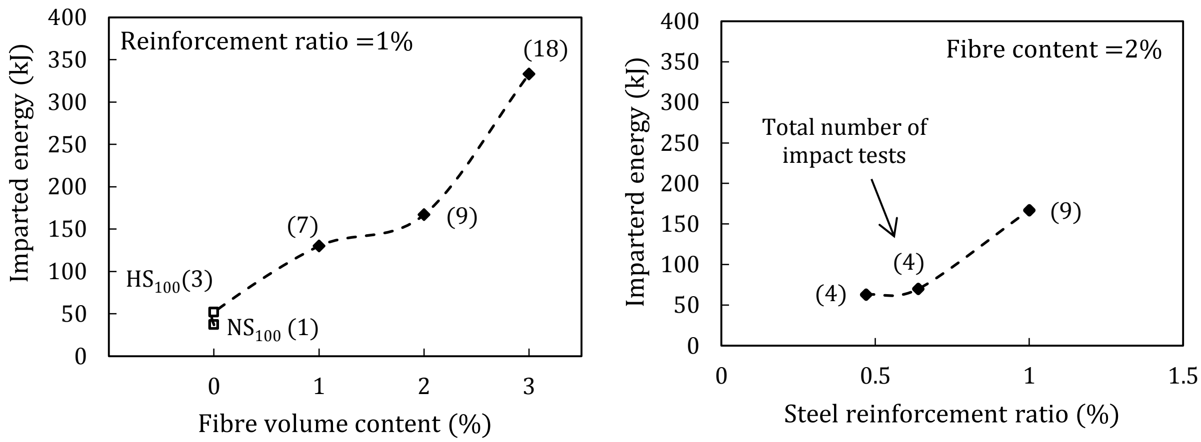

Figure 5.15 – Influence of fibre content and steel reinforcement ratio on impact capacity

5.3.3 Crack patterns and failure modes

Based on the observed damage and crack development in tested plates, the failure mode is found to be depending on the concrete material (i.e., NSC and HSC, or UHP-FRC) rather than reinforcement ratio and fibre content. Both NSC and HSC plates are failed in punching shear mode. The NSC plate (NS_{100}) is terminated after the first impact test due to concrete ejection in the impact zone with a residual displacement of 29.3 mm (**Figure 5.16-a**). HSC specimen sustained two more tests, The HS_{100} plate is terminated after the third impact test also due to severe concrete ejection with high probability of damage of instrumentation under additional impacts. The final residual displacement of HS_{100} is 47.5 mm.

a) NS_{100} (NSC, Steel spacing =100 mm)

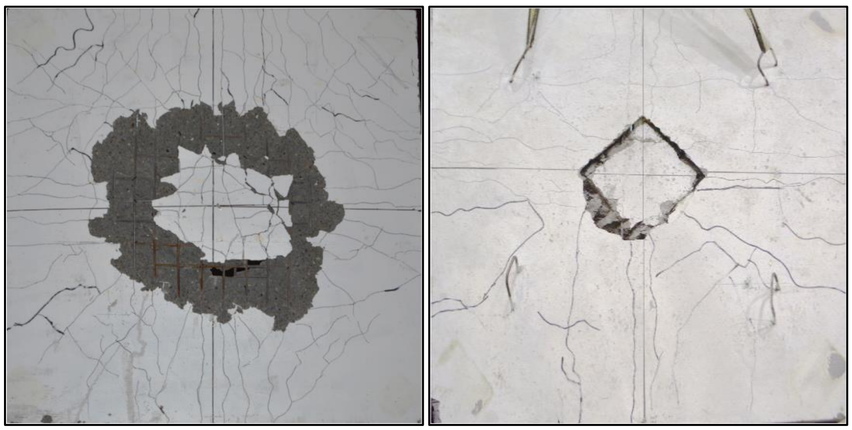

b) HS_{100} (HSC, Steel spacing =100 mm)

Figure 5.16 – Final crack patterns of control specimens (left: bottom surface; right: top surface)

The final cracking patterns for UHP-FRC plates are presented in **Figure 5.17**. Unlike predominated punching shear failure pattern observed in control specimens and HSC series, and reported in several experimental impact studies on RC plates (Murtiadi and Marzouk, 2001; Zineddin and Krauthammer, 2007; Chen and May, 2009; Hrynyk and Vecchio, 2014), all UHP-FRC plates exhibit pronounced ductility and are typically failed in pure flexural mode regardless fibre volume dosage and/or steel reinforcement ratio. Under repeated impact tests, all UHP-FRC plates reach the cumulative residual displacement of 65 mm and only bending cracks are observed.

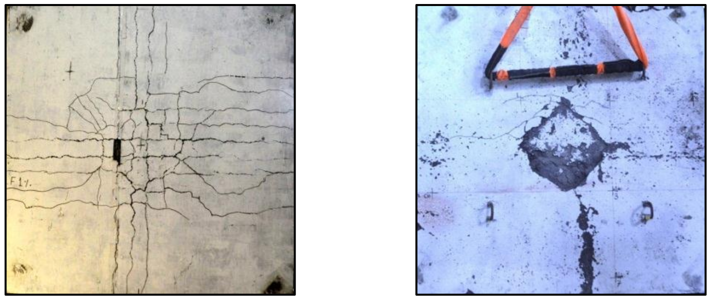

a) UF_1S_{100} (v_f =1%, Steel spacing =100 mm)

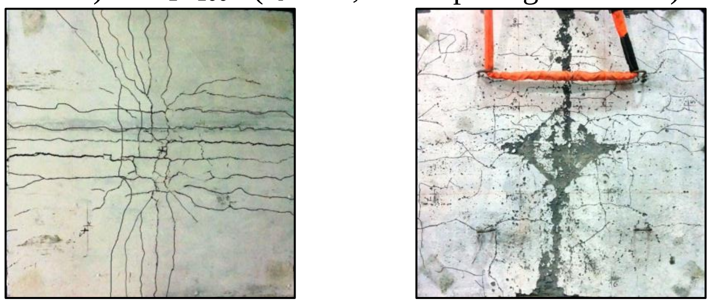

b) UF_2S_{100} (v_f =2%, Steel spacing =100 mm)

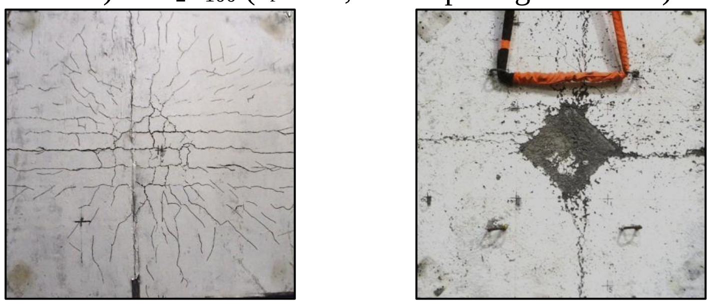

c) UF_3S_{100} (v_f =3%, Steel spacing =100 mm)

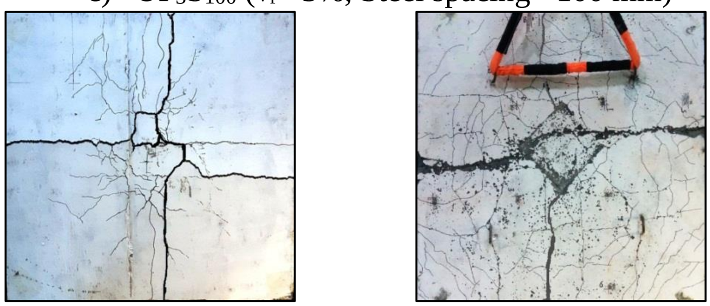

d) UF_2S_{210} (v_f =2%, Steel spacing =210 mm)

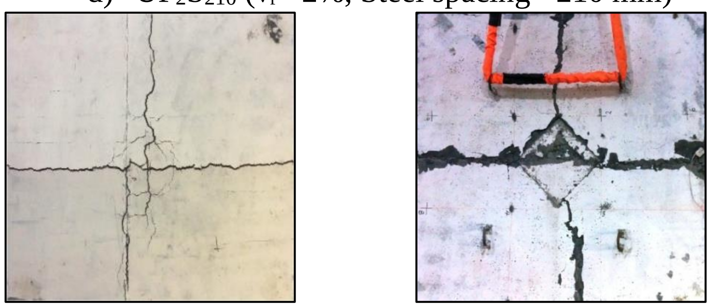

e) UF_2S_{158} (v_f =2%, Steel spacing =158 mm)

Figure 5.17 – Final crack patterns of UHP-FRC plates (left: bottom surface; right: top surface)

A worth of mentioning here that steel reinforcement ratio strongly influences the crack pattern. UHP-FRC plates containing a steel reinforcement ratio of 1% (UF_1S_{100}, UF_2S_{100}, and UF_3S_{100}) typically exhibit similar crack pattern. Multi-cracks aligned with steel reinforcement grids are developed in both directions on the bottom surface of plates regardless fibre volume content (**Figures 5.17**-a, b, and c). On the other hand, the major damage of plates reinforced with steel reinforcement of ratios less than 1% (UF_2S_{158} and UF_2S_{210}) is typically concentrated in a single wide crack at mid-span and failure crack pattern is consisted of four radial macro-cracks (**Figures 5.17**-d and **5.17**-e). It should be pointed out that fibre content plays an important role in limiting the extent of damage level. Increasing the fibre content has led to an increase in the number of cracks in the bottom surface of plates and a reduction in the width of cracks formed.

All UHP-FRC specimens showed enhanced damage control properties compared to NSC and HSC specimens. No spalling, scabbing, and/or significant large concrete fragmentations are observed under repeated impact tests. Even at failure, the fragments are in form of fine powder. Therefore, the use of UHP-FRC in structural members can effectively eliminate the possibility of sudden catastrophic failure that would cause injury to occupants in case of accidental extreme loading scenario. A comparison between damage progression under repeated impact load for the control HSC specimen (HS_{100}) and UHP-FRC specimen containing 2% fibres (UF_2S_{100}) is shown in **Figure 5.18** and damage characteristics of impact zone are illustrated in **Figure 5.19**. It should be pointed out that both specimens have same reinforcement ratio and layout.

1st impact test 3rd impact test

2nd impact test 6th impact test

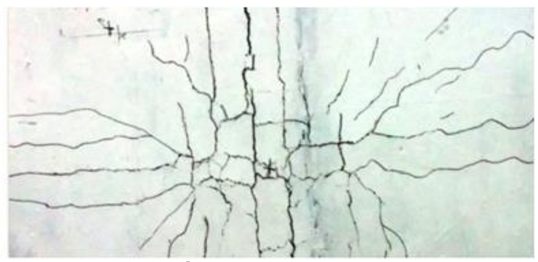

3rd impact test 9th impact test

Figure 5.18 – Damage progression under repeated impact loads (left: HS_{100}; right: UF_2S_{100})

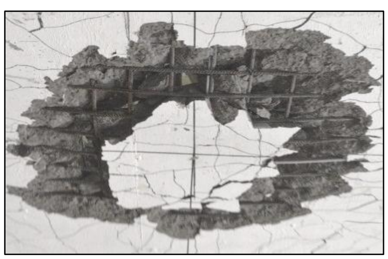

a) HSC plate after 3 impact tests

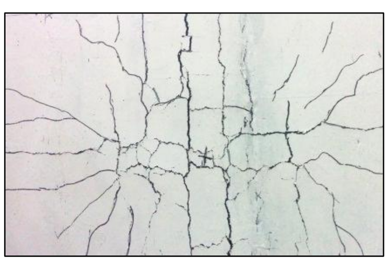

b) UHP-FRC plate after 9 impact tests

Figure 5.19 – Damage characteristics of impact zone (left: bottom surface; right: top surface)

5.3.4 Midpoint displacement response

The midpoint displacement-time histories for all plates are responded typically as shown in **Figures 5.20** – **5.22**. Under each impact, the midpoint exhibited progressively increasing peak followed by residual displacements and the plate vibrates at the equilibrium position. As mentioned before, when there is no plastic deformation or damage occurred in the plate due to impact, the plate is vibrated freely at zero equilibrium position. On the other hand, if the plastic deformation is occurred, the plate will vibrate at a new equilibrium position that called permanent displacement offset. It should be mentioned that displacement-time histories shown in **Figures 5.20 – 5.22** represent the results of individual impact tests that do not include the accumulation of residual displacements from previous impacts.

a) <u>Influence of concrete material on the midpoint displacement response</u>

Figure 5.20 shows the displacement response of plates NS_{100}, HS_{100}, and UF_1S_{100} for all preformed impact tests. It should be recalled that the plates are identical with exception of concrete materials. The results of even impact tests of specimen UF_1S_{100} are omitted for clear displaying purpose. The advantage of using UHP-FRC in impact resistance structures shows up clearly in this comparison; NSC and HSC plates exhibited excessive damage as it is reflected on the displacement response in the form of permanent displacement offset and significant increase in time period after each impact test (**Figure 5.20-a** and **b**). However, NSC specimen showed a more ductile response compared to HSC. The peak midpoint displacement of NSC is more than twice the HSC displacement. On the other hand, UHP-FRC plate (UF_1S_{100}) showed a pronounced ductility and enhanced elastic recovery response under repeated impacts (**Figure 5.20-c**). The UHP-FRC specimen has the ability to recover the displacement with slightly permanent displacement offset and lowers natural time period elongation. It should be clear in this comparison that the UF_1S_{100} specimen containing 1 % steel fibres is a lower-bound and other UHP-FRC specimens that containing 2 and 3% steel fibres showed more pronounced ductility and elastic recovery properties.

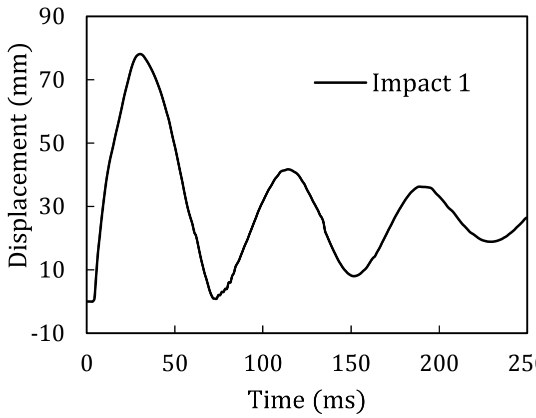

a) NS_{100} (NSC)

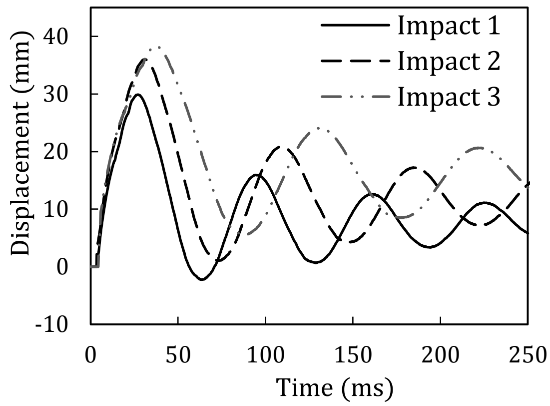

b) HS_{100} (HSC)

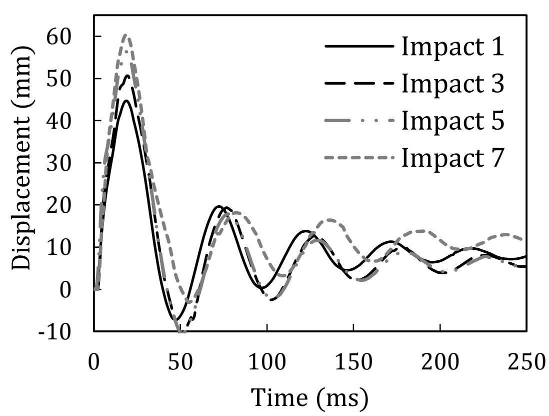

b) UF_1S_{100} (UHP-FRC, v_f =1%)

Figure 5.20 – Influence of concrete material on the midpoint displacement-time history

b) <u>Influence of steel fibre content on the displacement response</u>

Figure 5.21 shows the influence of steel fibre content on displacement response for first and fourth impact tests. It is clearly illustrated that the increasing of fibre dosage reduced the peak and residual displacements. Also, the time period is decreased with the increase of fibre content. **Figure 5.21** can be used to demonstrate the effect of fibre content on controlling damage level; plate containing 3% fibre (UF_3S_{100}) exhibited no permanent displacement offset compared to plates containing 1 and 2% fibres (UF_1S_{100} and UF_2S_{100}). It should be mentioned that increasing fibre from 1 to 2 % has limited effect on displacement response under first impact test (**Figure 5.21-left**). Same displacement response is observed in second and third impact tests. Both plates have almost similar response in terms of magnitude, time response, and residual displacement. Starting from fourth impact test (**Figure 5.21-right**), the displacement histories of plates UF_1S_{100} and UF_2S_{100} showed different peak and permanent displacement offset. The reason of such behaviour can be return to the effect of fibres distribution on micromechanical behaviour of UHP-FRC matrix. The number of fibres per unit volume of plate UF_3S_{100} (v_f =3%) are sufficient to effectively arrest the propagation of any potential micro-cracks at early stage. As a result, the first crack limit is increased and there is no significant plastic deformation offset in displacement response (**Figure 5.21-left**). On the other hand, fibres spatial distributions of plates containing 1 and 2% fibres are not enough to stop the development of micro-cracks paths under first three impact tests. Under fourth impact tests, the size of developed micro-cracks is large enough to be arrested by fibres in plate UF_2S_{100} (v_f = 2%) and fibres start to be active. However at this level of damage, the micro-cracks size still small to be resisted by fibres in plate UF_1S_{100} (v_f = 1%) and the plate suffer more plastic deformation offset (**Figure 5.21-right**).

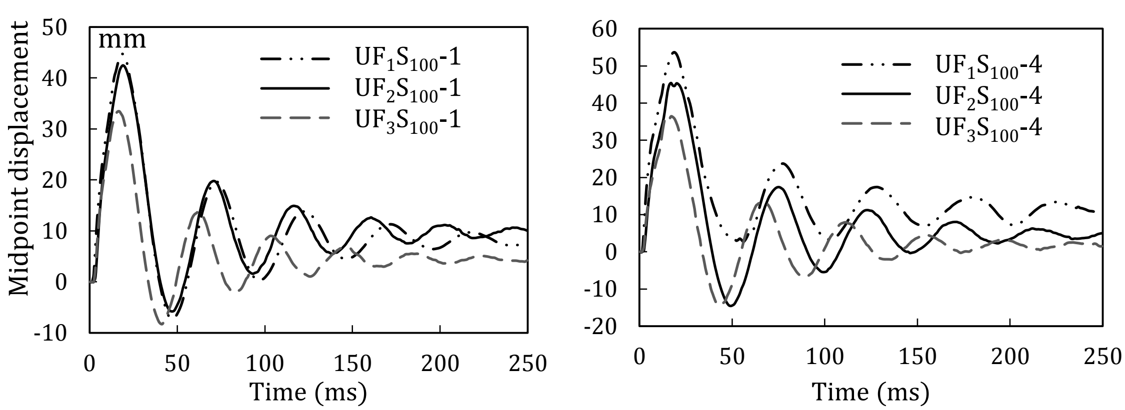

Figure 5.21 – Influence of fibre content on midpoint displacement (left: 1st test; right: 4th test)

c) Influence of steel reinforcement ratio on the displacement response

The effect of steel reinforcement ratio on displacement response is presented in **Figure 5.22**. In general, steel reinforcement ratio plays an important role in limit peak displacement and residual displacement especially for impacts tests performed on previously damaged plates, i.e., second, third impact tests, etc., (refer to **Figure 5.22-right**). Under first impact test on the other hand, there is no change in displacement response is observed when the steel reinforcement ratio increased from 0.64 to 1.00%. Additionally, there is no permanent displacement offset in which indicates only slight deformation took place compared to specimen UF_2S_{210}.

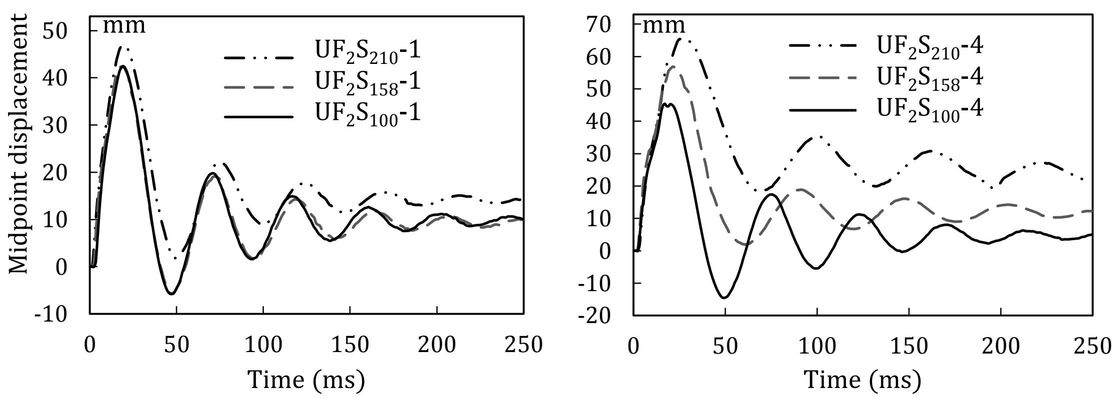

Figure 5.22 – Influence of reinforcement ratio on midpoint displacement (left:1st; right:4th test)

5.4 Dynamic Characteristics Results of Tested Plates

This section presents the experimental results of the dynamic characteristics (natural damped frequencies and damping ratio) of tested plates. The extracted values from this investigation are used later in numerical simulation (Chapter 6). As mentioned before in Chapter 4, the intact plates are excited using sledge hammer at their midpoint to generate free vibration and the plates' responses are captured by two ±500g accelerometers and the quartz load cells. **Figure 5.23** shows typical extracted damped free decay.

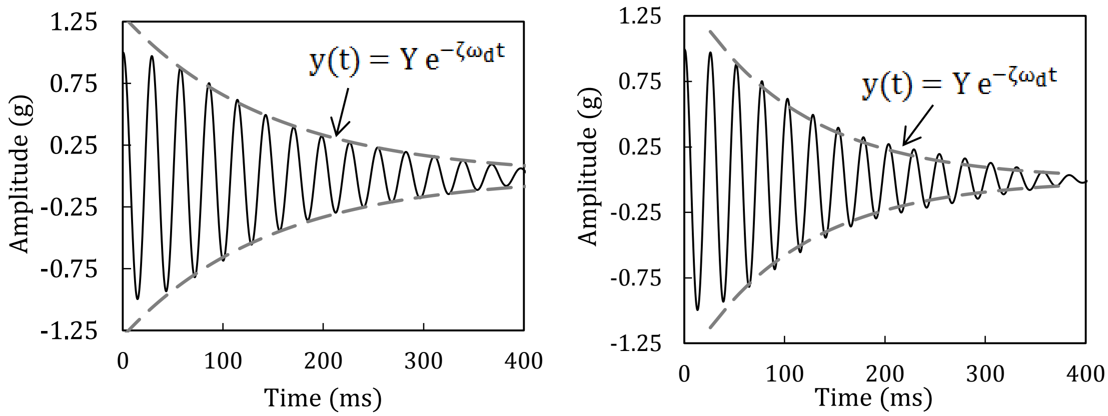

Figure 5.23 –Typical free decay response (left: HS_{100}; right :UF_1S_{100})

The extracted damped free decay curves are used to estimate the damped frequency and damping ratios of the plates. The damped period T_d is measured directly from the digitized graph using the average of the first six cycles. The natural frequency in Hertz is calculated using: $f_d = 1/T_d$ and in rad/s using: $\omega_d = 2\pi f_d$.

The damping ratio (ζ) is estimated using logarithmic decrement approach. The logarithmic decrement is rate of decay of free vibration response. Logarithmic decrement (δ) is calculated using two non-successive cycles of damped vibration as expressed in **Eq. 5.3** and the critical damping ratio (ζ) is estimated using **Eq. 5.4** (Clough and Penzien, 2003)**:**

$$n\delta = \ln \frac{Y_i}{Y_{i+n}} \tag{5.3}$$

$$\delta = \frac{2\pi\,\zeta}{\sqrt{1-\zeta^2}} \tag{5.4}$$

Where,

Y_i = response amplitude at time t_i; Y_{i+n} = response amplitude at time t_{i+n};

n = number of cycles between the two non-successive peaks Y_i and Y_{i+n}.

The estimated dynamic properties using aforementioned Equations are checked by implementing the extracted the natural damped frequency and damping ratio values into **Eq. 5.5** to generate fitting exponential envelope to the damped free vibration response (refer to **Figure 5.23**)

$$y(t) = Y\, e^{-\zeta \omega_d t} \qquad (5.5)$$

Where, Y is the maximum free vibration amplitude that decays exponentially with time t.

Table 5.6 summarizes the dynamic characteristics of all plates. It should be mentioned that all tested plates are responded in first vibration mode under drop-weight impact tests regardless concrete type, reinforcement ratio, fibre content, and level of damage. The first vibration mode is shown up clearly in the displacement shapes developed using the measurements of laser displacement sensors and confirmed by the analysis of recorded videos.

Table 5.6 – Dynamic properties of tested plates

Plate's ID		Period T_d,(ms)	Fundamental Frequency		Damping ratio ζ, (%)
			f_d, (Hz)	ω_d (rad/sec)	
HSC series	HS-1-D	28.15	35.52	223.18	2.95
	HS-2-D	28.08	35.61	223.74	2.96
	HS-3-D	28.00	35.71	224.37	2.97
	HS-2-S	28.11	35.57	223.50	3.01
	HS-3-S	28.13	35.55	223.37	3.01
UHP-FRC series	NS_{100}	33.96	29.45	185.0	2.91
	HS_{100}	28.90	35.64	223.93	2.95
	UF_1S_{100}	24.63	40.66	255.2	3.05
	UF_2S_{100}	22.88	43.70	274.8	3.53
	UF_3S_{100}	22.90	43.66	274.4	3.54
	UF_2S_{158}	23.11	43.27	271.0	3.50
	UF_2S_{210}	23.38	42.77	268.8	3.97

Figure 5.24 shows typical displacement shape of tested Plates at different time periods assuming zero displacement at supports. This figure can be used also to show the plate response

type, NSC specimens responded locally especially during first 15 ms compared to UHP-FRC specimen which responded globally. This observation is consistent with the obtained failure modes discussed before.

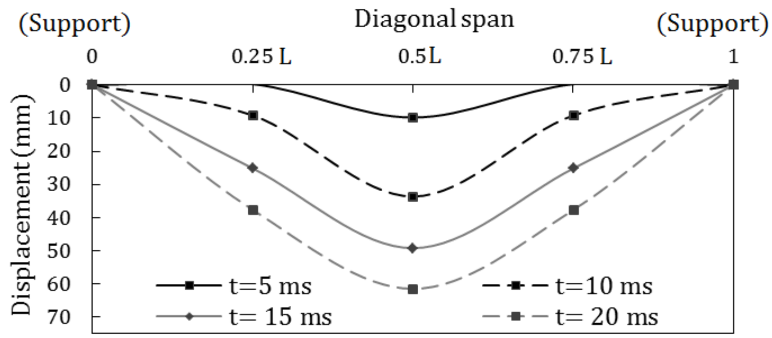

a) NSC specimen (NS_{100})

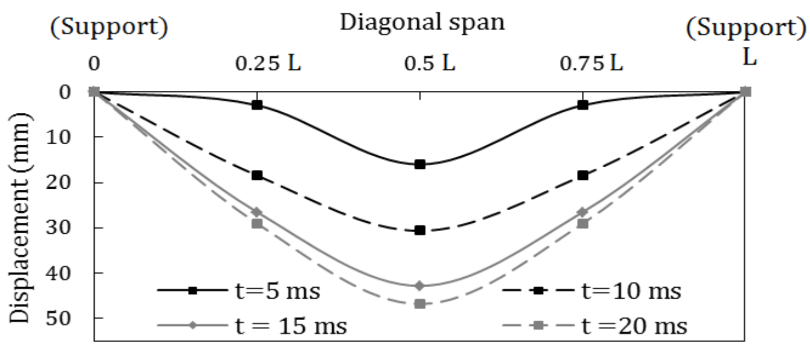

b) UHP-FRC specimen (UF_1S_{100})

Figure 5.24 – Time histories of deformed shape (1st impact test)

5.5 Summary of Full-scale Testing of RC Plates

The drop-weight low-velocity experimental program was successful in investigating the behaviour of two different series of RC plates with different objectives. The experimental program provides good information about dynamic experimental data evaluation, filtering, and validation. The first series tests of HSC plates enabled a better understanding of the steel reinforcement contribution in the behaviour of RC plates subject to impact loading. On the other hand, the second series of impact tests on UHP-FRC plates enabled a better understanding of the advantage of using UHP-FRC in impact resistance structures. Precision low-velocity impact test data were generated in a research area where no testing has been performed. The findings of the two experimental investigations can be presented separately as follows:

a) <u>The following conclusions can summarize the results of HSC series:</u>

1. The impulse of impact force is equal to the change of momentum of impact mass and does not affected by steel reinforcement ratio and/or arrangement.
2. The contact time duration of impact is inversely proportional to the plate stiffness for both single and doubly reinforced plates. The contact time duration was found to be longer for plates with lower reinforcement ratio, and for damaged plate (second impact test).
3. The peak displacement and residual displacement are inversely proportional to the reinforcement ratio for doubly reinforced plates. On the other hand, increasing steel reinforcement ratio has no significant effect on peak displacement of single reinforced plates.
4. Crack pattern was found to be depending on the reinforcement layout rather than reinforcement ratio. Single reinforced specimens typically failed by localized sudden punching. On the other hand, doubly reinforced plates were typically failed in a ductile punching mode. The addition of minimum top reinforcement layer plays an important role in limiting the damage. Additionally, scabbing mass is affected by reinforcement ratio. More concrete was ejected from the back surface of the plates with lower reinforcement ratio.

b) <u>The following conclusions can summarize the results of UHP-FRC series:</u>

1. The use of UHP-FRC instead of NSC or HSC successively changed the failure mode from punching shear to pure flexural mode under repeated low-velocity impact loads. The UHP-FRC plates exhibited superior damage control characteristics when compared to RC plate cast using NSC and HSC. No spalling, scabbing, and/or large fragmentations were observed.

2. All UHP-FRC plates responded globally with pronounced ductility compared to control specimens (NSC and HSC plate). Under repeated impact tests, all UHP-FRC plates regardless of the fibre volume content and/or steel reinforcement ratio reached the target cumulative residual displacement of 65 mm and only bending cracks were observed without any significant punching shear cracks.
3. Comparing the impact capacity of UHP-FRCs plates to NSC plate that was constructed using same steel reinforcement ratio, the total imparted energy to UHP-FRC plate containing 2% fibres by volume (commonly used fibre percent in the industry) was found to be in the range of 9 times the capacity of NSC plate.
4. The use of fibre content of 3% in impact resistance structures is more significant in enhancing the dynamic performance compared to the other used two steel fibre contents of 1 and 2%. The total impact energy of UHP-FRC plate containing 3% fibres was found to be double the capacity of UHP-FRC plate containing 2% fibres and 18 times the capacity of NSC plate.
5. Increasing steel reinforcement ratio has a positive effect on overall impact behaviour which reflected in less peak and residual displacements and higher impact energy capacity.

6 FINITE ELEMENT MODELLING

6.1 Introduction

The use of FE to predict the structural response of RC structures under impact loads is inevitable due to the limitation of empirical equations, complexity of analytical methods, and expensive experimental tests. However, numerical simulation of impact problems through FE method is a highly sophisticated process. There are many aspects still require wide discussion and exploration to accurately model RC structures under impact loading, such as defining strain rate effect on concrete and steel reinforcement materials models, including effect of damping, defining stiffness degradation under dynamic loads, mesh dependency of results, and modelling the dynamic contact between impacted bodies.

The main objective of this chapter is to develop an accurate 3D-FE model capable of analyzing and predicting the dynamic response of the RC structures. The FE analysis has been performed using a general-purpose program ABAQUS/Explicit software, version 6.14 (Simulia, 2016). The simulation results are validated using the results of experimentally tested RC plates presented in previous chapters. Concrete and steel reinforcement are represented by two separate built-in material models which are combined together to describe the behaviour of the composite RC material. Concrete Damage Plasticity (CDP) model is adapted to consider nonlinearity, stiffness degradation, and strain rate effects of concrete. CDP model is coupled with fracture energy to ensure mesh size independent results. The classical metal plasticity model is used to define the full response of the steel reinforcement. Each input parameter is investigated in order to establish a precise numerical method for impact analysis and identify the significance of various parameters on the numerical results. This chapter provides also an effective method for predicting the deformed shape of impacted plate using mass participation factor. The predictive capability of calibrated HSC model has been demonstrated by simulating different plates with different steel reinforcement ratios and arrangement. Thereafter, the calibrated HSC model is extended to model UHP-FRC plates in order to assess whether the existing (CDP) constitutive material model with adjustable material parameters may be able to accurately replicate the UHP-FRC member response under impact loads. The numerical simulation of UHP-FRC is only performed for plates containing 2% fibres because this fibre content is the commonly used percent in industry. Additionally, there are three tested specimens with different steel reinforcement that can be used to check the predictive capability of calibrated UHP-FRC model. The following sections present detailed explanation of the procedures implemented for modelling and calibrating the FE models.

6.2 Development of 3D-FE Model

On the basis of the main objectives of this chapter, 3D-FE models with identical dimensions and boundary conditions of tested plates are developed. Proper geometrical and material parameters are selected carefully so as to simulate the actual impact test as close as possible without any simplifications. The various items concerned with modelling will be addressed in the following subsections.

6.2.1 Geometric modelling

The 3D-FE model of the test setup is illustrated in **Figure 6.1**. Eight-node solid elements with reduced integration (C3D8R) are used to model concrete plates. C3D8R element is formulated based on Lagrangian assumption of the element deforms with material deformation. While first order elements such as C3D8R do not suffer from shear and volumetric locking of full integration elements, the combination of using a reduced integration technique with linear interpolation elements leads to zero energy model or hourglass numerical problem. To overcome hourglass problem, ABAQUS offers numbers of formulations to overcome this problem by using small elastic stiffness and/or viscous damping.

Longitudinal steel reinforcement is modelled using two node beam element (B31) using same arrangement and concrete cover as tested plates. The B31 element uses linear interpolation and has a constant stress. The embedded constraint is adopted to simulate the bond between steel reinforcement and surrounding concrete assuming perfect bond. The advantage of embedded constraint is that the meshes of concrete and steel reinforcement are not required to match. A comprehensive description of selected elements and embedded constraint can be found in ABAQUS Manual (Simulia, 2016).

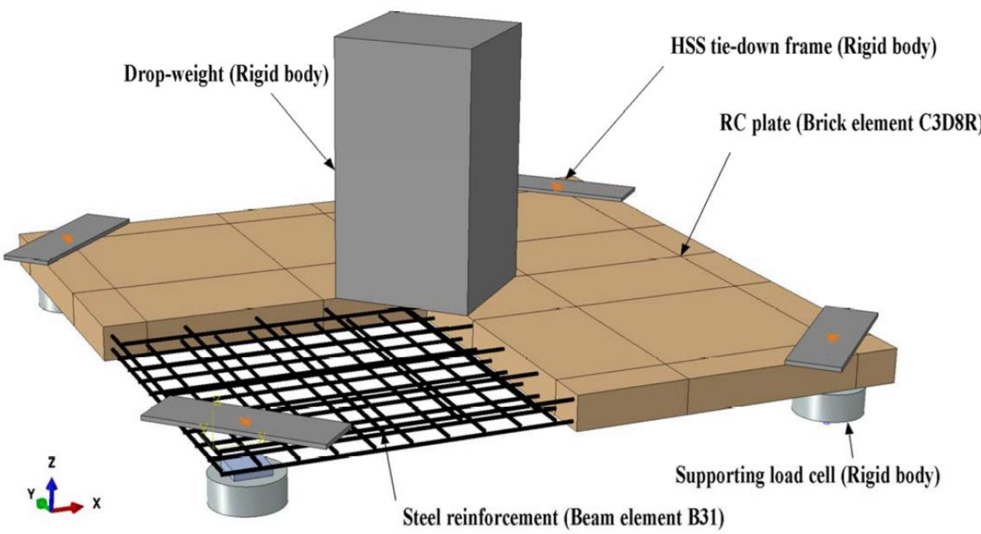

Figure 6.1 – Generated geometry of impact test (control specimen HS_{100})

The drop-weight and supporting systems are modelled with same dimensions and contact areas of the experimental setup using eight-node solid elements with reduced integration (C3D8R). Only supporting system parts in direct contact with the specimen are modelled to simulate their effect on test specimen and in same time reduce the computational cost of the analysis. Rigid body constraint is applied to drop-weight and supporting system since there was no deformation observed during experimental testing. Additionally, stresses are not required for these parts.

6.2.2 Contact interaction

In impact simulation, creating a proper mechanical interaction between different parts is important in order to generate an accurate normal and friction forces that arise during physical contact interaction. ABAQUS/Explicit has two sophisticated computational contact algorithms to model extremely discontinuous form of nonlinearity that involved in impact problems. The two contact algorithms are general contact and contact pairs. The general contact is a single unified contact algorithm that requires minimum user input. It is based on an automatically generated all-inclusive surface definition. Conversely, the contact pair is used to describe contact between two surfaces. It requires the explicit definition of pair surfaces that may potentially come into contact. Both algorithms require specification of contact properties between surfaces. More details regarding contact modelling can be found in (Simulia, 2016) for further understanding.

In the current numerical study, general contact is used since it allows defining contact between all parts of the model (i.e., drop-weight, the RC plate, and the supporting systems) with a single simple interaction. It should be pointed out that, nine contact pairs must be defined to replace the implemented general contact. The default ABAQUS/Explicit option of hard contact is utilized to describe the pressure behaviour of the contact interaction in the normal direction. The hard contact relationship does not allow the transfer of tensile stress across the interface. The friction between the different parts in contact is modelled using isotropic penalty friction formulation. This friction model uses the Coulomb friction model to relate the maximum allowable frictional stress to the contact pressure (Simulia, 2016). The friction coefficient between steel and concrete of 0.40 is adapted to model the friction between the steel parts and the RC specimen.

6.2.3 Loading and boundary conditions

In order to reduce the computational time, the drop-weight is modelled in an initial position very close to the specimen surface (1 mm offset) with initial impact velocity. The predefined impact velocities used in the simulations are taken equal to those extracted from image analysis of recorded videos. The gravitational acceleration is applied to both the drop-weight and the specimen to simulate gravitational effects. **Figure 6.2** illustrates the applied loads, and boundary conditions of the numerical model.

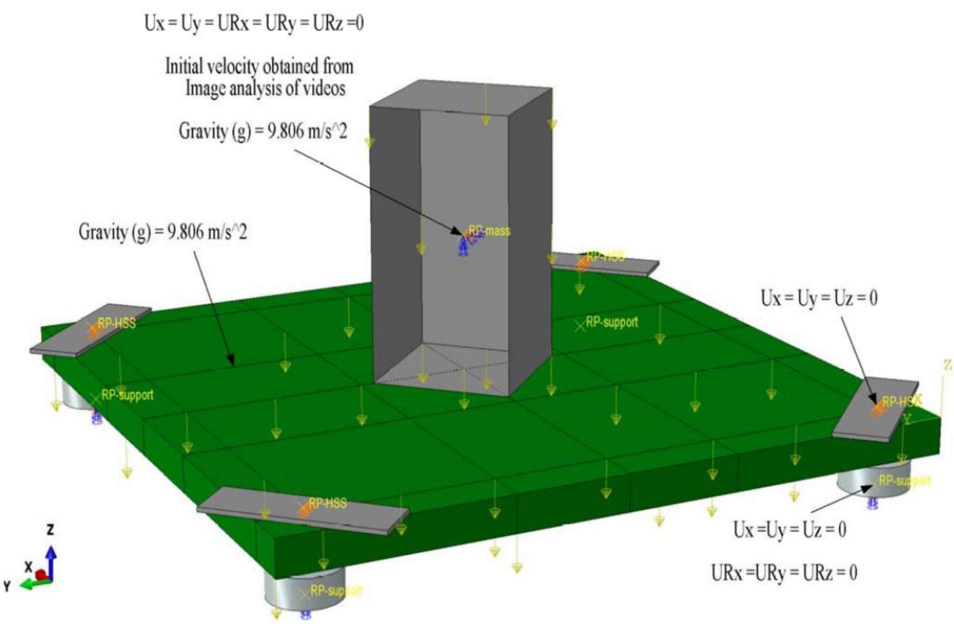

Figure 6.2 – External loads and boundary conditions of FE model.

6.2.4 Materials constitutive models

The adopted material constitutive model must be capable of tracing the development and propagation of the yielding and inelastic flow of the material up to the failure point. In addition, the strain rate effect is other important issue which should be investigated properly in low-velocity impact analysis. The following subsections provide in details the input data of concrete and steel reinforcement materials.

6.2.4.1 Concrete materials modelling

The material properties of HSC and UHP-FRC that used in the FE model are presented in **Table 6.1**. These values are extracted from the results of materials investigation tests presented in Chapter 3.

Table 6.1 – Static material properties of HSC and UHP-FRC materials

Property	Unit	HSC	UHP-FRC 2%
Density (ρ)	kg/m^3	2,540	2,650
Compressive strength (f_c')	MPa	83.10	162.40
Strain at peak stress (ε_o)	mm/m	2.50	4.35
Splitting tensile strength (f_{tsp})	MPa	4.51	11.11
Elastic modulus (E_c)	GPa	30.20	48.80
Poisson's ratio (υ)	---	0.2[1]	0.2[1]

[1] Reasonably assumed

The elastic behaviour of concrete is specified by defining elastic modulus and Poisson's ratio assuming isotropic material before cracking occurs. Additionally, density of concrete must be defined in order to form the lumped mass matrix in explicit analysis. The experimental measured geometrical and mechanical properties reported in **Table 6.1** are used to define these parameters.

Nonlinear behaviour of concrete has been defined using built-in Concrete Damage Plasticity (CDP) model available in ABAQUS. The four input parameters that are required to fully describe the yield surface and flow rule in the three-dimensional space of stresses include dilation angle (ψ) in degrees, plastic flow potential eccentricity (ϵ), ratio of the strength in the biaxial state to the strength in the uniaxial state (σ_{bo}/σ_{co}), and the shape factor that defines the yield surface in the deviatoric plane (K_c), are initially set to 30^o, 0.1, 1.16, and 0.67, respectively. Thereafter, each parameter is calibrated through a series of parametric studies and its effect on the numerical results is addressed. The strain hardening behaviour is modelled using isotropic hardening in which the increase in yield stress is assumed to be uniform in all directions with the increased plastic strain (Dunne and Petrinc, 2005; Simulia, 2016). Other parameters describing the performance of concrete are determined for uniaxial stress-strain curves.

a) Uniaxial behaviour modelling of HSC

Well-equipped experimental study was conducted by Marzouk and Chen (1995) to investigate the tension properties of HSC, including the post-peak softening response. The tested properties were uniaxial tension, splitting, modulus of rupture, and fracture energy. The HSC used in their investigation had the same mix proportions of HSC used in the current research and both mixes were developed following the recommendations of earlier research of Marzouk and Houssein (1990). Additionally, the reported mechanical properties of Marzouk and Chen (1995) are close to the measured mechanical properties reported in **Table 6.1**. Therefore, the uniaxial tensile strength f_t = 4.05 MPa and fracture energy G_F = 160 N/m reported in (Marzouk and Chen, 1995) are used to complement the material properties of HSC model.

Figure 6.3 summarizes the adapted uniaxial relationships implemented in CDP model side by side with tested uniaxial responses for both compression and tension. The uniaxial compressive stress-strain response of HSC is modelled by fitting the experimental quasi-static curve with piecewise linear model with three branches (**Figure 6.3**-a). Such simplifications are introduced to increase the computational efficiency of the FE model. The modelled uniaxial tensile stress-strain response is elastic linear up to the tensile strength. The post-peak tension stiffening behaviour is defined as stress-crack width response based on the tensile fracture energy criterion. The fictitious crack model proposed by Hillerborg (1985) is used to define the descending branch of uniaxial tensile stress-crack displacement response (**Figure 6.3**-b).

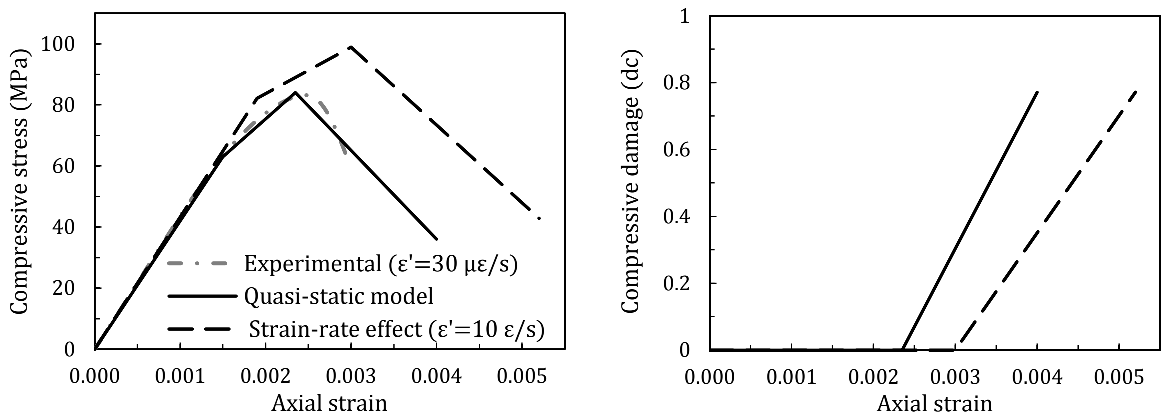

a) Uniaxial compression parameters (left: stress-strain; right: damage)

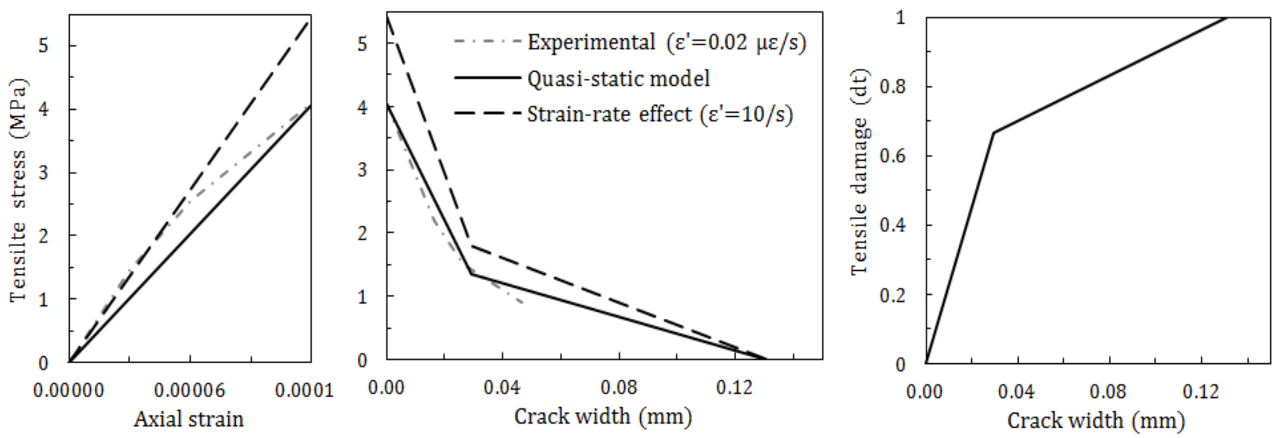

b) Uniaxial tensile parameters (left: stress-strain/crack width; right: damage)

Figure 6.3 – Adapted HSC uniaxial relationships for concrete damage plasticity model.

The results of stain rate investigation presented in Chapter 3 showed that CEB-FIP Model Code (2010) fits well with gained enhancement in both compression and tension of HSC. Therefore, the DIFs formulas of CEB-FIP (2010) are implemented to compute the enhancement in HSC constitutive model. Maximum strain rate considered is 10 s^{-1} since this rate is the highest recorded rate by steel strain gauges in all impact tests. The strain rate effect on crack opening width of the tensile descending response is not considered since the experimental results of Zhang et al. (2009) showed that G_F/f_t remains constant for loading rates less than 23 s^{-1}.

Damage is assumed to occur in the softening range in both compression and tension. The compression damage parameter (d_c) is simplified using a linear relationship with zero damage at strains corresponding to compressive strength and the maximum value of 0.80 at failure strain to avoid computational difficulties associated with zero stiffness at complete damage. On the other hand, the tension damage (d_t) is defined using a bilinear model as shown in **Figure 6.3**-b.

b) Uniaxial behaviour modelling of UHP-FRCs

The steel fibres are treated as a property of the UHP-FRC matrix since the fibres are assumed to be uniformly distributed throughout the matrix. The uniaxial compressive and tensile responses are defined following the same approach implemented in HSC model. Strain rate effects are defined using the dynamic material properties measured in Chapter 3. **Figure 6.4** illustrates the adapted uniaxial input compressive and tensile curves.

6.2.4.2 Steel reinforcement modelling

Unlike concrete, steel exhibits large plastic deformation associated with a substantial change in the cross-sectional area and the length. In such case, the uniaxial response must be expressed in terms of true stress-true strain curve rather than nominal stress-strain curve in order to take account of cross section change. The uniaxial stress-strain curve is defined based on coupon tests reported in Chapter 3. The classical metal plasticity constitutive model is adapted to define plastic behaviour using von Mises yield criterion assuming isotropic hardening (Simulia, 2016). The strain rate enhancement in yield and ultimate strength are estimated using Malvar and Crawford (1998) model (see, Section 2.3.2). **Figure 6.5** shows experimental nominal and true stress-strain, and the input plastic behaviour of classical metal plasticity model including strain rate effect.

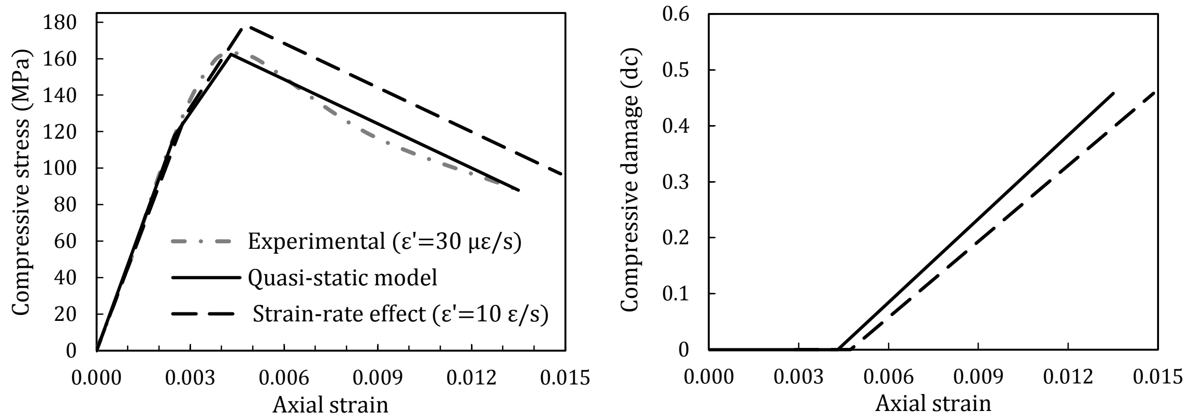

a) Uniaxial compression parameters (left: stress-strain; right: damage)

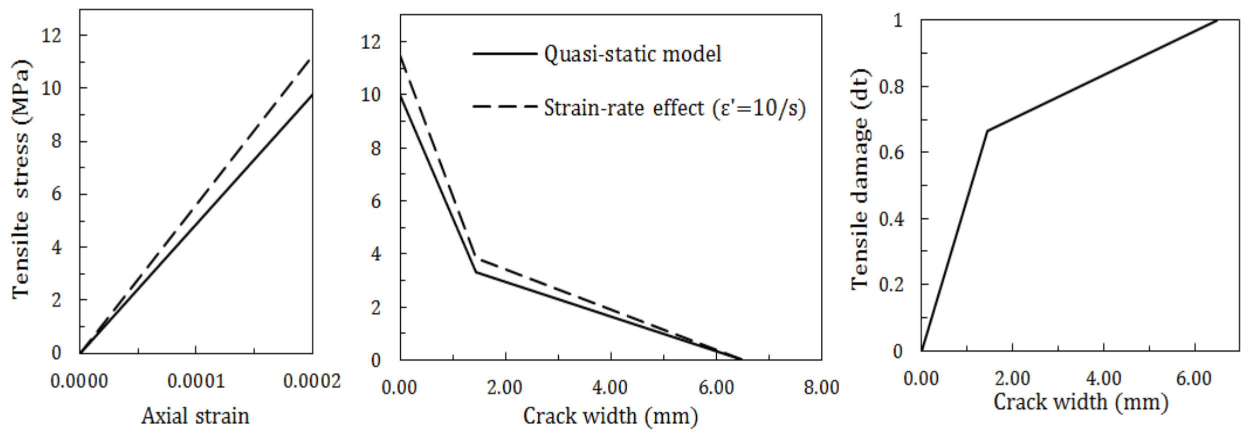

b) Uniaxial tensile parameters (left: stress-strain/crack width; right: damage)

Figure 6.4 – Adapted UHP-FRC uniaxial relationships for concrete damage plasticity model.

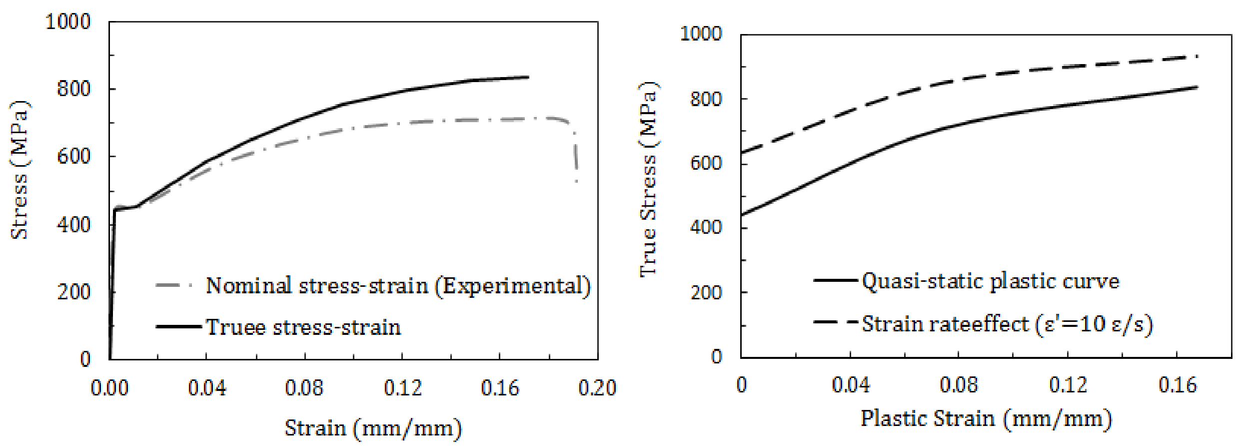

Figure 6.5 – Uniaxial stress-strain response of steel (left: experimental; right: plastic input).

6.2.4.3 Drop-weight and supporting system modelling

The drop-weight and supporting system are modelled assuming elastic material properties of steel since no plastic deformation was observed during testing. The adapted material properties of supporting system are: elastic modulus = 210 GPa, Poisson's ratio = 0.3, density = 7.85×10^3 kg/m^3. Same material properties are used for the drop-weight except for the mass density (3.77×10^3 kg/m^3). The density is evaluated by dividing the 475 kg mass by the volume of the drop-weight.

6.3 Mesh Convergence and Stability of Solution

It is important to use a sufficiently refined mesh in order to ensure the model produces a mathematical accurate solution. In general, numerical result of FE model tends toward a unique value as the mesh density increased. However, the computer resources required to run the simulation increase as the mesh is refined. The optimal mesh size should be selected in such a way that both accurate results are received and computational time is minimized. In nonlinear FE analysis, especially when the material is described by a softening constitutive relationship (same as the current model), the simulation results are critically dependent on the mesh size.

The dynamic response of the control plate (HS_{100}) with the complete definition of material properties is used to check the implemented fracture energy technique that used to minimize the mesh dependency of results. The plate is subjected to drop-weight impact with predefined velocity of 9 m/s. Three particular results are used in this convergence study, namely: midpoint displacement; total reaction force; and steel reinforcement strain at midpoint. To ensure best results, the plate is uniformly meshed such that the aspect ratios of all solid elements are unity with side length equal to mesh size of the beam element of steel reinforcement model. Five different mesh sizes are considered. Hourglass enhanced stiffness option has been used to stop the formation of zero energy modes. The convergence of the results is summarized in **Figure 6.6.** Results are normalized with respect to the values predicted by the finest mesh of size 10 mm. As shown the results are converging as the mesh is refined which indicate the results are mesh independent. Based on convergence study, a mesh size of 20 mm (5 elements through the plate's thickness) is adequate to ensure the model produces a mathematical accurate solution. The differences between results of models with mesh size of 20 mm and 10 mm are negligible. The mesh size of 10 mm (i.e., element characteristic length) is less than the coarse aggregate size of HSC and for this reason it cannot be considered in smeared cracking based model. It should be pointed out that the numerical results are convergent only when the solid elements have an aspect ratio of one (cube elements). The results showed mesh dependency when aspect ratio changed, especially displacement response.

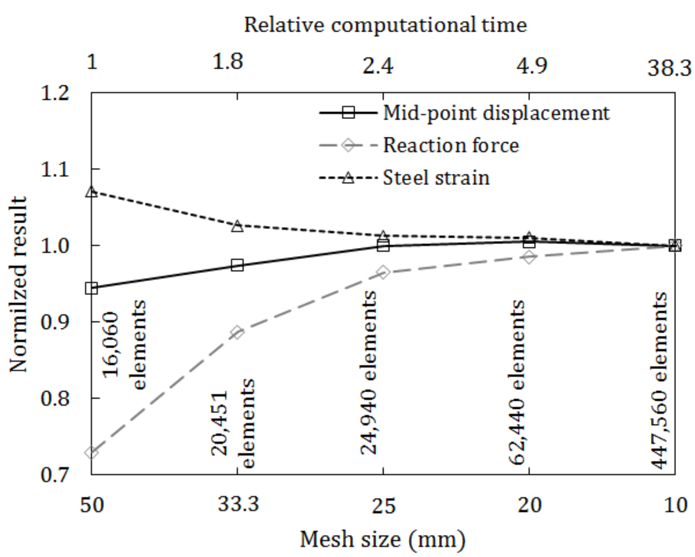

Figure 6.6 – Mesh convergence study

As discussed in details in Chapter 2, energy balance is an important tool to gauge the stability of explicit analysis. It can be used to validate the selected mesh size and implemented hourglass resistance technique. ABAQUS/Explicit has two limitations in order to ensure the stability of numerical solution. First, the variation total energy value throughout the entire solution must be less than 1%. Second, the artificial energy introduced by hourglass resistance control technique should be minimal, typically less than 5% of internal energy (Simulia, 2016).

Figure 6.7 shows the energy time histories of the initial 50 mm mesh size and the selected mesh size of 20 mm. As shown, the use of coarse mesh size of 50 mm resulted in unstable energy levels. The variation of total energy is more than 1% and the artificial energy is more than 20% of the internal energy which indicates an undesirable high level of mesh distortions (**Figure 6.7-left**). On the other hand, the adapted mesh size of 20 mm showed a constant total energy throughout the simulation time and low artificial energy level. Based on this study the FE model seems to be valid, from the standpoint of elements behaviour, and the accuracy of explicit mathematical solution. Details of the selected mesh configuration used throughout the subsequent simulations are shown in **Figure 6.8**.

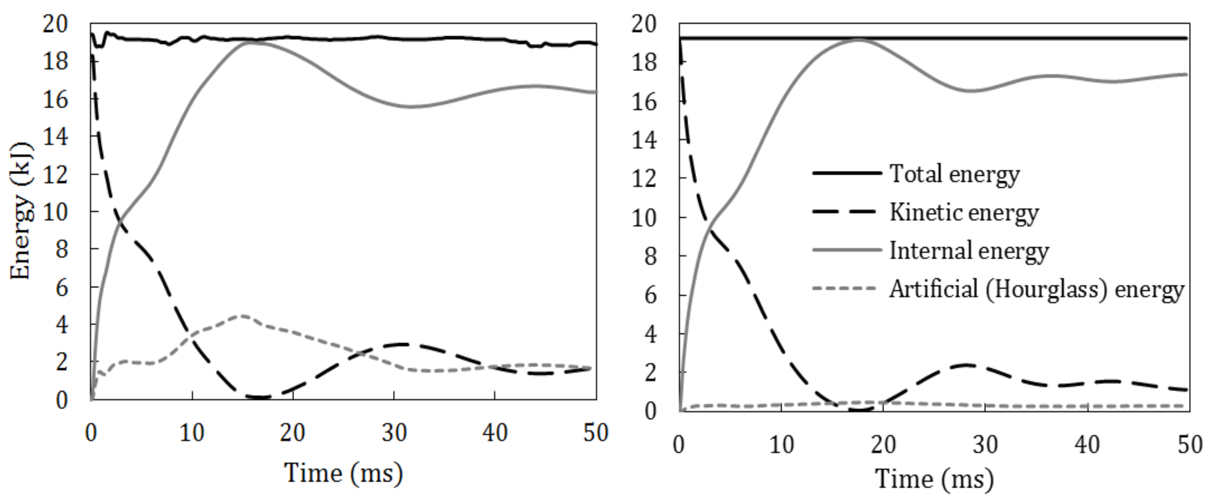

Figure 6.7 – Energy time histories (left: 50 mm initial mesh; right: 20 mm reference mesh)

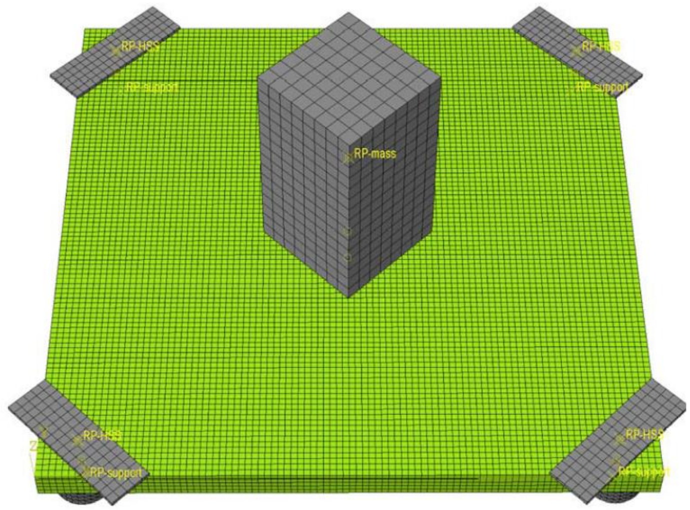

Figure 6.8 – Adapted mesh configuration of impact test

6.4 Modal Analysis

Modal analysis frequencies are dependent on the mass and stiffness of structures, and the boundary conditions (Chopra, 2012). The use of dynamic characteristics (natural frequencies and corresponding mode shapes) in the verification of FE models is a useful approach when experimental data are available. This stage of analysis is intended to verify that the overall elastic stiffness, mass distribution, and the modelled contact properties of boundary conditions.

In this section, the natural frequencies (eigenvalues) and corresponding mode shapes (eigenvectors) of tested plates are extracted numerically using linear perturbation frequency analysis (Lanczos solver) available in ABAQUS (Simulia 2016). **Figure 6.9** shows typical first mode shape and **Table 6.2** shows the comparison between fundamental natural frequencies extracted numerically and experimentally for all plates. It is evident from this table that, the fundamental natural frequencies of the FE model and tests are in good agreement with maximum difference less than 4%. This indicates that the mass, elastic stiffness and contact properties of supports are adequately modelled.

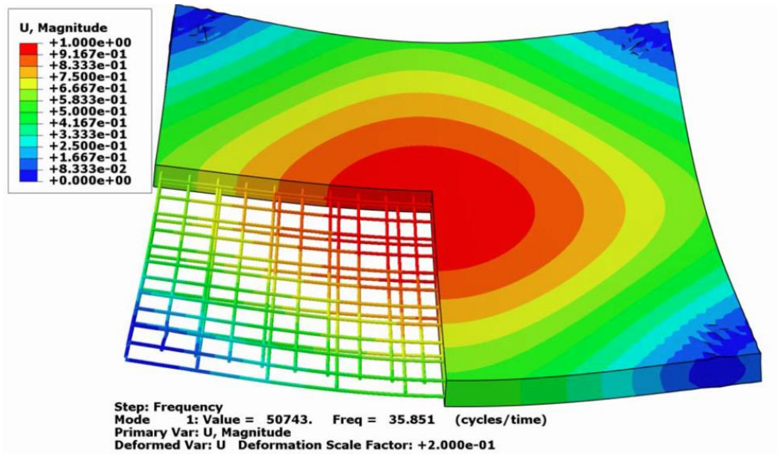

Figure 6.9 – First model shape of plate HS_{100} (f_d = 35.85 Hz)

The first ten mode shapes and corresponding natural frequencies of HS_{100} plate are shown in **Figures 6.9** and **6.10**. Mode shapes related to axial and torsional deformation are excluded. It should be pointed out that the predicted frequencies calculated using elastic material properties are upper-bound and the frequencies of damaged plates after applying impact loads are less.

Table 6.2 – Comparison between numerical and actual frequencies

Plate's ID		Fundamental natural frequency, f_d (Hz)		
		Model	Test	Difference[1] (%)
HSC series	HS-1-D	35.85	35.52	0.93
	HS-2-D	35.68	35.61	0.20
	HS-3-D	36.20	35.70	1.40
	HS-2-S	35.66	35.57	0.25
	HS-3-S	35.95	35.55	1.13
UHP-FRC series	HS_{100}	35.85	35.64	0.59
	UF_1S_{100}	43.22	41.60	3.89
	UF_2S_{100}	44.20	43.70	1.14
	UF_3S_{100}	44.60	43.66	2.15
	UF_2S_{158}	44.10	43.27	1.92
	UF_2S_{210}	43.65	42.77	2.06

[1] based on experimental natural frequencies

Generally, structure members have many natural frequencies corresponding to different deformed or mode shapes. However, low frequency modes mainly affect the member response.

Next step is to examine how many mode shapes are sufficient to capture the dominant dynamic response of RC plate under considered midpoint impact load and which modes are the main contributor to the plate's response. For such purposes, modal effective mass (known also as mass participation factor) is used to examine mass participation of the first ten mode shapes in vertical direction (direction of applied impact load). Modal effective mass provides a method for judging the significance of a particular mode shape based on the amount of system mass participating in this mode (Chopra, 2012).

Priesrley et al. (1996), among other authors, confirm that the cumulative effective mass for considered mode shapes should be at least 80% of total mass to ensure that the number of mode shapes is adequate to capture the dynamic response of a structure. In this investigation, the cumulative effective mass for considered first ten modes is 96%, well above the recommended limit, which means the first ten modes are enough and higher mode shapes have negligible contribution in the plate response.

Figure 6.10 illustrates the contribution of first ten mode shapes. It is evident that only first and ninth mode shapes have effective mass in vertical direction. However, first mode has a relatively high effective mass of 91 % compared to 0.90 % effective mass of ninth mode. Thus, the first mode can be readily excited by the vertical impact load. On the other hand, the ninth mode is negligible in this sense. From this modal analysis investigation, it can be concluded that the plates are only responded in first mode shape under considered midpoint impact load and supporting conditions. This conclusion matches the observed deformed shape of all tested plates. The first mode is shown up clearly in the displacement shapes developed using the measurements of laser displacement sensors reported in **Figure 6.11**.

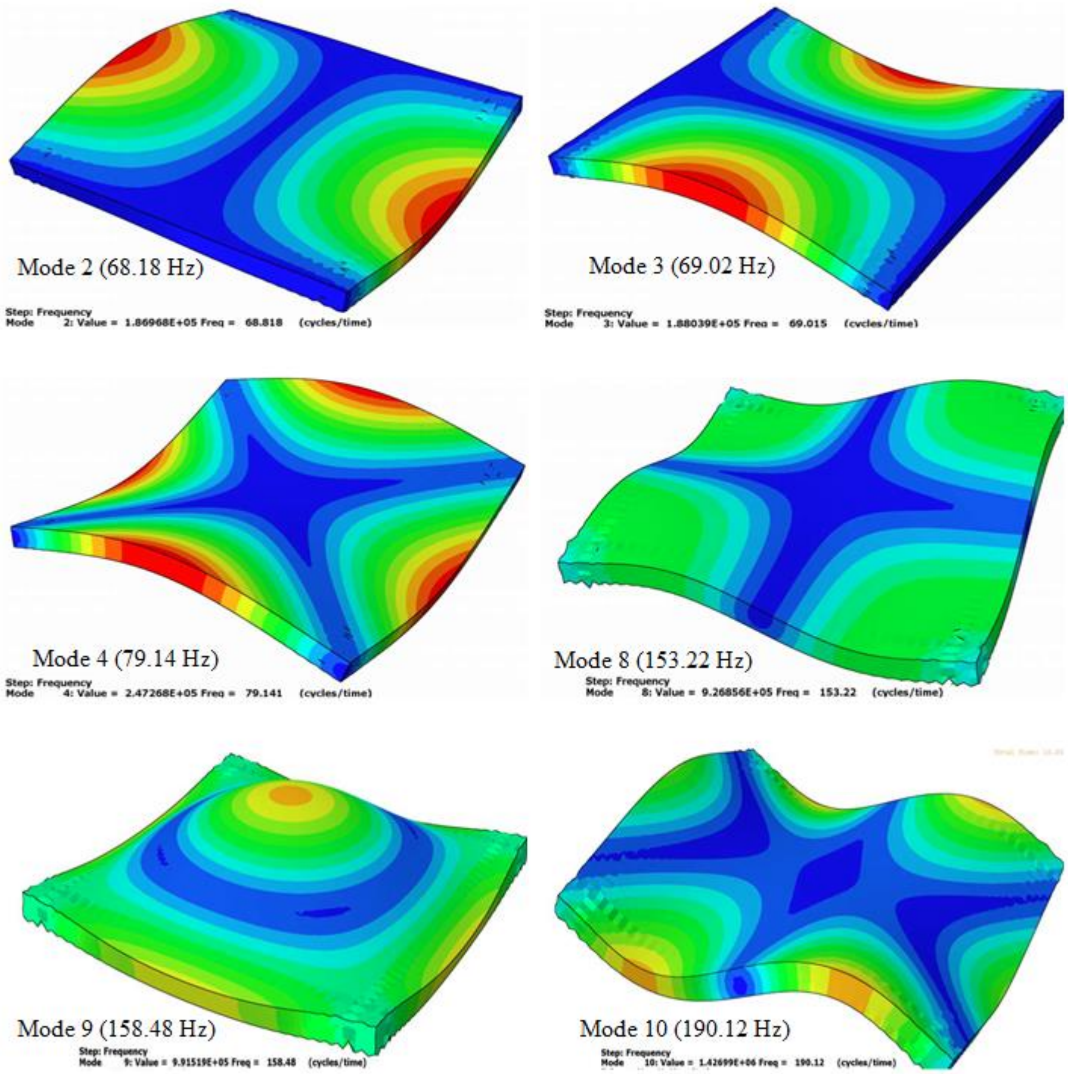

Figure 6.10 – Mode shapes and corresponding natural frequencies of plate HS_{100}

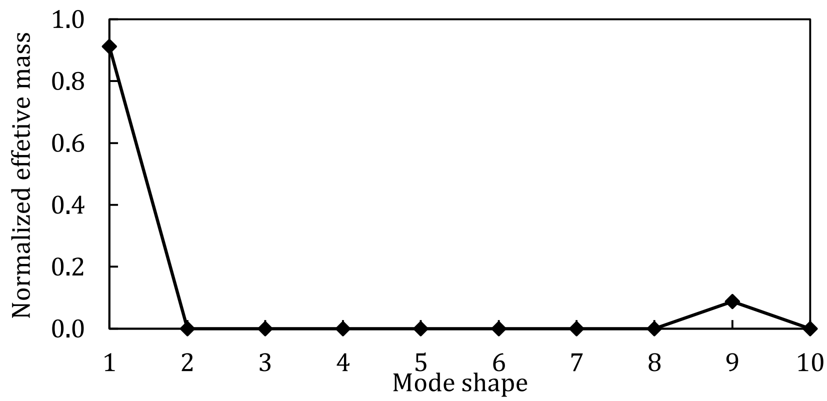

Figure 6.11 – Effective mass participation for first ten mode shapes

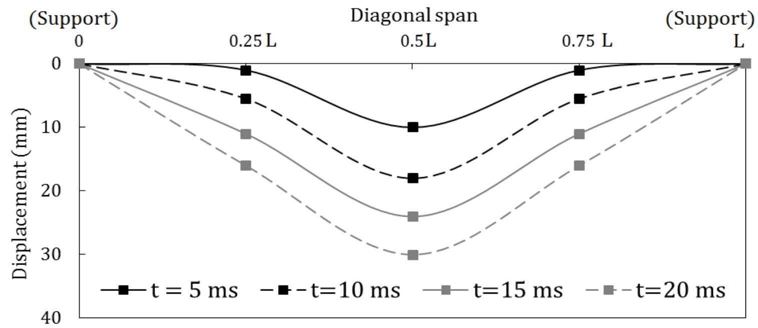

Figure 6.12 – Measured deformed shape of plate HS_{100} (1^{st} impact test)

6.5 Verification of Implemented Impact Loading Technique

The first impact test of plate HS_{100} is selected to perform this verification process. To examine the effect of defined gravity acceleration on rebound response of drop-weight, long analysis time period is considered starting with initial contact instant to the time of second impact due to mass rebounding. The quality of the implemented loading technique is shown up clearly in **Figure 6.13**. Both position and velocity of the drop-weight are reproduced numerically with very good accuracy in terms of time response, and amplitudes, with maximum discrepancies in position and velocity amplitudes being in order of 3 and 2%, respectively.

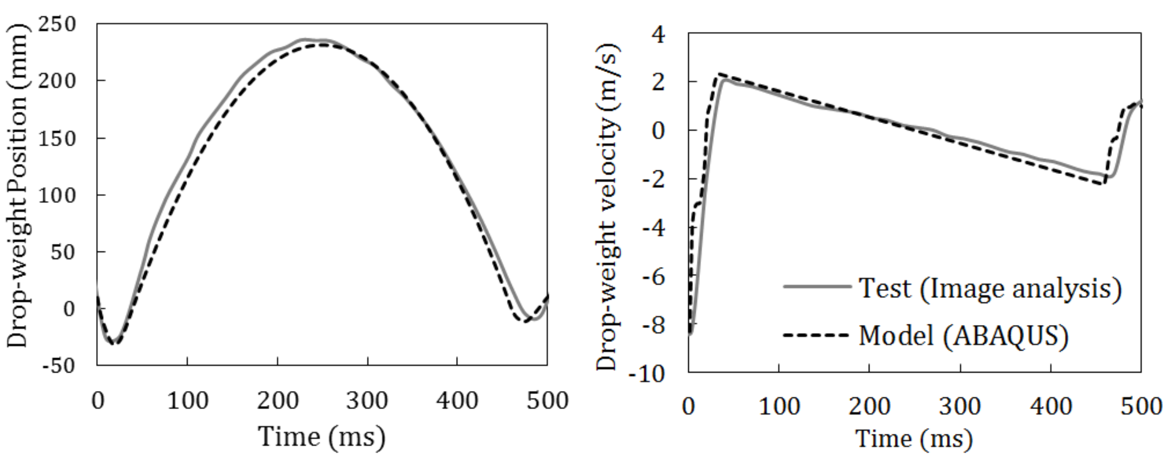

a) Position time history b) Velocity time history

Figure 6.13 – Comparison of kinmatic responses of drop-weight (HS_{100}, 1^{st} impact test)

6.6 Analysis Approach

In all subsequent analyses, the results of the FE models are compared to the experimentally measured impact force, total reaction force, midpoint displacement, and steel strain time histories. Output data curves of the simulations are collected with same sampling rates that have been used in experiments; impact and reaction forces are sampled at 100 kHz, while midpoint displacement and steel strain are sampled at 5 kHz. The impact force is calculated using the same technique of experiments by applying Newton's 2^{nd} law (drop-mass × drop-weight acceleration). The acceleration curves obtained from simulations are filtered using low-pass second order Butterworth filter with 5 kHz cutoff frequency same as experimental acceleration data.

In impact testing, the rebounding of the drop-weight was not prevented. The rebounding typically occurred after first 400 milliseconds with a maximum height of 250 mm (**Figure 6.13**). The analysis of recorded videos showed that the rebounding has insignificant effects on the crack pattern. Therefore, to minimize the required computation time, the numerical analyses are performed for only the initial 50 milliseconds of each impact test. This time period is enough to assess the computed responses up to end of impact contact. However, longer computational time periods are considered in some analyses to assess the effect of damping and gravitational acceleration on the responses. The time increment for all numerical calculations is approximately 1.3 microseconds estimated automatically by ABAQUS/Explicit. The total execution time of each explicit analysis (50 milliseconds) is approximately an hour and 49 minutes by a core i5 computer with 3.06 GHz processor frequency.

All specimens in the experimental program have been subjected to multi-impacts, it is necessary to incorporate this loading history into the FE modelling to examine the final crack pattern and check the applicability of proposed modelling approach to analysis consecutive impact load scenarios. Different analysis steps are defined to simulate multi-impacts. The "restart analysis" option available in ABAQUS is used to define the new initial impact velocity of drop-weight and to allow the model continues using material properties considering the plastic deformation and damage from the termination point of previous analysis step.

6.7 Numerical Analysis of HSC Plates

The FE model of HSC plates is calibrated based on the results of the first impact test of control plate HS_{100}. The influences of strain rate, and damping are addressed next. Then, the predictive capability of calibrated model is demonstrated by simulating other tested HSC plates with different reinforcement ratio and arrangement. The applicability of the proposed method to model consecutive impact loading is discussed as well.

6.7.1 Calibration of CDP model parameters

CDP model parameters with uncertainties, including dilation angle (ψ), deviatoric plane shape parameter (K_c), flow potential eccentricity (ϵ), and damage parameters are calibrated through a series of parametric studies in which numerical predictions are compared to the experimental measurements. The numerical results of the calibrated CDP model are shown in **Figure 6.13** along with the experimental measurements. As shown all measured responses are reproduced numerically with very good accuracy in terms of time response, and amplitudes. The CDP parameters that results in the best fit of the experimental responses are found to be $\psi = 40^o$, $\epsilon = 0.1$, and $K_c = 0.67$. The following subsections provide the details of the calibration process and the influence of each parameter on the analytical results. In the following parametric studies, each parameter is varied independently over its possible range to set an optimal value and to investigate its effect on the predicted response.

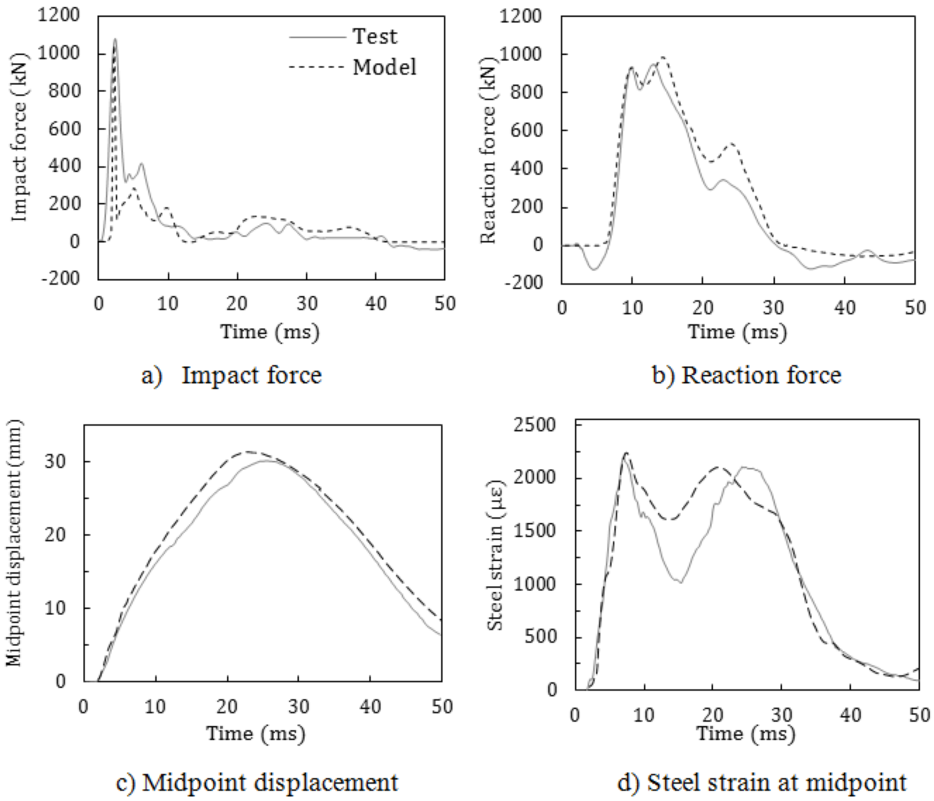

Figure 6.14 – Impact response time histories for HSC control plate (HS_{100}, 1st impact test)

6.7.1.1 Uniaxial compressive strength descending behaviour

The compressive stress-strain behaviour of HSC is well known for the ascending branch. However, the post-peak portion of HSC curve is more complicated. There are many factors that affect the post-peak behaviour of concrete during compression test, such as frictional end restraints between specimen and platen, quasi-static loading rate, and machine stiffness. Some researchers concluded that the softening response of HSC should not be treated as a material property (Mier 1984; Rabczuk et al. 2005). Therefore, the influence of descending branch of compressive stress-strain curve on the analytical results is investigated. Three different descending slopes are considered in this analysis. The variation in descending slope is achieved by changing the failure stress while failure strain is kept constant and equal to 4.0 ‰. **Figure 6.15** illustrates the different studied cases and their influences on the analytical results are shown in **Figure 6.16**. This investigation has been performed using the default CDP parameters (ψ = 30°, ϵ = 0.1, and K_c = 0.67).

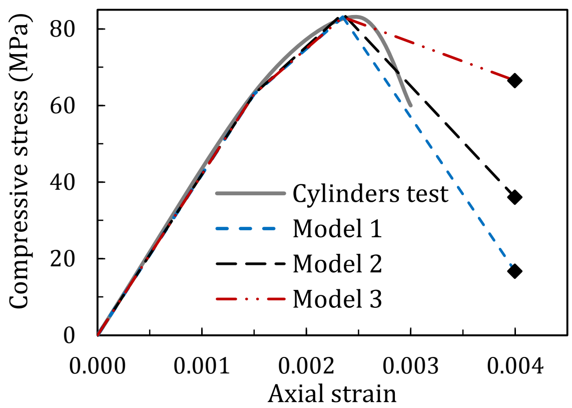

Figure 6.15 – Different studied cases of uniaxial compressive stress-strain curve

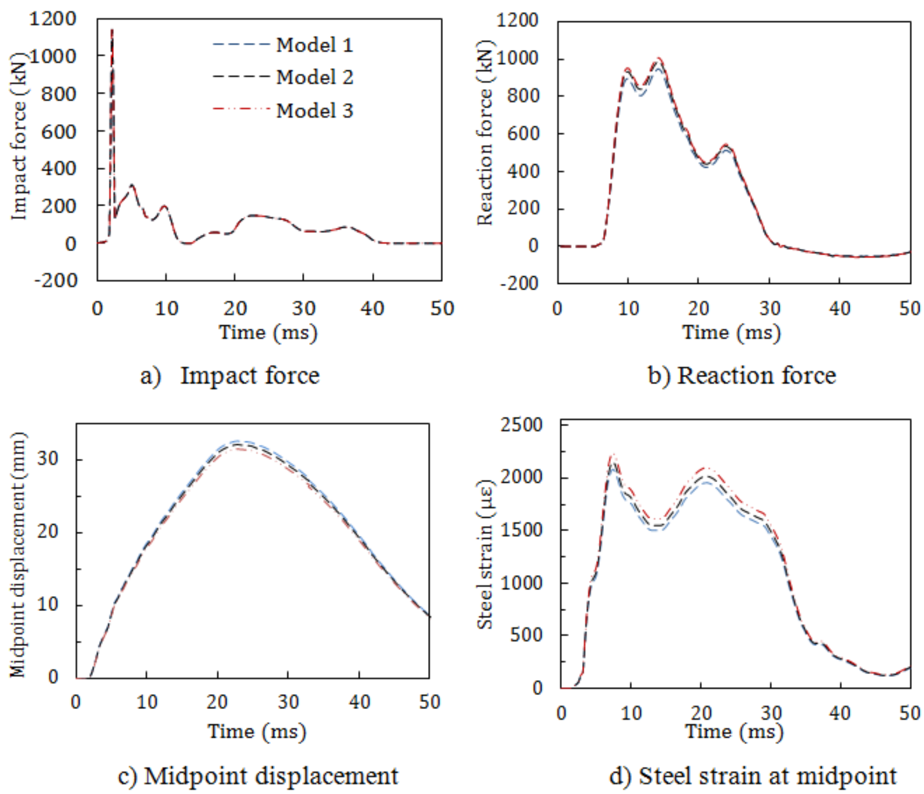

Figure 6.16 – Influence of uniaxial compression response (HS_{100}, 1st impact test)

It is evident from **Figure 6.16** that, the post-peak compressive behaviour has insignificant effect on the analytical response of HSC plate. This means that the compressive stresses in the model have not reached the compressive strength during impact simulation. This expectation is confirmed by checking the compressive stresses in the model. The minimum principal stresses under first and second impacts are 46 and 55 MPa. Consequently, the compressive stress-strain of Model 2 has been selected to be used as uniaxial compressive input for all the next analyses.

6.7.1.2 Dilation angle of HSC model

CDP model uses the dilation angle (ψ) parameter to control the amount of volumetric strain developed during plastic deformation. Typically, the dilation angle of concrete is in the range of 30° to 45°. Four different values of ψ (30°, 35°, 40°, 45°) with ϵ = 0.1, and K_c = 0.67 are considered in this study. **Figure 6.17** shows the influence of different values of dilation angle on the simulation results compared to experimental measurements.

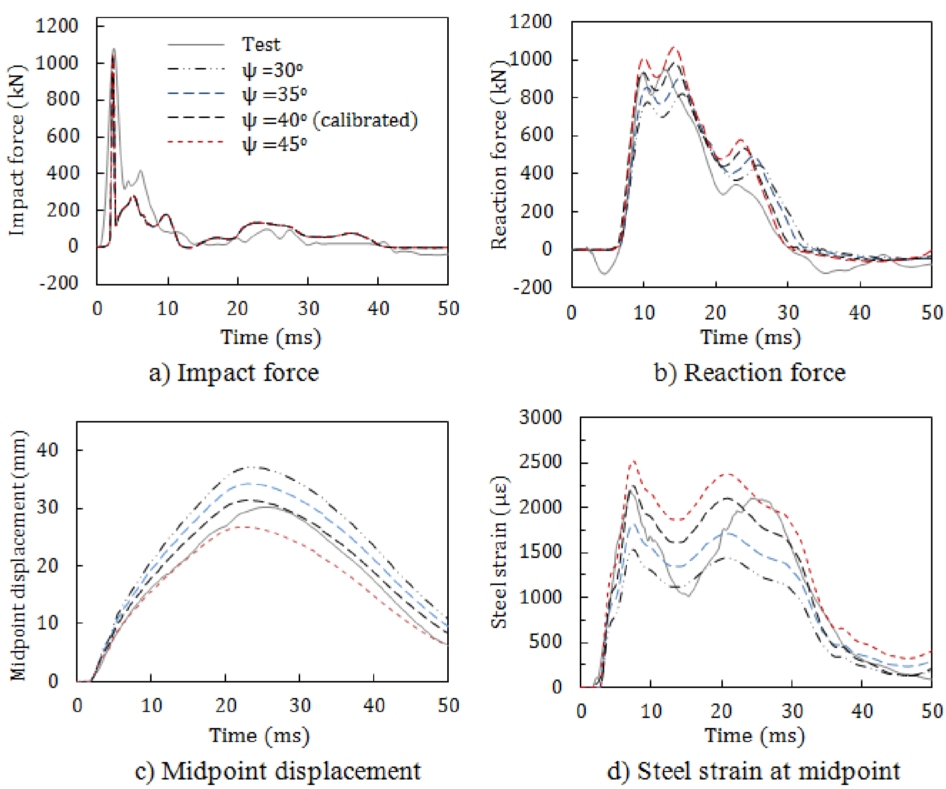

Figure 6.17 – Influence of dilation angle size ψ, (HS_{100}, 1st impact test)

It can be shown that dilation angle value has no effect on the impact force response. On the other hand, the displacement and strain time histories are significantly affected. Based on this investigation, the dilation angle size of 40^o has been selected to be used in all the following HSC simulations.

6.7.1.3 The deviatoric plane shape parameter

CDP model allows modifying the yield surface in the deviatoric plan in order to account for different yield tri-axial tension and compression stresses through the shape parameter (K_c). The K_c must be within the range of $0.5 \leq K_c \leq 1$ to ensure the convexity of the yield surface. **Figure 6.18** gives the comparisons among the different models. Three different values of K_c (0.5, 0.67, 1) with $\epsilon = 0.1$, and $\psi = 40^o$ are considered.

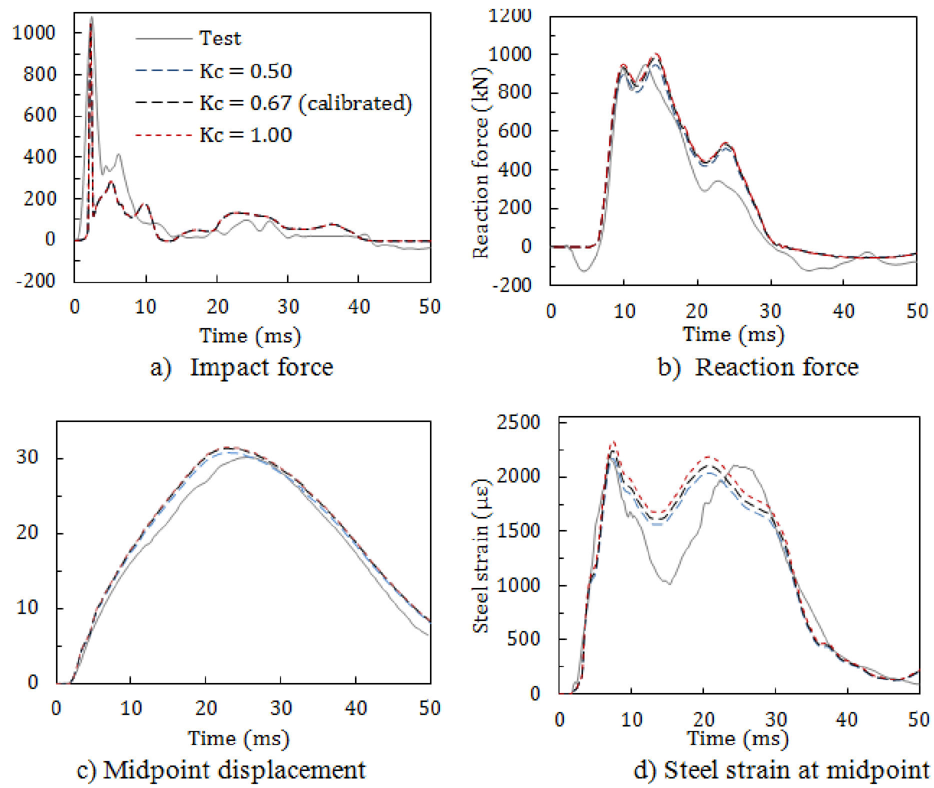

Figure 6.18 – Influence of shape factor K_c, (HS_{100}, 1st impact test)

As shown in **Figure 6.18**, the influence of deviatoric plane shape on the analytical impact response of RC plate is not significant. Therefore, using any value of K_c parameter in the specified range ($0.5 \leq K_c \leq 1$) is generally acceptable in impact analysis. Consequently, the shape parameter is defined with its default value ($K_c = 0.67$) for all the next analyses.

6.7.1.4 Flow potential eccentricity

Concrete material exhibits more volume expansion under compressive loading at low confining pressures close to pure shear and uniaxial compression. CDP model allows increasing the dilation angle at low confining pressures through the eccentricity parameter (ϵ). **Figure 6.19** gives the comparison among three different ϵ values and the experimental measurements. Three different values of ϵ (0, 0.5, 1) with $K_c = 0.67$, and $\psi = 40^{o}$ are considered in this investigation.

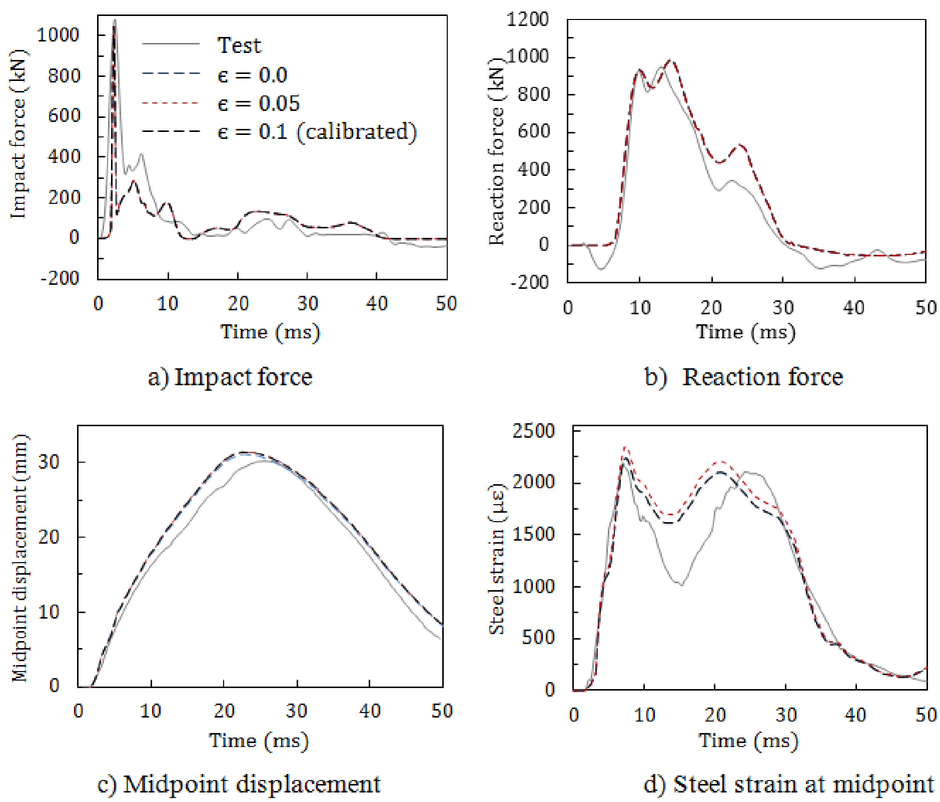

Figure 6.19 – Influence of default flow potential eccentricity ϵ, (HS_{100}, 1^{st} impact test)

As shown in **Figure 6.19**, the influence of flow eccentricity on analytical impact response of RC plate is not significant. This response is expected since this parameter characterizes the volume change at low confining pressures and the impact problems involve mostly stress state at high confining pressures (Park et al., 2001). Therefore, The default flow potential eccentricity (ϵ = 0.1) has been considered for all the next analyses.

6.7.1.5 Damage parameters of HSC model

The damage parameters in the CDP model play an important role in the response of RC members subjected to cyclic loading conditions such as fatigue or dynamic loads. The damage parameters take into account the degradation of stiffness after peak strength in strain-softening branch. The influence of the damage parameters on responses is illustrated in **Figure 6.20**.

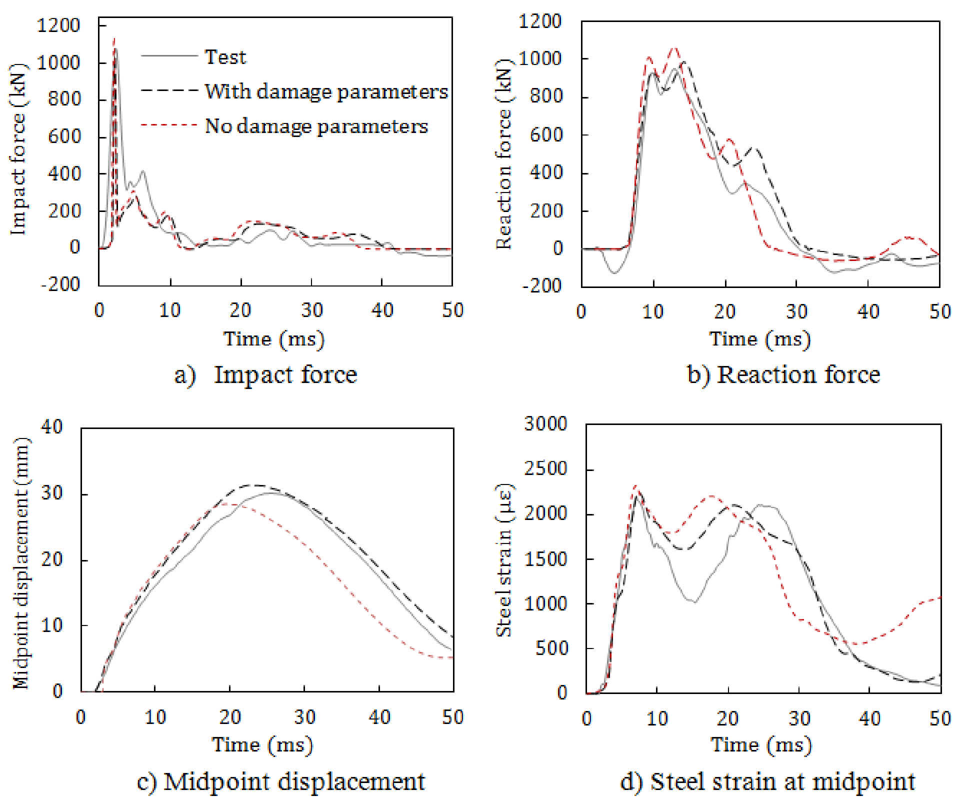

Figure 6.20 – Influence of damage parameters (HS_{100}, 1st impact test)

A good agreement between the results of the two models with the test results is observed during first 5 milliseconds because the materials in this range of loading are in elastic domain. It is evident from this comparison that the model without damage parameters, behaves stiffer than the experiment which reflected on shorter contact time duration and higher impact force (**Figure 6.20-a**), higher strain and reaction force (**Figure 6.20-b**, **d**), reduced midpoint displacement and time period (**Figure 6.20-c**). Thus, modelling the progressive degradation of concrete using damage variable is vital in modelling the impact response of RC members.

6.7.2 Strain rate effects

Figure 6.21 presents the analytical against the measured results for first impact test of the control specimen (HS_{100}). Analyses are performed with and without considering strain rate effects.

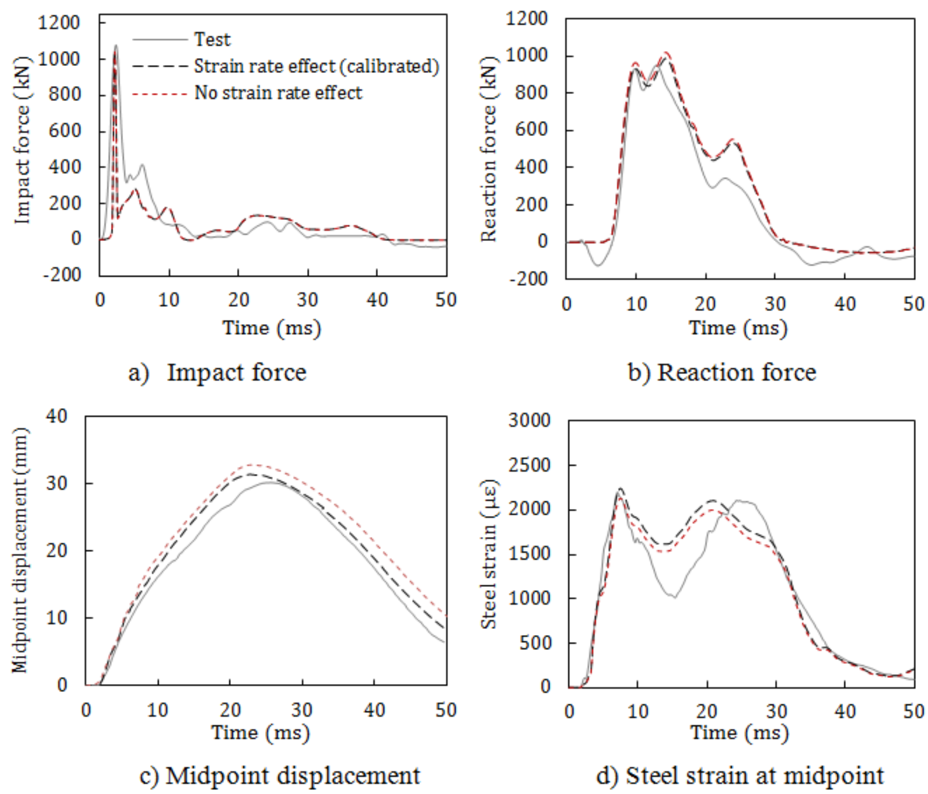

Figure 6.21 – Influence of strain rate effects on computed response (HS_{100}, 1st impact test)

It can be seen that the analysis considering strain rate effects resulted in slightly stiffer responses. The peak midpoint displacement and the time period of the response are reduced as a result of stiffness enhancement (**Figure 6.21-c**). The impact force, total reaction force, and reinforcement strain, however, are marginally affected by the inclusion of rate effects.

Figure 6.22 shows the influence of strain rate effects inclusion in the tension damage patterns in comparison with the observed crack pattern from the experiment. In FE damage patterns, elements with low damage level (< 25%) are left blank (white) for clear displaying purpose and the shown contours of the damage are ranging from 0.25 (blue) to 0.9 (red). The presented damage patterns are resulted after applying the same numbers of tests (three drops) using the measured initial impact velocities. As shown the material models enhanced by considering strain rate effects gives a better representation of the cracks.

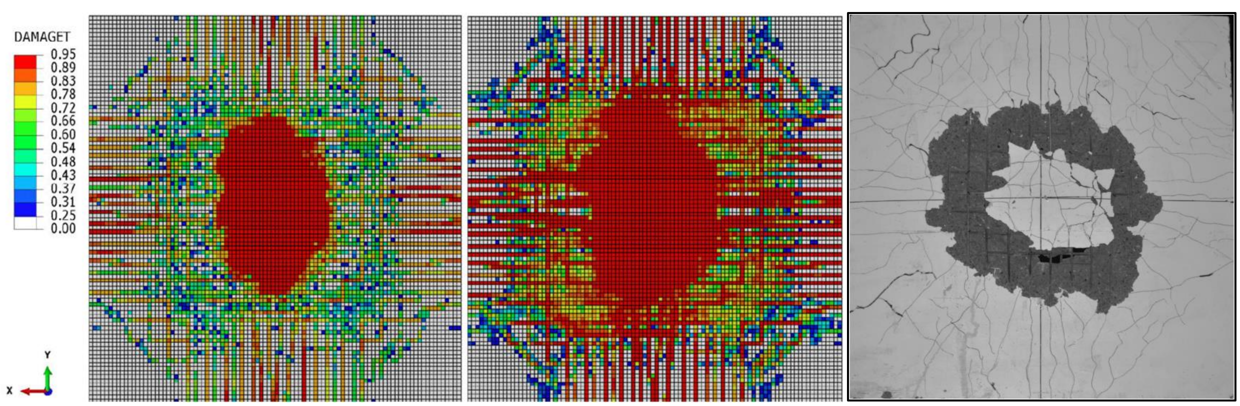

a) Strain rate effects b) No strain rate effects c) Experimental crack pattern

Figure 6.22 – Influence of strain rate effects on computed damage pattern (HS_{100})

Based on this investigation, under low-velocity impact conditions, strain rate enhancements have virtually a small influence on the impact force, reactions, and steel strain time histories. However, the inclusion of strain rate effect is essential in order to obtain a better estimation of midpoint displacement response and crack pattern especially in load case involves consecutive impact scenarios. It should be pointed out that strain rate effects are more significant for higher loading rates corresponding to blast and explosion (i.e., $\dot{\varepsilon} \geq 100\ \mathrm{s}^{-1}$).

6.7.3 Damping effect

Rayleigh damping is commonly used to model the damping in FE analysis (Chopra, 2012). In ABAQUS, Rayleigh damping matrix is defined using two parameters: the mass (α) and stiffness (β) proportional Rayleigh damping factors. It should be pointed out, for low frequency response as the case in this study (refer to Section 6.4), the mass proportional damping (α) dominates the damping effect and the contribution of the stiffness proportional damping (β) can be ignored (Chopra, 2012; Clough and Penzien, 2003; Simulia, 2016). The mass proportional damping (α) can be calculated using **Eq. 6.1**.

$$\alpha = 2\omega_{\mathrm{d}} \times \zeta \qquad (6.1)$$

Where, ω_{d} is the circular natural frequency in rad/s; and ζ the critical damping ratio.

In this section, the effect of damping is investigated. Two different analyses are performed with and without including the damping effect. The Rayleigh mass proportional damping factor α is taken equal to 13 determined using **Eq. 6.1** using the measured dynamic characteristics of RC plates reported in Chapter 5. **Figure 6.23** illustrates the influence of the damping effect on midpoint displacement response for the first impact test of specimen (HS_{100}). Relatively long computational time of 250 milliseconds is considered to assess the damping effect. It is evident from **Figure 6.23** that the simulated midpoint displacement time histories are nearly identical for first cycle (50 milliseconds), afterwards, the damped response has a magnified short-period response and more heavily damped compared to the experimental and undamped displacement responses. It should be pointed out that both simulated responses overestimate the plastic offset and residual displacement but they are more pronounced in damped response. Similar observations regarding poor estimation of residual displacement of nonlinear impact simulations are also reported in (Fujikake et al. 2009; Jiang et al. 2012).

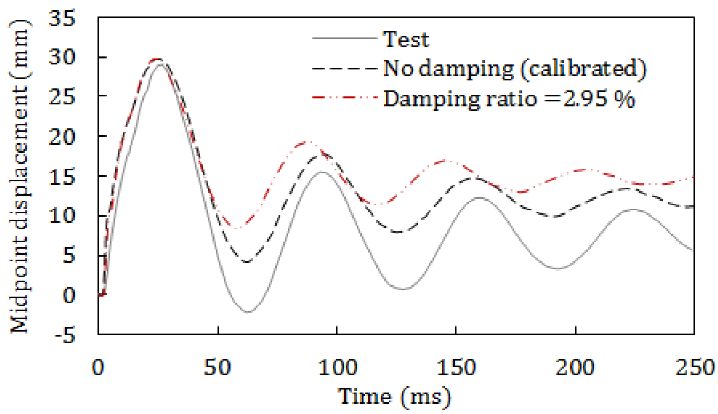

Figure 6.23 – Damping effects on midpoint displacement response (HS_{100}, 1st impact)

Based on this investigation, the effect of damping can be ignored in the nonlinear FE analysis of RC structures subjected to impact load due to the following reasons: the effect of damping on the first cycle of structural response is negligible, which is usually the interesting cycle of response (**Figure 6.23**); in nonlinear analysis, the dissipated energy through plastic deformation is greater than that dissipated by actual structural damping (Dunne and Petrinc, 2005); explicit analysis introduces a small amount of damping in the form of bulk viscosity to limit the numerical oscillations and ensure numerical stability (Simulia, 2016; Belytschko et al., 2014); and contact algorithms incorporate some damping to prevent numerical instabilities (Simulia, 2016).

6.8 Numerical Results of HSC Series

The predictive capability of the calibrated HSC model is addressed here by analyzing the impact response of HSC series that are constructed with different steel reinforcement ratios and arrangement. The simulated impact force-time, total reaction force-time, midpoint displacement-time, and steel strain at midpoint-time are plotted alongside the test results for the two conducted impact tests. Thereafter, discussions pertaining to the computed crack pattern are provided.

6.8.1 Numerical results of first impact load

The computed response-time histories of doubly and single reinforced plates under first impact test are presented in **Figures 6.24** and **6.25**, respectively.

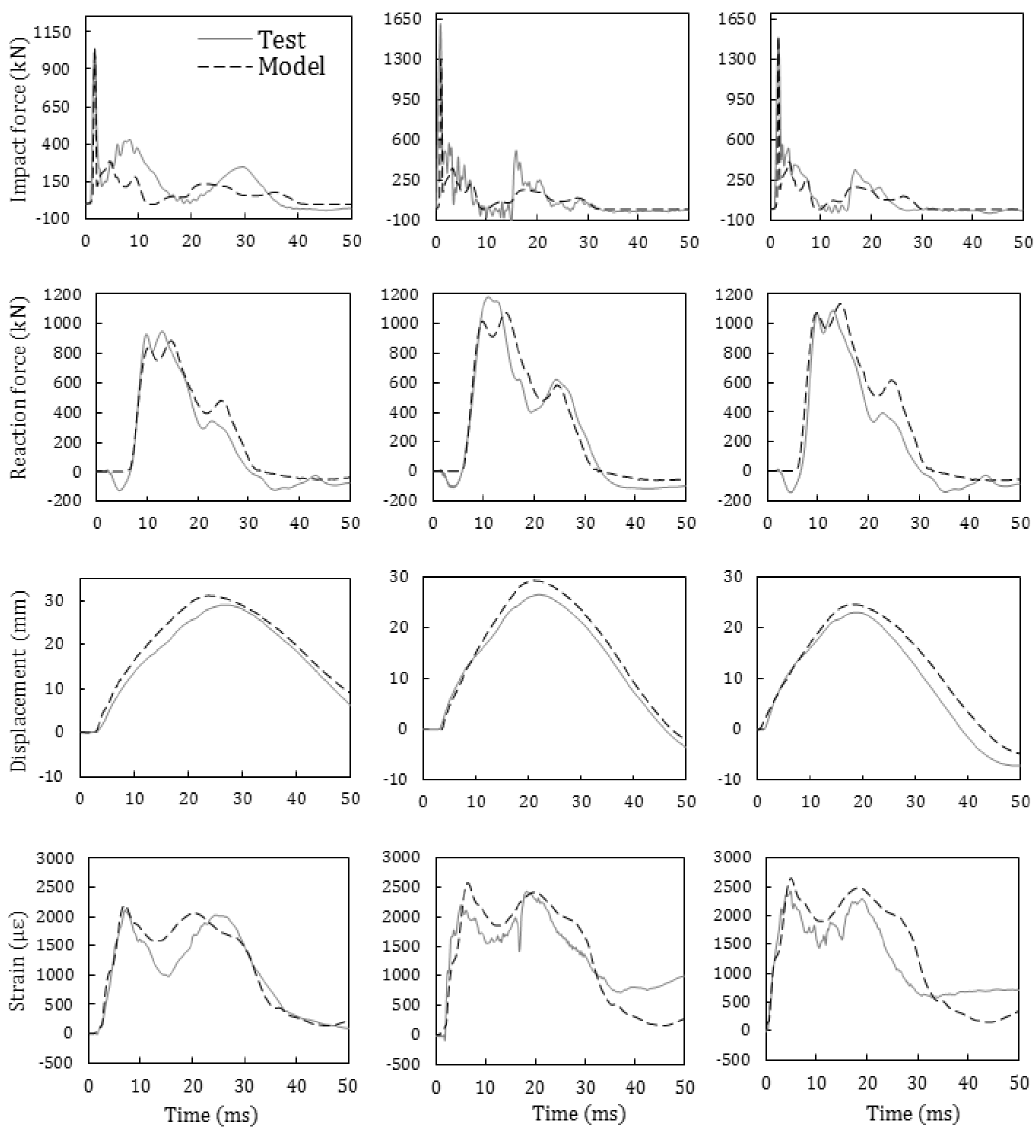

a) HS-1-D-1 b) HS-2-D-1 c) HS-3-D-1

Figure 6.24 – Comparison of model prediction to test results of doubly HSC plates (1st impact)

Generally, the model accurately estimates the time histories for all responses in terms of peak magnitudes and time responses. From the presented responses histories, it is evident that the computed peak impact forces agree well with the experimental data. The reaction responses match the shape of measured total reaction forces. The overall computed displacement responses are captured well. The steel strain time histories matched reasonably the experimental results.

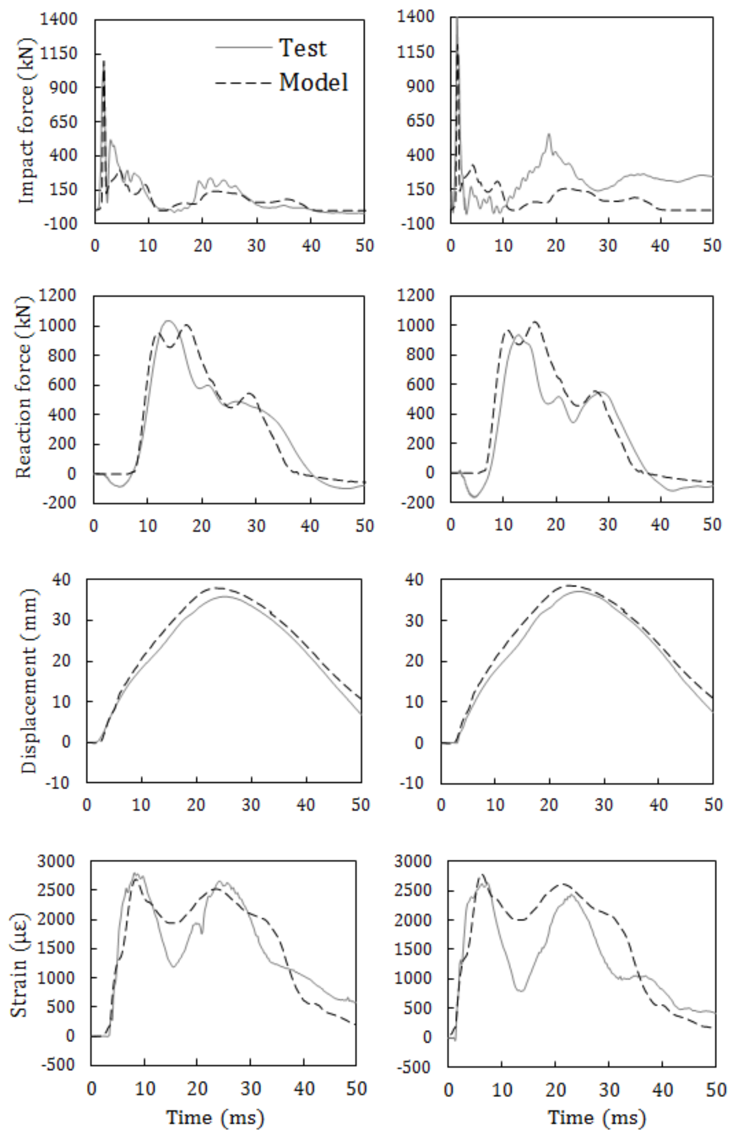

a) HS-2-S-1 b) HS-3-S-1

Figure 6.25 – Comparison of model prediction to test results of single HSC plates (1st impact)

The peak estimated and measured responses for all HSC plates under first impact are reported in **Table 6.3**, where the parameters of studied plates are also presented. From the tabulated data it can be observed that on average, the peak responses values are estimated with high accuracy. The mean model-to-test ratio for all responses is found to be in the range of 0.96 to 1.07 with a coefficient of variation (COV) ranging from 2.1 to 13.1%.

Table 6.3 – Comparison of model prediction to test results of HSC plates (1st impact)

Plate's ID	Reinforcement		Results type	Impact force (kN)	Reaction force (kN)	Midpoint displacement (mm)	Steel strain (με)
	Layout	Ratio					
HS-1-D	Doubly reinforced	1.00 %	Test	980.10	950.00	29.03	2117
			Model	1045.10	987.00	31.08	2193
			M/T[1]	1.07	1.04	1.07	1.04
HS-2-D		2.00 %	Test	1616.90	1182.00	26.51	2433
			Model	1306.40	1075.80	29.24	2686
			M/T[1]	0.81	0.91	1.10	1.10
HS-3-D		3.00 %	Test	1479.80	1089.95	22.99	2432
			Model	1515.50	1135.10	24.60	2730
			M/T[1]	1.02	1.04	1.07	1.12
HS-2-S	Single reinforced	2.00 %	Test	1065.00	1034.96	35.87	2804
			Model	1097.40	1006.70	37.98	2686
			M/T[1]	1.03	0.97	1.06	0.96
HS-3-S		3.00 %	Test	1464.05	938.75	37.15	2635
			Model	1201.90	1026.48	38.61	2820
			M/T[1]	0.82	1.09	1.04	1.07
Mean			M/T[1]	0.95	1.01	1.07	1.07
variance (COV [%])			M/T[1]	13.1	7.0	2.2	6.2

[1] Model-to-test ratio

6.8.2 Numerical results of second impact load

Similar levels of accuracy are achieved in the analyses of all HSC plates under second impact load. The computed response-time histories of doubly and single reinforced plates under second impact are shown in **Figures 6.26** and **6.27**, respectively.

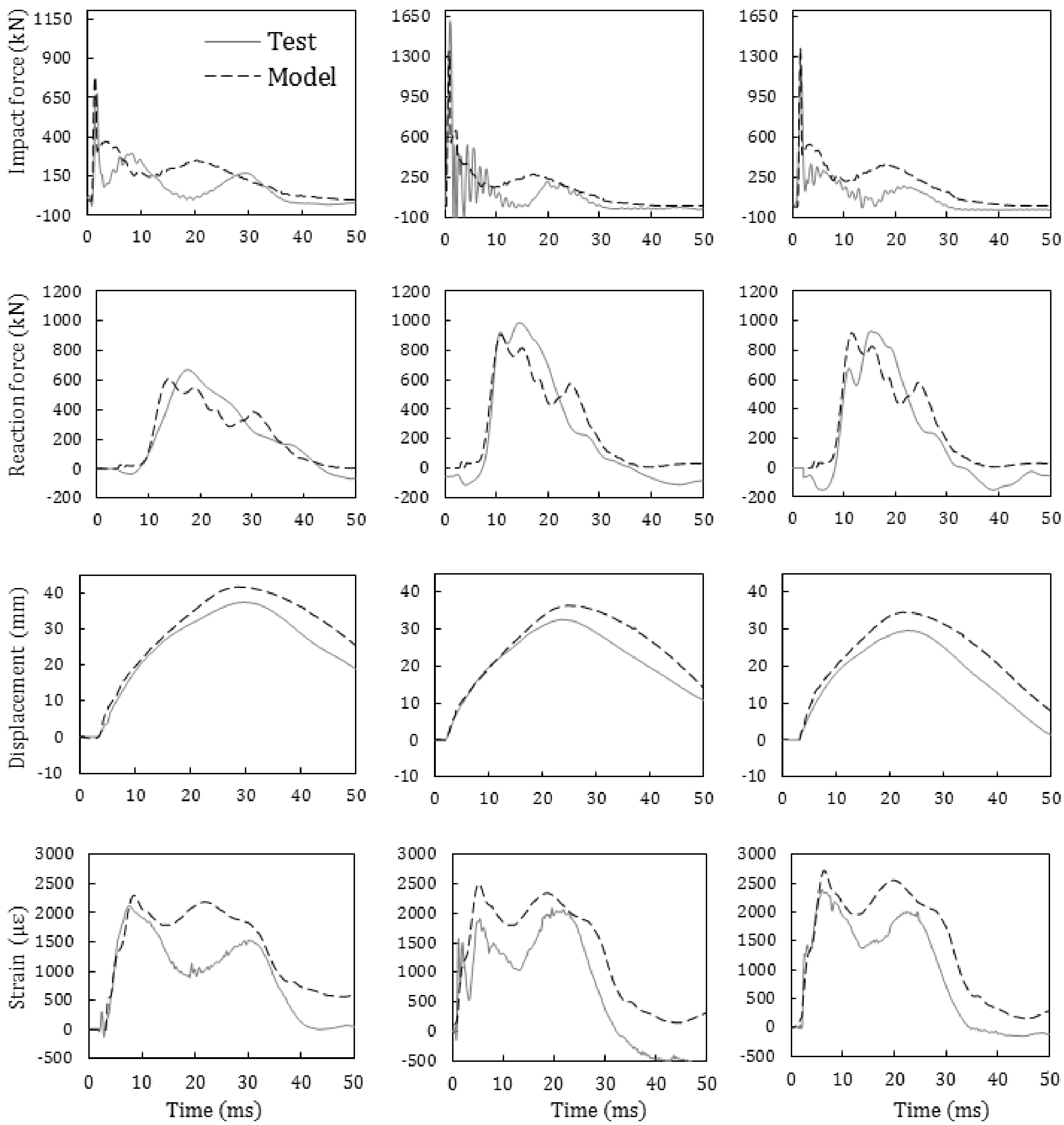

a) HS-1-D-2 b) HS-2-D-2 c) HS-3-D-2

Figure 6.26 – Comparison of model prediction to test results of doubly HSC plates (2nd impact)

It can be seen that the general shapes of computed impact and reaction forces are slightly changed compared to the obtained responses under fist impact load. However, seem to be in reasonable agreement with the experimental measurements. The overall computed displacement responses are captured well. The peak midpoint displacements are overestimated in all simulations and computed time periods are also larger than those of experiments. This may imply that the stiffness of the modelled plates is slightly lower than the experiment or the damage parameters are overestimated. The influence of fully bond assumption between concrete and steel reinforcement is shown up clearly in the steel strain time histories especially single reinforced plates (refer to **Figure 6.27**).

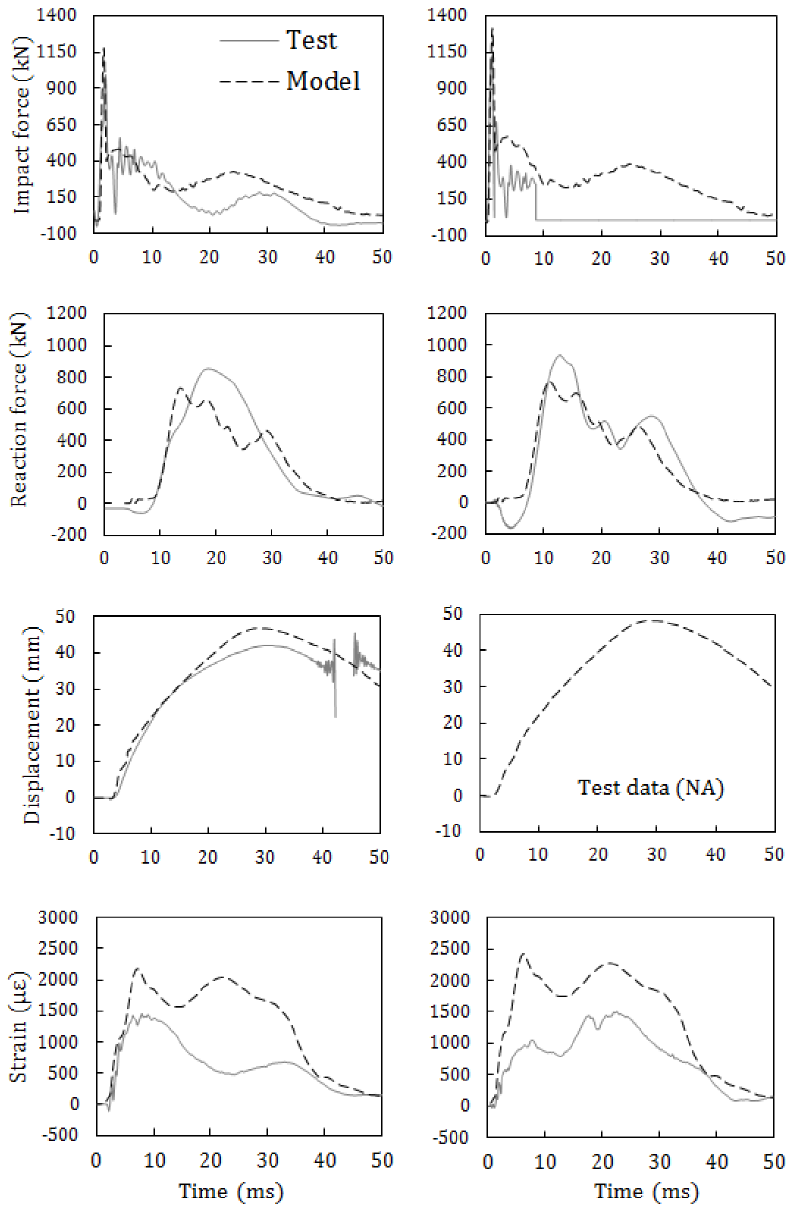

a) HS-2-S-2 b) HS-3-S-2

Figure 6.27 – Comparison of model prediction to test results of single HSC plates (2nd impact)

The peak estimated and measured responses for all HSC pates under second impact are reported in **Table 6.4**. Almost similar level of accuracy of first impact analysis is obtained for impact force, reaction force and midpoint displacement. Estimates of the steel strains, however, are not computed with the same level of accuracy. The mean model-to-test ratio of strains is 1.30 with a coefficient of variation (COV) of 17.8 % which indicates a relatively low level of accuracy.

Table 6.4 – Comparison of model prediction to test results of HSC plates (2nd impact)

Plate's ID	Reinforcement		Results type	Impact force (kN)	Reaction force (kN)	Midpoint displacement (mm)	Steel strain (με)
	Layout	Ratio					
HS-1-D	Doubly reinforced	1.00 %	Test	680.05	669.00	37.54	2114.00
			Model	781.20	609.50	41.75	2300.00
			M/T[1]	1.15	0.91	1.11	1.09
HS-2-D		2.00 %	Test	1613.15	987.65	32.52	2096.00
			Model	1345.00	905.30	36.34	2495.00
			M/T[1]	0.83	0.92	1.12	1.19
HS-3-D		3.00 %	Test	1237.30	929.60	29.52	2399.00
			Model	1367.10	917.20	34.51	2717.00
			M/T[1]	1.10	0.99	1.17	1.13
HS-2-S	Single reinforced	2.00 %	Test	996.80	852.10	42.11	1450.00
			Model	1171.80	730.80	46.80	2171.00
			M/T[1]	1.18	0.86	1.11	1.50
HS-3-S		3.00 %	Test	1128.35	806.00	NA	1510.00
			Model	1308.50	772.20	48.40	2417.00
			M/T[1]	1.16	0.96	---	1.60
Mean			M/T[1]	1.08	0.93	1.13	1.30
Variance (COV [%])			M/T[1]	13.2	5.3	2.5	17. 8

[1] Model-to-test ratio

6.8.3 Numerical damage patterns of HSC plates

In general, smeared cracking based model cannot represent the crack patterns perfectly. However, it can give a reasonable representation of the distribution and level of induced damage throughout the modelled structure. As reported in Chapter 5, single reinforced plates failed by localized sudden punching with sever scabbing. On the other hand, doubly reinforced plates failed by ductile punching shear mode in which both bending and shear cracks are developed.

Figure 6.28 presents the tension damage pattern obtained from the FE analyses and the observed crack pattern from experiments for both single and doubly reinforced plates containing 3% bottom steel reinforcement (HS-3-S and HS-3-D). The presented damage patterns are resulted after applying same numbers of impacts (two impacts).

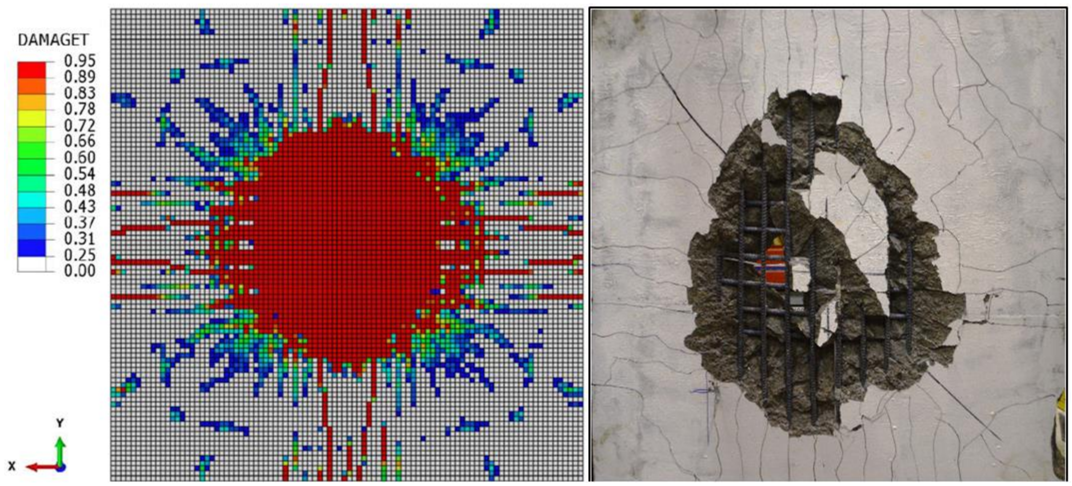

a) HS-3-S

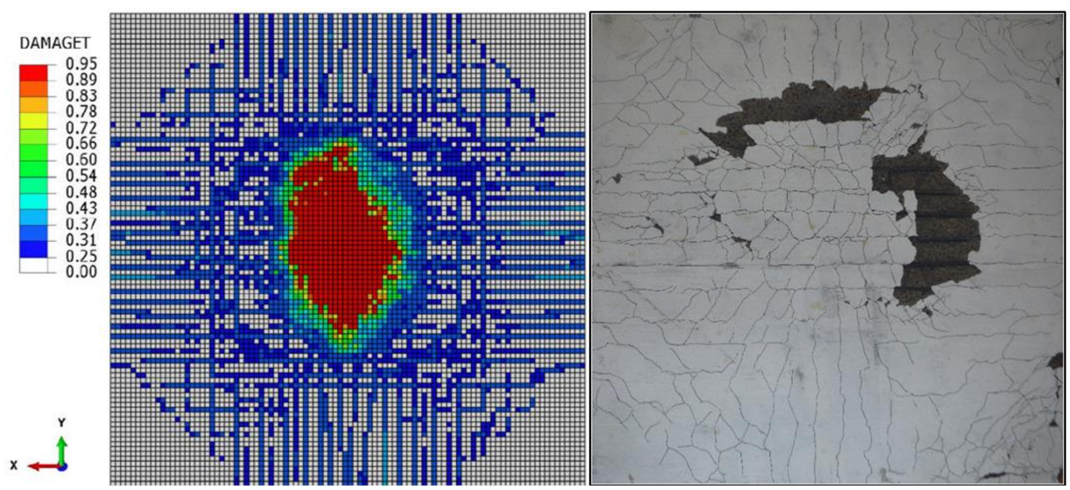

b) HS-3-D

Figure 6.28 – Final crack pattern of HSC plates (left: Model; right: test)

It is shown up clearly in **Figure 6.28** that the damage patterns of FE models are in good agreement with the observed crack pattern of experimental tests. The failure model of single reinforced plate is predicted well, element with high level of damage (> 0.90) are spread over a larger area in midpoint zone which gives an indication of punching shear failure model. For doubly reinforced plate, the elements severely damaged (> 0.90) are localized at the impact zone. Elements with moderate damage levels (0.25 to 0.50) are aligned in both directions indicate flexural bending behaviour.

6.9 Numerical Analysis of UHP-FRC Plates

The FE simulations of UHP-FRC plates are performed following the same procedures of HSC plates modelling with the exception of concrete material parameters. The CDP parameters are calibrated based on the results of the experimental test of plate UF_2S_{100} containing 2 % fibre and steel reinforcement ratio of 1%. Then, the predictive capability of calibrated model is demonstrated by simulating other UHP-FRC plates cast using same UHP-FRC (UF_2S_{158} and UF_2S_{210})

6.9.1 Calibration of CDP model parameters

Based on the experience gained from the previous HSC modelling, only the material parameters with significant effects are calibrated. CDP constitutive model parameters with high uncertainties, including fracture energy (G_F), uniaxial tensile strength (f_t) and dilation angle (ψ) are calibrated through a series of parametric studies using the experimental results of the first impact test of plate UF_2S_{100}. Other CDP parameters with marginal effect, including ϵ, σ_{bo}/σ_{co}, and K_c, are set to the default values of 0.1, 1.16, and 0.67, respectively.

As observed in the HSC calibration process, the influences of material parameters on the impact force and reaction results are generally limited. Therefore, only the results of midpoint displacement and bottom steel strain at midpoint zone are considered in the following parametric studies.

6.9.1.1 Fracture energy

In literatures, UHP-FRC of 140 – 180 MPa containing 1.5 – 2.5% short steel fibre by volume and cured under standard conditions, showed tensile fracture energies ranging from 14,000 to 21,000 N/m (Wille and Naaman, 2010; Voit and Kirnbauer, 2014; Xu and Wille, 2015; Tran et al., 2016). In this investigation, three different values of fracture energy (16000, 18000, and 20000 N/m) with f_t = 10 MPa, and ψ = 30° are considered. **Figure 6.29** illustrates the influence of the fracture energy on the computed responses. It is evident that the tension stiffening behaviour of concrete has a pronounced effect on the impact response of the plate. Both midpoint displacement and steel strain are inversely proportional to the fracture energy value. Smaller fracture energy inputs indicate that the material has lower deformation capacity. This means the cracks begin to propagate at lower stress values and steel reinforcement starts to arrest cracks at early stages which reflected in higher strain values as shown in **Figure 6.29-b**.

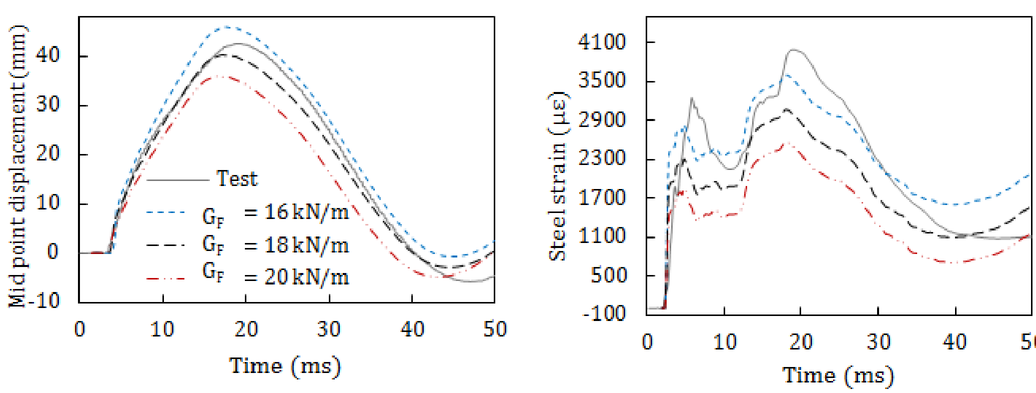

a) Midpoint displacement b) Steel strain at midpoint

Figure 6.29 – Influence of fracture energy, G_F (UF_2S_{100}, 1st impact test)

It worth noting that ultimate localized crack width of UHP-FRC is equal to half the fibre length (i.e., 65 mm) (Wille et al., 2012; Xu and Wille, 2015). Based on the used fictitious crack model of Hillerborg (1985), the maximum crack opening width corresponding to 20,000 N/m fracture energy is 72 mm in which over the theoretical crack opening capacity. On the other hand, the fracture energy of 18,000 N/m resulted in ultimate maximum crack opening of 64 mm, close to the deformation capacity limit. Therefore, the fracture energy of 18,000 N/m is selected to be used in all the following analyses.

6.9.1.2 Tensile strength

The tensile strength of UHP-FRC has been measured using splitting tensile tests. Thus, it is important to calibrate the estimated tensile strength. In this investigation, the uniaxial tensile strength variables in the range from 80 to 100 % of splitting tensile strength and the results are summarized in **Figure 6.30**.

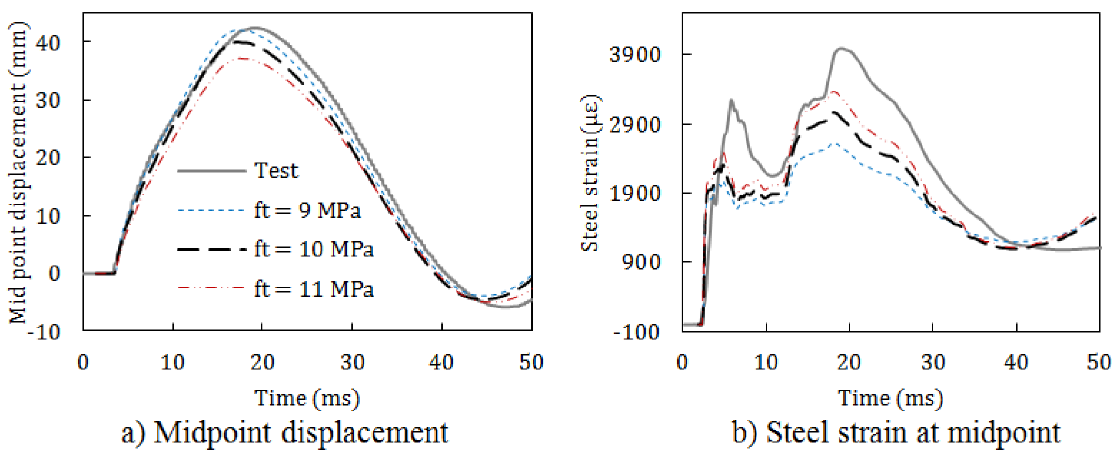

Figure 6.30 – Influence of tensile strength, f_t (UF_2S_{100}, 1st impact test)

The tensile strength has limited effect on both computed displacement and steel strain responses. It might be because the considered tensile strength values are close to each other. In general, the uniaxial tensile strength of nonfibrous concrete is estimated as 90 % of concrete splitting strength (CEB-FIP, 2010). Therefore, for all following simulations, the uniaxial tensile strength is taken equal to 10 MPa same like conventional concrete.

6.9.1.3 Dilation angle of UHP-FRC model

Three different values of ψ (10°, 20°, 30°) with G_F = 18000 N/m, and f_t = 10 MPa are considered in this study. **Figure 6.31** shows the influence of different values of dilation angle on the simulation results in comparison with experimental measurements.

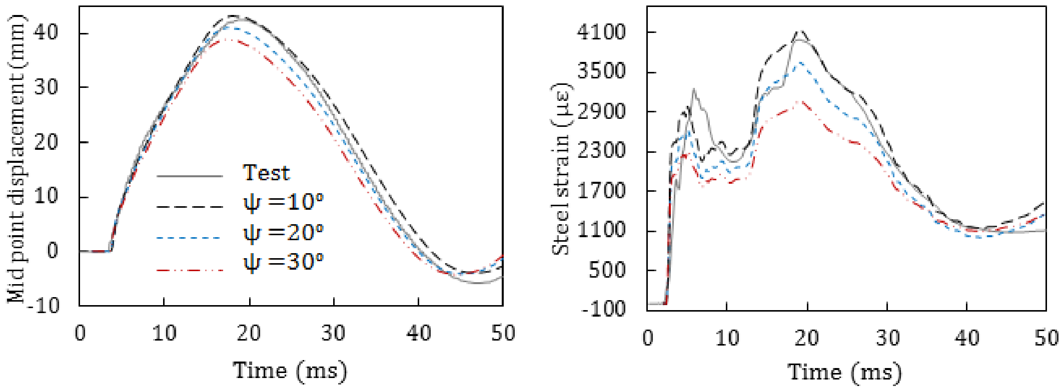

Figure 6.31 – Influence of of dilation angle size, ψ (UF_2S_{100}, 1st impact test)

As shown, the simulation results of 10° dilation angle fits well with the experimental data. The selected dilation angle here is close to 15° which was adapted to model UHP-FRC beam under static load using CDP model by Chen and Graybeal (2011). The significance of dilation to the mechanical response of UHP-FRC is not well understood and there is no available studied regarding the volumetric dilatancy of UHP-FRC. However, the results of this study are expected since UHP-FRC has enhanced dense microstructure and exhibits less volume changes compared to conventional concrete.

6.10 Numerical Results of UHP-FRC Plates

This section presents the computed responses for the UHP-FRC plates containing 2% fibre by volume: UF_2S_{100}, UF_2S_{158}, and UF_2S_{210}. The computed impact force-time, total reaction force-time, midpoint displacement-time, and steel strain-time histories are plotted alongside the test results for selected impact tests. Thereafter, the induced damage patterns are discussions. The responses-time histories of UHP-FRC plates under first and second impact tests are presented in **Figures 6.32** and **6.33**, respectively.

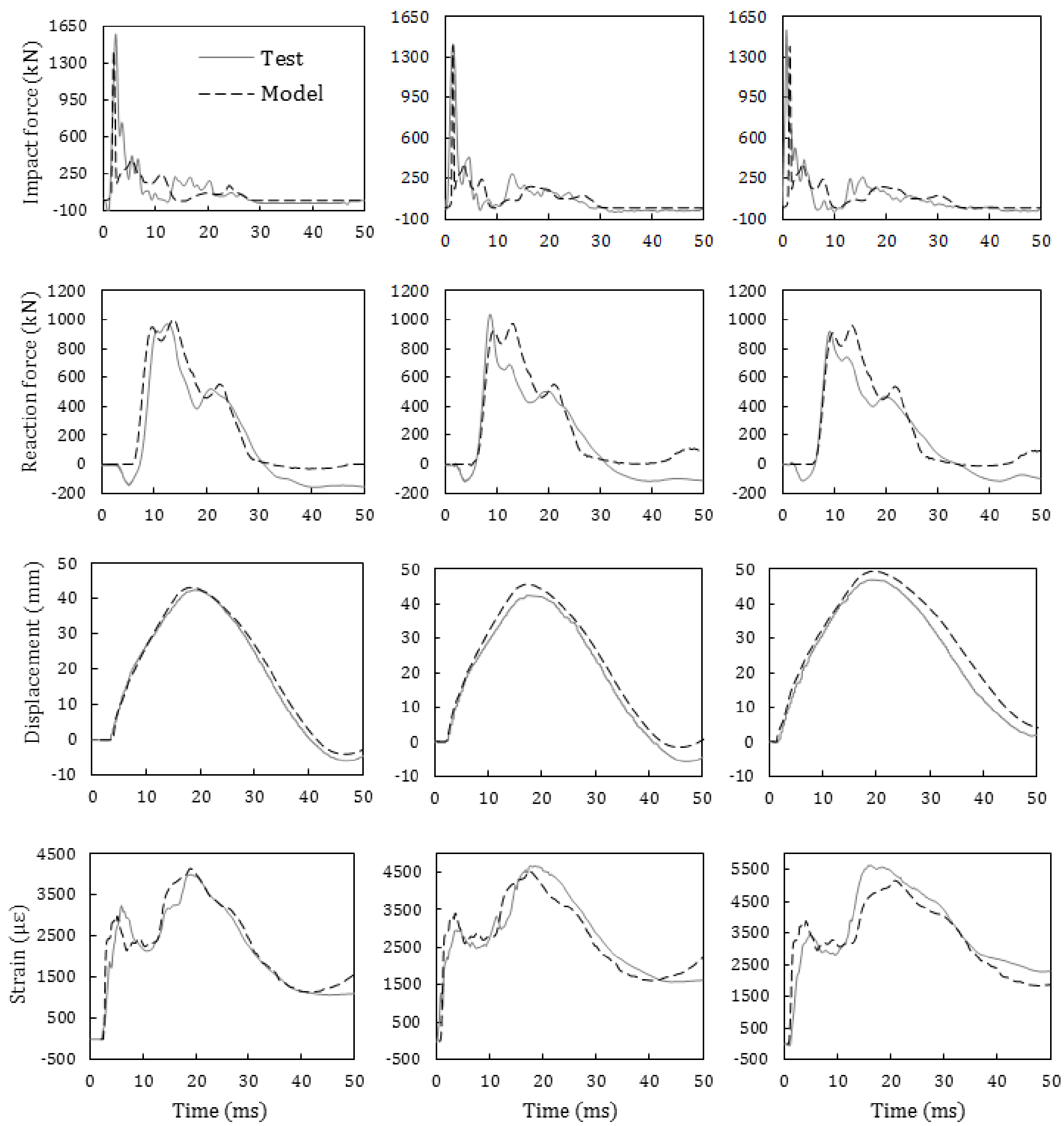

a) UF_2S_{100}-1 b) UF_2S_{158}-1 c) UF_2S_{210}-1

Figure 6.32 – Comparison of model prediction to test results of UHP-FRC plates (1st impact)

It can be seen that the analytical results achieved similar levels of accuracy as that attained in analyses of the HSC Plates. In general, the computed responses are in good agreement with experimental measurements in terms of peak values, time response, and overall shape.

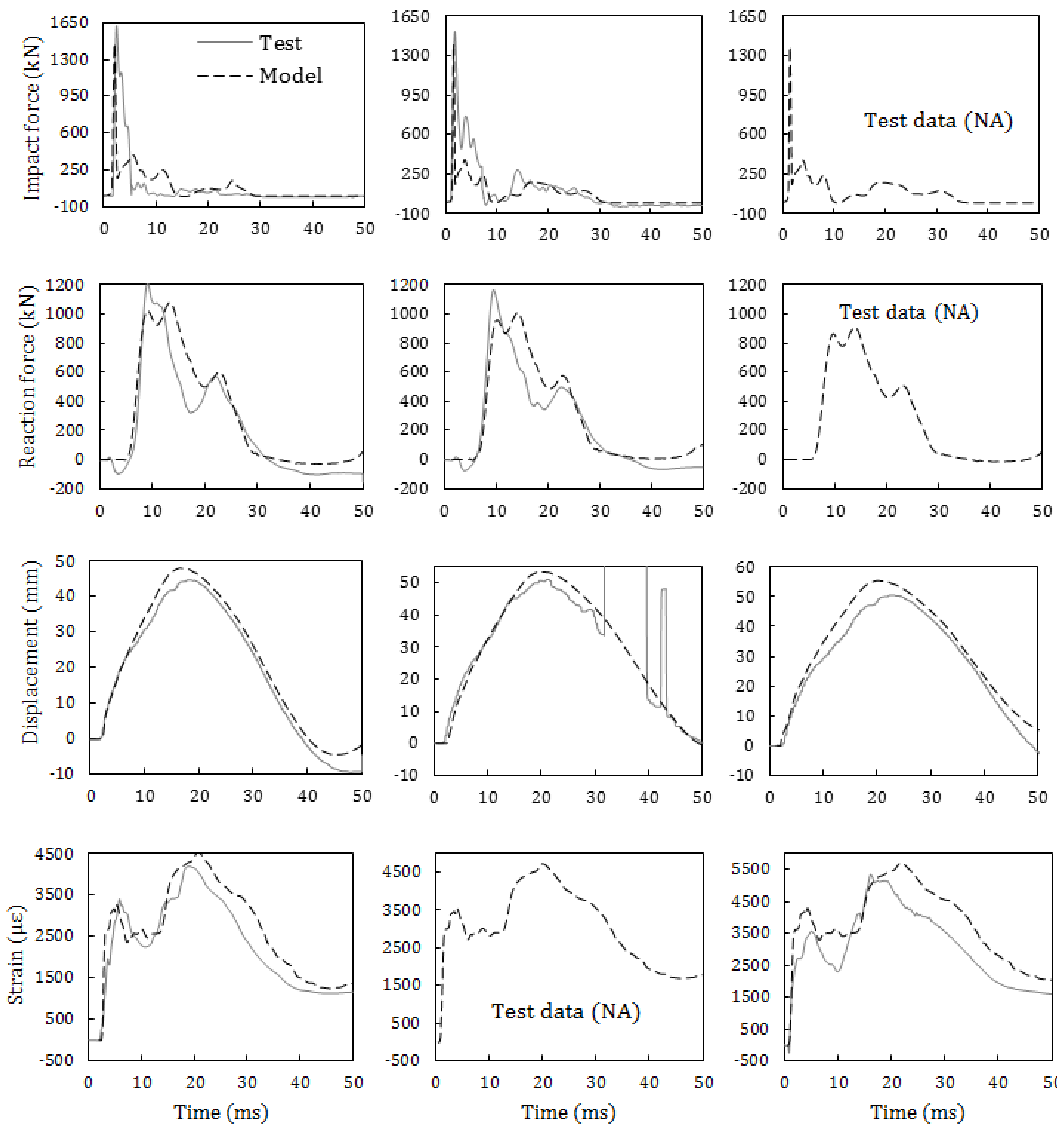

a) UF_2S_{100}-2 b) UF_2S_{158}-2 c) UF_2S_{210}-2

Figure 6.33 – Comparison of model prediction to test results of UHP-FRC plates (2nd impact)

The peak computed and measured responses for UHP-FRC plates under first and second impact tests are reported in **Table 6.5** and **6.6**, respectively. It is evident from the tabulated data that, the peak responses values are estimated with high accuracy. The mean model-to-test ratio for all responses is found to be in the range of 0.88 to 1.08 with a coefficient of variation (COV) ranging from 0.8 to 5.2 %.

Table 6.5 – Comparison of model prediction to test results of UHP-FRC plates (1st impact)

Plate's ID	Steel ratio	Results type	Impact force (kN)	Reaction force (kN)	Midpoint displacement (mm)	Steel strain ($\mu\varepsilon$)
UF_2S_{100}	1.00 %	Test	1576.50	969.56	42.49	3992
		Model	1410.39	1002.00	43.21	4142
		M/T[1]	0.89	1.03	1.02	1.04
UF_2S_{158}	0.64 %	Test	1550	1038.44	42.44	4701
		Model	1370.44	971.80	45.64	4533
		M/T[1]	0.88	0.94	1.08	0.96
UF_2S_{210}	0.48 %	Test	1534.76	918.87	46.96	5631.00
		Model	1345.26	956.80	49.41	5156
		M/T[1]	0.91	1.04	1.05	0.92
Mean		M/T[1]	0.88	1.00	1.05	0.97
Variance (COV [%])		M/T[1]	0.82	4.8	2.3	5.2

[1] Model-to-test ratio

Table 6.6 – Comparison of model prediction to test results of UHP-FRC plates (2nd impact)

Plate's ID	Steel ratio	Results type	Impact force (kN)	Reaction force (kN)	Midpoint displacement (mm)	Steel strain ($\mu\varepsilon$)
UF_2S_{100}	1.00 %	Test	1610.00	1210.6	44.70	4150
		Model	1452.75	1080.1	48.01	4536
		M/T[1]	0.90	0.89	1.07	1.09
UF_2S_{158}	0.64 %	Test	1513.3	1165.3	51.1	NA
		Model	1404.53	1010.8	53.52	4733
		M/T[1]	0.93	0.87	1.05	---
UF_2S_{210}	0.48 %	Test	NA	NA	50.0	5352
		Model	1379.58	910.1	55.42	5711
		M/T[1]	---	---	1.11	1.07
Mean		M/T[1]	0.92	0.88	1.08	1.08
Variance (COV [%])		M/T[1]	1.4	1.4	2.3	1.2

[1] Model-to-test ratio

The analytical results of the third and successive impacts showed less accurate estimates of the experimental responses. In general, the impact force and reaction are estimated with reasonable accuracy. On the other hand, the overall shape of the computed displacement and steel strain responses are found to significantly differ from the measured responses (**Figure 6.34**). The displacement and steel strain showed significant discrepancies in the form of larger time periods, unrecoverable response. Such differences in responses are mainly returned to the absence of modelling fibre contribution at microstructure level and the full bond assumption between concrete and steel reinforcement. The obtained humble numerical results should be correlated to the experimental observation of fibres contribution in limiting damage progression by bridging action after applying the fourth impact test (refer to, Section 5.3.4). The simulation of UF_2S_{100} plate, which was subjected experimentally to nine impact tests, is aborted in seventh impact simulation due to excessively distorted elements. This means that the CDP model can predict the dynamic response reasonably well for cases in which cracking is in the form of non-continuous micro-cracks in the cementitious paste. On the other hand, the model is not able to predict the response after the crack formation and fibres become active to stop the propagation of cracks by bridging action.

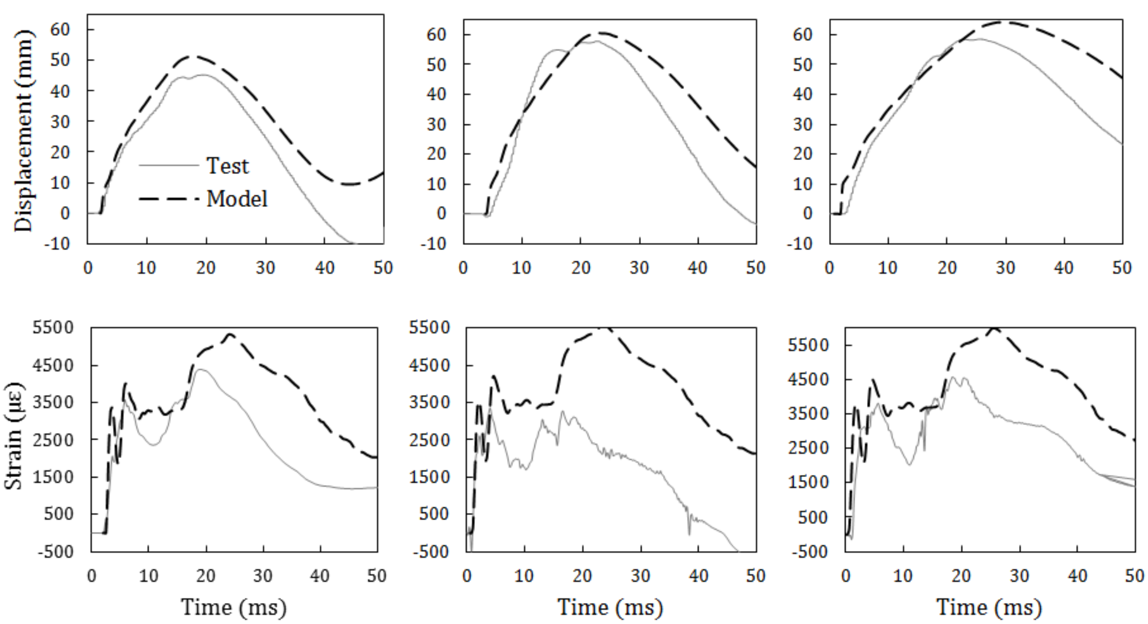

a) UF_2S_{100}-3 b) UF_2S_{158}-3 c) UF_2S_{210}-3

Figure 6.34 – Comparison of model prediction to test results of UHP-FRC plates (3rd impact)

Figure 6.35 presents tension damage patterns obtained from the FE analysis and the observed cracks from experiment for two UHP-FRC plates with different steel reinforcement ratios (UF_2S_{210} and UF_2S_{100}). Same damage display setting of HSC is used here. The only different is that the mesh size is decreased to 10 mm in order to obtain more representative damage patterns of cracks.

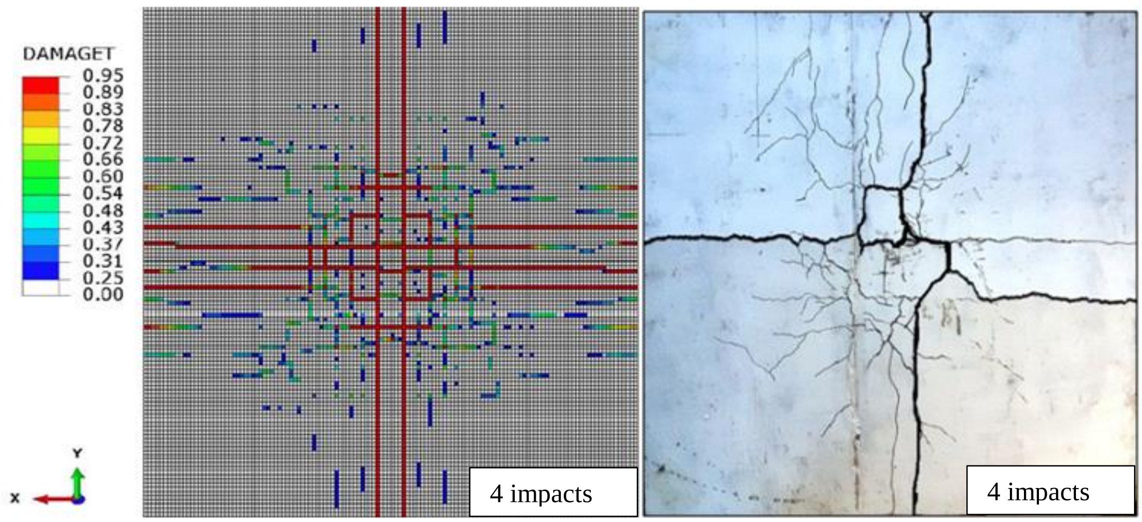

a) UF_2S_{210} (v_f =2%, Steel spacing = 210 mm)

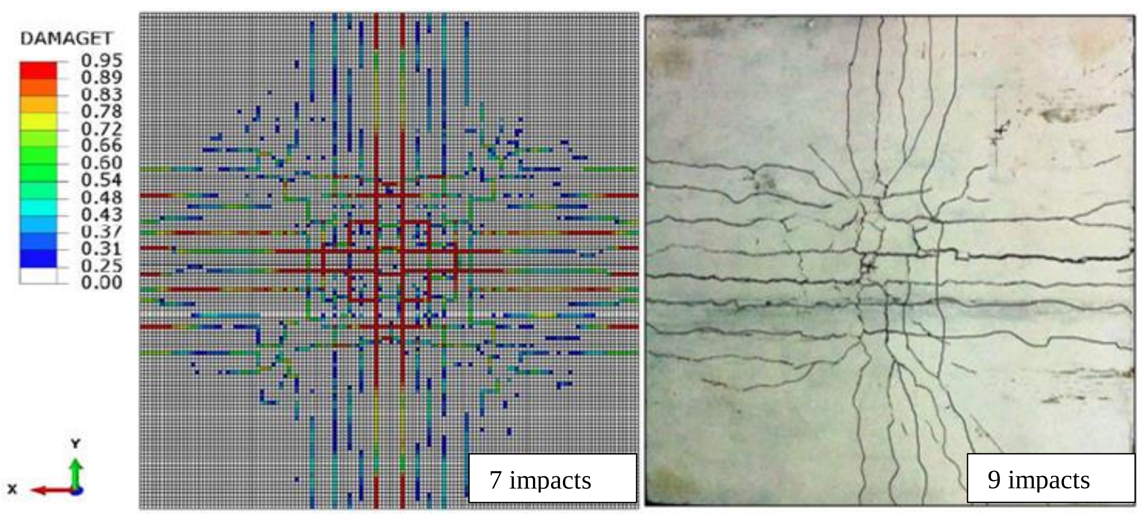

b) UF_2S_{100} (v_f =2%, Steel spacing = 100 mm)

Figure 6.35 – Final crack pattern of UHP-FRC plates (left: Model; right: test)

It can be said that the FE model cannot represent the crack patterns perfectly for all subsequent impact cases; however, it can at least give a reasonable representation of induced damage pattern and failure mode of UHP-FRC plates. The predicted damage patterns have not shown the localized sever damage of midpoint zone associated with punching shear observed in HSC model.

For UF_2S_{210} plate, elements with high damage levels are aligned in both directions indicate flexural bending behaviour. The aligned damage patterns are concentrated in the mid span as a continuous full damaged element which represents the single localized crack. On the other hand, the damage patterns of UF_2S_{100} distributed over larger number of cracks same as experimentally observed multi-cracks. Additionally, there is no continues element with high damage level in both direction (i.e., there is no localized cracks)

6.11 Summary of Finite Element Modelling

Numerical analysis procedures have been developed to model repeated low-velocity impacts on RC plates using ABAQUS/Explicit and the applicability was verified in comparison with existing experimental data. Different input parameters have been calibrated through a series of parametric studies and the significance of each parameter on the analytical results was addressed. An effective method for predicting the deformed shape of impacted plate using mass participation factor was provided. The proposed FE model has limitations regarding the estimation of steel strain time history for damaged RC members, since it was assumed prefect bond between steel reinforcement and surrounding concrete. The predicted responses of UHP-FRC plates show promise with regards to model UHP-FRC materials with the existing damage plasticity model. From the dynamic numerical study, the following conclusions are drawn:

1. The CDP model is a mesh dependent. The model must be coupled with fracture energy criterion and an appropriate mesh size with unity aspect ratio to ensure mesh size independent results. The artificial energy output must be considered as a quality check on mesh size and the stability of the explicit dynamic analysis.

2. The parametric investigations of CDP constitutive model parameters showed that the dilation angle, the inclusion of strain rates, and the use of the damage parameters are critical for an accurate FE modelling of the concrete behaviour under impact loading conditions, while the influence of the deviatoric plane shape, flow potential eccentricity, and damping effect are insignificant.

3. The numerical results of the six HSC plates with different steel reinforcement layouts and ratios confirm the ability of the calibrated HSC model for predicting the response and failure mode of dynamically loaded RC members with good accuracy.

4. The computed dynamic response of UHP-FRC was found to be significantly influenced by the fracture energy input than the uniaxial tensile strength value.

5. Based on the numerical results, the plastic volume change of UHP-FRC (dilation angle equal to 10^{o}) is small in comparison to HSC material (dilation angle equal to 40^{o})

6. The numerical results of UHP-FRC plates can demonstrate the feasibility of existing concrete damage plasticity constitutive model in estimating the dynamic response of new UHP-FRC materials. However, instabilities of results were observed in the later-impact analyses that corresponding to damage level of fibres bridging action stage.

7 CONCLUSIONS AND RECOMMENDATIONS

7.1 Conclusions

Two experimental testing programs and a major numerical investigation have been performed. The first experimental investigation is aimed to determine the static and dynamic mechanical properties of UHP-FRC materials. The second experimental investigation is focused on the advantage of using UHP-FRC in impact resistance structural members. The numerical investigation aimed to develop an accurate 3D-FE model capable of analyzing the dynamic response of RC structures under low-velocity impact loads. A second focus of the numerical investigation was to examine the ability of existing CDP to accurately replicate the dynamic response of reinforced UHP-FRC plates. For clarity purposes, conclusions of materials investigation, drop-weight impact testing, and numerical modelling are presented separately in the following subsections.

7.1.1 Materials investigation conclusions

1. UHP-FRC material is less strain-rate sensitive than HSC.
2. DIFs are higher for UHP-FRC matrices with lower strengths and decrease with the increase of matrix strength for compressive strength, elastic modulus, and flexural strength.
3. The dynamic enhancement of flexural tensile strength is inversely proportional to the fibre content. On the other hand, the effect of fibre content on dynamic enhancement in compression is insignificant.
4. The DIFs formulas of CEB-FIP Model (2010) fit reasonably well with HSC results in both compression and tension. On the other hand, the CEB-FIP Model (2010) overestimates DIFs

for all UHP-FRC matrices, especially matrices of compressive strength greater than 110 MPa.

7.1.2 Drop-weight impact testing conclusions

1. Precision low-velocity experimental measurements of reinforced UHP-FRC plates have been generated in a research area where no testing has been performed.
2. The UHP-FRC plates exhibit superior damage control characteristics when compared to RC plate cast using NSC and HSC. No spalling, scabbing, and/or large fragmentations were observed.
3. The use of UHP-FRC instead of traditional concrete materials successively changes the failure mode from punching shear to pure flexural mode under repeated impact loads.
4. The use of fibre content of 3% in impact resistance structures is more significant in enhancing the dynamic performance compared to the other used two steel fibre contents of 1 and 2%. The total impact energy of UHP-FRC plate containing 3% fibres was found to be double the capacity of UHP-FRC plate containing 2% fibres and 18 times the capacity of NSC plate.
5. Increasing steel reinforcement ratio has a positive effect on overall impact behaviour which reflected in less peak and residual displacements and higher impact energy capacity.

7.1.3 Numerical simulation conclusions

1. The numerical results of UHP-FRC plates can demonstrate the feasibility of existing concrete damage plasticity constitutive model in estimating the dynamic response of new UHP-FRC materials.
2. The parametric investigations of CDP constitutive model parameters showed that the dilation angle, the inclusion of strain rates, and the use of the damage parameters are critical for an

accurate FE modelling of the concrete behaviour under impact loading conditions, while the influence of the deviatoric plane shape, flow potential eccentricity, and damping effect are insignificant.

3. The plastic volume change of UHP-FRC (dilation angle equal to 10^o) is small in comparison to HSC material (dilation angle equal to 40^o).

4. The computed dynamic response of UHP-FRC was found to be significantly influenced by the fracture energy input than the uniaxial tensile strength value.

5. Instabilities of results were observed in the later-impact analyses that corresponding to damage level of fibres bridging action stage.

7.2 Recommendations for Future Work

While the undertaken research was successful in accomplishing the outlined objectives, there are a number of recommendations which would likely benefit the future studies. The following recommendations were identified over the course of this research:

1. An appropriate uniaxial tensile input model for UHP-FRC takes into account hardening and softening responses, and the fracture energy is required. Such research would allow improvement, development, and generalization of numerical constitutive models.

2. Comprehensive experimental investigations on the mechanical properties of UHP-FRC materials under high strain rates ($>10s^{-1}$) are required in order to develop mathematical models for the dynamic enhancement of such new materials.

3. The significance of volumetric dilatancy of UHP-FRC is in need to be investigated. The plastic volume change of UHP-FRC is not well understood and there is no available studied in this regard.

4. The use of accelerometer to determine the impact force presented several challenges as it requires extensive post-processing validation and filtering. Using a high capacity dynamic (quartz) load cell to measure the impact force is recommended.
5. The full-scale impact experimental data could be used by other researchers to assess the performance of currently existing analytical procedures or develop new analytical models for UHP-FRC material.
6. Improving the stability of explicit solution is in need to be investigated when the bond model is introduced.
7. Using calibrated HSC and UHP-FRC material models to investigate the response of RC structures with different geometries under low-velocity load conditions.
8. Extend the calibrated HSC and UHP-FRC constitutive models to simulate RC structural members under higher strain rates, such as explosion and blast loads.

Appendix A: STRAIN RATES CALCULATIONS

Sample calculation of different input displacement rates that have been used in the materials investigation (Chapter 3) are presented in this appendix. Additionally, the calculation of strain rates extracted from drop hammer tests is also given.

A.1. Input displacement rates of compression tests conducted using MTS 815:

Specimens of compression tests are cylinders with dimensions of 100×200 mm.

Example: the displacement rate corresponding to the basic quasi-static strain rate of 3×10^{-5} s^{-1} can be calculated using the following equation:

$$\dot{\varepsilon} = \frac{\dot{\Delta}}{L} \rightarrow \dot{\Delta} = \dot{\varepsilon} \times L \rightarrow \dot{\Delta} = 3 \times 10^{-5} \times 200 \times 60 = 0.36 \ {}^{mm}/_{minute} \qquad (A.1)$$

Where,

$\dot{\Delta}$ = displacement rate, mm/minute; $\dot{\varepsilon}$ = strain rate, s^{-1}; L = height of the specimens, mm.

A.2. Input displacement rates of three point bending tests conducted using MTS 793:

Specimens of three point bending tests are prisms with dimensions of 100×100×400 mm with a clear span of 300 mm. The displacement rate can be calculated assuming engineers' theory of bending using Eq. A.2:

$$\dot{\sigma} = \frac{\dot{M}y}{I} = \frac{3\dot{P}L}{2bh^2} \text{ and } \dot{\sigma} = E \times \dot{\varepsilon} \rightarrow \dot{\varepsilon} = \frac{3\dot{P}L}{2Ebh^2} \rightarrow \dot{P} = \frac{2Ebh^2\dot{\varepsilon}}{3L}$$

$$\dot{\Delta} = \frac{\dot{P}L^3}{48EI} = \frac{\dot{P}L^3}{4Ebh^3} \rightarrow \dot{P} = \frac{4\dot{\Delta}Ebh^3}{L^3}$$

$$\therefore \dot{\Delta} = \frac{\dot{\varepsilon}L^2}{6h} \qquad (A.2)$$

Where,

$\dot{\Delta}$ = displacement rate, mm/minute; $\dot{\varepsilon}$ = strain rate, s^{-1}; L = clear span, mm; h = depth of the Specimens, mm.

Example: the displacement rate corresponding to the basic quasi-static strain rate of 1×10^{-6} s^{-1} can be calculated using (Eq. A.2) as follows:

$$\dot{\Delta}=\frac{\dot{\varepsilon}L^2}{6h}=\frac{10^{-6}\times300^2}{6\times100}\times60=0.009\ \mathrm{mm/minute}$$

A.3. The three point bending dynamic tests using drop-hammer impact setup

Strain rate is calculated based on Young's modulus values resulted from compressive strength tests at the basic quasi-static strain rate using the following equation

$$\dot{\sigma}=\frac{\dot{M}y}{I}=\frac{3\dot{P}L}{2bh^2}\quad \text{and}\quad \dot{\sigma}=E\times\dot{\varepsilon}$$

$$\dot{\varepsilon}=\frac{3\dot{P}L}{2Ebh^2} \tag{A.3}$$

Where:

$\dot{\varepsilon}$ = strain rate, s^{-1}; P' = maximum loading rate, kN/s, = peak slope of reaction force time history; L = clear span, mm; b = specimen width, mm; h = specimen depth, mm; E = elastic modulus, kN/mm^2.

Example: for HSC impact test from a height =150 mm

The maximum loading slope (Figure A.1) $\dot{P}=21.5\ {}^{kN}/_{ms}=8.7\times10^6\ N/s$

$$\dot{\varepsilon}=\frac{3\dot{P}L}{2Ebh^2}=\frac{3\times21.5\times10^6\times300}{2\times30{,}200\times100^3}=0.32\ s^{-1}$$

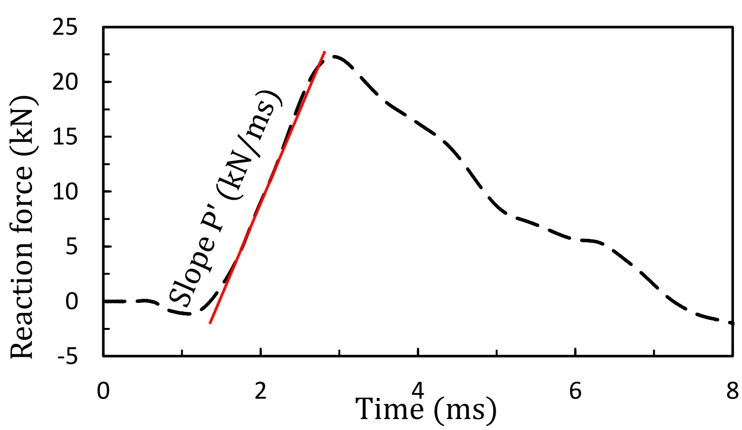

Figure A.1 – Typical reaction force time history (HSC, drop-height of 150 mm)

Appendix B: MATERIALS MECHANICAL PROPERTIES

B.1. Concrete Materials

Concrete matrix	Compressive strength f_c', (MPa)				COV [1]
	Specimen 1	Specimen 2	Specimen 3	Average	
HSC	79.2	83.0	87.1	83.1	4.75
UF_2-110	115.7	113.0	103.7	110.8	5.68
UF_2-130	137.6	127.3	133.2	132.7	3.89
UF_1-150	151.9	162.7	149.8	154.8	4.47
UF_2-150	174.1	160.0	153.1	162.4	6.59
UF_3-150	166.9	157.1	152.1	158.7	4.74

[1] coefficient of variation (%)

Concrete matrix	Elastic modulus E_c, (GPa)				COV[1]
	Specimen 1	Specimen 2	Specimen 3	Average	
HSC	29.7	29.1	31.8	30.2	4.69
UF_2-110	35.1	34.2	32.1	33.8	4.55
UF_2-130	40.3	40.8	36.8	39.3	5.55
UF_1-150	46.9	44.0	50.1	47.0	6.49
UF_2-150	51.1	48.4	46.9	48.8	4.36
UF_3-150	52.8	47.8	47.3	49.3	6.17

[1] coefficient of variation (%)

Concrete matrix	Flexural strength f_r, (MPa)				COV[1]
	Specimen 1	Specimen 2	Specimen 3	Average	
HSC	7.1	8.6	8.3	8.0	9.92
UF_2-110	13.2	11.3	11.8	12.1	8.14
UF_2-130	12.9	14.5	13.7	13.7	5.84
UF_1-150	8.9	8.2	8.4	8.5	4.24
UF_2-150	21.1	18.4	18.1	19.2	8.61
UF_3-150	30.2	26.9	27.8	28.3	6.03

[1] coefficient of variation (%)

Concrete matrix	Splitting strength f_{tsp}, (MPa)				COV[1]
	Specimen 1	Specimen 2	Specimen 3	Average	
HSC	4.1	4.8	4.6	4.5	8.28
UF_1-150	8.3	6.8	6.9	7.3	11.63
UF_2-150	12.1	9.9	11.3	11.1	9.88
UF_3-150	15.3	12.9	13.9	14.0	8.63

[1] coefficient of variation (%)

B.2. Steel Reinforcement

Steel bar size	Yield stress f_y, (MPa)				COV[1]
	Specimen 1	Specimen 2	Specimen 3	Average	
10M	436.2	422.7	441.3	433.4	2.22
15M	439.5	431.7	433.8	435.0	0.93
20M	463.8	438.9	450.9	451.2	2.76

[1] coefficient of variation (%)

Steel bar size	Ultimate strength f_{ult}, (MPa)				COV[1]
	Specimen 1	Specimen 2	Specimen 3	Average	
10M	630.2	621.6	613.3	621.7	1.36
15M	610.3	613.4	631.2	618.3	1.82
20M	618.2	647.0	622.1	629.1	2.48

[1] coefficient of variation (%)

Steel bar size	Elastic modulus Es, (GPa)				COV[1]
	Specimen 1	Specimen 2	Specimen 3	Average	
10M	199.3	199.3	204.7	201.1	1.55
15M	205.7	207.2	199.8	204.2	1.92
20M	201.9	193.1	200.8	198.6	2.41

[1] coefficient of variation (%)

Appendix C: ULTIMATE STATIC CAPACITIES OF HSC PLATES

C.1. Yield line analysis

Theoretically, there are several possible valid yield line patterns that could be applied to plates with same boundary and loading conditions. However, there is only one particular yield line pattern that gives the ultimate moment capacity or the least failure load, i.e., other mechanisms have a higher resistance. For this study, two yield line mechanisms with high probability of occurrence are examined and the critical case is selected to estimate the ultimate flexural capacity.

Pattern (1):

This failure pattern is formed in isotropic square plate simply supported at the corners, subjected to a concentrated load (P) at the midpoint. For this case, the yield lines extend from the midpoint to mid-spans of free edges (**Figure C.1-a**). By applying the virtual work principles for virtual maximum displacement (δ) at midpoint, the relation between the load capacity (P) and the ultimate moment capacity (M_u) can be calculated using Eq. (B.1).

$$\mathrm{P}.\delta = 4 \times \mathrm{M_u} \times \frac{\mathrm{L}'}{2} \times \frac{\delta}{\mathrm{L}'/2} \rightarrow \mathbf{P = 4\ M_u} \qquad (\mathrm{C}.1)$$

Pattern (2):

The second pattern is so-called fan mechanism. It formed when the plate subjected to heavy concentrated load (**Figure C.1-b**). This failure pattern is rare to be critical. However, a check is required in case of sudden concentrated load. The load capacity has been also calculated using the virtual work method. For doubly reinforced plates the positive moment (M_u) and negative moment (M_u') are assumed to be equal. However, for Plates with only positive reinforcement the negative moment is assumed to be zero.

$$\mathrm{P}.\delta = (\mathrm{M_u} + \mathrm{M_u}') \times 2\pi \mathrm{r} \times \frac{\delta}{\mathrm{r}} \qquad (\mathrm{C}.2)$$

For doubly reinforced plates (M_u = M_u')   **P= 12.57 M_u**

For single reinforeced plates (positive reinforcement only M_u' = 0.0)   **P= 6.29 M_u**

Based on the two studied yield line mechanisms, the most critical case is found to be pattern (1) where $\mathbf{P= 4\ M_u}$.

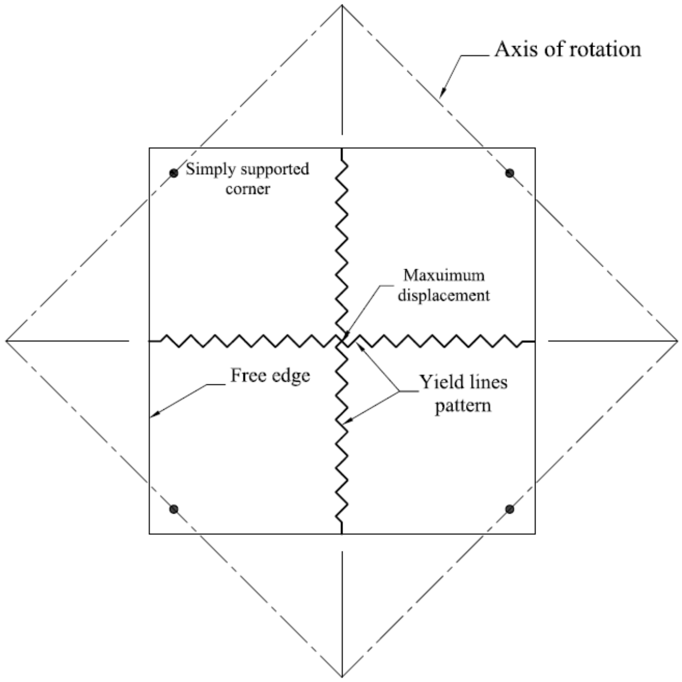

a) Pattern (1)

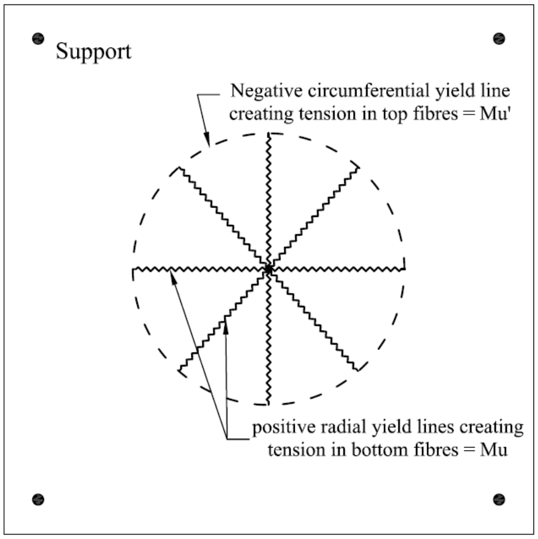

b) Pattern (2) Fan collapse

Figure C. 1– Typical fracture patterns of square plate simply supported at the corners and carrying a concentrated load at central point.

<u>Hint:</u> Isotropic means the plate equally reinforced in perpendicular directions

C.2. Ultimate static capacities of HSC plates

CSA A23.3 (2004) is followed to estimate ultimate flexural and punching static capacities of HSC plates. To get the ultimate resistance or section capacity, materials factors of safety are taken equal to unity, i.e., no reduction in material properties is considered.

C.2.1 Ultimate static moment and flexural load capacities

Concrete compressive strength (f_c') = 80 MPa; clear cover (b_c) = 15 mm;

steel yield stress (f_y) = 400 MPa.

$\alpha_1 = 0.85 - 0.0015 \times f_c{}' = 0.73, \qquad \beta_1 = 0.95 - 0.0025 \times f_c{}' = 0.77$

Assume initially that steel in tension is yield and materials factors of safety = 1 (to get the ultimate resistance)

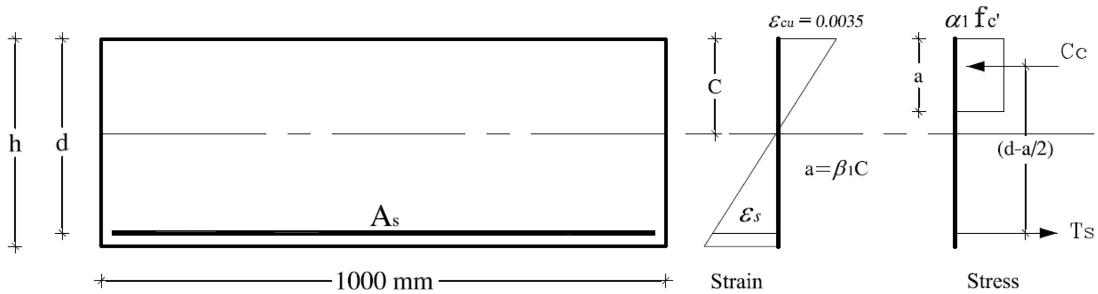

Figure B.2 − Typical ultimate flexural behaviour of RC slab according to CSA A23.3

a) Plates reinforced with 10M@100 mm

$$d = h - b_c - \frac{d_b}{2} = 100 - 15 - \frac{10}{2} = 80 \text{ mm}$$

Calculation of tension force in steel

$T_s = A_s \times f_y = 1000 \times 400 = 400$ kN

Calculation of compression stress block depth (a)

$$a = \frac{T_s}{\alpha_1 . f_c` . b} = 6.85 \text{ mm} \rightarrow \text{Neutral axis depth } C = \frac{a}{\beta_1} = 8.90 \text{ mm}$$

Check of steel yield

$$\frac{C_b}{d} = \frac{0.0035}{0.0035 + \varepsilon_y} = 0.6364 \rightarrow C_b = 0.6364 \times 80 = 50.90 \text{ mm}$$

$C < C_b$ steel is yield

Calculation of moment of resistance and ultimate flexural load

$$M_r = T_s\left(d - \frac{a}{2}\right) = 30.63\ \mathrm{kN.m}\ \rightarrow P_{usf} = 4\ M_r = 122.5\ \mathrm{kN}$$

b) Plates reinforced with 15M@100 mm

$$d = h - b_c - \frac{d_b}{2} = 100 - 15 - \frac{15}{2} = 78\ \mathrm{mm}$$

Calculation of tension force in steel

$T_s = A_s \times f_y = 2000\times 400 = 800$ kN

Calculation of compression stress block depth (a)

$$a = \frac{T_s}{\alpha_1.f_c`.b} = 13.70\ \mathrm{mm}\ \rightarrow \text{Neutral axis depth } C = \frac{a}{\beta_1} = 17.80\ mm$$

Check of steel yield

$$\frac{C_b}{d} = \frac{0.0035}{0.0035 + \varepsilon_y} = 0.6364\ \rightarrow C_b = 0.6364 \times 80 = 50.90\ \mathrm{mm}$$

$C<C_b$ steel is yield

Calculation of moment of resistance and ultimate flexural load

$$M_r = T_s\left(d - \frac{a}{2}\right) = 56.52\ \mathrm{kN.m}\ \rightarrow P_{usf} = 4\ M_r = 226.1\ \mathrm{kN}$$

c) Plates reinforced with 20M@100 mm

$$d = h - b_c - \frac{d_b}{2} = 100 - 15 - \frac{20}{2} = 75\ \mathrm{mm}$$

Calculation of tension force in steel

$T_s = A_s \times f_y = 2000\times 400 = 1200$ kN

Calculation of compression stress block depth (a)

$$a = \frac{T_s}{\alpha_1.f_c`.b} = 20.55\ \mathrm{mm}\ \rightarrow \text{Neutral axis depth } C = \frac{a}{\beta_1} = 26.69\ \mathrm{mm}$$

Check of steel yield

$$\frac{C_b}{d} = \frac{0.0035}{0.0035 + \varepsilon_y} = 0.6364\ \rightarrow C_b = 0.6364 \times 80 = 50.90\ \mathrm{mm}$$

$C<C_b$ steel is yield

Calculation of moment of resistance and ultimate flexural load

$$M_r = T_s\left(d - \frac{a}{2}\right) = 77.67 \text{ kN.m} \rightarrow P_{usf} = 4\,M_r = 310.70 \text{ kN}$$

C.2.2. Ultimate static punching load

The provision of CSA A23.3 (2004) expresses the punching strength of RC plates and footings in three categories. The smallest of three is considered as punching shear strength of the plate. Figure C.3 shows the punching perimeter of tested plates loaded by a 400 mm square loading area.

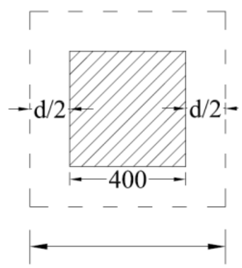

Figure C.3 − Critical perimeter for punching shear according to CSA A23.3

a) Plates reinforced with 10M@100 mm

$$\text{Depth of exterior reinforcement layer } (d_{max}) = 100 - 15 - \frac{10}{2} = 80 \text{ mm}$$

$$\text{Depth of interior reinforcement layer } (d_{min}) = 100 - 15 - 10 - \frac{10}{2} = 70 \text{ mm}$$

$$d = \frac{80 + 70}{2} \cong 75 \text{ mm},$$

$$\text{shear perimeter } (b_o) = 4\,(400 + 75) = 1900 \text{ mm}$$

- **Shear resistance (v_c) =** the least of

(1) $v_c = \left(1 + \frac{2}{\beta_c}\right) \times 0.19 \times \lambda\phi_c\sqrt{f_c'} = \left(1 + \frac{2}{1}\right) \times 0.19 \times \sqrt{80} = 5.10 \text{ N/mm}^2$

Where $\beta_c = 1$ for square column

(2) $v_c = \left(0.19 + \frac{\alpha_s d}{b_o}\right) \times \lambda\phi_c\sqrt{f_c'} = \left(0.19 + \frac{4 \times 75}{1900}\right) \times \sqrt{80} = 3.11 \text{ N/mm}^2$

Where $\alpha_s = 4$ for interior column

(3) $v_c = 0.38 \times \lambda\phi_c\sqrt{f_c{}'} = 0.38 \times \sqrt{80} = 3.40\ \mathrm{N/mm^2}$

The ultimate punching capacity of the plate

$$V_{us} = v_c \times b_o \times d = 3.11 \times 1900 \times 75 = 443.4\ \mathrm{kN}$$

b) <u>Plates reinforced with 15M@100 mm</u>

Depth of exterior reinforcement layer $(d_{max}) = 100 - 15 - \frac{15}{2} = 77.5\ \mathrm{mm}$

Depth of interior reinforcement layer $(d_{min}) = 100 - 15 - 15 - \frac{15}{2} = 62.5\ \mathrm{mm}$

$d = \frac{77.5 + 62.5}{2} \cong 70\ \mathrm{mm},$

shear permiter $(b_o) = 4\ (400 + 70) = 1880\ \mathrm{mm}$

- **Shear resistance (v_c)=** The least of

(1) $v_c = \left(1 + \frac{2}{\beta_c}\right) \times 0.19 \times \lambda\phi_c\sqrt{f_c{}'} = \left(1 + \frac{2}{1}\right) \times 0.19 \times \sqrt{80} = 5.10\ \mathrm{N/mm^2}$

(2) $v_c = \left(0.19 + \frac{\alpha_s d}{b_o}\right) \times \lambda\phi_c\sqrt{f_c{}'} = \left(0.19 + \frac{4 \times 70}{1880}\right) \times \sqrt{80} = 3.03\ \mathrm{N/mm^2}$

(3) $v_c = 0.38 \times \lambda\phi_c\sqrt{f_c{}'} = 0.38 \times \sqrt{80} = 3.40\ \mathrm{N/mm^2}$

The ultimate punching capacity of the plate

$$V_{us} = v_c \times b_o \times d = 3.03 \times 1880 \times 70 = 399\ \mathrm{kN}$$

c) <u>Plates reinforced with 20M@100 mm</u>

Depth of exterior reinforcement layer $(d_{max}) = 100 - 15 - \frac{20}{2} = 75\ \mathrm{mm}$

Depth of interior reinforcement layer $(d_{min}) = 100 - 15 - 20 - \frac{20}{2} = 55\ \mathrm{mm}$

$d = \frac{75 + 55}{2} \cong 65\ \mathrm{mm},$

shear perimeter $(b_o) = 4\ (400 + 65) = 1860\ \mathrm{mm}$

- **Shear resistance (v_c)** = the least of

(1) $v_c = \left(1 + \frac{2}{\beta_c}\right) \times 0.19 \times \lambda\phi_c\sqrt{f_c{}'} = \left(1 + \frac{2}{1}\right) \times 0.19 \times \sqrt{80} = 5.10\ \mathrm{N/mm^2}$

(2) $v_c = \left(0.19 + \frac{\alpha_s d}{b_o}\right) \times \lambda\phi_c\sqrt{f_c{}'} = \left(0.19 + \frac{4 \times 65}{1860}\right) \times \sqrt{80} = 2.95\ \mathrm{N/mm^2}$

(3) $v_c = 0.38 \times \lambda\phi_c\sqrt{f_c{}'} = 0.38 \times \sqrt{80} = 3.40\ \mathrm{N/mm^2}$

The ultimate punching capacity of the plate

$$V_{us} = v_c \times b_o \times d = 2.95 \times 1860 \times 65 = 356.6\ \mathrm{kN}$$

Appendix D: PUBLICATIONS

The following papers were extracted from this research program:

D.1 Published papers:

1. Othman, H. and Marzouk H., (2016). “Strain rate sensitivity of fiber-reinforced cementitious composites”, *ACI Materials Journal*, 113(2), pp. 143–150.
2. Othman, H. and Marzouk H., (2016). “An experimental investigation on the effect of steel reinforcement on impact response of reinforced concrete plates”, *International Journal of Impact Engineering*, 88, pp.12–21.
3. Othman, H. and Marzouk H., (2016). “Impact response of ultra-high performance reinforced concrete plates”, *ACI Structural Journal 2016* (Accepted and has been passed on to the publishing services department)
4. Othman, H. and Marzouk H., (2014). “Numerical investigation of reinforced concrete slabs under impact loading”, In: *10th fib International PhD Symposium in Civil Engineering*, Québec, Canada,: 2014, p. 263–270.

D.2 Submitted papers:

1. Othman, H. and Marzouk H., “Development of a drop-weight impact test setup”, Submitted to Experimental Techniques journal.
2. Othman, H. and Marzouk H., “Calibration of finite element simulation of reinforced concrete plates subjected to impact load”, Submitted to Computers and structures Journal.

REFERENCES

ACI Committee 544, (1988). "Measurement of Properties of Fiber Reinforced Concrete", American Concrete Institute, Report 544.4R-88, Reapproved 2009.

Acker, P. and Behloul, M., (2004). "Ductal® Technology: a large spectrum of properties, a wide range of applications", In *International Symposium on Ultra High Performance Concrete*. Kassel, Germany, pp. 11–24.

AFGC, (2002). "Ultra High Performance Fibre-reinforced Concretes – Interim Recommendations", France.

Asprone, D., Cadone, E. and Prota, A., (2009). "Tensile High Strain-rate Behavior of Reinforcing Steel from an Existing Bridge", *ACI Structural Journal*, 106(4), pp.523–529.

ASTM Standard C39/C39M, (2001). "Standard Test Method for Compressive Strength of Cylindrical Concrete Specimens", ASTM International, West Conshohocken, PA, USA, www.astm.org.

ASTM Standard C150/C150M, (2016). "Standard Specification for Portland Cement", ASTM International, West Conshohocken, PA, USA, www.astm.org.

ASTM Standard C469, (2002). "Standard Test Method for Static Modulus of Elasticity and Poisson's Ratio of Concrete in Compression", ASTM International, West Conshohocken, PA, USA, www.astm.org.

ASTM Standard C494/C494M, (2015). "Standard Specification for Chemical Admixtures for Concrete", ASTM International, West Conshohocken, PA, USA, www.astm.org.

ASTM Standard C496/C496M, (2004). "Standard Test Method for Splitting Tensile Strength of Cylindrical Concrete Specimens", ASTM International, West Conshohocken, PA, USA, www.astm.org.

ASTM Standard C1240/C1240M, (2015). "Standard Specification for Silica Fume Used in Cementitious Mixtures", ASTM International, West Conshohocken, PA, USA, www.astm.org.

ASTM Standard C1437, (2015). “Standard Test Method for Flow of Hydraulic Cement Mortar”, ASTM International, West Conshohocken, PA, USA, www.astm.org.

ASTM Standard C1609/C1609M, (2007). “Test Method for Flexural Performance of Fiber-Reinforced Concrete (Using Beam with Third-Point Loading)”, ASTM International, West Conshohocken, PA, USA, www.astm.org.

Banthia, N., Mindess, S. and Trottier, J., (1996). “Impact Resistance of Steel Fiber Reinforced Concrete”, *ACI Materials Journal*, 93(5), pp.472–479.

Barr, P., Carter, P., Howe, W. and Neilson, A., (1982). “Replica Scaling Studies of Hard Missile Impacts on Reinforced Concrete”, In *Symposium on concrete structures under impact and impulsive loading*, Berlin- Germany, pp. 329–344.

Bazant, Z., and Cedolin, L., (1980). “Fracture mechanics of reinforced concrete”, *Journal of the Engineering Mechanics Division*, 106(6), pp.1287–1306.

Belytschko, T., Liu, W., and Moran, B., (2014). “Nonlinear Finite Elements for Continua and Structures”, 2nd Edition, John Wiley & Sons Inc, West Sussex, England, 804 pp.

Bischoff, P., and Perry, S., (1991). “Compressive behaviour of concrete at high strain rates”, *Materials and Structures*, 24(6), pp.425–450.

Brown, D., (2016). “Tracker® Software V. 4.87 (video analysis and modeling tool)”, Available at: https://www.cabrillo.edu/~dbrown/tracker/.

Cavill, B., Rebentrost, M., and Perry, V., (2006). “Ductal®: An Ultra-High Performance Material for Resistance to Blasts and Impacts”, In *1st Specialty Conference on Disaster Mitigation (CSCE)*. Calgary, Canada, pp. 1–10.

CEB-FIP, (1988). “Concrete Structures under Impact and Impulsive Loading – Synthesis Report”, Comité EURO-International du Béton, Bulletin D’Information, Lausanne, Switzerland, 184 pp.

CEB-FIP, (2010). “Model Code for Concrete Structures”, Design Code, Comité EURO International du Béton, Lausanne, Switzerland, 350 pp.

Chanvillard, G. and Rigaud, S., (2003). "Complete Characterization of Tensile Properties of Ductal® UHPFRC According to The French Recommendations", In *4th International Workshop High Performance Fiber Reinforced Cement Composites (HPFRCC4)*. pp. 21–34.

Chen, L. and Graybeal, B., (2011). "Modeling Structural Performance of Ultrahigh Performance Concrete I-Girders", *Journal of Bridge Engineering*, 17(October), pp.754–764.

Chen, Y. and May, I., (2009). "Reinforced Concrete Members under Drop-weight Impacts", *Proceedings of the ICE - Structures and Buildings*, 162(1), pp.45–56.

Chopra, A., (2012). "Dynamics of Structures: theory and applications to earthquake engineering", 4th Edition, Pearson Education Inc., New Jersey, USA, 944 pp.

Clough, R. and Penzien, J., (2003). "Dynamics of structures", 3rd Edition, Computers and Structures Inc., Berkeley, USA, 752 pp.

Cowper, R. and Symonds, P., (1957). "Strain Hardening and Strain Rate Effects in the Impact Loading of Cantilever Beams", Technical Report no. 28, Brown University, USA, 52 pp.

CSA A23.3, (2004). "Design of Concrete Structures", Canadian Standards Association Mississauga - Canada, 214 pp.

Dunne, F. and Petrinc, N., (2005). "Introduction to Computational Plasticity", Oxford University press, Oxford, UK, 259 pp.

Ellis, B., DiPaolo, B., McDowell, D. and Zhou, M., (2014). "Experimental Investigation and Multiscale Modeling of Ultra-High-Performance Concrete Panels Subject to Blast Loading", *International Journal of Impact Engineering*, 69, pp.95–103.

Fehling, E. and Bunje, K., (2004). "Design Relevant Properties of Hardened Ultra High Performance Concrete", In *International Symposium on Ultra High Performance Concrete*. Kassel, Germany, pp. 327–338.

Fujikake, K., Li, B. and Soeun, S., (2009). "Impact Response of Reinforced Concrete Beam and its Analytical Evaluation", *Journal of Structural Engineering*, 135(8), pp.938–950.

Gao, X., Molyneaux, T. and Patnaikuni, I., (2006). "Dynamic Properties of Fibre Reinforced and Plain Ultra High Performance Concrete", In *19th Australasian Conference on the Mechanics of Structures and Materials*. Christchurch, New Zealand.

Genikomsou, A. and Polak, M., (2015). "Finite Element Analysis of Punching Shear of Concrete Slabs using Damaged Plasticity Model in ABAQUS", *Engineering Structures*, 98, pp.38–48.

Gopalaratnam, V. and Shah, S., (1986). "Properties of Steel Fiber Reinforced Concrete Subjected to Impact Loading" *ACI Materials Journal*, 83(14), pp.117–126.

Grassl, P. and Jirasek, M., (2006). "Plastic Model with Non-local Damage Applied to Concrete", *International Journal for Numerical and Analytical Methods in Geomechanics*, 30(1), pp.71–90.

Graybeal, B., (2005). "Characterization of the Behavior of Ultra-high Performance Concrete", PhD. Dissertation, University of Maryland, USA, 383 pp.

Graybeal, B., (2007). "Compressive Behavior of Ultra-high-performance Fiber-reinforced Concrete", *ACI Materials Journal*, 104(2), pp.146–152.

Guner, S. and Vecchio, F., (2013). "Simplified Method for Nonlinear Dynamic Analysis of Shear-Critical Frames", *ACI Structural Journal*, 109(5), pp.727–737.

Bache, H., (1981). "Densified Cement/ultrafine Particle-based Materials", In *2nd int. conference on superplasticizers in concrete*. Ottawa, Canada, pp. 10–12.

Habel, K., Charron, J.P., Braike, S., Hooton, R.D., Gauvreau, P. and Massicotte, B., (2008). "Ultra-high Performance Fibre Reinforced Concrete Mix Design in Central Canada", *Canadian Journal of Civil Engineering*, 35(2), pp.217–224.

Habel, K. and Gauvreau, P., (2008). "Response of Ultra-high Performance Fiber Reinforced Concrete (UHPFRC) to Impact and Static Loading", *Cement and Concrete Composites*, 30(10), pp.938–946.

Hillerborg, A., (1985). “The Theoretical Basis of a Method to Determine the Fracture Energy of Concrete”, *Materials and Structures*, 18(4), pp.291–296.

Hillerborg, A., Modéer, M. and Petersson, P., (1976). “Analysis of Crack Formation and Crack Growth in Concrete by Means of Fracture Mechanics and Finite Elements”, *Cement and Concrete Research*, 6(6), pp.773–781.

Hrynyk, T. and Vecchio, F., (2014). “Behavior of Steel Fiber-Reinforced Concrete Slabs under Impact Load”, *ACI Structural Journal*, 111(5), pp.1213–1224.

Hallquist, J., (2007). “LS-DYNA User’s Manual”, Livermore Software Technology Corporation, Livermore, USA.

Jiang, H., Wang, X. and He, S., (2012). “Numerical simulation of impact tests on reinforced concrete beams”, *Materials and Design*, 39, pp.111–120.

JSCE, (2008). “Recommendations for Design and Construction of HPFRCC with Multiple Fine Cracks”, Japan Society of Civil Engineers, 113 pp.

Kennedy, R., (1976). “A Review of Procedures for the Analysis and Design of Concrete Structures to Resist Missile Impact Effects”, *Nuclear Engineering and Design*, 37, pp.183–203.

Kennedy, G. and Goodchild, C., (2004). “Practical Yield Line Design”, 1st Edition, British Cement Association, Crowthorne, England, 175 pp.

Kishi, N., Mikami, H., Matsuoka, K. and Ando, T., (2002). “Impact Behavior of Shear-failure-type RC Beams without Shear Rebar”, *International Journal of Impact Engineering*, 27(9), pp.955–968.

Kishi, N., Matsuoka, K., Mikam, H. and Goto, Y., (1997). “Impact Resistance of Large Scale RC Slabs”, In *2nd Asia-pacific Conference on Shock and Impact loads on Structures*. Melbourne, Australia, pp. 213–220.

Kishi, N. Kurihashi, Y., Ghadimi Khasraghy, S. and Mikami, H., (2011). “Numerical Simulation of Impact Response Behavior of Rectangular Reinforced Concrete Slabs under Falling-Weight Impact Loading”, *Applied Mechanics and Materials*, 82, pp.266–271.

Kishi, N. and Bhatti, A., (2010). “An Equivalent Fracture Energy Concept for Nonlinear Dynamic Response Analysis of Prototype RC Girders Subjected to Falling-weight Impact Loading”, *International Journal of Impact Engineering*, 37(1), pp.103–113.

Kurihashi, Y., Taguchi, F., Kishi, N. and Mikami, H., (2006). “Experimental Study on Static and Dynamic Response of PVA Short-fibre Mixed RC Slab”, In *fib proceedings of 2 nd International Congress*. Naples, Italy, 10 pp.

Kwak, H-G. and Gang, H., (2015). “An Improved Criterion to Minimize FE Mesh-dependency in Concrete Structures under High Strain Rate Conditions”, *International Journal of Impact Engineering*, 86, pp.84–95.

Lafarge, 2016. “Lafarge North America”, Available at: http://www.ductal-lafarge.com.

Lee, J. and Fenves, G., (1998). “Plastic-damage Model for Cyclic Loading of Concrete Structures”, *Engineering Mechanics*, 124(8), pp.892–900.

Li, Q., Reid, S.R., Wen, H.M. and Telford, A.R., (2005). “Local Impact Effects of Hard Missiles on Concrete Targets”, *International Journal of Impact Engineering*, 32(1-4), pp.224–284.

Li, Z. and Huang, Y., (1998). “Effect of Strain Rate on the Compressive Strength Surface Cracking and Failure Mode of Mortar”, *ACI Materials Journal*, 95(5), pp.512–518.

Lok, T. and Zhao, P., (2004). “Impact Response of Steel Fiber-Reinforced Concrete Using a Split Hopkinson Pressure Bar”, *Journal of Materials in Civil Engineering*, 16(1), pp.54–59.

Lublinear, J., Oliver, J., Oller, S. and Onate, E., (1989). “A Plastic-damage Model for Concrete”, *Solids and Structures*, 25(3), pp.299–326.

Maalej, M., Quek, S. and Zhang, J., (2005). “Behavior of Hybrid-Fiber Engineered Cementitious Composites Subjected to Dynamic Tensile Loading and Projectile Impact”, *Journal of Materials* *in Civil Engineering*, 17(2), pp.143–152.

Malvar, L. and Crawford, J., (1998). “Review of Static and Dynamic Properties of Steel Reinforcing Bars”, *ACI Materials Journal*, 95(5), pp.609–616.

Malvar, L. and Ross, C., (1998). “Review of strain rate effects for concrete in tension”, *ACI Materials Journal*, 95(6), pp.735–739.

Mangat, P. and Azari, M., (1984). “Influence of steel fibre reinforcement on the fracture behaviour of concrete in compression”, *International Journal of Cement Composites and Lightweight Concrete*, 6(4), pp.219–232.

Martin, O., (2010). “Comparison of Different Constitutive Models for Concrete in ABAQUS/Explicit for Missile Impact Analyses”, JRC Scintific and Technical Reports, Luxembourg, 44 pp.

Marzouk, H., (1991). “Creep of High–strength Concrete and Normal–strength Concrete”, *Magazine of Concrete Research*, 43(155), pp. 121–126.

Marzouk, H. and Hussein, A., (1992). “Experimental Investigation on the Behavior of High-Strength Concrete Slabs”, *ACI Structural Journal*, 88(6), pp.701–713.

Marzouk, H. and Chen, Z., (1993a.) “Finite Element Analysis of High-Strength Concrete Slabs”, *ACI Structural Journal*, 90(5), pp.505–513.

Marzouk, H. and Chen, Z., (1993b). “Nonlinear Analysis of Normal- and High-strength Concrete Slabs”, *Canadian Journal of Civil Engineering*, 20(4), pp.696–707.

Marzouk, H. and Chen, Z., (1995). “Fracture Energy and Tension Properties of High-strength Concrete”, *Journal of Material in Civil Engineering*, 7(May), pp.108–116.

Marzouk, H. and Houssein, A., (1990). “Properties of High-strength Concrete at Low Temperatures”, *ACI Materials Journal*, 87(2), pp.167–171.

MathWorks, (2015). “MATLAB® program”.

Mier, V., (1984). “Complete Stress-Strain Behavior and Damaging Status of Concrete under Multiaxial Condition”, *International Conference on Concrete under Multiaxial Condition*, 1.

Millard, S., Molyneaux, T.C., Barnett, S.J. and Gao, X., (2010). “Dynamic Enhancement of Blast-resistant Ultra High Performance Fibre-reinforced Concrete under Flexural and Shear Loading”, *International Journal of Impact Engineering*, 37(4), pp.405–413.

Miyamoto, A., King, M. and Fujii, M., (1991). “Nonlinear Dynamic Analysis of Reinforced Concrete Slabs under Impulsive Loads”, *ACI Structural Journal*, 88(4), pp.411–419.

Murtiadi, S. and Marzouk, H., (2001). “Behaviour of high-strength concrete plates under impact loading”, *Magazine of Concrete Research*, 53(1), pp.43–50.

Naaman, A., (2007). “High performance fiber reinforced cement composites: classification and applications”, In *CBM-CI International Workshop*. Karachi, Pakistan, pp. 389–401.

Ngo, T., Mendis, P. and Krauthammer, T., (2007). “Behavior of Ultrahigh-strength Prestressed Concrete Panels Subjected to Blast Loading”, *Journal of Structural Engineering*, 133(11), pp.1582–1590.

Ong, K.C., Basheerkhan, M. and Paramasivam, P., (1999a). “Behaviour of Fibre Reinforced concrete slabs under low velocity projectile impact”, *ACI Special Publication*, 172(December), pp.993–1011.

Ong, K.C., Basheerkhan, M. and Paramasivam, P., (1999b). “Resistance of fibre concrete slabs to low velocity projectile impact”, *Cement and Concrete Composites*, 21(July), pp.391– 401.

Othman, H. and Marzouk, H., (2014). “Numerical investigation of reinforced concrete slabs under impact loading”, In *10th fib International PhD Symposium in Civil Engineering*. Québec, Canada, pp. 263–270.

Pajak, M., (2011). “The Influence of The Strain Rate on The Strength of Concrete Taking into Account the Experimental Techniques”, In *Architecture Civil Engineering Environment*. Gliwice, Poland, pp. 77–86.

Parant, E., Rossi, P., Jacquelin, E. and Boulay, C., (2007). “Strain Rate Effect on Bending Behavior of New Ultra-high-performance Cement-based Composite”, *ACI Materials Journal*, 104(5), pp.458–463.

Park, S., Xia, Q. and Zhou, M., (2001). “Dynamic Behavior of Boncrete at High Strain Rates and Pressures: II. Numerical simulation”, *International Journal of Impact Engineering*, 25(9), pp.887–910.

Priesrley, M., Seible, F. and Calvi, G., (1996). “Seismic Design and Retrofit of Bridges”, Jhon Wiley & Sons Inc, New Yourk, USA, 704 pp.

Rabczuk, T., Akkermann, J. and Eibl, J., (2005). “A Numerical Model for Reinforced Concrete Structures”, *International Journal of Solids and Structures*, 42(5-6), pp.1327–1354.

Reinhardt, B., Cornelissen, H. and Hordijk, D., (1986). “Tensile Tests and Failure Analysis of Concrete”, *Journal of Structural Engineering*, 112(11), pp.2462–2477.

Richard, P. and Cheyreezy, M., (1995). “Composition of reactive powdeandr concretes”, *Cement and Concrete Research*, 25(7), pp.1501–1511.

Riisgaard, B., Ngo, T., Mendis, P., Georgakis, C. and Stang, H., (2007). “Dynamic Increase Factors for High Performance Concrete in Compression using Split Hopkinson Pressure Bar”, In *Proceedings of the International Conference of Fracture Mechanics of Concrete and Concrete Structures*. Italy, pp. 1–4.

Rong, Z., Sun, W. and Zhang, Y., (2010). “Dynamic Compression Behavior of Ultra-high Performance Cement Based Composites”, *International Journal of Impact Engineering*, 37(5), pp.515–520.

Ross, C., Tedesco, J. and Kuennen, S., (1995). “Effects of Strain Rate on Concrete Strength”, *ACI Materials Journal*, 92(1), pp.37–47.

Rossi, P., Arca, A., Parant, E. and Fakhri, P., (2005). “Bending and Compressive Behaviours of a New Cement Composite”, *Cement Concrete Research*, 35(1), pp.27–33.

Roth, M., Rushing, T., Flores, O., Sham, D. and Stevens W., (2010). “Laboratory Investigation of the Characterization of Cor-Tuf Flexural and Splitting Tensile Properties”, *Report ERDC/GSL TR-10-46*, Vicksburg, MS, USA, 57 pp.

Roy, D., Gouda, G. and Bobrowsky, A., (1972). “Very High Strength Cement Pastes Prepared by Hot Pressing and Other High Pressure Techniques”, *Cement Concrete Research*, 2, pp.349–336.

Saatci, S. and Vecchio, F., (2009). “Effects of shear mechanisms on impact behavior of Reinforced Concrete Beams”, *ACI Structural Journal*, 106(1), pp.78–86.

Sangi, A. and May, I., (2009). “High-mass Low-velocity Impacts on Reinforced Concrete Slabs”, In *7th European LS-DYNA Conference*. Salzburg, Austria.

Sawan, J. and Abdel-Rohman, M., (1987). “Impact Effect on RC Slabs: Experimental approach”, *Journal Of Structural Engineering*, 112(9), pp.2057–2065.

Schmidt, M. and Fehling, E., (2005). “Ultra-high-performance Concrete: Research, development and application in Europe”, *Concrete, ACI Special Publication*, 228, pp.51–78.

Simulia, (2016). “ABAQUS 6.14 User’s Manuals”, *Dassault Systèmes Simulia Corp.*

Sinha, B., Gerstle, K. and Tulin, G., (1964). “Stress-strain Relations for Concrete under Cyclic Loading”, *ACI Journal Proceedings*, 61(2), pp.195–212.

Soleimani, S., Banthia, N. and Mindess, S., (2007). “Behavior of RC Beams under Impact Loading: Some new findings”, In *Proceedings of the 6th International Conference on Fracture Mechanics of Concrete and Concrete Structures*. Catania, Italy, pp. 867–874.

Soleimani, S. and Banthia, N., (2014). “A Novel Drop Weight Impact Setup for Testing Reinforced Concrete Beams”, *Experimental Techniques*, 38(3), pp.72–79.

Suaris, W. and Shah, S., (1982). “Strain-rate Effects in Fibre-reinforced Concrete Subjected to Impact and Impulsive Loading”, *Composites*, (April), pp.153–159.

Tran, N., Tran, T.K., Jeon, J.K., Park, J.K. and Kim, D.J., (2016). “Fracture Energy of Ultra-high-performance Fiber-reinforced Concrete at High Strain Rates”, *Cement and Concrete Research*, 79, pp.169–184.

Tue, N.V., Schneider, H., Simsch, G. and Schmidt, D., (2004). Bearing Capacity of Stub Columns Made of NSC, HSC and UHPC Confined by a Steel Tube”, In *Proceedings of the International Symposium on Ultra High Performance Concrete*. University of Kassel, Germany, pp. 339–350.

Gokoz, U. and Naaman, A., (1981). “Effect of Strain-rate on the Put-out Behaviour of Fibers in Mortar”, *International Journal of Cement Composites and Lightweight Concrete*, 3(3), pp.187–202.

Vebo, A. and Ghali, A., (1977). “Moment-curvature Relation of Reinforced Concrete Slabs”, *Journal of the Structural Division*, 103(3), pp.515–531.

Voit, K. and Kirnbauer, J., (2014). “Tensile Characteristics and Fracture Energy of Fiber Reinforced and Non-reinforced Ultra High Performance Concrete (UHPC) ”, *International Journal of Fracture*, 188(2), pp.147–157.

Walraven, J., (2009). “High Performance Fiber Reinforced Concrete: Progress in knowledge and design codes”, *Materials and Structures*, 42(9), pp.1247–1260.

Weerheijm, J. and Van Doormaal, J., (2007). “Tensile failure of Concrete at High Loading Rates: New test data on strength and fracture energy from instrumented spalling tests”, *International Journal of Impact Engineering*, 34(3), pp.609–626.

Wille, K., Kim, D. and Naaman, A., (2010). “Strain-hardening UHP-FRC with Low Fiber Contents”, *Materials and Structures*, 44(3), pp.583–598.

Wille, K. and Naaman, A., (2010). “Fracture Energy of UHPFRC under Direct Tensile Loading”, In *FraMCoS-7 international conference*. Jeju, Korea.

Wille, K. Naaman, A., and Parra-Montesinos, G., (2011). “Ultra-High Performance Concrete with Compressive Strength Exceeding 150 MPa (22ksi) : a simpler way”, *ACI Materials Journal*, 108(1), pp.46–53.

Wille, K., Naaman, A., El-Tawil, S. and Parra-Montesinos, G., (2012). "Ultra-high Performance Concrete and Fiber Reinforced Concrete: achieving strength and ductility without heat curing", *Materials and Structures*, 45(3), pp.309–324.

Williams, M., (1994). "Modeling of Local Impact Effects on Plain and Reinforced Concrete", *Structural Journal*, 91(2), pp.178–187.

Xu, M. and Wille, K., (2015). "Fracture energy of UHP-FRC under Direct Tensile Loading Applied at Low Strain Rates", *Composites Part B: Engineering*, 80, pp.116–125.

Yazdizadeh, Z., (2014). "Use of Fiber Brag Gating Sensors in Civil Engineering Applications", MSc. thesis, Ryerson University, Toronto, Canada, 103 pp.

Yi, N-H., Kim, J.H., Han, T.S., Cho, Y.G. and Lee, J.H., (2012). "Blast-resistant Characteristics of Ultra-high Strength Concrete and Reactive Powder Concrete", *Construction and Building Materials*, 28(1), pp.694–707.

Yudenfreund, M., Odler, I. and Brunauer, S., (1972). "Hardened Portland Cement Pastes of Low Porosity", *Cement and Concrete Research*, 2(3), pp.313–330.

Zhang, X. Ruiz, G., Yu, R.C. and Tarifa, M., (2009). "Fracture Behaviour of High-strength Concrete at a Wide Range of Loading Rates", *International Journal of Impact Engineering*, 36(10), pp.1204–1209.

Zineddin, M. and Krauthammer, T., (2007). "Dynamic Response and Behavior of Reinforced Concrete Slabs under Impact Loading", *International Journal of Impact Engineering*, 34(9), pp.1517–1534.